Conception, design and evaluation of a self-pressurizing propulsion storage module for a PocketQube-class satellite using compliant mechanisms

E. Chatzimanolis

Technische Universiteit Delft

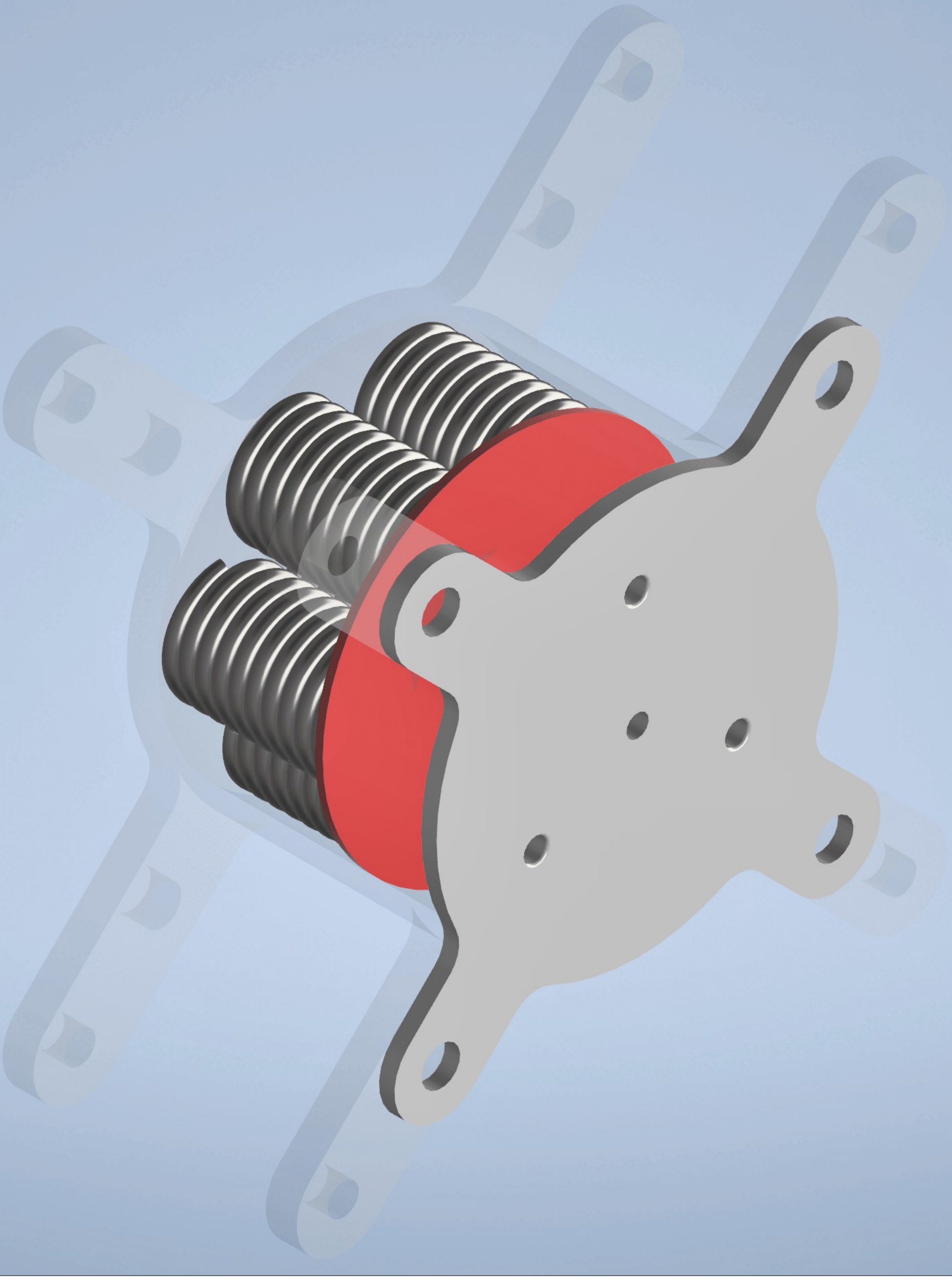

Delft University of Technology

Challenge the future

Conception, design and evaluation of a self-pressurizing propulsion storage module for a PocketQube-class satellite using compliant mechanisms

by

E. Chatzimanolis

in partial fulfillment of the requirements for the degree of

Master of Science
in Aerospace Engineering

at the Delft University of Technology,
to be defended publicly on Tuesday June 2, 2020 at 12:00 PM.

Student number:	4499980	
Project duration:	October 18, 2017 – June 2, 2020	
Supervisor:	Dr. A. Cervone	
Thesis committee:	Dr. A. Cervone,	TU Delft - LR-SSE (Chair)
	Dr. A. Menicucci,	TU Delft - LR-SSE
	Prof. Dr. Ir. J. L. Herder,	TU Delft - 3mE-PME

Preface

The last five years were marked by an intensive effort to earn the Master's Degree of Science in the field of Aerospace Engineering, the culmination of which is expressed in this thesis. Brimming with technical challenges, this work has spurred my growth both as a mechanical engineer, recollecting past experiences and knowledge, and an aerospace engineer using a newly acquired skillset to provide a candidate solution to a relatively new problem in the field of microsatellite propulsion, propellant storage and management. Undertaking a thesis project is not limited to sharpening technical skills, but has a strong impact on a more personal level, especially in my case with this two-year long project. The perseverance and dedication to bringing one's own goal to fruition, the curiosity and passion one cultivates whilst exploring ideas and literature, and above all, the maturity to reflect and react on unforeseen circumstances have been refined to an extent that will accompany my professional and personal life.

I am credited as the sole author for this study. This could not be further from the truth, as my accomplishments are the result of the people who led me this far. I would like to express my profound gratitude to Dr. Cervone, a supervisor with unwavering belief in my abilities and inexhaustible patience, for entrusting me this work and providing his guidance and vast knowledge whenever asked and whatever asked. I would also like to express my appreciation towards the assessment committee members, who showed interest in this endeavor of mine and were willing to share their opinion on its outcome.

I would be ungrateful if I did not mention the friends I have made in this long academic journey, be it in the university or in the grounds of TU Delft. The list would exceed this preface, but I would like for each and everyone to know that the thoughts, feelings and experiences we have shared are imprinted forever in the person I have become, and for that I am truly thankful.

Unarguably, though, the most important people to which I owe not only this work, but my entire life, are my parents. Not enough words can be used to describe the love and support that overcomes any hardship for the sake of raising a child, and a man.

E. Chatzimanolis
Delft, June 2020

In memory of
my grandmother (1936-2018)

Abstract

The advent of miniaturized satellites has sparked an interest in effective methods of exploiting their capabilities. Potential has been found in propulsion-enabled units, and TU Delft is at the forefront of researching and developing suitable propulsion modules for thrust generation or attitude control of small satellites classified as *Cubesats* and *Pocketqubes* for the purpose of technology demonstration, presenting an open platform for students to provide their ideas.

Acknowledging the challenges in power budgeting and distribution, the current thesis presents the conception, design and numerical evaluation of a passive, self-pressurized propellant storage system for use with the in-house microthrusters. Target components for which the storage must be suitable are the *Vaporizing Liquid Microthruster (VLM)* and the *INKX0511400AA5 VHS Solenoid Lee Valve*, an off-the-shelf component already at the disposal of the faculty. Starting from the notion of passive pressurization, an extensive review of literature is used to decide on exploring the idea of compliant mechanisms as a pressurizing method. The scientific output of this work aims to extract productive conclusions on the design and performance level achievable by this concept and open a new design avenue for propellant storage modules.

Expanding upon the definition of compliant mechanisms, a considerable amount of design concepts were evaluated under the premise of a two-stage trade-off strategy, aiming to balance creativity and practicality. Proclamation of the explored pressurizing mechanism is followed by individual trade-off procedures for material, shape and configuration of the entire module, leading to a complete preliminary design concept to be evaluated.

Traditional and unconventional analytic models are implemented to materialize the design concept, measuring its static and dynamic response in both idle and thrust conditions. They delve into the fields of structural and fluid dynamics and are validated against more advanced and accurate Finite Element (FE) and Computational Fluid Dynamics (CFD) models. Both outputs are compared with the mission, system and subsystem requirements to fully assess the performance levels obtained.

Regulated for pressure drops of $500\ Pa$ and $50\ Pa$ from tank to valve, the former is capable of concluding a self-actuated expulsion within $25\ ms$ in both cases, failing to achieve target values for thrust duration. The conservative design approach has led to a $27.4\ gr$ wet tank mass, with a $2.9\ gr$ propellant capacity. As a first implementation of compliance-based pressurization in propellant storage, the results highlight its viability and the field should be further explored.

Table Of Contents

List of Tables

List of Figures

List of Symbols

Latin Letters

A	Cross-section Area
b	Width
C_d	Discharge coefficient
c	Damping Constant
D	Diameter
d	Diameter (Small)
E	Young’s Modulus
F	Force
G	Shear Modulus
GA	Geometrical Advantage
g_0	Grav. Acceleration
h	Thickness/Height
I	Moment of Inertia
K_B	Bergstrasser corr. factor
K_W	Wahl corr. factor
k	Stiffness
L	Length
l	Length (Small)
M	Bending Moment
MA	Mechanical Advantage
m	Mass
N_e	Element Count
N_n	Node Count
P	Pressure
p	Pitch
Q	Element Quality
q	Force per unit length
R	Radius
T	Torque
t	Time
u	Fluid velocity
V	Volume
v	Spacecraft velocity
w	Normalized Displacement

Latin letters (Ch. 1)

c_P	Isobaric sp. heat
c_V	Isochoric sp. heat
e	Sp. internal energy
f	Fanning factor
H	Altitude
I	Electric current
I_{sp}	Sp. impulse
Ma	Mach number
M_r	Molecular weight
n	Gas number density
Q	Volumetric flowrate
q	Heat flowrate
R	Electric resistance
r	Radius
Re	Reynolds number
T	Temperature

v'	Thermal velocity

Greek Letters

α	Radius factor
δ	Displacement/Deformation
$\Delta()$	Difference in ()
ϵ	Energy
η	Energy Efficiency
ν	Poisson's Ratio
ρ	Material Density
σ	Axial Stress
τ	Shear Stress

Greek letters (Ch. 1)

α_{T}	Thermal acc. coefficient
α_{V}	Momentum acc. coefficient
δ	Mean mol. spacing
ϵ	Emissivity
Γ	Vanderkerckhove function
γ	Sp. heat ratio
γ_s	Strain rate limit
$\bar{\mathrm{I}}$	Identity tensor
κ	Thermal conductivity
λ	Mean free path
μ	Dynamic viscosity
Kn	Knudsen number
ν	Kinematic viscosity
Φ_s	Sphericity factor
$\bar{\tau}$	Shear stress tensor

Constants

GM	Grav. coefficient
$\mathbb{K}$	Boltzmann constant
$\mathbb{R}$	Universal gas constant
σ	Stefan-Boltzmann constant

1

Introduction

The beginning of the twenty-first century has been marked by a new philosophy in satellite development, shifting the interest from large, complex and expensive singular spacecrafts to small, simple and affordable entities. Part of this shift is related to miniaturized propulsion modules that unlock many capabilities for a satellite. Be it a stand-alone unit or belonging in a group of satellites, the vehicle needs to perform various orbit and attitude maneuvers to enhance the mission capabilities, such as improving pointing stability in monitoring missions, or engaging in relative orbit maneuvers for render-vouz or docking missions. An important application aiming to the future of earth observation missions are the *Distributed Satellite Systems*, in which multiple satellites operate in unison to perform the same (or more) tasks as their larger counterparts. The usefulness of propulsion can for example be seen in moving certain units to another orbit to improve the constellation's coverage. At present, propulsion-enabled nano- and pico-satellites are extremely limited, emphasizing the need for development of suitable modules. In response to this need, the *Delfi-PQ* satellite acts as a technology demonstrator for propulsion-enabled, PocketQube-class satellites. Taking inspiration from the idea of small-scale propulsion systems, this project will attempt to reach the following objective:

> **Generation of a propulsion design candidate for a PocketQube-class satellite such as the *Delfi-PQ*, using in-house thruster technologies.**

In order to build up a complete and thorough answer compliant with said objective, several sub-objectives are used to cover all the aspects of the research question.

1. *Mission characteristics*: Contrary to well-known frameworks and standards that apply down to Cubesat-level satellites, there is a lack of definitive standards for the Pocketqubes. As a result, a preliminary guideline for propulsion must be defined. Hence, the first sub-question can be formed as: *What are the design constraints inherent to such a small scale satellite regarding propulsion? What are the main requirements to be met in the Delfi-PQ mission?*
2. *Fluid flow*: The down-scaling of propulsion modules gives rise to fluid flow phenomena that are otherwise not accounted for in larger scale thrusters. A well-defined theoretical

background is required for enabling subsequent description of the thruster technologies employed and their parameters. It is then possible to ask: *How can fluid flow be accurately described? How does it vary in different components of the module?*

3. *Thrusters*: To date, the university has been actively involved with the development of two types of micro-thrusters, namely the *Vaporizing Liquid Microthruster (VLM)* and the *Free Molecule Micro-Resistojet (FMMR)*. The two concepts are of similar 'age', but are significantly different from one another, thus requiring investigation on their capabilities, limitations and evolution over time. Important questions to be tackled are the following: *What analytic and numerical models accurately describe each thruster? What is the development status of each thruster?*

4. *Module design:* To properly place the thesis work in the research framework, a conceptual design candidate must be generated, making use of all knowledge acquired. One can reinstate the argument as: *Based on all gathered information, what is the best configuration for a propulsion module for Delfi-PQ?*

1.1. Literature Review

The introductory part as well as the current section is an excerpt from the companion literature review (see [28]). A tentative answer to each of the aforementioned research questions is given by gathering information existing samples of micro-propulsion modules, while simultaneously learning the fundamentals of microfluidics and gathering information on the two in-house thruster models, namely the Vaporizing Liquid Micro-thruster (VLM) and the Free Molecule Micro-Resistojet (FMMR). Mission analysis is aimed at deriving a complete set of system requirements once the design candidate is set, whereas a brief study on the feed and storage systems is conducted to complete the picture. From there, a trade-off analysis gives rise to the conceptual design that will be tackled in the remainder of the thesis.

1.1.1. Propulsion System Requirements and Constraints

PocketQube Description

The last two decades have been marked by efforts in satellite miniaturization down to what is known as *pico-* class satellites, represented by vehicles with a mass lower than $1\ kg$. The ultimate goal is the drastic reduction of costs, development times and the simultaneous increase in mission generation by introducing COTS technology and exploiting satellite network capabilities. To date, these efforts are culminated in *Cubesats*, satellites comprised of fundamental units sized at a $10\ cm$ cube and arranged in different forms, but further miniaturization opportunities are being considered. One promising candidate is found in the so-called *PocketQubes*. Originally proposed by [35] in 2009, they are cubical satellites in the femto-/pico- class range, having a linear dimension of $5\ cm$. Spec-wise, a PocketQube is equivalent to 12.5% of a Cubesat volume and approximately 20% of its mass, while the internal architecture follows the same principle of its progenitor. A serious question has been raised during the PocketQube Workshop [98], in that a universal architecture standard may not be applicable to all types of missions and relevant satellites, mostly on the electrical interfacing department. Despite that, details and specifications on dimensions of the first proposed 'standard' are given in Figures 1.1 and 1.2.

This architecture is more advantageous over alternatives at this scale, the reason being the modular unit format that enables flexible combinations of components and subsystems

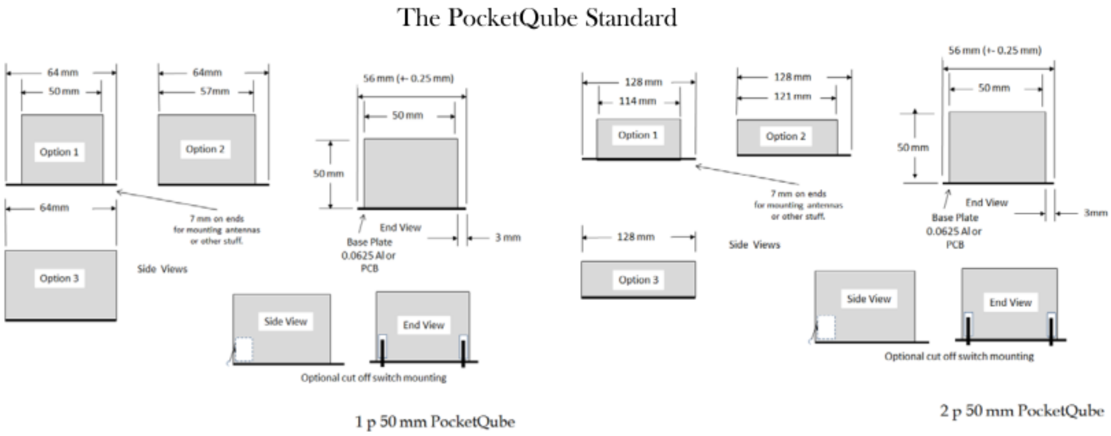

Figure 1.1: The *Pocketqube* standard external dimensions (source: [35])

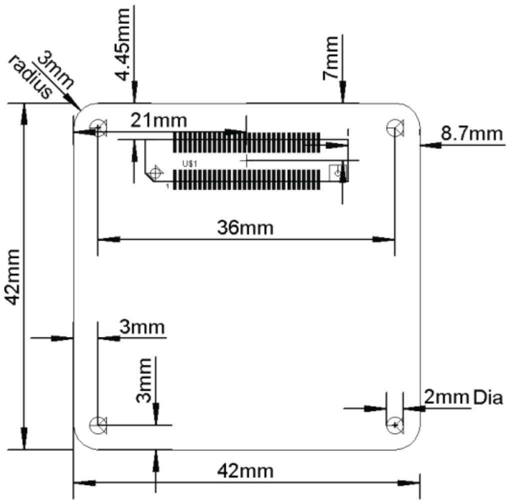

Figure 1.2: The internal PCB dimensions according to the PQ60 standard (source: [38])

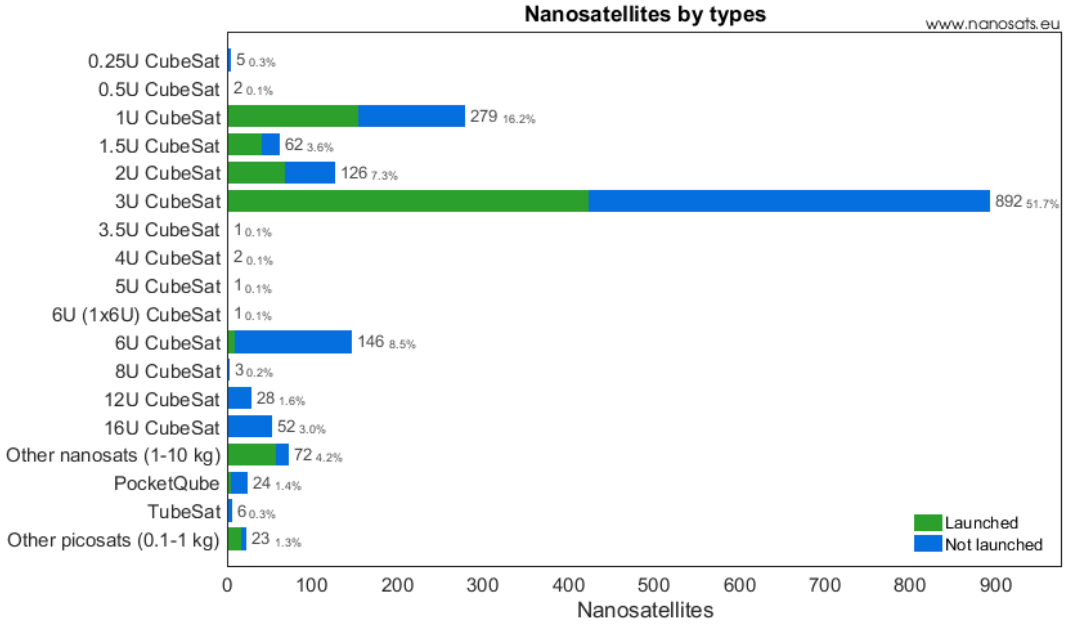

Figure 1.3: Statistical analysis of launched nano- & pico-satellites (source: [63])

in order to meet *Distributed Satellite Systems (DSS)* mission requirements. For instance, missions that are based on satellite formations (swarms, constellations etc.) need high redundancy levels to preserve the functionality that the mission was designed for, even if one of more units are lost due to failures. This obviously could not be done with large satellites, but even Cubesats have not been able to fill this gap. The author believes that Pocketqubes, being so small, easy to assemble and consequently easily replaceable, are far more suitable to multi-satellite operations (such as Earth Observation) than Cubesats and above. Just by sheer numbers, for a single Cubesat the equivalent of 6-8 Pocketqubes can be employed at a lower cost and complexity. At the same time, a strong preference towards multi-unit Cubesats (see Fig. 1.3) indicates that a similar trend would be widely-accepted by the space community.

In light of this trend, the *Delfi-PQ* project was conceived. Developed by the chair of Space Engineering, the *Delfi-PQ* is a 3-unit Pocketqube satellite aiming to display a reliable core bus platform and flight-proven subsystems [2]. The project is focused on showcasing the promising capabilities of the Pocketqube format, which in the first stage is reflected in supporting a scientific payload or an advanced subsystem. Out of the available options, this study is directed towards a modular propulsion subsystem, generated by primarily in-bred thruster technologies. The benefits from such a small propulsion module allow for minute and controlled orbit and attitude maneuvers.

Unfortunately, among the very limited number of Pocketqubes successfully flown, only one is known to be equipped with a propulsion subsystem, in the form of a μPPT. Simultaneously, the work of [70] emphasized the lack of detailed literature on propulsion progress for Cubesats, either due to publicly restricted documentation or the low number of flight heritage components. Therefore, data extraction from reference missions was discarded, generating the need for a tailor-made set of requirements.

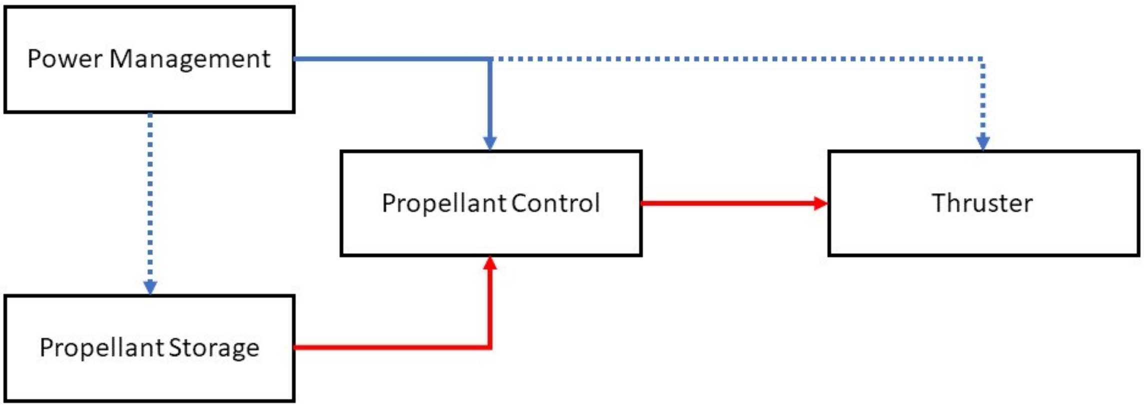

Figure 1.4: Typical configuration of a propulsion system. The dashed arrows indicate optional power flow.

System requirements

On a system level, two are the driving requirements for a propulsion module: it shall fit within the Pocketqube and it shall display thrust capabilities. Both are self-explanatory but vague in terms of technical, measurable requirements. The former can be interpreted in two ways: first, being a modular design, it is possible to think of the propulsion module as a single-unit (1p) component that can be combined with other modules to form a Pocketqube. Second, the more classical, mission-dependent approach drives the module sizing, with most probable values (including propellant storage) being between 0.5p and 1.5p. As for the latter, the technology demonstration purpose was clarified, thus no strict Δv has been defined. However, some guidelines from [27] can be used about the thrust. While referring to a Cubesat-related propulsion system, a thrust range of $0.5 - 9.5\ mN$ seems a reasonable requirement for a propulsion module that enables swift yet accurate orbital maneuver, especially when compared to conventional alternatives. Still, mass and power budgets are fundamental to the design process. Estimated values from the SSE Micropropulsion Group have been taken as reference and are summarized in Table 1.1.

Table 1.1: Mass, size and power budgets for the propulsion module

Type	Value	Units
Wet Mass	75	g
Peak Power	4500	mW
Peak Power (+30%)	5850	mW
Idle Power (+30%)	65	mW
Length	40	mm
Cross-Section	42 x 42	mm

The power requirements mentioned can be used for estimating the energy required from the electrical subsystem for an orbit. A thrust duty cycle of 1% was hypothesized, while the remaining 99% is allocated to the idle state. The total required energy - including the contingency margin - for the propulsion system can be calculated by partial multiplication of the states' power consumption with the respective time in each state and addition. It follows that for an orbital period of $1.5\ hrs = 5400\ s$, provided by the Micropropulsion Group:

$$Total\ energy = (0.01 \cdot 5850 + 0.99 \cdot 65) \cdot 1.5 = (58.5 + 64.35) \cdot 1.5 \simeq 184.3\ [mWh]$$

Design Constraints

While the pocket-sized format is attractive for several mission types and opportunities, the design of such a propulsion module is challenging. Even if the aforementioned requirements are feasible with current technology, the concept itself is subject to design constraints that require mindful decisions for the individual parts. The following constraints have been identified from a first approach:

- *Downscaling*: Downscaling a propulsion system is not limited to physically miniaturizing already available parts, as the effects on propellant flow might give rise to effects otherwise neglected on a larger system (e.g thick boundary layers). Hence, just downscaling an existing system may require a complete redesign of some components, specifically adapted to the micro-fluidic scale.

- *Component Availability*: Aside from performance metrics and operational stability, an important factor in a module is the availability of flight-ready components. The findings of [70] regarding Cubesat propulsion showed that proprietary modules are being developed, so a scarcity in COTS parts is safely assumed, further restricting design options.

- *Integration*: Following from above, it can be easily seen that the most viable option is found in custom-made parts. With the exception of valves - they fall within the COTS category - and probably connections, the module's constituents are tailor-made to mission requirements. Consequently, the integration process mandates additional constraints in terms of positioning and routing, unless clever design techniques are implemented. However, integration also refers to the harmonious function of the components, and for a propulsion system, the thruster is prioritized. As such, all other parts are selected/designed to meet the thruster requirements on propellant, pressure and power, thus creating part dependencies that cannot be satisfied unless a thruster type is chosen.

1.1.2. Fluid Flow Overview

The evaluation of thruster alternatives is done in a range of analytic and numerical models, as well as in experimental results. In order to keep up with knowledge required for each specific system and mentioned in separate chapters, a brief analysis on the expected fluid flows is given in this chapter. The outcome will bridge the gap between analytic and numerical models from a general fluid dynamics perspective.

Starting from the reasoning explained in [86], fluid transport devices are described by the *continuum hypothesis*, which is valid for liquids and most gases at atmospheric pressures. However, this hypothesis is questionable under vacuum environment conditions, especially at the thruster exit section, and the micro-fluidic scale. In order to verify or disprove the continuum assumption, a set of parameters must be used as a reference to flow characterization.

Gas Flows

Regardless of system employed, gaseous propellants are expected at the exit, due to more desirable thermodynamic properties. In particular, the thermal energy content, expressed by the gas temperature, acquired during the heating process is converted to kinetic energy and hence high velocity during the expulsion. To this, the lower heat capacity of gases compared to liquids enables greatly higher thrust outputs for a specific amount of power provided. Consisting molecules that rarely collide with each other, they are well described by the *Kinetic Gas Theory*:

$$P = n\mathbb{K}T$$

where n is the number density of the gas, $\mathbb{K}$ is the Boltzmann constant and T is the gas temperature. The cube root of the number density is called the *mean molecular spacing* δ, quantity corresponding to the average distance between gas molecules. When divided by the molecule diameter d, a density ratio is formed that defines whether a gas is dilute of dense. This ratio is important for the dimensionless parameters that follow.

Speaking of parameters, the most useful aside from classical dimensionless parameters is the *mean free path* λ, the distance that is traveled by molecules before any collision. Mathematically, it is expressed below:

$$\lambda = \frac{1}{\sqrt{2}\pi d^2 n} \tag{1.1.1}$$

Aside from, λ, a characteristic length scale L_{sc} is needed. This value is either taken from geometrical parameters present in the device under study (e.g. nozzle diameter), or from the working medium itself (such as the molecular diameter). On an approximative scale, [86] has discerned the different length scale limits depending on point and transport fluid quantities, using only the definition of the mass density within a sampling volume. Yet when involved with complex geometries, this length scale is not applicable, thus employing a characteristic dimension. From the aforementioned, the most critical parameter in defining the flow regime within a flow path is derived, the *Knudsen* number. This ratio is expressed as follows:

$$Kn = \frac{\lambda}{L_{sc}} \tag{1.1.2}$$

It is possible to relate the Knudsen number to more manageable parameters like the *Mach* and *Reynolds* numbers. From [86], the kinematic viscosity is defined as:

$$\nu = \frac{\lambda\bar{c}}{2} = \frac{\lambda\sqrt{3\mathbb{K}T}}{2} \tag{1.1.3}$$

The Mach and Reynolds numbers can be inter-related by:

$$Ma = \frac{u}{\sqrt{\gamma\frac{\mathbb{R}}{M_r}T}}, \quad Re = \frac{uL_{sc}}{\nu} \rightarrow \frac{\nu}{L_{sc}} = \frac{Ma}{Re}\sqrt{\gamma\frac{\mathbb{R}}{M_r}T} \tag{1.1.4}$$

With some re-formatting, Equation 1.1.2 obtains its new form:

$$Kn = \sqrt{\frac{4\gamma\frac{\mathbb{R}}{M_r}}{3\mathbb{K}}}\frac{Ma}{Re} \tag{1.1.5}$$

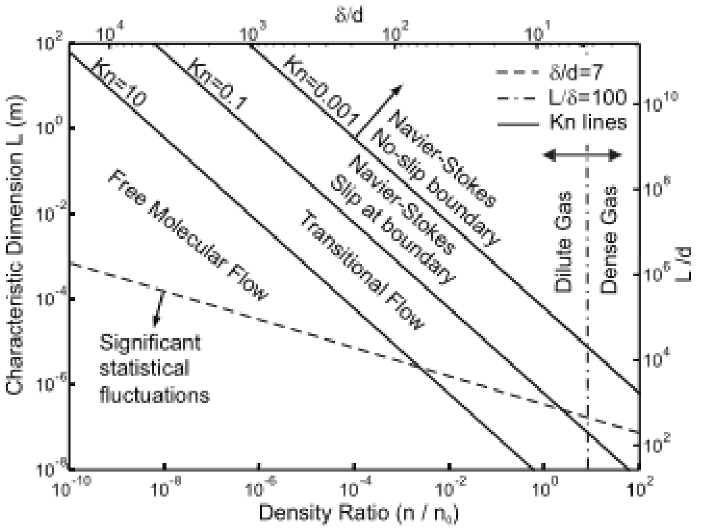

Figure 1.5: Flow regimes based on Knudsen number (source: [86])

where Ma is the local Mach number and Re is the local Reynolds number. The effect of the *Knudsen* number is reflected on the flow consideration. When $Kn > 10$, the flow is assumed to be comprised of individual molecules that virtually do not interact, or are unaffected by, neighboring molecules when in collision with surfaces. A transitional flow is detected for $0.25 < Kn < 10$, where collisions start to affect the flow field, and for $0.001 < Kn < 0.25$, the slip flow regime applies, where a slip velocity and temperature jump are noted between fluid and adjacent surface. Finally, a continuum flow assumption is valid when $Kn < 0.001$. Conveniently, [86] provides a detailed graphical presentation of aforementioned regimes, as a function of the dimensionless parameter characterizing gas flows. Much information can be extracted from the figure using a logical reasoning and a parameter correlation process.

- $Kn - P$: Using both forms of the Knudsen number's definition, the strong dependence on pressure (via the number density and velocity formulations) is noted, and thus is progressively increased when moving from the storage tank to the thruster exit, in total vacuum. As a result, any analytic or numerical models will only be accurate when applied to the correct flow regime.

- $Kn - Ma, Re$: Again, starting from the definition, a high Kn can be achieved by either an increase in Mach numbers (usually in nozzle expansion processes) and/or a reduction in Reynolds numbers (common in laminar flows). Conversely, an ever increasing Kn translates to analogous changes of both Ma and Re numbers, which in turn translate to re-consideration of laminar and turbulent flow modeling. In a similar fashion, boundary conditions and compressibility effects can be discerned.

According to the theory developed so far, a continuous fluid is described by well-known transport equations. Especially in the case of a compressible Newtonian fluid, that is described by the density ρ and the velocity vector $\mathbf{u}$, the *Navier-Stokes* equations in [65] hold:

$$\begin{aligned}
&\textit{Continuity Equation}: \frac{\partial \rho}{\partial t} + \nabla \cdot (\rho \mathbf{u}) = 0 \\
&\textit{Momentum Balance}: \frac{\partial}{\partial t}(\rho \mathbf{u}) + \nabla \cdot (\rho \mathbf{u}\mathbf{u}) = -\nabla P + \nabla \cdot \overline{\tau} + \rho g \\
&\textit{Thermal Energy}: \frac{\partial}{\partial t}(\rho E) + \nabla \cdot (\mathbf{u}(\rho E + P)) = -\nabla \cdot (\kappa \nabla T + (\overline{\tau} \cdot \mathbf{u}))
\end{aligned} \tag{1.1.6}$$

To the aforementioned set, the total energy E and shear stress tensor $\overline{\tau}$ are defined respectively, with e the specific internal energy and $\overline{I}$ the identity tensor.

$$\begin{aligned}
E &= e + 0.5|\mathbf{u}|^2 \\
\overline{\tau} &= \mu \left[(\nabla \mathbf{u} + \nabla \mathbf{u}^T) - \frac{2}{3}(\nabla \mathbf{u})\overline{I} \right]
\end{aligned}$$

Liquid Flows

Contrary to gases, liquids consisting in molecules that exist in a state of continual collision [86], which renders flow regime characterization impossible with the parameters described up to this point. For instance, no mean free path can be defined and hence no Knudsen numbers. What can be used though is the *strain rate limit* equation showing that Newtonian liquids can 'break' when sheared beyond a certain point, defined in the following equation:

$$\dot{\gamma}_s = \frac{\partial u}{\partial y} \geq \frac{2}{\tau}$$

With Newtonian, the fluids with viscous stresses $\overline{\tau}$ linearly proportional to the strain rate $\dot{\gamma}_s$ are intended, according to τ is a time scale associated with inter-molecular forces, so the inverse value is a collision frequency. It is understood by the author that, a too high velocity gradient separates fluid molecules by overcoming the inter-molecular forces that induce the collisions described by this frequency above. As a result, the viscosity μ defining a fluid is changed, and for a Newtonian fluid, this means a non-constant viscosity, thus breaking the assumption.

Piping and Other Components

The micro-fluidic devices assessed in this study obviously include some form of piping that transfers propellant from storage to vacuum. The pressure drops inherent to this event can be simply described by flow field equations. Assuming an isothermal, incompressible, isotropic, Newtonian fluid with an arbitrary cross section and an infinitely long channel (fully developed flow), the following expressions hold:

$$0 = -\frac{\partial P}{\partial x} + \mu \left(\frac{\partial^2 u_x}{\partial y^2} + \frac{\partial^2 u_x}{\partial z^2} \right) \tag{1.1.7}$$

$$0 = \frac{\partial P}{\partial y} = \frac{\partial P}{\partial z} \tag{1.1.8}$$

Transformation into polar coordinates (circular cross-section) and double integration with no-slip conditions results in the expressions for fluid velocity u_x and volumetric flow rate Q, with r_0 being the maximum radial distance from the walls.

$$u_x = -\frac{dP}{dx}\frac{(r_0^2 - r^2)}{4\mu} \rightarrow Q = \frac{\pi r_0^4}{8\mu}\frac{dP}{dx} \tag{1.1.9}$$

Then, Equation 1.1.9 can be transformed using a finite tube of dimensions L and D, giving the useful form of Equation 1.1.10, where $\overline{u} = Q/A$ os the average fluid velocity and $f = 64/Re$ the *Fanning* friction factor.

$$\Delta P = \frac{8\mu Q L}{\pi r_0^4} = f Re \overline{u}\frac{\mu L}{2D^2} = \frac{1}{2}\rho f \overline{u}^2 \left(\frac{L}{D}\right) \tag{1.1.10}$$

A particularly useful conclusion is the correlation of pressure drop with length-to-diameter ratio, Reynolds number and the propellant itself. In reality, this is a direct result of altering the friction factor, which dependent on aforementioned parameters. What can be briefly said is that the dimensionless number $\zeta = f(L/D)$ is defined as the *loss factor*, a parameter extremely useful in estimating pressure drops in components other than piping, such as corners and valves. Various sources provide tabulated and graphical expressions to estimate both the friction and the loss factor per component, but they will be revisited during the thesis development with selected parts.

1.1.3. Vaporizing Liquid Microthruster

The first thruster alternative evaluated in the scope of the study is the so-called *Vaporizing Liquid Microthruster (VLM)*, originally conceived by [82]. The main principle is straightforward: a liquid propellant is fed into a heated chamber and vaporized. The resulting gas is then ejected through a nozzle to generate thrust. The thruster is similar to both nozzle expansion systems and resistojets,in that vapor is expelled through a nozzle just like a rocket engine, but a simple heat transfer mechanism - typical to resistojets - is employed for the vaporization instead of the classical combustion. A typical setup is shown in Fig. 1.6. The VLM has been reported to be advantageous in more than one aspects:

- *Leak rate*: Since the propellant is stored in liquid form, the propellant viscosity becomes significantly higher and as a result the total leak rate from the tank is drastically reduced compared to a gas-related thruster. In turn, propellant volume margins are reduced allowing for smaller packages. The authors of [43] argue that the VLM might suffer by a small increase in mass, due to propellant storage. This seems implausible for a system with low (if not zero) leak rates that reduces propellant mass margins, not to mention that the higher density of liquids does instead decrease the tank size and mass.

- *Reliability*: The thruster operates through a very simple heat transfer mechanism instead of complex combustion processes found in most rocket engines. In practical terms this means that moving parts and associated mechanical failures are limited to valves, vastly improving the system's operational reliability. Furthermore, it will be shown that material selection and thruster designs have also improved electrical and thermal reliability, ensuring long-lasting, stable functionality.

- *Flexibility*: The envisioned blow-down mode of operation [49] and the dependence of thrust on power input allow for continuously variable levels of Δv and therefore fine-tuning for different maneuvers. Moreover, a constant-pressure mode of operation is also tunable, by means of burn duration, pulsed heating etc. The result is a limitless amount of combinations to get the optimal Δv per maneuver.

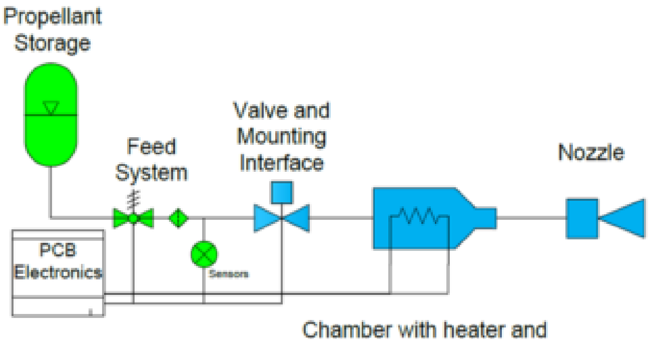

Figure 1.6: Schematic of a VLM system, with feed components in *green* and thruster components in *blue* (source: [27])

In this chapter, analytic and numerical models describing the physics of a VLM thruster, whereas the most notable variants of the latter are presented in terms of design and performance as a means to identify possible design parameters for the other components.

Model Description

The VLM thruster is essentially divided in two fundamental components: the heated chamber, where the vaporization occurs, and the nozzle, responsible for the gas expulsion. In modeling the vaporization process, an energy balance system is formulated for steady-state conditions, as presented in the work of [79]:

$$\frac{I^2R - q_w}{\dot{m}} = \underbrace{\frac{m}{\rho V_c}\left[c_{_{P,L}}\Delta T + q_{_{LV}}\right]}_{heat\ \&\ vaporize} + \underbrace{c_{_{V,L}}(T_c - T_c^{'})}_{overheat} + \underbrace{\frac{1}{\rho V_c} q_0}_{residual fluid} \qquad \left[\frac{J}{kg}\right]$$

In the equation above, I^2R is the power input converted to heat provided, q_w the losses through chamber walls, V_c the chamber volume, $c_{_{P,L}}$ the specific heat, $\Delta T = T_c - T_i$ the temperature difference between chamber T_c and inlet T_i, $q_{_{LV}}$ the latent heat, $T_c^{'}$ the chamber temperature at full vaporization, C_v the isochoric gas specific heat and q_0 the heat required for any residual propellant in the chamber. Judging from the formulation, it is implied even for an open system, the overheat occurs within a fixed amount of volume, thus increasing the gas pressure. When studied separately, this may hold true by considering an almost stationary gas that is being heated and later on expanded. But having an open system contradicts this assumption, as the total flow from the inlet to the nozzle is uninterrupted, implying that the isobaric heat capacity may be more adequate. Perhaps, the isochoric heat capacity can be applied in transient conditions, where the chamber is still building up heat and gas, slowly increasing the pressure until the steady state.

Under ideal conditions and a certain power input level, complete vaporization occurs at the temperature $T_c = T_c^{'}$. In this limit case, no residual propellant exists ($q_0 = 0$), and $\frac{m}{\rho V_c} = 1$, leading to the reduced form of the energy model:

$$\frac{I^2R - Q_w}{\dot{m}} = c_{_{P,L}}(T_c^{'} - T_i) + q_{_{LV}} \quad \left[\frac{J}{kg}\right] \tag{1.1.11}$$

While according to [79] the effects of all assumptions on the model accuracy are non-trivial, the principles are still valid and straightforward enough to derive the chamber temperature and in turn the chamber pressure P_c required for thrust estimation.

Regarding the nozzle section, the *Ideal Rocket Theory* is used as a 1-D approximation of an isentropic flow to obtain a first estimate of bulk performance. Note that for this derivation it is assumed that the fluid flowing through the nozzle is fully evaporated, in other words in gaseous state, and can be described using the ideal gas law [49]. Starting from an energy balance that neglects storage and potential energy terms, the next equation applies:

$$c_{_P} T + 0.5\rho u^2 = c_{_P} T_c + \cancelto{0}{0.5\rho u_c^2} = const. \rightarrow u = \sqrt{2c_{_P}(T_c - T)} \tag{1.1.12}$$

in which $c_{_P}$ is the isobaric heat capacity. Then, assuming an isentropic flow, the *Poisson* expressions apply:

$$\left(\frac{T}{T_c}\right) = \left(\frac{P}{P_c}\right)^{\frac{\gamma-1}{\gamma}} = \left(\frac{\rho}{\rho_c}\right)^{\gamma-1} \tag{1.1.13}$$

with $\gamma = c_{_P}/c_{_V}$. Combination of the above equations allows for extraction of the exhaust velocity u_e:

$$u_e = \sqrt{2\frac{\gamma}{\gamma-1}\frac{\mathbb{R}}{M_r} \cdot T_c \left[1 - \left(\frac{P_e}{P_c}\right)^{\frac{\gamma-1}{\gamma}}\right]} \tag{1.1.14}$$

where R_u is the universal gas constant, M_r the propellant molecular weight and T_c, P_c the chamber conditions calculated in the heater model. In addition, it is useful to make use of the pressure-area relation for a *de-Laval* nozzle:

$$\frac{A_e}{A_t} = \Gamma \cdot \left\{2\frac{\gamma}{\gamma-1}\left(\frac{P_e}{P_c}\right)^{\frac{2}{\gamma}}\left[1 - \left(\frac{P_e}{P_c}\right)^{\frac{\gamma-1}{\gamma}}\right]\right\}^{-0.5} \tag{1.1.15}$$

Here, the subscript t corresponds to the throat section, the fraction $\frac{A_e}{A_t}$ is the nozzle expansion ratio, and Γ is the *Vandenkerckhove function*, given by:

$$\Gamma = \sqrt{\gamma}\left(\frac{2}{\gamma+1}\right)^{\frac{\gamma+1}{2(\gamma-1)}}$$

To the above considerations, a *choked flow* condition is superimposed for optimal performance. For a choked flow in a convergent-divergent nozzle geometry, sonic level velocities can be achieved ($Ma = 1$) and then the gas can be further accelerated to supersonic conditions, without the risk of shock waves and flow instabilities that would disrupt the velocity profile. Note that for Equation 1.1.16, inputs from previous formulas have been calculated.

$$\dot{m} = \frac{\Gamma \cdot P_c \cdot A_t}{\sqrt{\frac{\mathbb{R}}{M_r} \cdot T_c}} \tag{1.1.16}$$

In an attempt to include the effects of boundary layers situated at the nozzle walls, the *discharge coefficient* c_D is introduced (shown in [49]), correcting Equation 1.1.16:

$$\dot{m} = c_D \cdot \frac{\Gamma \cdot p_c \cdot A_t}{\sqrt{\frac{\mathbb{R}}{M_r} \cdot T_c}} \tag{1.1.17}$$

Having found all constituents from Equations 1.1.11, 1.1.14, 1.1.15 and 1.1.17, it is now possible to estimate the thrust levels produced by the VLM through Equation 1.1.18, which defines the thrust as a result of the rate of change of momentum associated with the exit velocity of the propellant flow and the differential pressure at the exit point with respect to the surrounding [79]:

$$F_{_{VLM}} = \dot{m}u_e + (P_e - P_\infty)A_e \tag{1.1.18}$$

The aforementioned derivation relies on a one-dimensional flow assumption, so accuracy errors are expected compared to multi-dimensional phenomena. However, for known propellant, power requirements, chamber thermodynamic conditions and geometrical configuration of the nozzle, thrust can be easily derived. In fact, [79] have worked on an iterative scheme from which thrust is calculated even for non-ideal conditions.

An improvement is again mentioned by [49] after evaluating the velocity and pressure profile results of [64], introducing a parameter called *velocity efficiency* (η_u), that measures the boundary layer effects on average exit velocity. Then, the thrust equation is reformulated:

$$F_{_{VLM}} = \eta_u \dot{m}u_e + (P_e - P_\infty)A_e \tag{1.1.19}$$

Numerical models

Regardless of the time efficiency of one-dimensional approximations, the analytic models presented are based on somewhat arbitrary premises and tend to oversimplify the problem. In order to improve modeling accuracy, a shift to multi-dimensional flows is required, which is more tangible with numerical simulation.

The leading alternative employed by researches and industries for continuum fluid applications is the development of *Computational Fluid Dynamics (CFD)* software. The core principle is that the simulation space is divided into finite-sized, fictitious volumes of fluid represented by the coordinates of the center. All transport equations mentioned in Chapter 1.1.2 are solved within these cells by numerical solvers. Depending on the application, different solvers or techniques can be used to lead the system to convergence and reach a stable solution, but all require a suitable time step (for transient conditions) to maintain numerical stability. Under simple models (e.g. Poiseuille flow), time is not a critical component and is only useful in improving the solver performance. More complex flows such as the VLM chamber that include several fluid phenomena in the same space and time instant (two-phase flows, heating processes, flow redirection etc.) need a very accurate time step in order to grasp the changes within the flow.

In Fig.1.7 the main software elements of a full CFD model are presented. For the scope of this study, only the solver block is interesting to explore, as all other components are standard regardless of the application. Even at this level, the only actual variation found in relevant publications is focused on the models, rather than the solver itself. The most common approach for a VLM chamber seems to be a turbulent model with no-slip wall conditions, under the premise of idealized and unmixable fluids. The latter is applied in the VLM by separating water from water vapor by an impenetrable interface, essentially splitting the fluid domains. Regarding the turbulence consideration, the work of [64] is reported to have used a Turbulent $\kappa - \epsilon$ model, while [61] employed a SST $\kappa - \omega$ model, with the assumption of a fully compressible single-phase flow. The difference in the aforementioned turbulence models is related to a trade-off between speed and accuracy in the flow field estimation in

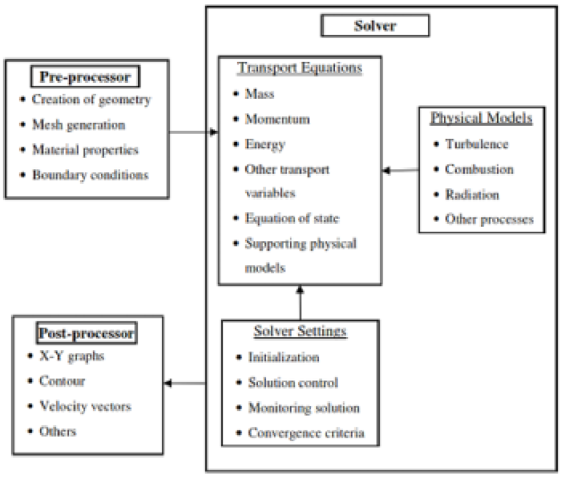

Figure 1.7: Schematic of CFD software architecture (source: [61])

boundary layers. The former is faster but rather unsuitable for boundary layer flows, which according to [61] can amount to 30% of the total flow, whereas the latter is far superior in terms of accuracy but more resource intensive. Prior experience of the author with CFD software showed that current desktop and portable computers are able to keep up with resources needed, so the SST $\kappa - \omega$ model is much more suitable. One caveat in this approach is the fine-tuning of some model parameters with respect to the region of interest (bulk or wall), which may be difficult.

Development Status

Since its conception, the VLM has underwent several changes that are either related to the geometric configuration (mostly shown in Fig. 1.8), the component materials or the manufacturing processes.

Despite the great emphasis on fluid flow phenomena, the thruster in [29] is representative of multi-channel chambers, practice expanded further in [26]. In particular, the notion of incorporating pillars into the chamber was mentioned, similarly to a packed bed formation, as an improvement over microchannels. Such a strategy was intensively applied by the chair of Space Engineering, through various iterations of in-house VLM thrusters [93], in which the concept of modular structuring was introduced. One of the proposed shapes for the internal pillars is shown in Fig. 1.8b, while alternatives have been evaluated in [93].

Visual representations of thrusters found in literature are gathered and depicted in Fig. 1.8. The pictures themselves are unclear regarding the thruster orientation, but it can be speculated that sub-figures 1.8a and 1.8d are in side view, sub-figures 1.8c and 1.8e are in isometric view and sub-figure 1.8f is in top view.

As far as performance metrics are concerned, the authors of [43] have preceded this study in gathering comparative results for many of the works mentioned so far. In Table 1.2, their output is compared to the university's thruster, as it was presented in [98]. The results clearly indicate the high versatility of the model, with the in-house variant displaying superior performance metrics. Sadly, they only represent theoretical predictions, so successive testing may confirm of disprove these values. Nonetheless, the current thruster developed is based on multiple heater sections, which implies a significantly wider range of performance according to the number of sections combined.

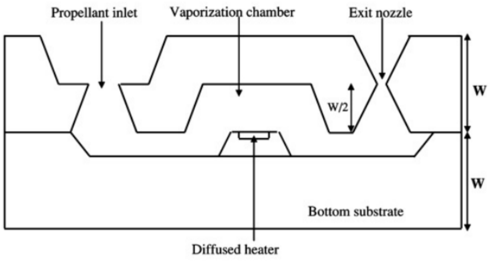

(a) source: [78]

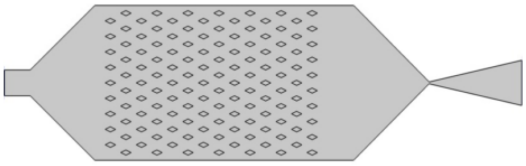

(b) source: [49])

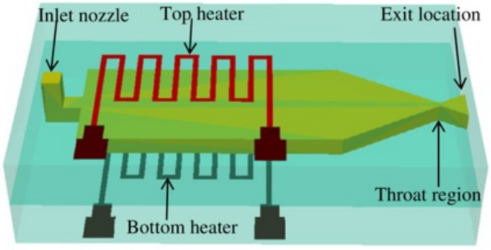

(c) source: [64]

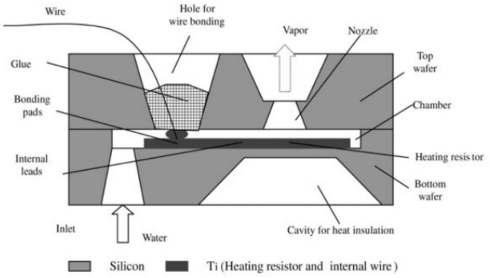

(d) source: [118]

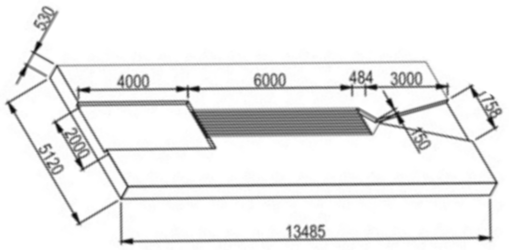

(e) source: [26]

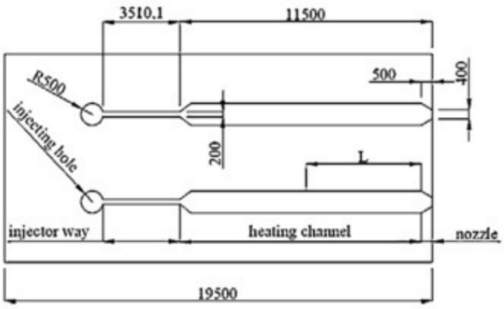

(f) source: [29]

Figure 1.8: Different variants of VLM thrusters

Table 1.2: Performance comparison of various VLM thrusters

Authors	Material	Throat Size (μm)	Propellant.	Mass flow (mg/s)	Power (W)	Temp. (K)	Thrust (mN)	I_{sp} (s)^a
[83]	Silicon	-	Water	90	5	-	0.15 - 0.46	5
[118]	Silicon	-	Water	0.038	30	573	0.0029	76.32
[78]	Silicon	30 x 30	Water	1.16	2.4	-	0.005 - 0.12	75
[29]	Silicon	-	Water	$< 8.\overline{33}$	-	573	0.5 - 3	-
[26]	Silicon	150 x 120	H_2O_2	100 - 500	-	413 - 613	2 - 6.5	105
[64]	Silicon	130 x 100	Water	0.2 - 2.04	3.6	$\simeq$ 470	0.15 - 1.014	105
[57]	LTCC	220 x 220	Water	1	7.1 - 9.2	399 - 421	0.034 - 0.068	6.9
SSE	Silicon	25 (circ.)	Water	1.5 - 3.5	4 - 10	550 - 773	1.7 - 4.2	100

[a] Values from max. thrust divided by max. mass flow

1.1.4. Free Molecule Micro-Resistojet

The second in-house alternative technology considered is the *Free Molecule Micro-Resistojet (FMMR)*, more recently called the *Low Pressure Micro-resistojet (LPM)*. Proposed by [58], the system operates under extremely low pressures and relies on collisional processes. Gaseous propellant from a tank flows into a plenum and then into an electrically heated chip with micro-machined expansion slots. Vibrational energy is transferred from the slots to directly interacting molecules, which after being expelled to the environment at high temperature and speed, generate thrust [69],[77]. A schematic of the resistojet is given in Fig. 1.9:

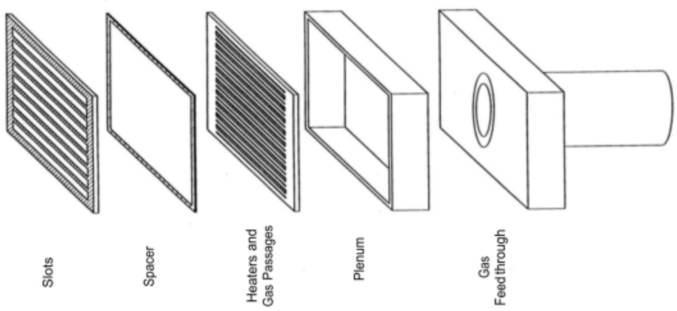

Figure 1.9: Exploded view of a FMMR system (source:[58])

Being largely different from conventional forms of propulsion system, no direct comparison can be made. It is yet possible to note some of the most obvious traits found in a FMMR.

- *Size*: As seen in the figure, the orientation of the chip allows for very small modules that are dependent on storage and control component packaging.
- *Flexibility*: The heating element design allows for great fine-tuning of the system's thrust levels by varying the number, shape and size of the expansion slots, while power and hence temperature modification effects the specific impulse levels, for an immense amount of flexibility with respect to Δv and impulse bit requirements.
- *Reliability*: Operating at almost vacuum conditions, even if gaseous propellant is used, pressure requirements on valves are minimized. Since they are the only moving part of the system, reliability issues are unlikely to occur. Furthermore, the long expansion slots prevent clogging and plugging issues[115].

In this chapter, analytic and numerical models describing the physics of a FMMR thruster, whereas the most notable variants of the latter are presented in terms of design and performance as a means to identify possible design parameters for the other components.

Model Description

Based on the operational principle, thruster performance can be correlated to the mass, momentum or energy flux through the expansion slots [69]. Before setting up the analytic model, several assumptions are required:

1. One-directional flow of molecules. While the individual molecules move at random directions, the bulk propellant is assumed to move from the plenum towards the vacuum

through the expansion slots in a direction perpendicular to the heating element, with no back-flow.

2. Thermodynamic Maxwellian velocity distribution
3. Infinitely thin expansion slot
4. Gas temperature equal to chip temperature

Under the above assumptions, the mass flow is given by the following:

$$\dot{m} = m_p n \frac{\overline{v'}}{4} A_s$$

By n, the number density is defined as the number of particles per unit volume (similar to the mass density), A_s the slot cross-section area, m_p the particle mass and $\overline{v'}$ the averaged thermal velocity:

$$\overline{v'} = \sqrt{\frac{8\mathbb{K}T_0}{\pi m_p}}$$

In reality, the expansion slot has a finite thickness, no matter how small. This thickness affects the number of exiting molecules, so an *accommodation coefficient* (α) is used to determine the fraction of molecules interacting with the walls that ultimately leave the system. In Fig. 1.10, the phenomenon is described, indicating the effect of slot thickness to exiting molecules. Hence, the mass flow equation is modified accordingly:

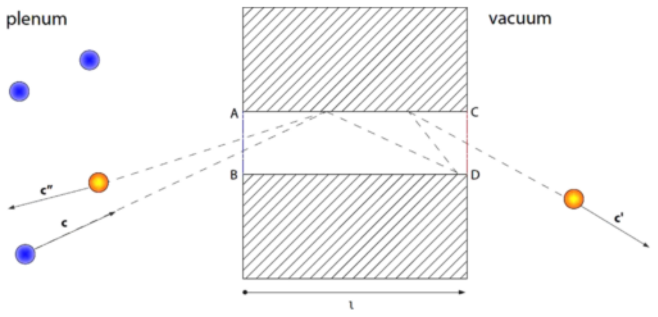

Figure 1.10: Schematic representation of the possible collisions with the expansion slot walls (source:[27])

$$\dot{m} = \alpha m_p n \frac{\overline{v'}}{4} A_s$$

Substitution of the number density [69] gives rise to another expression for the mass flow, based on the plenum pressure:

$$\dot{m} = \alpha m_p \frac{P\overline{v'}}{4\mathbb{K}T} A_s \tag{1.1.20}$$

The average exit velocity is given by an integral form that can be compressed to the equation:

$$u_e = \sqrt{\frac{\pi \mathbb{K} T_w}{2m_p}} \tag{1.1.21}$$

Then, the classical thrust equation is easily calculated and compacted to a form that is solely dependent on thermodynamic conditions and slot configuration:

$$F_{FMMR} = \dot{m} u_e = \frac{\alpha}{2} \frac{\sqrt{T_0 T_w}}{T} p_0 A_s \tag{1.1.22}$$

The 3 different temperatures appearing in the equation represent the stagnation/plenum (T_0), slot wall (T_w) and molecular (T). It should also be noted that the aforementioned mass flow and thrust levels are amplified by the number of expansion slots N_s. Regardless, this is an incomplete form of the thrust equation, according what is described in [27]. A numerical study in [109] concluded that the pressure term vanished above is not negligible and thus should be restored in the equation.

Wall Temperature

So far, this section was focused on the expansion process through which molecules are expelled. Equation 1.1.22 proves the dependence on wall temperature T_w, which requires a separate analysis. Following the approach of [116] for a control volume and applying an energy balance model, Equation 1.1.23 is formulated, where the subscript c stands for 'chip element'.

$$\frac{I^2 R_c - \epsilon\sigma\left(T_c^4 - T_\infty^4\right) A_c}{\Delta V_c} + \kappa \nabla^2 T_c = \rho c_P \frac{\partial T}{\partial t} \tag{1.1.23}$$

The term $I^2 R_c$ corresponds to power input, $\epsilon\sigma\left(T_c^4 - T_\infty^4\right)$ are the radiative losses with ϵ the chip emissivity and σ the Stefan-Boltzmann constant. A_c and ΔV_c are the chip's solid cross-section and volume respectively, while κ is the thermal conductivity. Then, the left hand side represents the power input to the chip via Joule Heating, minus the radiative and conductive losses to the environment. The right hand side is the power stored within the chip, described by the density ρ, isobaric heat capacity C_p and the time-dependent temperature rate $\frac{\partial T}{\partial t}$. The equation displays a transient character, but also reveals some information regarding the effects of radiation on operational properties of the thruster.

Numerical models

The oversimplified theoretical background provided earlier is effective and gives quite the insight on performance parameters, such as the slot configuration that defines both the cross-section area and the accommodation coefficient. Nonetheless the assumptions made at the beginning of this chapter are for the most part questionable. To begin with, a one-dimensional flow would imply a fluid that behaves uniformly. This is not true in a three-dimensional plenum, where molecules scatter in all directions, effectively limiting the amount of initial energetic molecules that get heated and expanded. Moreover, the equality of gas and wall temperatures can be only valid once the system reaches a steady-state condition, in which enough thermal energy stored in back-flowing molecules is released in the plenum, and even then this is not certain. The only assumption that may hold true is the Maxwellian velocity distribution, considering that the molecules will indeed reach a thermodynamic equilibrium. In fact, the analytic model for the expansion slot given above is only able to provide accurate results for basic shapes. Hence, the numerical approach is mandatory.

As in the VLM presented in Chapter 1.1.3, the numerical models have to be selected based on the appropriate flow regime. The original name assigned to the thruster (Free Molecule) gives a straightforward answer as to what regime to use. The most commonly implemented strategy to predict the flow field is the *Direct Simulation Monte Carlo (DSMC)* model. Originally developed by G.A. Bird, the method computes the position and velocity states of discrete particles, each of which represents a predetermined number of molecules in the real flow. As a result, the path (position) and energy content (velocity, temperature) needs not be calculated for every single molecule, but just for a small statistical sample [65], reducing computational effort.

Development Status

The FMMR is still considered a very 'young' thruster, so much that flight heritage is null, and consequently no literature could be found on actual working units. Instead, the development progress is mostly based on experimental units or numerical equivalents that have been published.

A diverse approach proposed by [77], and then implemented on the current version of the in-house FMMR system, was the use of ice as propellant. As shown in Table 1.3, this was the first thruster of this category exploring the possibility of propellant storage in solid form. In the concept proposed, a *Peltier* device would sublimate ice, with the resulting vapor operating as predicted through the heater chip and expansion slots. The advantages of a solid propellant are primarily found in a self-pressurized system with lower overall storage pressures, minimized requirements on valves and a more compact storage envelope.

More recently, the SSE chair has been experimenting with different types of expansion slots. Again following the optimization performed by [77], circular expansion slots have proven that common practices of rectangular slots might need a revision. From a physical perspective, the circular shape has the following traits:

- The radial symmetry of the circular slots inherently enforces uniform fluid properties (e.g. temperature), regardless of the particle-wall collisions. This also improves the overall molecule flow by removing re-circulation zones often present in rectangular geometries, so a better velocity distribution is expected.

- From a manufacturing viewpoint, creating a divergent nozzle by tapering a hole seems much easier to achieve than etching out perfectly aligned sections and then slanting them towards the desired shape. In the same fashion, creating two-dimensional arrays of circular slots is less prone to misalignments compared to rectangular shapes.

- One aspect that cannot be verified at this level of study is the change in the total available collision area. It is expected that one rectangular slot can be replaced by multiple circular slots, the number of which depends on the space available and the hydraulic diameter sought out. The challenge lies in fitting all these slots in such a way that the slot direction is still perpendicular to the chip, unless otherwise requested.

Table 1.3 reflects the achievements of aforementioned groups in the development of FMMR technology, at least on the chip/thruster side. Sadly, the table is not complete given the lack of performance values in located publications, however the superiority of the in-house variant, theoretical as it may be, is still present.

Table 1.3: Performance comparison of various FMMR thrusters

Authors	Propellant (Phase)	Material (heat.)	Chip size (mm) Slot size (mm)	Slot count	Pressure (Pa)	Temp. (K)	Power (W)	Thrust (mN)	Max. I_{sp} (s)
[58]	NH_3 (l)	-	10 x 10 x 0.9 0.1 x 8.7	9	20	1400	0.24 (pulsed)	1	-
[115]	Water (l)	-	25 x 25 x - 0.1 x -	100	195	600	$<$ 20	10	70.3
[116]	N/A	Cr/Pt/Au	13 x 42 x 0.4 0.1 x 3-5	50	-	600	2.9	-	-
[88]	N/A	Ni	9.5 x 9.5 x 0.5 0.1 x 4.6	16	900	573	1.6	1.07	54
[69]	Water (l)	Cr/Ti/Au	18.6 x 18.6 x 0.5 0.1 x 6.5	44	260	575	$<$ 5	1.7	65
[68]	Water (l)		smaller version of previous			580	$<$ 3	0.129	79.2
[77]	Ice (s)	Au	10 x 10 x 0.5 - x 5	10	50-200	573 - 1173	0.8-5.6	1-1.6	110
SSE	Ice (s)	Au/Pt/Rh	10 x 10 x 0.5 10^{-2} mm^2 (circ.)	67^2	-	573 - 1173	4.51	0.86 - 1.4	109.9

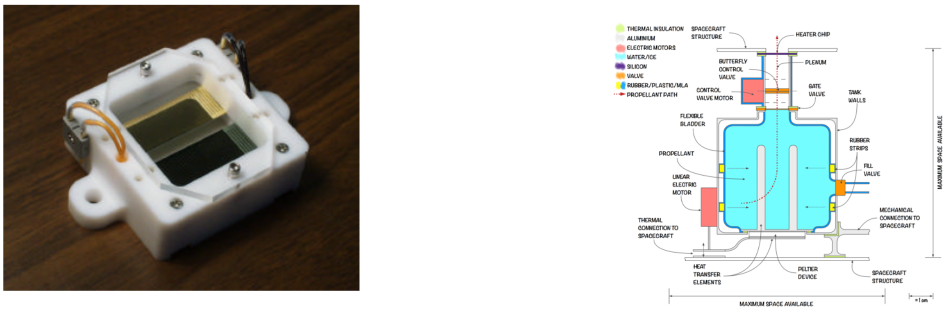

(a) source: [116]

(c) source:[77]

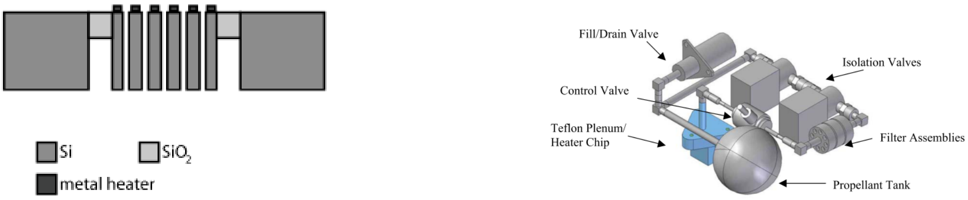

(b) source: [89]

(d) Technology Demonstrator from [68]

Figure 1.11: Different variants of FMMR thrusters

1.1.5. Non-thruster Components

Piping System

The piping system is required to transport the fluid from the storage to the plenum of each thruster. As seen in Chapter 1.1.2, piping is associated with pressure drops, analogous not only to the working medium, but to the pipe shape too. Speaking of shape, the *loss factor* was introduced, linking the effects of length and diameter to pressure loss. What should be clarified at this point is the meaning of 'length', which does not correspond to the geometrical length measured, but rather the equivalent length a straight pipe of the same diameter would have to induce the same pressure loss. Of course, the more complex the piping, the more equivalent length is increased. In that sense, straight connections should be preferred where possible, but the sizing requirements of the system necessitate some bends and corners. To that, a clever positioning of tanks and valves may relieve the system from such constraints. Indeed, the optimal solution would be the complete omission of piping and directly connect the different parts. However, a flow control system that does rely on piping is discussed later in this chapter, so some investigation must be made.

Onto the selection process, a dilemma between rigid and flexible tubing is posed. Hardline piping is more compact, but it needs careful fabrication to preserve a smooth surface in pipe extremities and curves. Conversely, flexible tubing might be more manageable, yet it requires fixtures, which is not always possible in small satellites. Out of the two types, the rigid tubing seems a more suitable option.

Performance-wise, the pressure drop across piping may be different per system. Starting from the VLM, the analysis performed in [93] for a similar type of module has proven that regardless of bends and transition sections e.g. valve fittings, the pressure drop is completely negligible ($O(10^{-4})$ $[bar]$) compared to the operational pressures of $1-5$ $[bar]$ encountered in the thruster. It can be easily seen that in the case of a VLM, piping is not an obstacle. For the FMMR though, some calculations must be made given the low working pressures

($O(10^{-3})$ $[bar]$).

The following assumptions are used for estimating the pressure drop:

- Mass flow: $O(10^{-7})$ $[kg/s]$
- Cross-section: $O(10^{-6})$ $[m^2]$
- Density: $O(10^{-3})$ $[kg/m^3]$
- Loss factor: $O(10)$ $[1]$
- Initial pressure: $O(10^2)$ $[Pa]$

The application of 1.1.10 is invalid, as vapor flows in microchannels can not regarded as incompressible. Instead, the compressible form of the momentum equation is integrated to derive the equation shown in [53].

$$\Delta P = \frac{1}{2}\rho\overline{u}^2\left[f\frac{L}{D} + 2ln\left(\frac{P}{P - \Delta P}\right)\right]$$

Then $u = \dot{m}/\rho A = O(10^2)$ $[m/s]$, and the iterative pressure equation gives a result of at least $O(10^2)$ $[Pa]$. Certainly, this brute approximation is not totally accurate but the order of magnitude stands within reason and more impressively is in the same order of the initial pressure. Therefore, the use of piping for the FMMR must be limited, if not completely omitted.

Microvalves

Having already determined multiple thrust firings as part of the mission objectives, the propulsion module should consist of a set of valves that regulate or completely cut off the propellant feed into the thruster. Moreover, the isolation of tanks from the rest of the system is imperative during the launch phase, translating to strong requirements on pressure levels the valves must withstand. At the same time, mass and power savings are most beneficial to the limited budgets inherent of a Pocketqube. The selection of suitable microvalves becomes then very intricate. Below, the driving requirements defined by [101] for microvalves have been listed:

- *Size, Weight and Integration*: Mass and volume savings allow for budget redistribution into other components, whereas the integration capability of a valve enable more compact and reliable modules. In the case of the Delfi-PQ, the size parameter affects the valve placement in the module, hinting towards a perpendicular orientation.
- *Power Consumption*: Given the limited power budget, and depending on the thruster type, the power management for valve operations is critical. According to [101], a preference in bi-stable valves that need power only in transient operations (e.g. switching states) is noted.
- *Voltage*: Valve voltage is a straight derivative of the system allowed voltage, rated at $8\ V$.
- *Resolution and Impulse Bit*: Thrust resolution is dependent on the impulse bit, which in turn is dependent on the valve's reaction time (transition between states) and stability in intermediate positions.

- *Pressure*: As explained earlier, the valve must be able to operate over certain pressure levels, defined by the tank, also considering shocks during shutoff. In addition, a pressure gradient must be ensured during operation.

To the above, launch regulations make the use of valves mandatory, so that the propellant tank is isolated from the system until the spacecraft reaches orbit. Due to the low operating pressure, the FMMR does impose any additional constraints, whereas for the VLM high sealing capabilities are required to prevent leakage of water droplets. Consequently, at least one valve is needed for integration, but the set of requirements indicates the use of two valves, for on/off functions and mass flow regulation.

As a starting point, the thorough work of [101] is used, where various COTS and MEMS technologies were examined based on performance and property metrics. The main conclusions drawn from the report are extended to facilitate the selection process:

- The COTS market is dominated by solenoid-type valves, which despite suffering from coil miniaturization issues, are generally compliant with the requirement set. Indeed, the testing systems used so far employ a *VHS Lee* flight-qualified solenoid valve for controlling the mass flow, first designated by [61]. In the current configuration it is combined with two MINSTAC fluid ports and PEEK filters, but they can be omitted if no pressurant is used, thus minimizing contamination risks. The total valve length is then reduced, to a reported $21\ mm$. This is half the allowed linear dimension of the Delfi-PQ, so a sideways positioning on top of the tank lid may be advantageous, especially if welding is possible. On the downside, the actuation voltage does not respect the voltage requirement, so an alternative was sought in the valves referenced by [101], to no avail.
- An alternative to COTS valves is found in custom MEMS valves, where different actuation methods and geometries proposed by various researchers can be implemented to improve performance with minimal size, weight and power consumption. Among them, piezo-electric and electrostatic actuators are the most promising, but again the voltage limitations create obstacles to overcome.

Both options belong to category of active microvalves, translating to current-powered devices. However, it is possible to replace the control valve with a passive feed mechanism that relies on tubing and fluid properties, the capillarity. The extensive research by [92] on the effects of surface tension to microfluidic systems proved that a set of tubes with varying diameters (either with a meniscus-type discontinuous step or tapering) is able to transport fluid and simultaneously preventing unwanted feed, due to the properties of viscous fluids. In Fig. 1.12a the principle of capillary control is shown, whereas Fig. 1.12b displays an example setup along with its pressure profile. The angles shown in the chart are characteristic to the propellant and the tube, enabling flow control be restabilizing the pressure to match the initial value. Aside from the benefit of budget savings, the generation of scaling laws through non-dimensional parameters nullifies down-scaling implications. Indeed, the experimental tests on five different fluids with varying viscosity were close to the analytic model, after the latter was corrected for gravity effects. A similar analysis was conducted in [68], where phase separation occurred via membranes and hydrophobic materials that exploit surface tension. The research on capillary effects in micro-thrusters has also resulted in the prototype units of engines presented by [40]. The principle of capillarity has been integrated in the heating section of the thruster and the viscosity difference between water and water vapor is used to generate thrust. The schematic presented in Fig. 1.13 is not to scale, but it is expected by the author that improvements already mentioned in Chapters 1.1.3 and 1.1.4 about nozzles will be implemented. Undeniably, both analytic and experimental results indicate that a capillary-based system can replace both piping and valves.

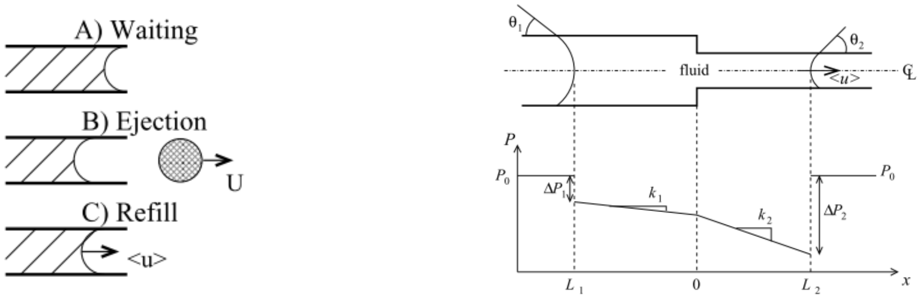

(a) Operation principle (source: [92])

(b) Pressure profile (source: [92])

Figure 1.12: Capillary control of propellant flow

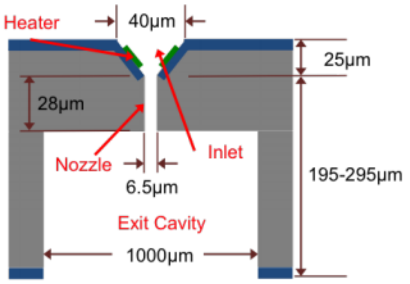

Figure 1.13: A capillary-based film evaporation thruster (FEMTA). Dimensions not to scale. (source: [40])

Tank Design

The storage component of the system must by default withstand the launch loads and push the propellant towards the tank exit. This is common in both systems, which simplifies the process of design selection. An additional requirement that applies for the FMMR is the heat management during the sublimation process, due to power constraints. Placement of sensor slots and attachment points will follow once a design has been determined. The research conducted by [93] in variable propellant volume tanks resulted in 6 different types, shown in Table 1.4, with a more generic representation of the various pressurization methods shown in Figure 1.14.

Among the options evaluated, a bladder-type tank seems the most applicable to both systems. The overall design involves a rigid external structure with a flexible internal bladder. In the VLM, it is expected to act as a divisor between the propellant and the pressurant, while in the FMMR it is intended as a contracting piston that pushes ice towards the heating system for the sublimation. As far the auxiliary mechanisms are concerned, [93] evaluated the feasibility of automotive industry gas generators used in airbag systems for the VLM water pressurization, and the results seemed promising on paper, but the unexpected explosions of 3 of the 4 generators tested questioned the product reliability and thus were not further discussed. The main downside to this option is the increase in power and weight budget consumption. During the same period, [77] developed a concept for the FMMR where the ice was sublimated through a Peltier device. Both systems are unsuitable because of down-scaling

Table 1.4: Characterization of propellant storage types

Type	System	Verdict	Reasoning
Mixed Prop./Pres.	VLM	Discarded	• Requires filters (added mass) • Compromise vaporization performance
Piston	Both	Discarded	• Moving part (reliability) • Leakage/Contamination risks
Bladder/Membrane	Both	Accepted	• Pressure stability • No power requirements
Propellant heating	FMMR	Accepted	• Required by system
Propeller/Screw	Both	Discarded	• Moving parts
Rotating tank	Both	Discarded	• Same as above

issues. Currently, other heating devices are considered and modeled by fellow students, but the level of progress is unknown to the author.

One plausible alternative might be the implementation of a *compliant* flexible tank, as indicated by Figure 1.14. The concept of compliance relies on exploiting a material's elastic capabilities in order to generate some translational or rotational motions, going against the common approach of rigid envelopes. An example displaying the difference between a classical and a compliant (jointless) mechanism is seen in Fig. 1.15. Such a tank would be advantageous in multiple ways: to begin with, no additional energy is required to push the bladder, since the natural position of the tank leverages can be fine-tuned to maintain the operational pressure designated. Moreover, the flexible system can withstand all launch loads with minimal mass, using *topology optimization* algorithms, whereas combination with piezoeletric systems is also possible. The greatest challenge in compliant systems is the materialization of a satisfying design, which boils down to trial and error methods, despite the capabilities of computer software. Based on the requirements imposed and the designs of [93] and [77], the author envisions a lidded tank with flexible sides housing the bladder, with pressurization automatically happening when the gate valve is open. A more detailed explanation is depicted in Fig. 1.16. Given the design complexity and time allocated to this study, a more detailed architecture is not feasible yet. Upon interest and time/resource availability, such an option could be investigated.

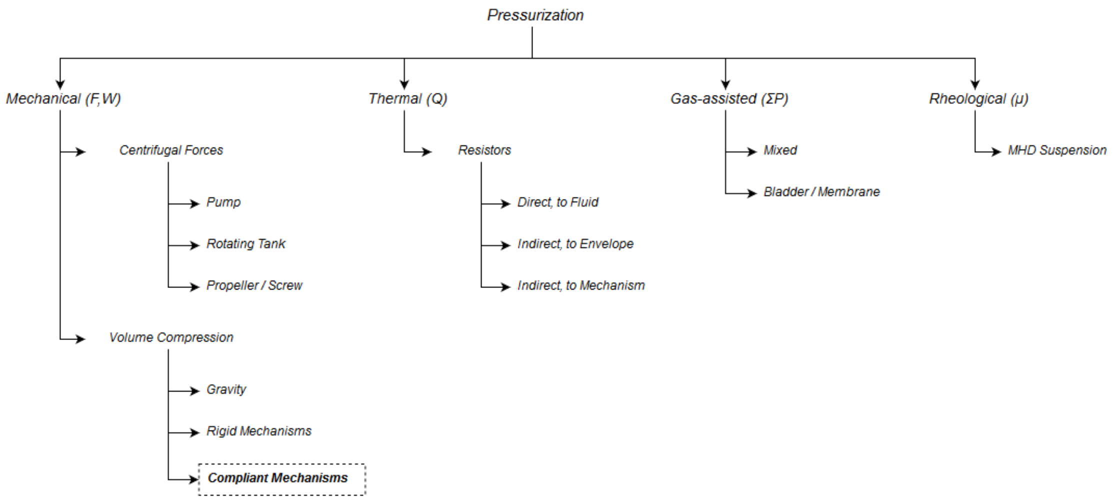

Figure 1.14: Identified methods of propellant pressurization.

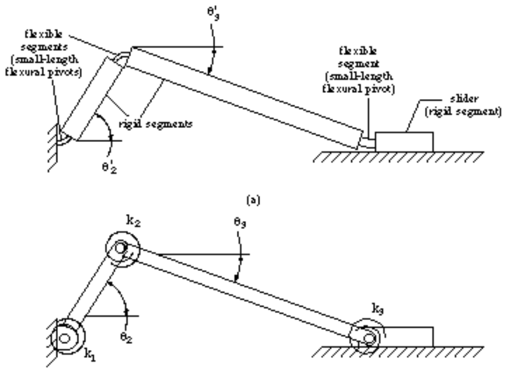

Figure 1.15: A slider mechanism. Top: compliant, bottom: pseudo-rigid model. (source: [1])

1.1.6. Design Candidate

The information gathered from previous chapters is put into use by means of a trade-off analysis, in an effort to find a propulsion design for the Delfi-PQ, and further down the line for any system. Individual components have been analyzed earlier, without a conclusive answer, therefore design concepts must be generated by examining all possible combinations.

Using Fig. 1.4 as a reference, three building blocks are being compared: propellant storage, control and thruster. The reason for omitting the power management is that from a manufacturing perspective, the standardized properties have already been determined, as shown in Fig. 1.2. Following from the results of previous chapters, two options per block have been identified:

- *Storage*: Pressurized w. gas generators / Compliant mechanism
- *Control*: Proportional valve / Custom capillary tubes
- *Thruster*: VLM / FMMR

In the control block, isolation valves have been left out of the analysis, as there is a

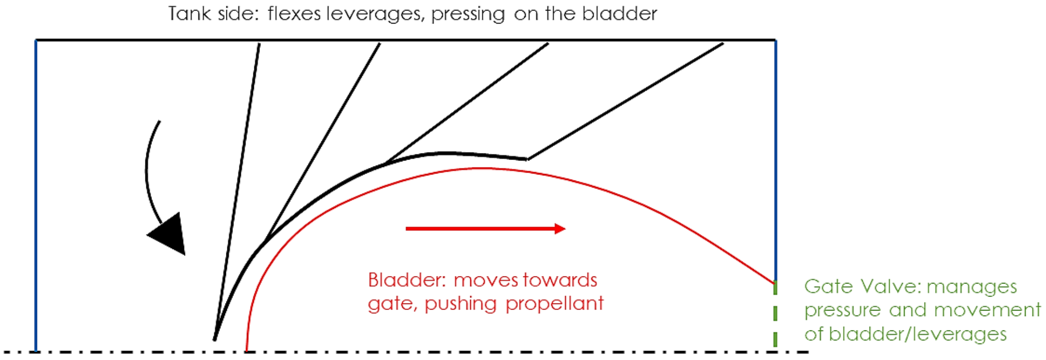

Figure 1.16: Schematic of a possible self-pressurizing tank, at a concept level.

possibility of being integrated with the tank lid, upon future discussion. Moreover, with proportional valve, the COTS solenoid valve is intended, although this is still debatable. Then, the number of possible combinations amounts to 8. An open question regarding the moment of inertia exists, the reason being the effects of inertia control on the placement of parts. In order to keep track of the configurations, Table 1.5 has been set up:

Table 1.5: Identified design concepts

ID	Storage	Control	Thruster
A	Pressurized	Proportional	VLM
B	Pressurized	Capillary	VLM
C	Compliant	Proportional	VLM
D	Compliant	Capillary	VLM
E	Pressurized	Proportional	FMMR
F	Pressurized	Capillary	FMMR
G	Compliant	Proportional	FMMR
H	Compliant	Capillary	FMMR

Trade-off analysis

It is clear that some configurations suffer from incompatibility with the goals of this review. The FMMR module proposed by the university relies on a sublimating ice system which by default is self-pressurized, so a dedicated mechanism is not required. As a result, configurations E & F participate with a handicap that can be overturned if the trade-off rating is convincing. For comparing the different options, the following design criteria seem adequate:

- *Performance*: Being a technology demonstrator, the module launched will reflect the maturity and performance level of the system developed.

- *Budgeting*: Having in mind the limitations of the small scale factor, an compact solution is also a more efficient solution.

- *TRL*: Despite only qualitatively, the technology readiness level of the selected components will directly impact the reliability of the module, as well as the development time/-cost.
- *Module Management*: Beyond the technical aspect, some operational characteristics are affected. For instance, the system pre-heating will also affect the transient behavior of thrust levels and propellant efficiency.

Starting from pure performance metrics, the data from [27] and [98] are used and replicated in Table 1.6. Despite the higher absolute metrics, the total power draw as well as the lower propellant efficiency are somewhat prohibitive for the limited budget of the Delfi-PQ. In this context, the FMMR can be more easily implemented.

Budget-wise, the thruster envelope and weight are similar in both cases, and they amount to a small percentage of the system, so they cannot be accounted in the trade-off. On the contrary, the tank and valve volume are non-negligible. Especially in the FMMR case, replacing the Peltier device with a heating mechanism might give more room for valve placement. Yet, more promising in this case seems to be the development of the capillary tubes. Only disadvantage of the option is the potential reduction in proportional capabilities.

Table 1.6: Comparative performance of the VLM and FMMR thrusters

Parameter	Liquid water resistojet (min-max)	Free molecule resistojet (min-max)	Unit
Chamber/channel temperature	550 - 773	300 - 900	K
Chamber/plenum pressure	5 x 10^5 - 7 x 10^5	50 - 150	Pa
Mass flow rate	1.5 - 3.5	0.5 - 2.7	mg/s
Power transferred to heaters	4 - 10	0 - 2[a]	W
Thrust	1.7 - 4.2	0.5 - 3.0	mN
Specific impulse	110 - 130	80 - 120	s

[a] For total power draw, 2 W of sublimation are assumed to be added.

As far as development time/cost is concerned, anything but the solenoid valve requires development, testing and integration time, compromising the launch date. From a design point of view, the pressurized tank has already been studied for Cubesats [107], facilitating the process of miniaturization to the new standards, whereas the compliant needs intensive research in force distribution. Moreover, the manufacturing process is more difficult with complex shapes such as the leverages in the latter design, but the final result is most favorable and advantageous in all terms. In a similar fashion, both MEMS valve technologies mentioned by [101] and the capillary tubes are resource-expensive. The mass and power savings have a higher return value than the bulky solenoid valve, but given the time allocation for the propulsion prototype, components with which past experience is available are preferred.

Another point to take into account is the module management during the launch and operational phases. To begin with, the FMMR relies on ice, and therefore it is not possible to fill the tank with ice and then transport the spacecraft for launch. Even if it were, only launching sites with temperature low enough to prevent melting are suitable for this system, unless a strong insulation keeps tank temperature in check. On the other hand, the VLM is more embracing in the matter, given that atmospheric conditions can be used for storage.

More, the system pre-heating phase is more forgiving for the FMMR, with simultaneous sublimation and chip heating, whereas the VLM requires a precise timing between pre-heating and water flow.

Based on these points, a qualitative trade-off table has been set up in Microsoft Excel, shown in Fig. 1.17. This table does not represent an absolute decision, but rather a guideline with which options can be ranked according to the previous argumentation. The trade-off criteria were used to evaluate the storage, control and thruster separately in order to discern the various pros and cons of each individual solution with respect to other components.

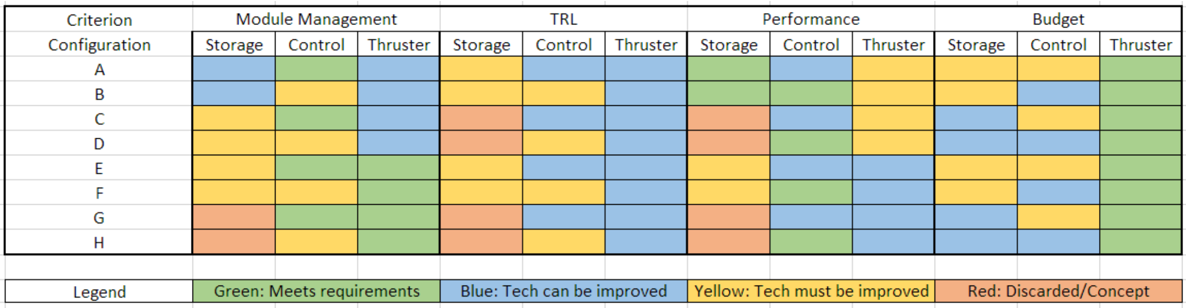

Criterion	Module Management			TRL			Performance			Budget		
Configuration	Storage	Control	Thruster	Storage	Control	Thruster	Storage	Control	Thruster	Storage	Control	Thruster
A	🟦	🟩	🟦	🟨	🟦	🟦	🟩	🟦	🟨	🟨	🟨	🟩
B	🟦	🟨	🟦	🟨	🟨	🟦	🟩	🟩	🟨	🟨	🟦	🟩
C	🟨	🟩	🟦	🟥	🟦	🟦	🟥	🟦	🟨	🟦	🟨	🟩
D	🟨	🟨	🟦	🟥	🟨	🟦	🟥	🟩	🟨	🟦	🟦	🟩
E	🟨	🟩	🟩	🟨	🟦	🟦	🟨	🟦	🟦	🟨	🟨	🟩
F	🟨	🟨	🟩	🟨	🟨	🟦	🟨	🟩	🟦	🟨	🟦	🟩
G	🟥	🟩	🟩	🟥	🟦	🟦	🟥	🟦	🟦	🟦	🟨	🟩
H	🟥	🟨	🟩	🟥	🟨	🟦	🟥	🟩	🟦	🟦	🟦	🟩

Legend	🟩 Green: Meets requirements	🟦 Blue: Tech can be improved	🟨 Yellow: Tech must be improved	🟥 Red: Discarded/Concept

Figure 1.17: Graphical trade-off table of considered options

Selected Design

From a first impression, the table hints that Combination A seems the most promising design. However, a closer inspection at the table proves that the absolute weakest point of the whole system is the propellant storage. To date, no tank of this size is known to exist, so regardless of the thruster selected, much effort is required to create a compact part. It can then be said that, if an opportunity for developing a thruster-independent storage module exists, it should be considered. Out of the alternatives presented, Combinations C,D and F are equally interesting as a full propulsion module, but the low TRL of compliant-based tanks highlights a gap in this research field. This an excellent opporunity for a student to fill this gap with a productive research within the scope of a Masters' Thesis. Between C and D, the author is inclined to propose Combination C over D, considering the well-studied behaviour of a proportional valve in [101]. The positioning of individual components is illustrated in Fig. 1.18.

1.2. Motivation

The literature review is partially successful in understanding the needs and complexities of a miniaturized micro-propulsion system that is applicable to an emergent form factor. Theoretical knowledge as well as practical aspects of the two in-house thruster technologies have been investigated, proving the promising capabilities of both VLM and FMMR thrusters in minute and accurate maneuvers. Surprisingly, the development status of thruster systems is not followed by an equivalent progress of the feed system. As a matter of fact, the majority of literature sources found by the author did not include information on experimental units of feed systems. Different conventional and innovative approaches for the tank, valve and piping components were described, opening a possibility for a fully controllable, passive pressurization and transport feed system that has minimal power consumption. These passive mechanisms include bladders, tanks with compliant mechanisms and tubes with desired capillary effects, but none of them has yet been encountered in propulsion units, so their

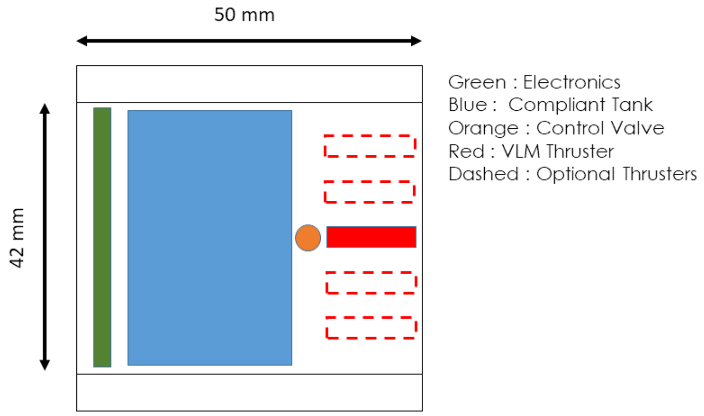

Figure 1.18: Strawman architecture of the propulsion module (side view)

performance is questionable. In light of such information, this MSc. thesis will focus on that specific part, stated as follows:

> **Development of a self-pressurizing storage system that can be implemented within a Pocketqube-sized propulsion module and is compatible with a Vaporizing Liquid Microthruster (VLM) and a standard off-the-shelf microvalve, using compliant mechanisms.**.

The aforementioned objective must be progressively accomplished through reasonable milestones/tasks, shown in the following list:

- *Requirements*: A notable lack of adequate requirements concerning such a small component must be overcome by the generation of quantifiable sub-objectives that the storage system must satisfy. To name a few, mass and volume budgets, structural integrity as well as propellant capacity are of paramount importance.
- *Compliance Theory and Applicability*: While from a concept perspective the proposed storage solution is enticing, no practical application in small satellites has been recorded to date. A research on the fundamentals of compliance and its currently prominent applications will provide information on the design approach to be followed.
- *Sizing and Optimization*: Taking into account the previous items, an optimization model is in order. The intent is to find an optimal configuration of flexible and rigid elements in the tank, so that the latter can meet the requirements above both in idle and thrust firing conditions.
- *Modeling and Simulation*: While calculations by hand, or even by analytic models provide a clear view of the design, a software-based approach is expected to question the foundations and the outcome of the sizing process, acting as a validation study.

Research Questions

Following from the milestones described previously, some questions must be formulated and answered during the thesis project, aiming to give measurable observations for the tank design and its materialized counterpart.

1. *What are the minimum requirements that the proposed storage solution must meet? What mass and volume budget can be allocated to the tank, taking into account any tolerances?*
2. *How does a compliant system operate? How can this principle be integrated to the system in discussion?*
3. *What is the optimal shape and configuration for the tank design? How does this configuration vary between idle and thrust conditions?*
4. *What performance can be achieved by the proposed design? How well is the output replicated in a software simulation?*

1.3. Thesis Outline

The report is divided into four distinct phases and seven chapters, aimed at giving a complete answer to the research questions presented.

Phase 1 deals with the background knowledge required for coming up with a promising tank design. Chapter 2 introduces the reader to the notion of Compliant Mechanisms, explaining the fundamental operation principle, known applications and the most prominent features a compliant mechanism can have, positive or negative. Chapter 3 sets the framework with which the tank design must operate through common Systems Engineering practices, mainly in the form or requirements or design constraints.

Phase 2 is focused on converting the knowledge acquired into a tangible design idea. In particular, Chapter 4 presents a two-level trade-off strategy with which a number of potential design candidates undergo comparison based on user-defined criteria. The unavoidable bias introduced by the criteria is evaluated through sensitivity analyses. Secondary aspects of the design, namely the materials, the shape and the configuration are also subject to trade-off analysis, giving rise to a complete preliminary design proposal.

Phase 3 is dedicated to advancing the design concept into a set of tangible metrics, such as size and compliance properties, and to giving an estimation of the storage module's performance for the requirements set previously. Chapter 5 employs a series of theoretical/analytic models found in engineering literature and size and shape optimization study to materialize the pressurizing mechanism and the envelope components, emphasizing on the former, using custom MATLAB scripts. A largely simplified *Fluid-Structure Interface* (FSI) model is constructed in SIMULINK to predict the expulsion performance during a single thrust cycle. The analysis is repeated in Chapter 6, but under much more advanced models and with the use of Computer-Aided Engineering (CAE) software, being in essence a validation study. A three-way comparison between analytic models, CAE simulations and system requirements gives conclusive evidence on the design suitability.

Phase 4 declares the end to this design cycle, and of course the thesis. Design choices, model shortcomings and recommendations for future endeavors are discussed in Chapter 7 effectively characterizing the success or failure of the study in terms of performance and/or viability. This is followed by a concluding note about non-academical aspects of a MSc. Thesis that have affected the overall approach to this final part of the MSc. program.

2

Compliant Mechanisms

The research proposal obtained from the literature study, briefly reported on Chapter 1, focuses on the implementation of a propellant storage and expulsion system based on the concept of a *compliant mechanism*. This chapter is by logical consequence a foray into understanding what is defined as a compliant mechanism, its basic properties and functionality and its benefits and caveats. Lastly, known and potential applications are mentioned to justify the consideration of a compliant mechanism in a propulsion system.

2.1. Definitions

To introduce and describe the inner workings of a compliant mechanism, one must first understand the basic concepts behind its name: what does it mean to be *compliant*, and what it means to be a *mechanism*?

Starting from the latter, mechanisms are defined as mechanical devices used to transmit force, motion or energy [51]. Using the term *transmit* implies that mechanisms are essentially mediators between mechanical/thermal/electrical inputs and outputs, hinting a relationship between transmission efficiency and overall performance. Then, according to [3], compliance is the ability to yield, to submit under a request. In the engineering world, the definition is refined to *the ability of an object to yield elastically when a force is applied*. An additional point to make would be the replacement of the term 'transmission' with the more appropriate (in the author's opinion) term 'conversion', as such phenomena are apparent in contemporary mechanisms. In thermal actuators and thermostats, for instance, heat is converted into force and then into motion. Merging all the above results in a better definition for identifying a compliant mechanism, alas

> *A mechanical device that converts an applied force, motion or energy into a desired output through elastic yielding.*

The fundamental property of compliant mechanisms is the elastic deformation of constitutive elements to produce a motion or a force. This is achieved either by deflection of the entire mechanism, in which case the compliance is *distributed*, or by localized deflection of

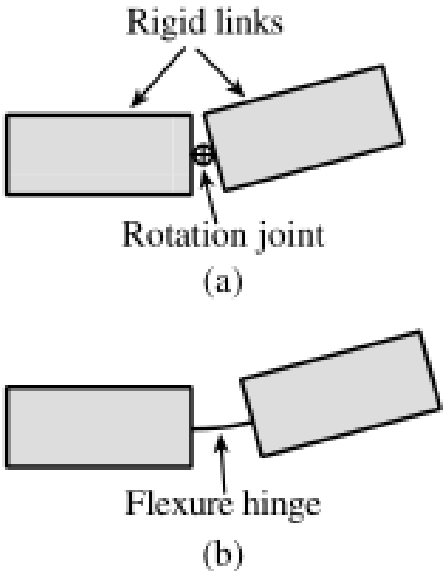

Figure 2.1: Joints enabling relative rotation in mechanisms: (a) Traditional joint, (b) flexure hinge. Source: [73]

thinner segments called flexure [1] hinges, hence the compliance is *lumped* [42]. From an engineering viewpoint, they perform a similar function to bearings, though to a limited degree, as reported by [73]. Figure 2.1 proves the point with a geometrical representation of the differences between traditional joints and flexures.

2.2. Basic Properties

Compliant mechanisms perform one particular function, that is transferring a force or displacement input (referred to as F_i and δ_i), through a combination of rigid and flexible members, to a force or displacement output (F_o and δ_o). The interaction of these members results in the emergence of unique kinematic and dynamic behaviours that need identification and grouping. A typical set of grouping principles encountered in literature is presented:

1. *Deflection*: A rather self-explanatory categorization, based on the deflection magnitude observed in actuated flexures. In [72], a *large-deflection* mechanism undergoes displacement levels above 20% of the structural dimension, as the latter is defined per system. It follows that displacement levels below the threshold number correspond to *small-deflection* mechanisms, although no acknowledged literature has mentioned something similar.
2. *Function*: Reported in [52], classification between compliant systems is applied based on the function they serve. *Kinematic* types are used in cases where following a motion or path is prioritized, whereas *Kinetic* types are most suitable for transferring forces and energy through a mechanism, regardless of displacement magnitudes. A third branch is mentioned, with no clear orientation and called *Basic*, but these mechanisms are not of any particular interest, hence not further discussed in this study. In Figure 2.2, a mechanism tree is depicted with the most notable categories.

---

[1] From the words 'flexible' and 'structure'

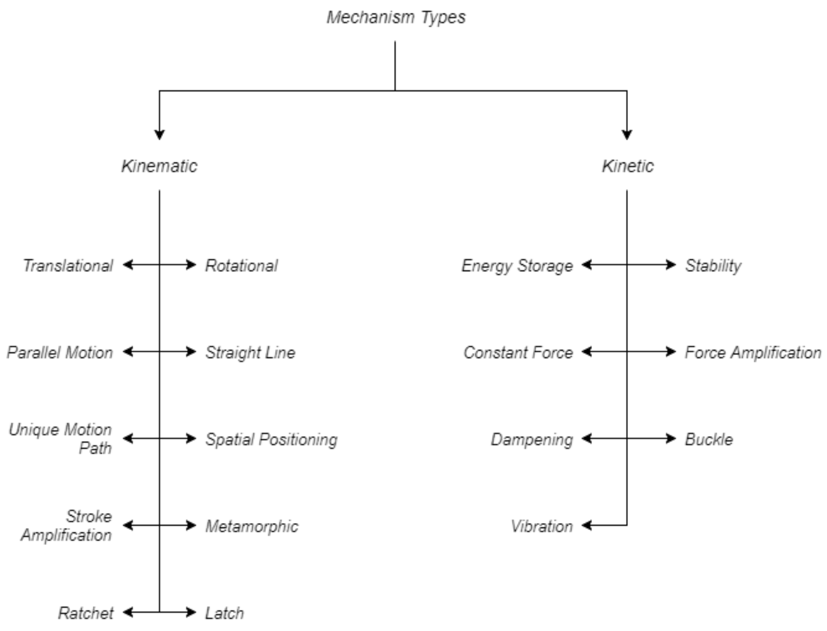

Figure 2.2: Function-based classification scheme of compliant mechanisms. Source: [52]

3. *Stress distribution*: Already seen in Section 2.1, another way to classify compliant systems is stress distribution, with two types being discerned. Mechanisms with stress forces being concentrated at the flexure extremities, essentially at the connection points with rigid elements, are said to display *lumped* compliance. On the other hand, mechanisms with stress forces spread out over the entire body, or in other words, mechanisms where all components participate in the deflection, are said to display *distributed* compliance. Both types are useful in their own rights: lumped compliance mechanisms enable more precise motions, as deflections are geometrically simple to predict. Distributed compliance mechanisms are better used in instances with cyclic loads and load-bearing applications, as stresses are absorbed by the whole system.

The classification allows for recognizing certain types of mechanisms from a qualitative viewpoint, in that they correspond to how they achieve a prescribe motion or force transfer. For example, metamorphic mechanisms – as the name suggests – change their topology and configuration during the actuation progress to obtain different motions (see Figure 2.3). Latching and release mechanisms deploy from a locked position to a deflected state, which must be reactivated manually. Stability mechanisms go beyond simple latches and transit from one locked position to another, based on the strain energy stored within participating flexures. One can easily find bi-stable mechanisms in common switches of electric appliances. Amplification systems use flexure combinations to multiply (or divide) the input magnitude, while constant force mechanisms reverse the procedure by utilizing flexures to induce additional stiffness, effectively reducing inputs to a constant output. A typical instance of constant force can be noticed in the resistance training equipment.

The principal functionality is a good criterion to discern the most qualified mechanism category for the case in study, but output differences between variants within the same

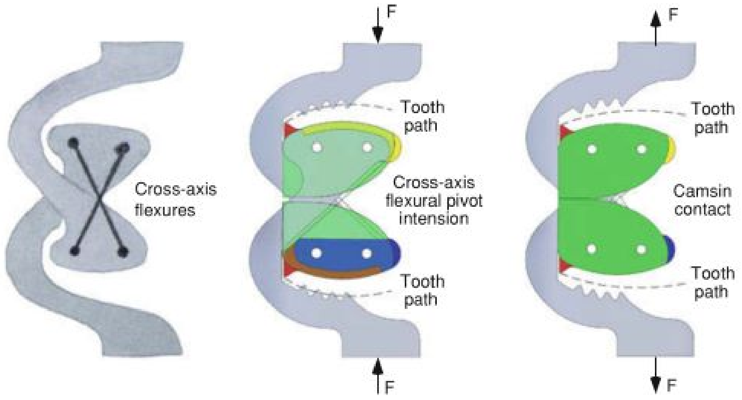

(a) Functional sketch (b) Behavior1 (c) Behavior2

Fig. 36.2 The two behaviors are illustrated in the context of Design 1. In Behavior 1, the cross-axis flexures are in tension when the compressive load is applied. The teeth (*in red*) engage and lock the mechanism. In Behavior 2, when a tensile load is applied from the weight of the shank, the cams come into contact and the cross-axis flexures are slack. The teeth do not engage so the prosthetic can rotate freely

Figure 2.3: A prosthetic knee based on a metamorphic compliant mechanism. Source: [123]

category are quite noticeable, meaning that more tangible references are needed. In [76], a set of performance numbers serving the purpose has been devised for large-deflection, linear-motion compliant mechanisms (LLCMs), the details of which are shown in Table 2.1. This work's author is inclined to believe the numbers are applicable to any compliant mechanism, since there seem to be no strict requirements on the deflection level.

Table 2.1: Typical performance metrics of LLCMs

Metric	Symbol	Expression	Purpose
Displacement	δ^*	δ/x	Deployed to stowed footprint ratio
	x	$\sqrt{b^2+l^2}$	Structural dimension (b: width, l: length)
Transverse Stiffness	k_t^*	$k_{t,min}/k_{a,virt}$	Normalized Off-axis stiffness
	$k_{a,virt}$	$F_{a,max}/\delta$	Virtual axial stiffness
Torsional Stiffness	k_{tor}^*	$k_{tor,min}/T_{char}$	Normalized torsional stiffness
	T_{char}	$F_{a,max}\cdot x$	Characteristic torque

An expansion to the above is found in [110], under the umbrella term of *advantage*. Taking the definition of conversion factors, performance numbers applicable to any mechanism can be generated to represent the capabilities of compliance. Namely, the *Mechanical Advantage* (MA) and the *Geometrical Advantage* (GA) are given in Equation 2.2.1. The *Energy Efficiency* (η) factor is the ability of a mechanism to convert input energy (usually in the form of mechanical work) into output energy, again in the form of work. Its mathematical formulation is explained:

$$MA = \frac{F_o}{F_i} \quad , \quad GA = \frac{\Delta\delta_o}{\Delta\delta_i} \tag{2.2.1}$$

Starting from the general definition of mechanical work, force times displacement, the energy efficiency is defined as $\eta = MA \cdot GA$. For a rigid-link mechanism that suffers no friction or inertia phenomena, $\eta = 1$, but this does not apply to compliant mechanisms. The reason is straightforward: flexures absorb part of the work provided at the input to get deflected, effectively reducing the mechanical work output. This comes with a penalty to the energy efficiency, as shown in equation (2.2.2),

$$MA = \frac{F_o}{F_i} = \frac{\Delta\delta_i}{\Delta\delta_o} - \frac{\Delta\epsilon}{\Delta\delta_o \cdot F_i} = MA_{rigid} - MA_{strain} \rightarrow$$

$$\eta = MA \cdot GA = (MA \cdot GA)_{rigid} - (MA \cdot GA)_{strain} \rightarrow \eta = 1 - \frac{\Delta\epsilon}{\Delta\delta_i \cdot F_i} \tag{2.2.2}$$

where $\Delta\epsilon$ represents the change in strain energy stored in the flexures, MA_{strain} is the associated advantage losses and $\Delta\delta_i \cdot F_i$ is the mechanical work at the input.

2.3. Assets and Drawbacks

The structural appearance and operation principle of compliant mechanisms offers some assets, as well as drawbacks, compared to counterparts based on joints and linkages. The following lists provide necessary information found in literature (see [42, 51, 124]):

Assets

Little/no assembly required: Due to the principle of deflecting members, motion is generated without the need for articulated joints, so the effective number of components and associated assembly is reduced. In monolithic [2] mechanisms (as the name implies) no assembly is required, which accentuates other advantages of compliant mechanisms.

No friction or wear: Contrary to joints, flexures are directly integrated to the rigid components, so the motions achieved do not cause interactions between moving parts, and consequently decrease friction levels. For monolithic mechanisms, friction is eliminated and so is mechanical wear in the long run.

No need for lubrication: The lack of friction between moving elements removes any necessity for lubricants, or for any liquid mediator for that matter. This realization is critical in space environments, where predominantly low pressure induces evaporation and may cause contamination of other spacecraft parts, or perhaps failure, due to the lack of lubricant.

No vibration and backlash: The constrained deflection of the various elements must be within the elastic region, which is assumed to be linear in most cases. An immediate effect of said assumption is the elimination of backlash – if no impact conditions arise – as well as vibration. Indeed, this elastic deflection results in a much higher movement precision and force sensing accuracy.

---

[2] from the words 'μονός' and 'λίθος' literally meaning 'single stone'

Lightweight and compact: The low-part count, the material optimized distribution and the ability of planar configuration/stowage, all contribute towards non-trivial mass and volume savings compared to rigid mechanisms. This is particularly useful in budget-oriented projects where miniaturization of components is crucial, such as the MEMS/NEMS scale.

Integrated functions: As with natural systems, all compliant mechanisms possess to some degree both motion and return-spring function, and can be further augmented to include other functions, depending on the application. For a conventional mechanism, the same functionality is usually achieved by additional components.

Manufacturing processes: The lower part count, the planar configuration and the strength distribution achieved through geometry handling all contribute towards an easier manufacturing procedure for compliant mechanisms. According to Howell[52], even a single sheet of material can be converted into a full mechanism.

Drawbacks

Limited rotation: The bending nature of the flexures does not allow full rotation like traditional joints like bearings or pins, which for revolutionary mechanisms is crucial. Depending on the design, it should be possible to concatenate multiple flexures to get a comparable rotation angle, at the expense of volume and mass.

Entanglement/Overlapping risks: Having such compact designs, which may consist of multiple separate mechanisms, the risks of either overlapping, touching or entangled flexible elements are higher with respect to rigid parts.

Non-linear kinematics: While the force-deflection relationship is assumed to be linear, the assumption for the deflection itself is not valid. If anything, the motion of flexures under large deflections is primarily non-linear, which further complicates the design process. On the other hand, traditional mechanisms are in most cases examined through linear beam equations.

Fatigue analysis: Compliant mechanisms are designed for a prolonged use, which undeniably exerts some more pressure on the design requirements. Thin components such as the flexures are known to suffer from fatigue or even creeping in long-term cyclic loads.

Energy efficiency: A difficult challenge seems to be the energy efficiency of compliant mechanisms. Despite the spring-like functionality of compliant systems, the elastic yielding of flexures converts some of the input energy into strain energy, stored within the flexures as localized deformations. Equation (2.2.2) proves the point, with $\eta_{comp} < \eta_{rigid}$.

Design challenges: Rigid mechanisms are usually designed with very basic methods, granted that individual components perform just one function. On the contrary, the intricacy involved with designing compact systems with enhanced functionality from fewer components is much higher, to the point where basic methods do not apply. In some applications, trial-and-error approaches have been reported, though more recently systematic analyses have emerged.

Mathematical Complexity: Contrary to traditional mechanisms, where the geometry and force equations are separate mathematical systems, the kinematic and dynamic aspect of bending flexures are to be treated simultaneously as they are mutually affected, so the complexity increases exponentially, also depending on the non-linearities introduced.

2.4. Practical Applications

The properties of compliant mechanisms may have been extensively studied for a few decades, but the concept itself originates in the pre-historic times, with notable examples in both human and natural environments. The branches of trees and plants have evolved over time to become compliant, serving multiple purposes: progeny dispersal, foliage weight management and weather adaptation through elastic yielding [42], while all animals can macroscopically be considered compliant 'super-organisms', as cells, muscles, tissues and even cartilages are in essence elastic mechanisms(e.g. the deployable tongue of chameleons, honeybees [117]). Most primitive weapons exploited the elasticity of wood to store and release strain energy provided by hunters at will, towards either increasing the ammunition velocity (bow) or trajectory corrections (see arrows and spears).

The advantages of compliant mechanisms are more pronounced in the modern era, as multidisciplinary studies of industrial and commercial products create many trade-offs between performance, cost and resource management, more often than not compromising on the resulting quality. Ranging from large-scale projects (e.g. aeronautical industry) to miniaturized precision systems (e.g. MEMS), a wide field of applications may benefit from the transition to flexible components. A small sample of the reported applications has been compiled from a brief literature survey:

Automotive Industry: Suspensions [18, 122], windscreen wipers [17], trunk lid latching mechanisms [121] and mirror actuators [103] can be made out of compliant-based parts with non-trivial weight, volume and part count savings compared to traditional rigid link systems. Ultimately, the cost-performance curve is shifted towards the latter.

Aeronautical Industry: Aircraft wings and wind turbine blades make use of aerodynamic profiles to generate lift, each with its own purpose. A major aspect in aerodynamic efficiency is the control of induced drag that is often done by manipulating the leading and trailing edges of airfoils through concatenated sliding mechanisms. Because of their link and joint-based nature, they are heavy and voluminous. Different academic [66, 85, 96] and commercial efforts [4, 5] have brought into the spotlight the concept of an adaptive trailing edge that bends according to the wind loads. Again, the weight and part count savings improve the overall performance while simultaneously reducing the cost of manufacturing and assembly.

Medical/Biomedical Sciences: Compliant mechanisms also find their use in the medical sciences in multiple forms: be it surgical tools such as grippers and cutters [55, 74], or rehabilitation devices [81], or even implants [52] the friction and backlash-free movement of compliant components allow for precise handling of tissues and injured parts of the human body during either operation or recovery.

MEMS/NEMS: An ever-increasing effort in miniaturized mechanisms emphasizes the importance of clever and efficient solutions that respect the tight size and weight budgets. Regardless of the shape or form, flexible elements are ideal to be employed in MEMS technologies, such as force amplification actuators [33] and thermal actuators [22].

Commercial Items: A less prominent area to look for compliant mechanisms is the consumer market, with quite a few products being compliant or having a compliant part. Shampoo lids for instance use a flexure to allow opening of the bottle, yet keeping the lid connected to the main body. Clothespins and desktop staplers [56] perform their action by using springs - a compliant element - while foldable desks and chairs that follow the compliance principles would be quite beneficial for space saving [52] with simultaneous mass savings by omitting pins and joints.

Space Applications: The space industry could make use of compliant mechanisms to enhance the functionality of spacecrafts and vehicles in general, especially considering the advancements in pico-satellite technology. Release and deployment mechanisms [124] for solar array panels, traction wheels for rovers [120] and precision cryogenic mirrors [54] for instance can be adapted with flexible elements, effectively replacing lubricated joints and as a result eliminating contamination risks, and mechanical failure due to friction. Compliant mechanisms lend themselves well to vibration isolation applications [41], as the backlash-free displacement eliminates unwanted vibrations during launch, separation and deployment phases of a mission.

2.5. Conclusion and Remarks on Chapter

A general introduction of the concept of compliant mechanisms has been given in this chapter, based on literature sources. The original definitions of the notions ’compliance’ and ’mechanism’ are reviewed and adapted to better reflect the manifestation of physics events that ultimately constitute a compliant mechanism. The abundance of unique mechanisms found in literature is condensed into classified groups based on the level of deflection, the main function served and the type of stress distribution/management, aiming to reduce the design space into the more useful alternatives. Basic properties and functions are seen in both qualitative and quantitative metrics as a reference, while advantages and disadvantages provide a background for the known and potential applications found.

Despite all of the notable information acquired, the scope of compliant mechanisms as provided by literature sources is limited to flexure-based elements that solely rely on bending actuation or combinations of them. Strain energy, the source for elastically deflecting elements, is not constrained by bending forces, while the definition of compliance itself does not specify such an actuation as a criterion for the notion to apply. It is safe to assume that the compliant mechanism design space is a superset of flexured-based solutions, and based on this Chapter 4 is structured. At the same time, not all options are practical for a Pocketqube-sized propulsion system, so the design domain is bound by mission-specific needs. The process of identifying all relevant items is explained in detail in Chapter 3.

3

Requirements

The need to confine a compliance-based propulsion storage module has become apparent in Chapter 2, as the relevant design space is quite expanded. The mission requirements themselves are not sufficient to explicitly ask for solutions about propellant storage, but any selected design is driven by a set of *system requirements* in order to meet a system-specific aim, as part of the mission goal. In a very abstract manner, one can state the aim as:

> *The compliance-based storage module shall be compatible for use in a Pocketqube-class propulsion system.*

In this chapter, an effort to collect any piece of information regarding the requirement framework needed to compare the candidate design options, and collect them into well structured and clearly defined system requirement groups. Furthermore, any known design challenges about the proposed technology are presented as a non-technical set of constraints that do not constitute a requirement.

3.1. Requirement discovery and analysis

A common Systems Engineering practice when defining requirements for the candidate designs is the *Requirement Discovery* [45]. The designer starts from an objective that must be reached and expands it in all possible directions with the aim of reducing the problem to a concrete, measurable list of lower-level requirements, such that all designs have a reference with which they are compared. This objective may be anything related to the design, so long as it can be characterized a ’parent’ of the needed requirement list, with typical examples being mission requirements, flow-down charts and technical documents. This natural approach to deriving requirements is reminiscent of a branching tree, hence the most familiar way of representing the process is the Requirement Discovery Tree (RDT). Similar to a logic AND diagram, the RDT gives a clear view of the requirements the candidate designs must meet in order to be studied. The subsequent step to take after the compilation of the RDT, a requirement analysis is needed. The generated requirements are checked for consistency with other documents, systems and subsystems, provided the availability of information, and then discussed with stakeholders to evaluate whether said requirements meet the expectations of the latter. This being an independent study not directly involved with other projects, a discussion with the primary stakeholder, in this case the supervisor of this study, has taken place to kickstart the procedure.

3.2. Propellant storage system requirements

In implementing the aforementioned approach, the work performed by [46] applied to a propellant storage system for the DelFFi project is used as a guideline, while the sizing was done based on the *Delfi-PQ* PocketQube satellite. Shown in Figure 3.1, color-coded branches visualize the classification and grouping of identified subsystem requirements. A brief explanation for the different branches, as well as the requirement definition are given:

Budgets

The problem statement given above refers to *PocketQubes*, rather small entities. Weight, size and power limitations are to respected, yet performance must be maximized for the system to prove its advantages over larger scales. Requirements for this branch have been generated based on information from various sources, with numerical adaptations included to fill the gaps where necessary.

- *PROP-TNK-1.1*: *The total (wet) mass of the tank shall be less than* 32 *gr.*
  Rationale: data from [98] describe the mass allocation per component of the propulsion subsystem. By simple subtraction, the allowed wet mass for the tank is obtained.
- *PROP-TNK-1.2*: *The total (footprint) volume of the tank shall be less than* $10.584\ cm^3$.
  Rationale: $30\ \%$ allocation of the total available volume (4.2 x 4.2 x $2.0\ cm^3$). The $4.0\ cm$ from the literature review was updated to half the size, hence $2.0\ cm$.
- *PROP-TNK-1.3*: *The total power consumption of the tank shall be less than* $450\ mW$.
  Rationale: $10\ \%$ allocation of total available normal power ($4.5\ W$). Percentage determined after discussion with the supervisor as a first estimate.
- *PROP-TNK-1.4*: *The total cost of tank shall be less than TBD.*
  Rationale: for a technology demonstrator, cost management is relatively flexible, so no bounds are needed.
- *PROP-TNK-1.5*: *The tank design shall maximize the availability of* Δv, *within the constraints of Requirement PROP-TNK-1.2*
  Rationale: for this system, there is no specific velocity increment required, but the ratio between Δv and propellant capacity is strong, giving an incentive to design a better tank.

Components

The following components of a propellant storage system have been assumed to exist, according to [46]:

- *PROP-TANK-2.1*: *The tank shall be equipped with a fill/drain port.*
  Rationale: the port allows for propellant replenishment during testing phases, and potentially re-usable tanks.
- *PROP-TNK-2.2*: *The tank shall be equipped with pressure and temperature sensors of the stored propellant.*

Rationale: monitoring the propellant thermodynamic conditions assists the active parts of the module in thrust control.

- *PROP-TNK-2.3*: *The tank shall store non-hazardous propellant.*
  Rationale: safety regulations on Cubesats (see [70]) are limiting the propellant selection in terms of toxicity, pressure and energy density. Those are assumed to hold true for PocketQubes as well.

- *PROP-TNK-2.4*: *The tank shall allow the insertion of an optional bladder.*
  Rationale: an optional bladder may compensate for the lack of sealants in certain design concepts where capillary effects are not sufficient.

Material

A crucial aspect of this specific tank is material selection. Legal constraints as well as compliance requirements pose a limit to the available options.

- *PROP-TNK-3.1*: *The material(s) employed shall be qualified for use in space.*
  Rationale: Standard guidelines from [39]

- *PROP-TNK-3.2*: *The material(s) employed shall display a resilience value higher than TBD.*
  Rationale: A strong and flexible material is guaranteed to offer a greater performance during both containment and expulsion of propellant.

- *PROP-TNK-3.3*: *The difference in electric potential of selected material(s) shall be less than TBD.*
  Rationale: IF more than one materials are employed, the propellant acts as an electrolyte that may induce phenomena of galvanic (bimetallic) corrosion. Materials with similar potential and/or corrosion treatment are guaranteed to prevent contamination of either the tank or the propellant.

- *PROP-TNK-3.4*: *The selected material(s) shall have absorptivity and emissivity factors less than TBD.*
  Rationale: In case of a thermal control failure, the tank material shall minimize the radiation exchanged with the space environment so as to preserve the propellant's composition and thermodynamic condition.

Structure

Dealing with launch and internal loads translates into a sturdy structure frame that supports the mechanism function with minimal amount of mass and volume waste.

- *PROP-TNK-4.1*: *The tank shall be able to withstand a Maximum Expected Operating Pressure (MEOP) of* $5.5\ bar$.
  Rationale: The propulsion system thruster is expected to operate in the range of $1-5.5\ bar$.

- *PROP-TNK-4.2*: *The tank shall be able to withstand longitudinal acceleration loads between* -5 g_0 *and* +1.8 g_0.
  Rationale: 3.1. Sourced by [46].

- *PROP-TNK-4.3*: *The tank shall be able to withstand lateral acceleration loads between* -1.8 g_0 *and* +1.8 g_0.
  Rationale: 3.1. Sourced by [46].
- *PROP-TNK-4.4*: *The tank shall be able to withstand the sine equivalent dynamics.*
  Rationale: 3.1. Sourced by [46].
- *PROP-TNK-4.5*: *The tank shall be able to withstand the expected random vibrations.*
  Rationale: Rationale: 3.1. Sourced by [46].

Integration

Being a component of the propulsion subsystem, integration with the other components is a key factor for the design effectiveness.

- *PROP-TNK-5.1*: *The tank structure shall support integration with the propulsion module.*
  Rationale: In spite of the many assembly options, simplicity is prioritized.
- *PROP-TNK-5.2*: *The fill/drain port(s) shall be accessible after assembly and integration.*
  Rationale: The tank must be refillable during testing and forced failure conditions.

Performance

As in all products, accurate characterization of assets and shortcomings of the design is possible with a few performance metrics obtained by testing procedures.

- *PROP-TNK-6.1*: *The tank shall provide a positive pressure gradient in the range of* $1 - 5.5\ bar$.
  Rationale: The thruster is known to operate within a pressure range, so the tank must provide the needed pressure drop. Pressure values obtained from [100].
- *PROP-TNK-6.2*: *The tank shall display a stable operation for at least 1 year, or the equivalent of at least 6000 thrust cycles.*
  Rationale: The thrust cycles may vary in time and performance state, but the tank must react accordingly.
- *PROP-TNK-6.3*: *The tank shall display a stiffness ratio higher than TBD, in all off-axis directions.*
  Rationale: Deformations in degrees of freedom other than the desired lower the performance of the tank mechanism.
- *PROP-TNK-6.4*: *The tank design shall have a yield safety factor greater than 1.6.*
  Rationale: safety regulations obtained from [112].
- *PROP-TNK-6.5*: *The tank design shall have an ultimate safety factor greater than 2.0.*
  Rationale: safety regulations obtained from [112].
- *PROP-TNK-6.6*: *The tank shall maintain its functionality over a temperature range TBD*
  Rationale: The module is subject to temperature fluctuations, to which the mechanism must be resistant in order to provide a stable output.

A Requirement Discovery Tree is finalized by the identification of key and killer requirements. Killer are the requirements that force some solutions to be excluded from the selection

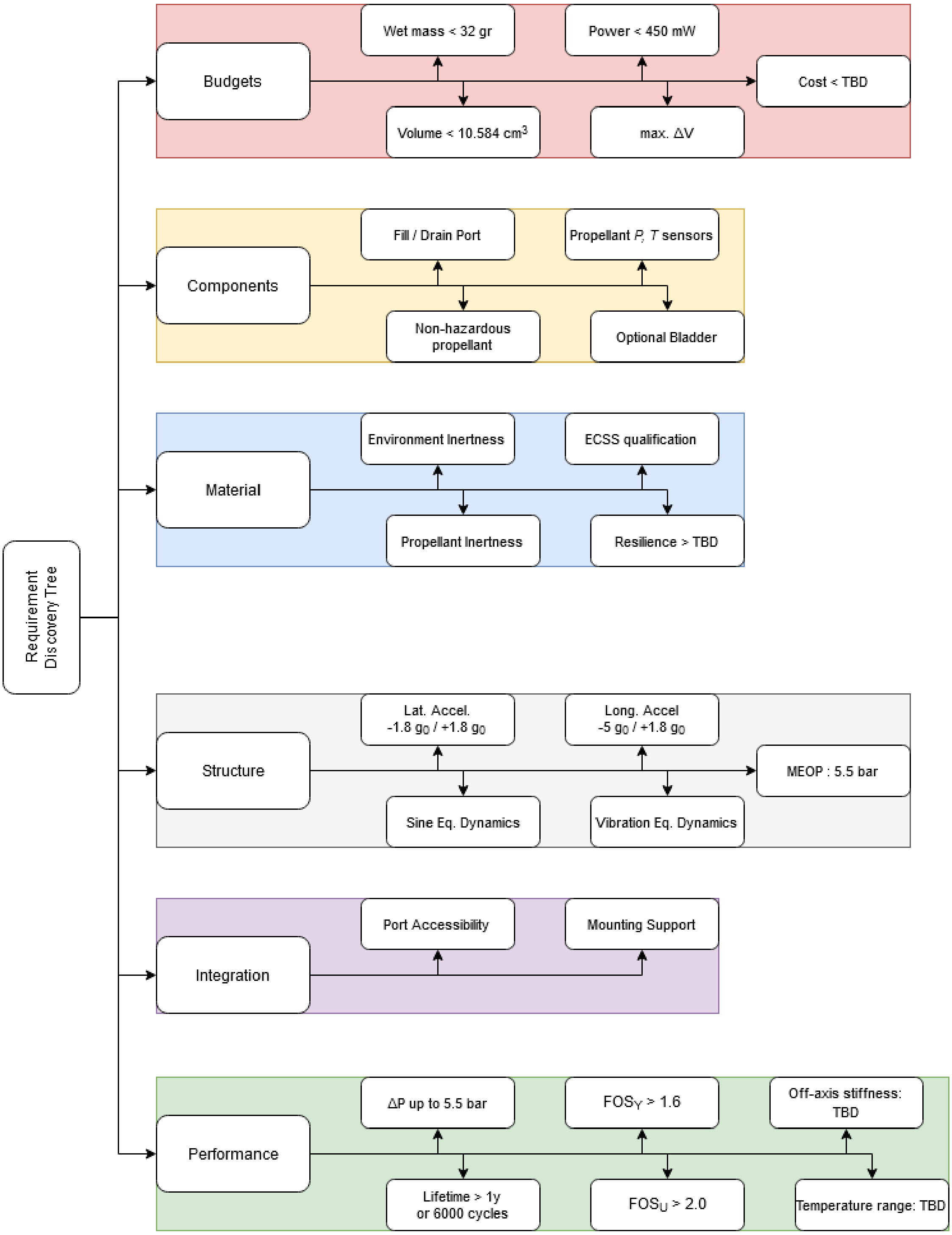

Figure 3.1: Requirement Discovery Tree for the propellant tank assembly.

process, reducing the design domain. Key are the requirements that drive the selection process, irrespective of other complementary or even conflicting requirements. In this work, they are highlighted in Figure 3.1 with blue and red respectively. Requirements 1.2 and 1.3 are obviously killers, being budget limits, while 3.1 is paramount for the safety of the tank and the satellite. As key requirements, 3.3, 4.1 and 6.1 seem to be excellent representations. 3.3 ensures an optimal chemical performance of the propellant when injected to the thruster, 4.1 drives the structure of the tank system and 6.1 is the leading performance metric that responds to the thruster's pressure demands.

Table 3.1: Soyuz user manual: vibration and sine equivalent dynamics. Sourced by [46].

Sine equivalent dynamics

Direction	Longitudinal			Lateral		
Frequency band (Hz)	5-10	10-30	30-40	1-5	5-30	30-40
Sine Amplitude	0.5	1.0	0.6	0.3	0.8	0.6

Random vibrations

Duration (s)	120	480	875
RMS Acceleration (g_0)	4.94	3.31	1.36

3.3. Design Challenges

Requirements in this work have been defined as standards that the resulting product must meet to be sufficient, but only represent part of the constraints imposed. Additional constraints are derived from design challenges pertaining to the product in discussion, in this case a PocketQube-sized water tank. One could consider as the primary contributor the limited know-how on PocketQube propulsion modules. Despite the rapid advances in large-scale and more recently Cubesat-level designs, which have resulted in commercialized propulsion units and the existence of thruster and valve modules as explained in Chapter 1, down-scaling the tank itself while including an expulsion component and providing good propellant capacity is still a question to answer. The limited amount of PocketQube launches (seen in Figure 1.3) partially proves the point, then complemented by cross-checking satellite catalogs [60], [104] for propulsion-enabled entities. The results are obvious: out of the 32 PocketQubes developed, only 4 have been launched as of August 2018, and none possesses a fuel-powered propulsion unit.

Setting aside the physical aspects of down-scaling existing designs, performance compromises are equally noteworthy to mention. Current generation propellant tanks at the Cubesat scale are expelling propellant via gas generators or pistons, which require power provision and control, increase the system complexity and negatively affect the performance reliability. Another important challenge to consider is the lacking flight heritage of compliant mechanisms as a whole. Despite some space applications relying on compliance have been proposed, they only relate to release/deploy mechanisms or vibration isolation [41], [124]. To date, no propulsion system is known to employ compliant mechanisms in any form or shape, and Cubesat-level systems are still based on classical approaches. Both factors highlight the difficulty in generating a well-performing and innovative design.

3.4. Conclusion and Remarks on Chapter

In this chapter, an extensive requirement framework was established to achieve the goals set in Chapter 1. Using a common systems engineering approach, the Requirements Discovery Tree (RDT), and a past project of high relevance with this study, the technical requirements are generated, justified and categorized based on the prominent aspect they describe, resulting in six groups. Key and killer requirements are found among the requirement set, such that the design options are reasonably limited and have a measurable figure to compare with. The poor or non-existent flight heritage of compliant mechanisms and the physical down-scaling of a propulsion storage system to this extent are the principal design challenges to take into account when assessing the potential design candidates. As a result, no immediate conclusion can be drawn about the expectations for the envisioned propulsion system, but it will be possible once a detailed design proposal is generated and tested, either from a theoretical or experimental perspective. The first step into this direction is taken in Chapter 4, where design candidates are discovered and evaluated under a two-stage trade-off analysis.

4

Trade-off Process

With the minimum specifications of a compliance-based propulsion storage system set in Chapter 3 and the essential knowledge on compliant mechanisms available in Chapter 2, the thesis must progress in the design selection process. Starting from a broad range of design ideas, this chapter unfolds based on the premise of concluding to a preliminary design, at a conceptual level. A two-stage trade-off strategy is constructed and executed to progressively reduce the design domain space, while each stage includes a dedicated sensitivity analysis to eliminate any bias towards any particular concept. The procedure is repeated for less prominent aspects of the design, namely materials, shape and configuration, leading to a finalized concept that can be fully analyzed in subsequent parts of the thesis.

4.1. Trade-off Strategy

The fundamental strategy in choosing a design consists in presenting the candidates, evaluate them under user-defined criteria and based on the individual and overall scores, advancing the highest-scoring design. In this case however, a more segmented approach is preferred. The reasoning behind the decision stems from the objective of this trade-off process, it being the smallest, lightest and fuel efficient tank. Having to select a concept based on numerical values would require an enormous amount of potentially fruitless research, given that some concepts may not even have been considered as liquid storage devices. The use of qualitative criteria to reduce the number of concepts into a manageable research scope is a more compelling idea. From that point, the trade-off according to measurable criteria is possible. On this basis, a two-level trade-off strategy is followed:

1. The design candidates, along with some background information on their common functionality, are presented.
2. The first level of the trade-off process makes use of abstract criteria to evaluate the capabilities of each candidate, to confirm whether the latter is suitable enough to be studied or not.
3. The best first-level candidates advance to the second level, where technical criteria are employed to quantified their characteristics.

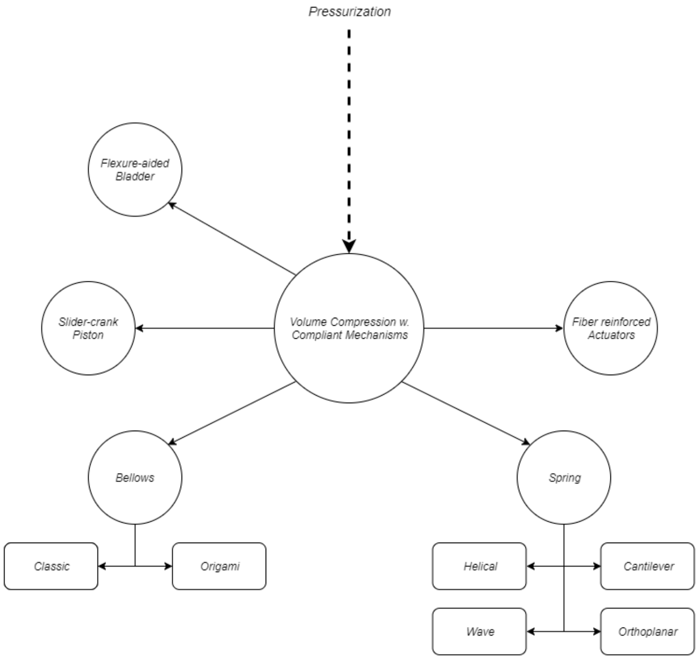

Figure 4.1: Design concepts participating in the trade-off

4. The best second-level concept is selected and the complementary trade-off processes for the main material and the design configuration take place.

4.2. Design Candidates

Executing the aforementioned process needs an acceptable amount of design concepts that enable the two-level selection. A brainstorming session and a literature survey were combined to derive a candidate list, with passive activation and low part count being the key aspects considered. The result is depicted in Figure 4.1, with a rudimentary structure-based classification to better display the differences between mechanisms. In the following parts, a brief overview of each mechanism is given.

4.2.1. Flexure-aided Bladder (FB)

The first concept to consider in the trade-off is a flexure-assisted bladder. Starting from the proposition of [93], that is a rubber bulb commonly found in medical applications, the design would augment the bulb's expulsion force through a clamping/squeezing mechanism composed of flexures. In [52], an extended catalogue of compliant mechanical elements provides ample ground for a suitable clamping mechanism, while original components can also be synthesized once the design is studied from a more technical aspect. The main point to acknowledge in this design is the lack of any relevant literature, setting a handicap against proven solutions.

4.2.2. Fiber-reinforced Actuators (FR)

Fluid storage and actuator devices may also come from the field of Biomedical Engineering. In particular, the famous *McKibben* actuator belongs to a group of pneumatic/hydraulic devices that are studied and tested with the aim of creating artificial muscles and in turn robotic entities like the ones reported in [30]. The traditional operation principle requires fluid to enter or leave the actuator, causing deformation and subsequently deflection along the central axis. Such a behaviour is feasible according to the structural schematic shown in Figure 4.2: an elastic tube is enclosed within a sleeve made of fibers that extend or contract when fluid is forced into or out the tube. The use of fibers is important in increasing the actuator's strength without sacrificing any of the flexibility.

Following the same reasoning, a propellant expulsion mechanism through fiber extension and contraction is possible, with any design issues to be overcome. For example, a hydraulic actuator contained in a light but rigid structure should be sufficient for the desired assembly, while preventing over-expansion/contraction caused by the axial deflection.

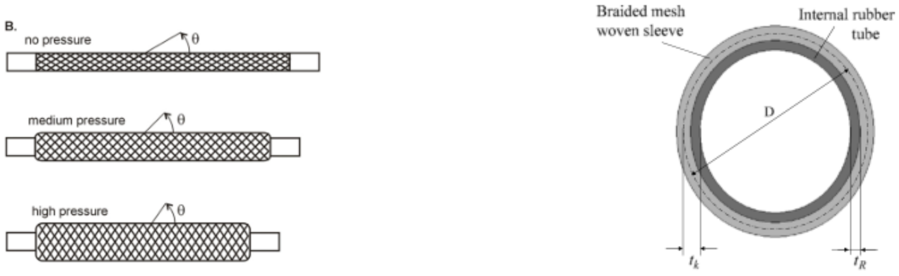

(a) Operating principle. Source: [30]

(b) Cross-section view. Source: [108]

Figure 4.2: Overview of a McKibben actuator and related fiber-reinforced actuators.

4.2.3. Crank-Slider Piston (CSP)

A well-developed volume compression mechanism can be found in the automotive industry and specifically Internal Combustion Engines (ICEs). Standard 4-stroke engines consist of four stages, one of which is the exhaust stage [94]. Figure 4.3 is indicative of the chamber state: right before the exhaust begins, there is a pressure buildup and the piston is contracted. During the exhaust phase, the piston extends due to the crankshaft rotation and expels gases, emptying the chamber. This particular stage could be replicated in the envisioned tank mechanism, on the condition of certain technical issues being tackled:

- In order for the candidate to be in accordance with the prerequisites of a compliant mechanism, the rotary aspect must be exchanged for a flexure-based equivalent.
- The difference between exhaust gases and the liquid propellant may translate in variation of the loads exerted at the piston, therefore the design must be able to cope with any additional loads.

A tentative answer is found in a crank-slider piston. The principle is similar to the ICE's exhaust stage, with the actuation happening due to the elastic deformation of linking flexures between the tank wall and the piston. The slider component is introduced to maintain alignment when operating. Different variants of a crank-slider piston have been reported in [31], [34] and [90].

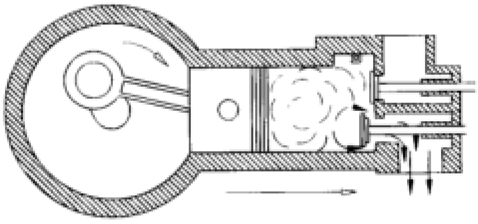

Figure 4.3: The exhaust stage of an ICE. Source: [94]

4.2.4. Classical Bellows (BEL)

Another form of body-changing fluid expansion is observed in bellows, an elastic corrugated shell that is found in a broad spectrum of applications, such as the ones reported in [87] and [23]. Of particular praise is the work of [75], discussing the capabilities of a bellows to act as a reusable and collapsible propellant storage device. The operation principle is dual: when force is applied to one extremity of the bellows (see Figure 4.4a), the corrugations bend incrementally, causing a longitudinal compression or extension, which in turn expels fluid. This can either happen internally, meaning that the expelled fluid corresponds to the internal volume change of the bellows, or externally in a similar to piston compression method.

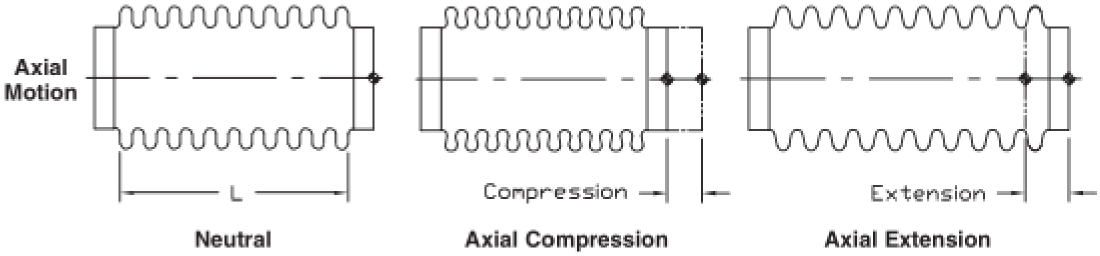

(a) The working principle of a bellows. Source: [6]

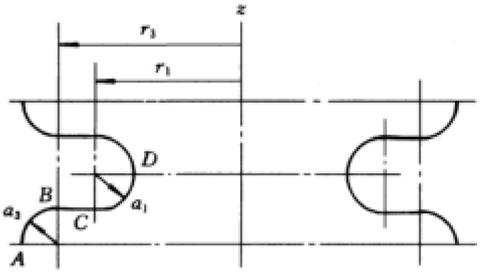

(b) Single corrugation set of a U-shaped bellows. Source: [126]

Figure 4.4: Overview of a classical bellows mechanism.

4.2.5. Origami Bellows (ORB)

The art of creating shapes from folding a single piece of paper, *Origami*, has sparked great interest among scientists and engineers, due to the possibilities this material manipulation technique offers. An Origami mechanism is created from a thin sheet of material folded at designated locations, converting a 2D entity into a functional 3D mechanism. Theoretical and practical examples discussed in [48] support the strong connection between Origami and

(a) Deployed. (b) Compressed.

Figure 4.5: Volume footprint of an Origami Bellows. Source: [25]

compliant mechanisms, both acquiring functionality through deflection of flexible elements. One could argue that the Origami - and the extended Kirigami method - is one of the possible techniques of synthesizing compliant mechanisms.

Applying the principles of folding material within a computerized framework enables the generation and optimization of several types of mechanisms, all being lightweight and collapsible into small volumes, trait that is particularly useful in a wide range of applications: solar arrays [125], heat dissipation fin enhancers [111] and soft active robots [71] are but a few instances showcasing the feasibility of deployable, functional designs. For the goal of this study to create a fluid container, a more attractive application has been presented by [25] and [97], namely the *Origami Bellows*. Expanding upon the idea of a classical bellows, folding the thin shell in an adequate manner allows a greater deflection of the walls and hence a higher amount of fluid is displaced. Figure 4.5 proves the point, while noteworthy is the fact that the Origami bellows reported in said literature have already been designed for space applications and harsh environments, highlighting the affinity of the concept with the author’s vision of an Origami-based tank.

4.2.6. Cantilever/Leaf Spring (SL)

Cantilever-type springs are a playful nomenclature for free-hanging thin material stripes, essentially behaving as flexures from their free ends. While simple in their operation, cantilever-type springs have found wide application in precision instruments such as Atomic Force Microscopes [67]. A variant more suited to this study is the double-cantilever spring, or as it is known in the automotive industry, the leaf spring $\left(\text{[62], [99], [102]}\right)$. Consisting of a single or multiple thin beams, the leaf spring was the original suspension system in land vehicles, and is still used in trucks and other heavy-duty vehicles for its resilience to high loads and impact forces, as well as its manufacturing simplicity.

A major issue connected to the leaf spring as a concept is the end geometry. In Figure 4.6b, a typical leaf spring used in automobiles is shown. Focusing on its extremities, one can notice the so-called ’eyes’, that convert any axial motion of the leaves into bending, so from a design viewpoint, this is a pinned-pinned beam problem. However, this is not possible (or at the very least not advisable) as the insertion of contact points to enable the rotation not only renders the tank assembly more difficult to manufacture, but adds friction and failure points in the structure, voiding the purpose of compliant mechanisms. A workaround accepted at this stage is affixing this mono-leaf spring into the tank walls, at the cost of some deflection and stress performance.

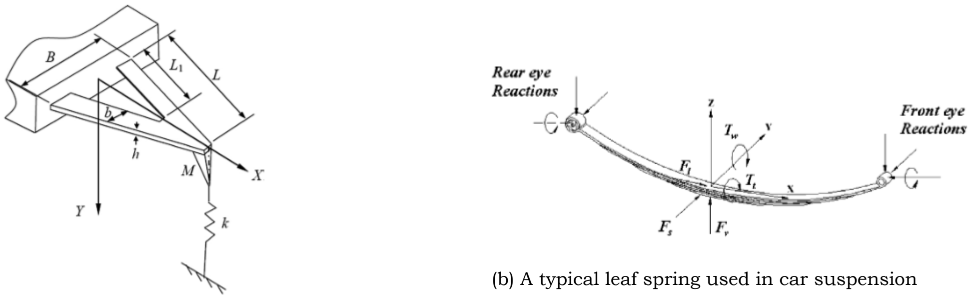

(a) Schematic of a V-shaped cantilever used in Atomic Force Microscopy. Source:[67]

(b) A typical leaf spring used in car suspension systems. Source: [99]

Figure 4.6: Different variants of a cantilever spring.

4.2.7. Helical/Coil Spring (SH)

The quintessential form of springs. The helical spring is a continuous flexure made out of wire that, contrary to the usual bending deflection occurring in compliant systems, it is locally subjected to torsion. This minor difference does not go against the definition given in Chapter 2, so it is treated as part of the candidate list. Applications of helical springs are abundant, ranging in scale, environment and shape, so any background information is somewhat unnecessary. For the tank assembly, a coil spring connected to an interface platform should provide the required load capacity and elastic deflection to act as an expeller.

4.2.8. Wave Spring (SW)

A less prominent form of spring, focused on applications with strict volume budget, is the wave spring. Coined by *Smalley Inc.*, this component is an arrangement of wave-like spring washers stacked on top of each other, as shown in Figure 4.7. The trade-off between a wave and a coil spring is reduced to a preference between deflection and volume footprint, since the flexure-like pattern of the washers occupies less space than a single turn of the coil for the same load capacity, but in exchange creates more contact points between the different levels and thus deflection is minimized.

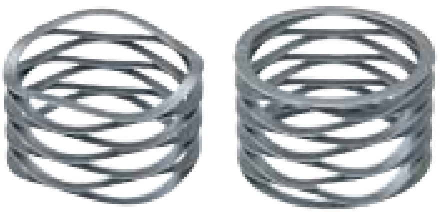

Figure 4.7: Smalley's *Crest-to-Crest* wave springs. Source: [9]

Figure 4.8: A Compliant Ortho-Planar Spring (COPS) design. Source: [91]

4.2.9. Ortho-planar Spring (SOP)

Discussed in [52] and [91], the ortho-planar spring is the amalgamation of three fields of study: lamina emergent mechanisms (LEMs), planar springs and compliant mechanisms. A standard design is shown in Figure 4.8: the base profile is connected with the center profile through a number of internal flexures. When in the undeformed state, the planar structure occupies minimal volume within the tank. The flexures bend when either profile is loaded and the other profile is thus extended in the axial direction. No practical applications have been reported in literature to validate its performance other than the piezo-electric harvester reported in [36] and the force/torque sensor of [113], but they are indicative of the spring's performance.

4.2.10. Eliminated options

Aside from the accepted candidate designs, the brainstorming session also resulted in other, less satisfactory alternatives which were discarded even before the first trade-off. A brief explanation for excluding some of the ideas is given:

Elastic bladder: The proposition in [93] for an elastic bladder containing the propellant would be sufficient for the purposes of this study, assuming the bladder is fully stretched (hence, maximum energy stored) when filled. Understandably this comes with potential burst risks, or contraction failure due to creep. Most elastic bladders are made out of elastomers, which are notorious for their time-dependent energy losses [20] and consequently are prone to local tearing or loss of their spring-like functionality. Without the use of a gas to pressurize, hence to create a high force imbalance, the bladder itself is theoretically insufficient.

Squeezer tank: Among the possible methods of inducing volume compression, a squeezing action has been considered. Within the fixed envelope of the tank, internal platforms would deploy during thrust from the walls and create a volume change that corresponds to propellant expulsion. The approach is rather problematic, for a few reasons: having deployable parts in the assembly not only contributes to failure risks, but creates a greatly complex design, relying on various geometry aspects such as the orientation and the gradual flexure length increase. In addition, the operation principle lends itself to asymmetric volume compression, which can cause propellant to leak into the deploying flexures, possibly blocking the actuation.

Torsion spring: Another path to store and release energy relies on torsion springs. Attached to a screw for instance, such a release system might be able to resolve symmetry loading issues. However, the inclusion of rotating components to such a small and self-activated system can only bring negative consequences in design simplicity, safety and in particular performance, as the propellant capacity may be heavily affected.

4.3. First-level criteria

For the first level of the trade-off process, a qualitative set of criteria is used to reduce the number of concepts. This set looks into the functional aspects of each design without getting into time-consuming technicalities, based on the desired properties a passive tank mechanism should have, while promoting simple solutions that allow for quick sizing of the advancing concepts later in the process. An iterative process of criteria selection concluded in the list hereby presented:

Design Function: How can the concept be used for propellant expulsion purposes. Depending on the modifications needed to achieve desired functionality, the design may increase in complexity and budget footprint. The following characterizations are deemed suitable:

- *Direct*: The design operates as-is, with the loaded state being equivalent to the full capacity condition of the tank.
- *Modified*: The design is modified such that is acquires the Direct functionality.
- *Dual*: The design is flexible enough to be utilized with or without any modifications to achieve the same level of performance.

Compliance Type: How stresses are managed when the mechanism is loaded. During operation, concentrated stresses may give rise to failure unless carefully designed, with the cost of added mass or complexity. The following characterizations are deemed suitable:

- *Lumped*: The developed stresses are concentrated on the flexures, much like traditional mechanisms display higher stresses at the linking joints.
- *Distributed*: The stresses are spread throughout the mechanism body.

Expulsion Type: How the mechanism achieves the propellant expulsion. Depending on the method, the propellant capacity and overall mass budget are affected due to integration of different components. The following characterizations are deemed suitable:

- *Internal*: The mechanism is housed in a rigid envelope and moves relatively to it. The volume distribution between mechanism and propellant changes during the expulsion process.
- *External*: The mechanism is the envelope itself, connected at mounting points. At thrust, the envelope/mechanism collapses into the smallest volume, effectively expelling propellant.
- *Dual*: The design can operate either as internal or external.

Literature Background: How well the concept has been studied and developed. Scientific articles and technical brochures with cataloged figures of merit should allow the reader to better understand the assets and drawbacks of each design. The following characterizations are deemed suitable:

- *Conceptual*: Literature found is limited to student works or the abstract description of design ideas.
- *Theoretical*: The design has been studied enough to produce approximate models and numerical predictions for the merit figures of interest. The models are either equation-based, or Finite Element related.
- *Experimental*: Articles in this category include manufactured prototypes for testing and possibly commercial products with verified performance metrics.

Analytic Model Support: How well can the concept be approximated by simple analytical (equation-based) models. While all candidates are expected to have been studied sufficiently for the reader to draw some conclusions, approximate analytical models that enable quick calculations are a significant aid towards avoiding excessive article research and generating tailor-made data for the tank in discussion. The following characterizations are deemed suitable:

- *None*: In literature found, the proposed cannot be reduced to quick calculations of performance characteristics. This includes analytic models, high-order differential equations and Finite Element solutions.
- *Limited*: While analytical models seem to be present, they are quite complex and rely on many unverifiable assumptions and thus variables. Calculations are possible, but highly inaccurate.
- *Extended*: The concept is well defined through simple analytical approximations. Assumptions are reduced to the absolute necessary, whereas results are in good agreement with experimental counterparts.

Motion Control: How well can the concept perform a uni-directional movement. This ensures that the energy stored in the mechanism when loaded with propellant is released back into the propellant via its expulsion. Unwanted, perpendicular to the expulsion direction, motions may subtract useful energy and thus reduce the propellant capacity. Corrections are possible in the form of guiding devices/rails, acknowledging the effects on mass and volume. The following characterizations are deemed suitable:

- *Insufficient*: Motion in the mechanism is predominantly uni-directional, but unless controlled by rigid supports, off-axis displacements are definitely noticeable.
- *Sufficient*: Motion in the mechanism is uni-directional within a range of loads, but can be further improved with minor design modifications.
- *Inherent*: The design is intended for uni-directional motion, with sideways movements controlled by symmetry.

As seen from the criteria, the qualitative ratings given for each design candidate create some imbalance when comparing their suitability. An efficient countermeasure to this imbalance is the quantification of the ratings with an agreeable metric. In this instance, the contribution of each criterion to the design complexity is weighed in depending on how well the criterion serves the purpose of identifying simple design solutions. In addition, the individual criteria are assigned to a range of numerical values from 1 to 3, so a weighted sum of the values should give an overall score representing the mechanism's usefulness and design simplicity. The rating scheme is shown in Table 4.1:

The contribution factors shown in the table are derived from a tuning strategy aimed at countering any initial bias, as well as showing a logical dependency of the criteria. Starting

Table 4.1: Quantification of first-level criteria

Criterion	Attribute	Rating	Contribution (%)
Design Function	Modified	1	25
	Direct	2	
	Dual	3	
Compliance Type	-	-	15
	Lumped	2	
	Distributed	3	
Expulsion Type	Internal	1	5
	External	2	
	Dual	3	
Literature Background	Conceptual	1	10
	Theoretical	2	
	Experimental	3	
Analytical Model Support	None	1	30
	Limited	2	
	Extended	3	
Motion Control	Insufficient	1	15
	Sufficient	2	
	Inherent	3	

from a random distribution of 20% and 10% values that sum to 100%, a 5% in/decrement is iteratively re-distributed from one factor to another, reflecting their impact either on the concept complexity or on different criteria. In essence, this is a quantified promotion-demotion scheme. In addition, all factors are capped at 30% to prevent instances where two factors would outweigh the remaining four by a large margin, inducing unwanted bias. Insofar as the criterion dependency goes, a tentative argumentation is given:

The development stage of a concept reported in literature, even at larger amounts, is somewhat worthless if the design does not lend itself to quick sizing estimates. That said, the *Literature Background* criterion is unimportant in terms of design simplicity, whereas the *Analytical Model Support* criterion was given the greatest contribution. The *Expulsion Type* criterion follows a similar logic, in that regardless of the way propellant is moved out of the tank, the design complexity is overall unaffected at this stage. Contrarily, the *Compliance Type* and *Motion Control* criteria have a slightly stronger impact on the design choice, with different models being needed for each circumstance. Lastly, the *Design Function* criterion is almost as crucial as the *Analytical Model Support*. The reason is quite apparent: a design requiring modifications poses a new challenge to the designer related to which modification is more suitable, more feasible etc.

4.3.1. First TO results

According to the methodology described so far, the first level trade-off is presented in Table 4.2. The overall scores derived from weight-averaged summation are in turn averaged and compared to the mean value, ensuring that better performing designs are sure to be qualified for the second, more technical, trade-off. From the values observed, 4 designs belonging to 2 categories are qualified: a bellows-type mechanism (BEL) and three springs, namely the cantilever/leaf (SL), the helical/coil (SH) and the wave (SW). Surprising is the fact that purely flexure-based compliant mechanisms are underperforming, contrary to the author's expectations. The simple analytical model proposed by [51], the strong point of flexures when thinking about the design process, cannot supersede the shortcomings related to their functionality. For instance, modifying the concept to operate in the opposite direction (tension instead of compression) is impacting the stresses developed in flexures, hence requiring stronger and perhaps more intricate designs. This is not a conclusive note, but rather an indication that with the current criteria, compliant mechanisms that go by the original definition are not as suitable for the purpose of volume compression.

A particular case is the Origami Bellows (ORB), which is mostly affected by the low score on Analytic Model Support. Despite the exemplary work of [25], the multi-variable analytic model that relies on foldable tesselation units does not lend itself to a quick performance estimate. Instead, the concept seems better suited to a detailed thesis project similar to the cited one that will better reflect the scores given for the remaining criteria.

4.3.2. Sensitivity Analysis

The scores in Table 4.2 reflect the performance of each concept from a qualitative viewpoint, but have been correlated to numbers based on a subjective contribution factor scheme. Countering the issue, a *Sensitivity Analysis* is used to validate the rationale used. Various methods of conducting this analysis exist, but for a simple case like the trade-offs reported in this work, the *One-Factor-At-a-Time (OFAT)* method is more than sufficient. Each criterion contribution factor is swept within a range of values while the others remain constant and

Table 4.2: Results of first trade-off

	CSP	FB	FR	BEL	ORB	SL	SH	SW	SOP
Design Function	2	2	1	3	3	2	2	2	1
Compliance Type	2	2	3	3	3	2	3	3	2
Expulsion Type	1	2	2	3	3	1	1	1	1
Lit. Background	1	1	3	2	3	3	3	3	1
An. Model Support	3	3	2	2	1	3	3	3	3
Motion Control	1	1	2	2	2	3	2	3	3
Overall Score	2.00	2.05	2.00	**2.45**	2.25	**2.50**	**2.50**	**2.65**	2.05

the effect is imprinted on the overall concept score. The assumption required to perform the analysis derives from the trade-off rationale of one criterion not outweighing the rest. If this were violated, then there would be no trade-off and the designer would only look for a concept based on the criterion with the highest weight value. That said, each criterion factor is swept from 0% to 50%. The analysis results in the charts of Figure 4.9.

A few conclusions can be drawn from this chart set, related to the trade-off orientation and the concepts involved. To begin with, the results are quite uniform across the board, proving that the qualified designs would most likely have been chosen under different weight contributions and the less performing ones always discarded. One could consider this as a two-tier option set of designs. Moreover, the overlaps occurring between various options (e.g. *SH* and *SL*), as well as the appearance of turning points allow the designer to notice this: the concept selection in this work has operated in two main poles, namely the Design Performance and the Design Simplicity. By varying the contribution factors of the criteria, a qualified concept can respond better to performance aspects like Motion Control, or to limitations imposed by the product at hand, such as the Design Function. Since this is a project run by a student, the balancing of weights promoted simple solutions at the expense of some performance. An interesting point to have in mind is the superiority of the SW concept seen in almost all charts, hinting towards a potential winner that may be verified by calculations in the second trade-off.

4.4. Second-level criteria

For the second level of the process, the advancing designs are materialized by means of performance metrics. The criteria employed provide these metrics through analytical models found in relevant literature, primarily focused on the mass and volume footprint of each solution. In addition, the quantification of metrics is derived from logical assumptions that lay a common ground for all concepts and are listed as follows:

- For designs based on an internal expulsion system, the required containment envelope is to be made out of Aluminum 6061-T6, a lightweight and common material. Properties obtained from [7].
- For the mechanism itself, the 17-7 PH variant of stainless steel is used, with excellent properties and suitability for aerospace applications. Properties obtained from [8].
- Going by the size limitations of the Pocketqube platform, each of the tank dimensions

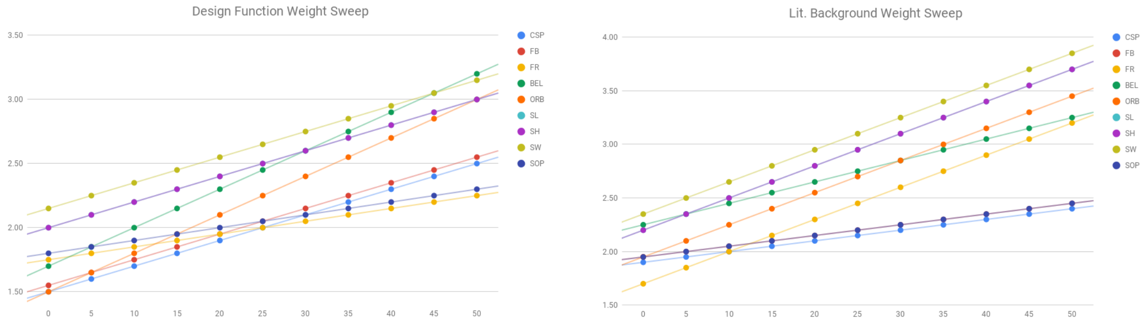

(a) Design Function

(d) Literature Background

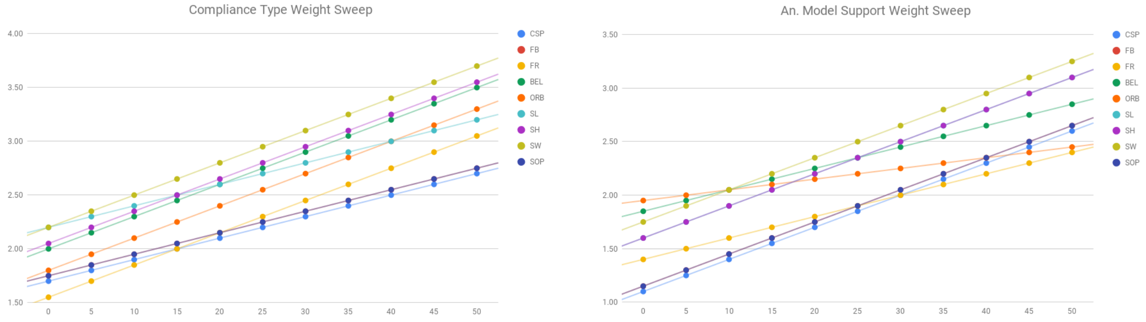

(b) Compliance Type

(e) Support of Analytical Model

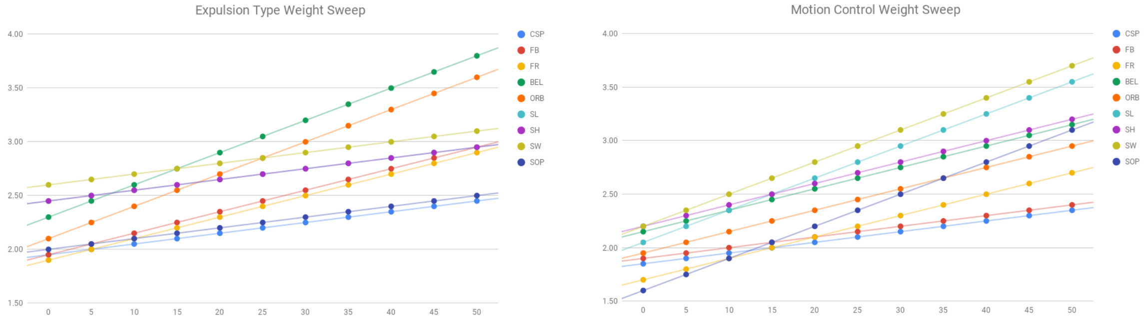

(c) Expulsion Type

(f) Motion Control

Figure 4.9: Sensitivity analysis of first trade-off

is limited to less than $3\ cm$, to also account for any interfaces/mounting or other components.

- Contrary to the expulsion coefficient introduced in [93], the system is assumed to fully expel the available propellant, allowing the estimation of the maximum capacity. For the latter (though somewhat inaccurate) a cylindrical volume with the deflection corresponding to its length is assumed, in line with the anticipated mechanism and tank shapes.
- While the highest load is expected to come from the pressure developed in the tank, the lack of a predefined contact area for this pressure to be transmitted in the mechanism complicates the calculations. A force load of $200\ N$ is imposed to circumvent the issue.

Just like the first level, the selection of suitable criteria was not straightforward, but concluded after taking into account different measurable parameters, as well as the system requirements. Below, the chosen criteria are described:

Operating Deflection: As explained in Chapter 2, all compliant mechanism showcase deflection towards one or multiple directions. Following the assumption of propellant capacity being directly connected with deflection levels, it is natural to include the latter as a trade-off criterion, with an important remark: the operating deflection is the mechanism's maximum deformation that does not compromise its mechanical properties, such as the yield or shear stress.

Propellant Capacity: The quintessential criterion of the trade-off, being one of the objectives. Calculated by obtaining the deflection levels (see above), as well as maximizing the mechanism's cross-sectional area through stress formulas.

Volume Footprint: Aside from the internal volume, expressed by the propellant capacity, the volume budget is equally affected by the tank's footprint when integrated in the propulsion module. The tank housing (or mechanism for external-type) is used to determine its value, approximated by a thin cylindrical shell. Accounting for the mechanism, the propellant and housing walls, the volume footprint is checked against the assumptions made earlier.

Dry Weight: Another system objective, the tank's dry weight must be contained, minimizing its footprint for the mass budget. Essentially, all non-propellant parts are summed to generate the criterion value from the assumptions made so far. The weight contributions come from the mechanism and the envelope (for the internal-type), since auxiliary parts like sealants can be neglected.

Similarly to the first-level scoring scheme, weighted ratings are summed to extract the overall score, but with a different method. For each criterion, the individual scores are averaged to obtain a reference point. Then, these scores are remapped to a 0-10 range based on how well each design performs compared to the mean value, the latter corresponding to 5. The results are weighed and summed according to the contribution factor of each criterion to obtain the final score. The equation set 4.4.1 is indicative of the process. The contribution factors follow the pattern of the first level trade-off, but they are tuned to promote maximum Δv and fulfillment of Requirement 1.5 (see Ch. 3). Starting from an equal 25% weight, a 5% in/decrement is reassigned to factors until a sufficient bias towards the requirement is ensured. In particular, the *Propellant Capacity* criterion is dominant in this trade-off, as it has been proven in [46] that a change in available propellant affects the $Deltav$ more than an equal change in the total dry mass. The *Dry Weight* and *Volume Footprint* criteria are almost equally important in respecting Requirements 1.1 and 1.2, with a small priority to the mass factor. The *Deflection at Load* criterion is given the last priority, for two reasons: first, it is complementary to the *Propellant Capacity* and to preserve balance in the trade-off, it was assigned a lower weighting factor. Second, while the study is concerned with flexible mechanisms, the key objective is to create a tank within a specific budget. That said, a design subject to higher deflection is of little use if heavy or voluminous, hence the lower factor.

$$Mean\ Value = \frac{Sum\ of\ Individual\ Scores}{Number\ of\ Designs} \tag{4.4.1}$$

$$Remapped\ Score = 5 + 5 \cdot \frac{Individual\ Score - Mean\ Value}{Best\ Score - Mean\ Value} \tag{4.4.2}$$

Table 4.3: Quantification of second-level criteria

Criterion	Limit Values	Contribution (%)
Deflection at Load	-	15
Propellant Capacity	Req. 1.5	40
Volume Footprint	Req. 1.2	20
Dry Weight	Req. 1.1 - Prop. Capacity	25

4.4.1. Second TO results

The first trade-off relied on basic literature search to draw conclusions on the design candidates, with qualitative/abstract criteria being adequate for the purposes. At this level, however, the quantification of design parameters is imperative and thus needs their extraction from the available analytical models. In this section, the equation sets for each qualified design are implemented to derive the trade-off criteria values. For the sake of consistency, the model-independent equations are presented below:

$$V_{to} = \pi \cdot (\frac{D_{o,mech}}{2} + h)^2 \cdot (L_{free} + 2h) \tag{4.4.3}$$

$$m_p = \frac{\pi}{4} \cdot D_{o,mech}^2 \cdot \delta_{mech} \tag{4.4.4}$$

$$m_{dry} \simeq m_{shell} + m_{mech} \tag{4.4.5}$$

$$m_{shell} = \rho_{al} \cdot (V_{to} - \pi \cdot \frac{D_{o,mech}}{4}^2 \cdot L_{free}) \tag{4.4.6}$$

where $D_{o,mech}$ is the outer cross-sectional dimension of the mechanism and δ is the operational deflection at the work height. L_{free} is the mechanism's free length and h is the envelope sheet thickness. Speaking of the latter, a quick sizing method has been set up, based on a thin cylindrical shell with external volume V_{to} and internal volume V_{ti}. A companion *MATLAB* script file called *SizeTank* is found in Appendix B.

Classical Bellows

Regarding the prediction a bellows' behaviour under load, the quite detailed work of [126] is exemplary. The mechanism is treated as an arrangement of thin corrugated shells, each extending or contracting in a uniform manner. For a single corrugation set, the following equation applies:

$$h_1 = \frac{h}{\sqrt{12(1-\nu^2)}} \qquad \delta = \frac{2q_o}{E_s h \cdot h_1^2} \cdot f(a_1, a_3, b) \tag{4.4.7}$$

In Equation 4.4.7, f is a set of functions with arguments the corrugation radii a_1 and a_3, the width of the annular plate b, and the thicknesses h and h_1, with ν being the Poisson ratio. Moreover, q_o is the axial force F per unit length of the mean bellows radius R_o. The reader is referred to Figure 4.4b for the schematic used in the calculations. The equation format is the result of a multi-page analysis of the toroidal shell equation: starting from a toroidal shell approximation, a corrugation is segregated into distinct deformable elements, each subject to either an tensile force or a moment. The stress analysis of all elements is then simplified to obtain the form above, based on these f functions. For all mathematical expressions, the reader should consult the work of [126].

Cantilever/Leaf Spring

For a mono-leaf spring, the standard cantilever beam theory is used, with a fixed-fixed boundary condition. It is an excessively simplified method and does not reflect real-world applications where leaf springs are modeled after pinned-pinned boundaries, but for the scope of this trade-off, a magnitude scale of the desired properties should be sufficient for safe conclusions. The methodology is summarized in Equation 4.4.8, with L_o the spring's horizontal length, b the width, h the spring thickness, and the subscript s refers to the stainless steel employed.

$$h = \sqrt{\frac{6F}{\sigma_{y,s}}} \cdot \sqrt{\frac{L_o}{b}} \qquad \delta = 6F \cdot \frac{1}{bE_s} \cdot \left(\frac{L_o}{h}\right)^3 \tag{4.4.8}$$

Direct calculation of properties from this point is possible by replacing $D_{o,mech}$ with L_o.

Helical/Coil Spring

The classical coil spring is an extensively studied mechanism with a simple geometry format. While the spring is subject to torsion, the deflection is still within the elastic region, hence the compliance. Among the vast literature, the spring design guide in [24] facilitates the determination of the criteria values. Using Figure 4.10 as a guideline, the stress of a helical spring is calculated as a superposition of axial tension/compression and torsion. Using Castigliano's theorem, the deflection formula is derived as a function of geometrical and material properties. In summary, the equation set 4.4.9 is shown below, with a more in-depth discussion present in the aforementioned source. Among the variables, d is the spring wire diameter, D the mean spring diameter, K a stress-correction factor and N is the number of deflecting turns.

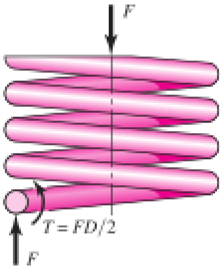

Figure 4.10: A helical spring model. Source: [24]

$$\tau = K \cdot \frac{8FD}{\pi d^3} \qquad \delta \simeq \frac{8FD^3N}{d^4G} \tag{4.4.9}$$

Wave Spring

The wave spring is a well defined mechanism based on multiple flexures stacked upon each other. Assuming equivalent turns, the multiplicative method applies by solving the equations for a single turn and transferring the outputs to the number of turns. As a starting point, the equations from [37] are implemented for a single wave spring washer. Briefly speaking, each washer is a ring comprised of crests and valleys. A circular ring approximation converts said waves into additional torsion and bending moments that contribute to the main axial compressive force. Using Castigliano's theorem, analytic expressions for the stress and deflection profile of said washer arise in the form of parametric functions of its shape and 'waviness'. The mathematical context is discussed at a deeper level in [37] with a multi-page derivation of load conditions, stresses and so forth.

Final results

In the following table, all sizing calculations are gathered and compared according to the proposed averaging and re-mapping strategy. The best-scoring candidate is marked with bold letters.

The results of the second level trade-off provide ample content for discussion, with both expected and unexpected numerical values. To begin with, the values obtained for the leaf spring are too distant from the average components. The author is inclined to accredit the anomaly to the oversimplified model used, as well as the concept itself. On the one hand, the model can only predict the properties of a straight beam, ignoring the thickness parabolic variation that is described in mono-leaf springs of available literature. On the other hand, the leaf spring as a physical object displays high length-to-width and length-to-thickness ratios. This calculated design is not in agreement with the general concept, so inaccuracies were expected.

An additional point must be made about the comparison between a helical and a wave spring. The initial expectation when studying the wave springs was their potential superiority over the helical spring, because the space saved from the more compact part would be occupied by propellant. However, the analytical models are in agreement with common sense: with load capacity taken as constant, the spacing between the turns of the helical spring enables the part to deflect significantly. Contrarily, the sinusoidal wave pattern of each turn of the wave spring creates more contacts points for the load to be dissipated, ef-

Table 4.4: Results of second trade-off

	BEL	SH	SL	SW	Mean Values
Prop. Capacity (g)	1.2	3.3	0.09	1.2	1.43
Dry Weight (g)	16.9	13.2	2.9	14.2	11.8
Deflection (mm)	3.2	9	0.02	4.1	4.08
Vol. Footprint (cm^3)	8.64	8.87	2.29	8.8	7.13
			Criteria Scoring		
Prop. Capacity	4.39	10	1.21	4.39	
Dry Weight	2.13	4.21	10	3.65	
Deflection	4.1	10	0.88	5.02	
Vol. Footprint	3.43	3.3	10	3.27	
Overall Score	3.63	**7.55**	4.66	4.16	

fectively reducing the deflection. In fact, it can be proven that an increase in the number of waves is inversely analogous to the turn axial deflection.

Further, one can notice that, with the exception of the leaf spring, the dry weight and volume footprint of the design candidates are highly comparable. This may indicate the range within which the final mechanism may lie, but it may also imply that an equivalent mechanism with a better load-deflection relationship could replace all the above.

4.4.2. Sensitivity Analysis

Similar to the first trade-off, the scoring system is affected by subjective preferences for certain criteria to be more important. The smaller group of criteria set forced some imbalance between the criteria, with a great emphasis towards propellant capacity, so an *OFAT* analysis is employed. The graphical depictions in Figure 4.11 are presented below.

This instance presents both similarities and differences with respect to Figure 4.11, due to the criteria differences and the overall performance of each concept. The introduction of measurable values in the trade-off evaluation creates a larger gap between the alternatives, such as the one seen in Figure 4.11b, however the general trend remains for the most part unchanged: the best performing design (*SL)* maintains its advantage over the other candidates within a large fraction of the sweeping range. An surprising point to acknowledge in this trade-off is the peculiar behaviour of the leaf spring (*SL*). Looking at the individual scores, it performs poorly in the most crucial aspects (Deflection and Propellant Capacity) and excellently in the Dry Weight and Volume Footprint aspects. The summation leads to an average result, which misleading as it may be, places the concept above the wave spring (*SW*) and the bellows (*BEL*). In addition, the poor performances in Deflection and Volume Footprint seem to be unaffected by the weight sweep, indicating a potentially erroneous model used for the approximation. Safe conclusions about the specifics of the SL cannot be drawn, so a comparison of the other three may be more beneficial for the study, which again promotes the Helical Spring (*SH*) as the design to employ for the generation of a self-pressurizing tank.

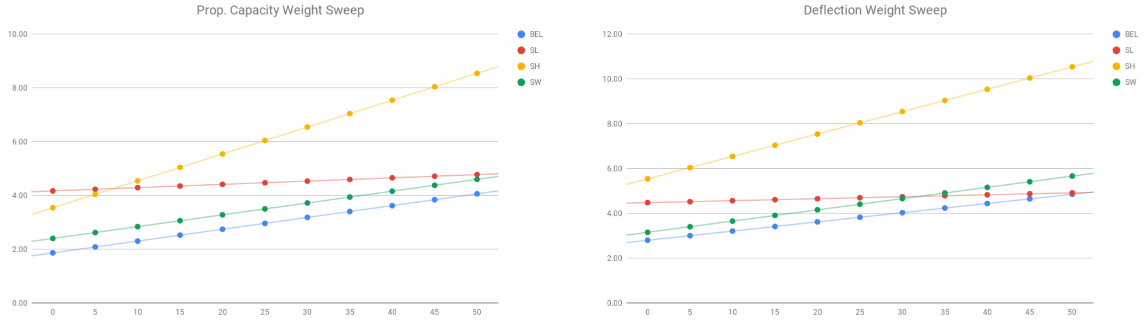

(a) Propellant Capacity

(c) Deflection

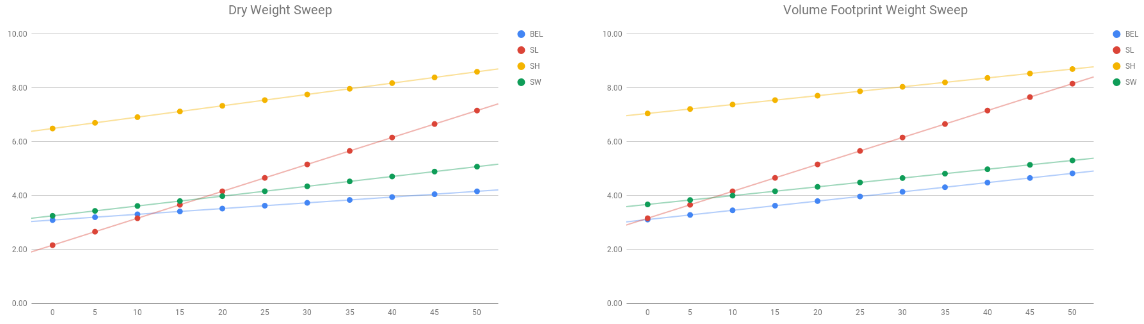

(b) Dry Weight

(d) Volume Footprint

Figure 4.11: Sensitivity analysis of second trade-off

4.5. Practical Design Trades

With the general concept of the tank defined, the study can now proceed to the next stage, the realization of a preliminary design. A multitude of options can be considered for this stage, so a well-defined framework is needed to organize the design options. This can be done by identifying characteristics that drive the design towards unique options, choosing appropriate technical criteria that enable comparison of the options and selecting the most appropriate design. To further clarify the selection, one should not only maximize the usability of the design, but also respect any requirements and production limitations imposed. In this study, it is possible to discern three factors that fully describe the tank assembly design:

Material: Already been hinted from Chapter 3, selecting proper materials for both the tank envelope and the pressurizing mechanism ensures mass and volume advantages, as well as facilitating the manufacturing of a physical object.

Shape: The main geometry of the tank, along with any prominent features. The overall propellant capacity, as well as the manufacturing procedures strongly benefit from an efficient and simple shape.

Configuration: The arrangement of primary and secondary features to further improve the design, especially with respect to their interaction and attachment to the main module.

4.5.1. Material Selection

The existence of two separate components, each serving its own mechanical purpose, drives the designer to look for suitable materials with tailor-made criteria per component in addition to the common properties shared from a product standpoint. For this instance, the latter may be conveniently summarized in *Manufacturing Feasibility* (MF), *Cost* (C_m), *Thermal Response* (α_T) and *Flight Qualification* (FQ). Worth mentioning is that MF is used as a comparative metric based on the material's processing capabilities rather than encompassing acquisition and logistic costs, as seen in [46]. The C_m factor is sufficient to discern the economic differences between materials, regardless of available manufacturing infrastructure, so MF gives a rating on the actual handling of the material. Moreover, FQ is a boolean metric to comply with Requirement 3.1:

> *PROP-TNK-3.1*: *The material(s) employed shall be qualified for use in space.*

That said, the requirement is probably redundant for the purpose intended. Since the materials sought after are intended for use in space, the author is intuitively guided towards flight-qualified alternatives even before entering the trade-off stage, so FQ is already taken into consideration. For the part-dependent criteria, the use of *Material Indexes* is convenient. They are numbers describing the effect of material properties on a certain performance aspect (e.g. beam stiffness) and are derived from problem-specific equations, after isolating the material parameters. Table 4.5 catalogs the needed parameters for the study, the material indexes that can be constructed and their application.

Selection Process

1. The first figure set is used to explain the formation of material indexes from the material properties situated at the x-y axes. Moving towards the top and right of each chart improves the individual properties, while moving perpendicular to the line slope improves

Table 4.5: Table of material properties and indexes for intended applications. Source: [47]

Material Property	Symbol	Application
Fracture Toughness	K_{1c}	Both
Yield Strength	σ_y	Both
Density	ρ	Both
Young's Modulus	E	Helical Spring

Material Index	Form	Application
Yield Resistance	$Y.R = \frac{K_{1c}}{\sigma_y}$	Tank Envelope
Specific Strength	$S.St = \frac{\sigma_y}{\rho}$	Tank Envelope
Resilience (per vol.)	$R_v = \frac{\sigma_y^2}{E}$	Helical Spring
Resilience (per mass.)	$R_m = \frac{\sigma_y^2}{E\rho}$	Helical Spring
Toughness	$G_c = \frac{K_{1c}^2}{E}$	Helical Spring

the material index. A benefit from this chart type is the separation of good and bad material families for the application at hand, in case the indexes become misleading.

2. The second figure set is used to refine the selection based on detailed performance numbers. For the index charts, the best materials are found towards the top and left side, whereas for the thermal coefficient charts, they are found towards the bottom and right. Exact numerical values are taken from Appendix A.

3. Color-coded tables with some promising candidates are set up. Owing to the wide range of index values even within the same material, the color scheme is used to accentuate the magnitude difference of material indexes, based on their average value. An initial three-color segregation is used: green marks the best, blue the moderate and red the worst value. If any noticeable difference requires additional characterization, the yellow color is added to mark sub-moderate values. Then, based on the reader's opinion about the index importance, one of the materials is selected from the table.

Pressure Vessel

The tank envelope functions as a pressure vessel, containing the fluid at its maximum available pressure. Subject to internal and external loads, its structure is anticipated to develop localized fractures, which propagate over time. The rate at which these fractures move through material layers is dependent on a property called *Fracture Toughness*. Nonetheless, fracture propagation occurs under the assumption that the material is allowed to reach the state of plastic deformation, which is prohibitive for a critical component bound by safety requirements such as safeguarding the propulsion module from propellant leakage. Preventing the development of fractures, a material with good *Yield Strength* is required to provide sufficient elastic deformation while the envelope is stressed.

The material index charts for the yield resistance and specific strength are depicted in Figures 4.12a and 4.12b. For the sake of completion, all available material families are shown, but in reality some are not needed. Natural materials are easily contaminated by water, foams and elastomers cannot be used for rigid structural components, while glasses and ceramics are too brittle for the purpose intended. As a result, only polymers, composites and metal alloys are considered for the next stage, fact that should not be surprising to the reader, as these are also superior in terms of raw performance.

Distinguishing materials from said families is not as intuitive. Figures 4.12c and 4.12d sort the materials based on the yield resistance and the specific strength respectively, with some materials being labeled for the sake of this argument. Tin and copper, for instance, are highly resistant to fractures because of their ductile nature, but this inflicts on their poor specific strength. On the other hand, the brittle nature of CFRP can only be advantageous in mass savings. To facilitate the selection, the thermal response chart of Figure 4.12e is used. Polymers are clearly inferior because of the high thermal expansion coefficient and low yield resistance, and only display moderate specific strengths that cannot compete with commonly used metals or composites.

With this in mind, the final selection is done between the metal and composite families, slightly prioritizing the specific strength. Under the assumption that the pressure developed within the tank is low, an excessively high yield resistance is met by heavy materials that would compromise the mass budget for a component that should amount to a smaller mass fraction. Based on numerical values obtained reported in Appendix A, plausible candidates for the pressure vessel are compared in Table 4.6, with the most promising alternative being a wrought and age-hardened Aluminum alloy. Despite not having the best scores in individual categories, it has a much lower density than steel, which translates to a lightweight structure for similar strength levels and has a much better yield resistance compared to Titanium alloys, improving on the safety margins. An intriguing alternative is Copper, with its exceptional yield resistance. Copper is also reported in [20] to be suitable small scale tanks, proving its application heritage. The downside is of course the very high density that impacts both the specific strength and the mass footprint of the envelope.

Helical Spring

The helical spring implemented as the pressurizing mechanism has an obvious function: store and release energy when interacting with the propellant. Towards achieving this function, the constituent wire of the coils undergoes torsion, which may induce internal stresses. For the spring to retain its normal operation over a prolonged period of time, the stresses developed must be kept within the elastic region of the material, defined by the Yield Strength, σ_y. Further, the deformation behaviour of the spring is strongly dependent on its ability to absorb length changes without breaking, the Young's Modulus, E. Both parameters are equally important for understanding the energy transfer to and from the spring, as the main point of deformation, strain, is given by σ_y/E, but of paramount importance is also the preservation of the spring even under failure conditions (overload, thermal control issues etc.), from which can be inferred that materials should also display a moderate fracture toughness, K_{1c}.

The material index charts for the resilience and toughness are depicted in Figures 4.13a and 4.13b respectively, both represented by the dashed lines. For the sake of completion, all available material families are shown, but again a simplification can be made. Natural

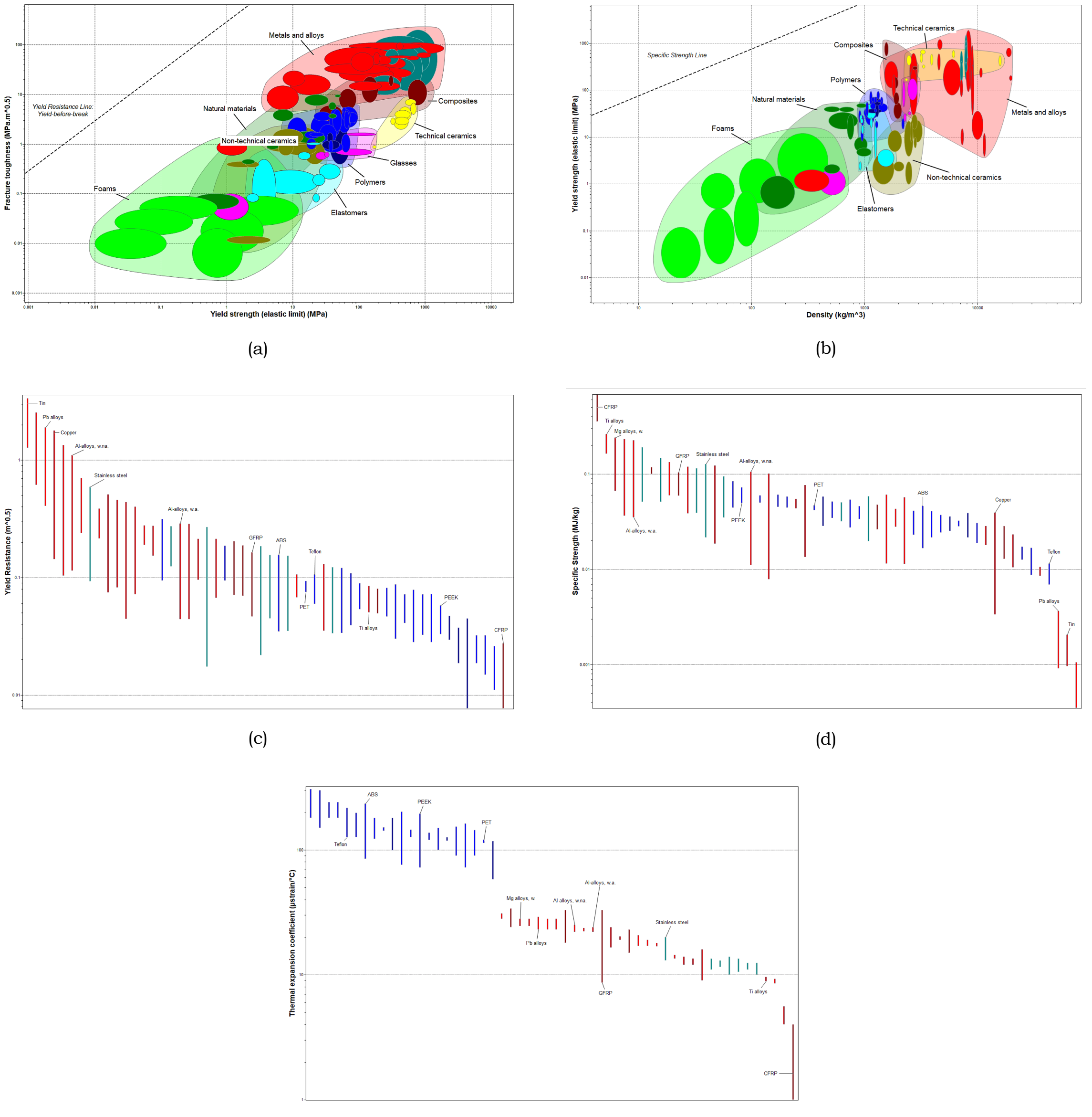

(a) (b) (c) (d) (e)

Figure 4.12: Material charts for the tank envelope.

Table 4.6: Material candidates for the pressure vessel

Material	$Y.R$ $[m^{0.5}]$	$S.St$ $[MJ/kg]$	α_τ $[\mu/m/^oC]$
Al alloys WA[a]	0.044 - 0.288	0.0353 - 0.227	22 - 24
Al alloys WNA[b]	0.115 - 1.11	0.0111 - 0.106	22 - 25
Copper	0.144 - 0.79	0.003 - 0.0392	16.9 - 18
GFRP	0.0466 - 0.164	0.059 - 0.104	8.64 - 33
Stainless steel	0.0925 - 0.592	0.0217 - 0.127	13 - 20
Ti alloys	0.0505 - 0.0847	0.163 - 0.262	8.9 - 9.6

[a] WA: wrought, age hardened (2xxx, 6xxx and 7xxx alloys)

[b] WNA: wrought, age hardened (1xxx, 3xxx, 5xxx and 8xxx alloys)

materials are extremely prone to water contamination or inversely soak up water, hence reducing the available propellant, so they are automatically excluded. The elimination of better suited materials, such as elastomers and polymers, is due to the loss factor found in these materials being quite high, leading to energy dissipation during unloading of the spring and thus lower pressurization capabilities. Ceramics and glasses are of brittle nature, and that inflicts on the spring's reliability, as a single coil can collapse and ruin the mechanism. While implausible, the risk outweighs any performance advantages these materials can bring.

Table 4.7: Material candidates for the helical spring

Material	R_v $[MJ/m^3]$	G_c $[kJ/m^2]$	α_τ $[\mu/m/^oC]$
Al alloys WA	0.122 - 5.05	5.96 - 16.7	22 - 24
GFRP	0.563 - 1.89	2.37 - 26	8.64 - 33
Ni superalloys	0.469 - 18.9	21.4 - 65.1	9 - 16
Stainless steel	0.145 - 5.02	19.3 - 113	13 - 20
Ti alloys	0.489 - 12.5	26.3 - 42.8	8.9 - 9.6

Similarly to the pressure vessel case, contradictions are unavoidable for the material index comparison. Both material indexes are obtained from fundamental properties, namely the fracture toughness and the yield strength, as shown in Table 4.5, so any trade-off done between those two is automatically transferred to the resilience and toughness, not to mention the squaring factor that amplifies the difference. That said, one index must be prioritized over the other, and in making the final decision, the mission objective is taken into account. Being a technology demonstrator, the tank assembly is more focused on displaying the potential of spring-loaded pressurizing systems rather than obtaining the ultimate performance, which may come from subsequent optimization of the initial design. Based on numerical values obtained from [47] and reported in Appendix A, plausible candidates for the helical spring are compared in Table 4.7, with a winner found in Stainless steel. It may be underwhelming in terms of performance, but it is a staple material as far as springs are concerned and its high volumetric toughness guarantees a safe and durable operation of the tank. Should more performance be needed, two design avenues are possible: either selecting a more resilience-oriented material from the table (e.g. *Ni* superalloys), or altering the geometry of the helical spring towards a more space-efficient variant.

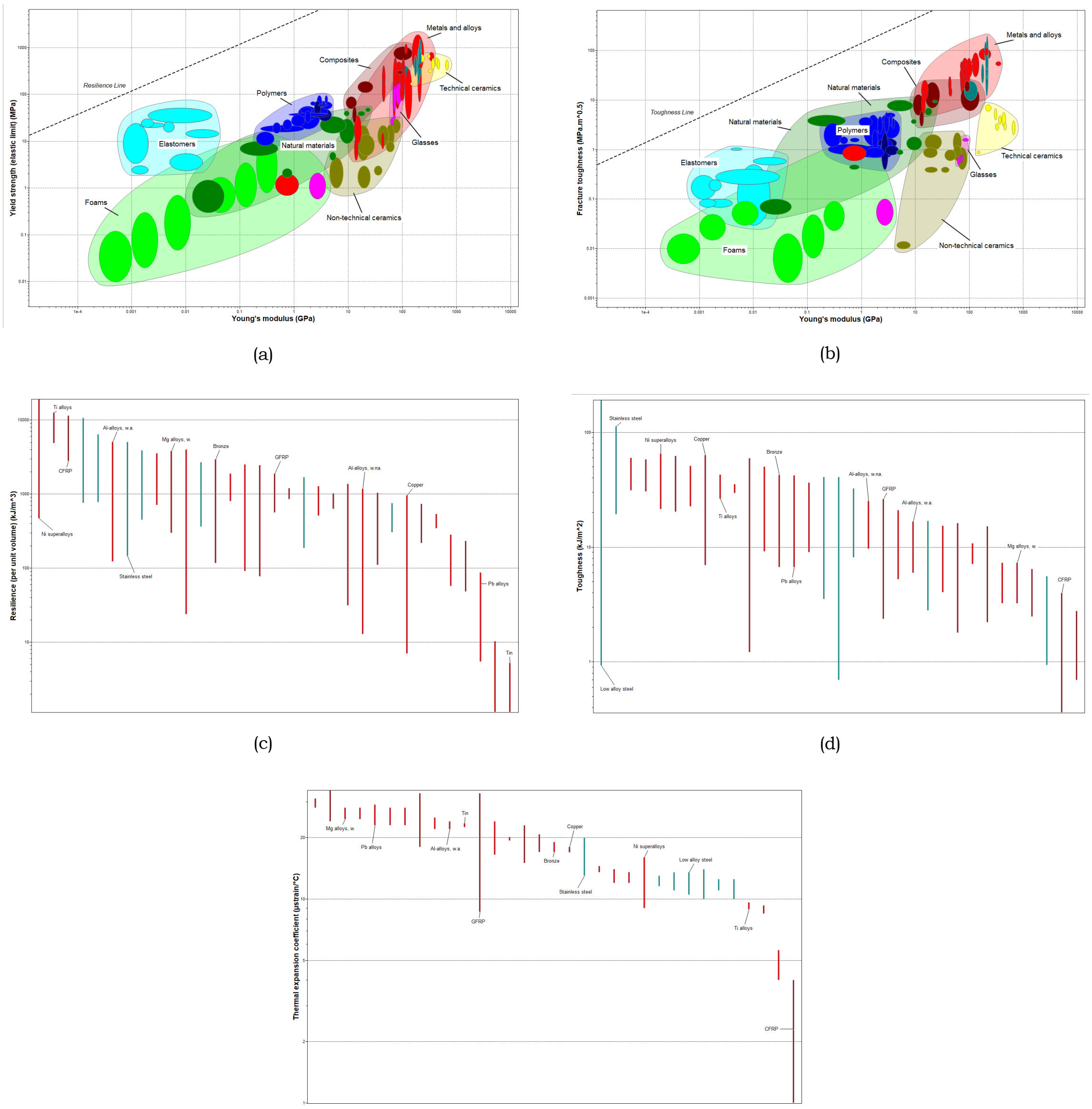

(a) (b)

(c) (d)

(e)

Figure 4.13: Material charts for the helical spring.

Manufacturing Feasibility

The trade-off process for both the pressure vessel and the helical spring draws conclusions from performance-oriented data, which are limited to the design stage and relevant simulation tests. Nonetheless, the goal of this is study is a materializable object, meaning that any materials involved must allow the transition from paper to end product. To this end, a short feasibility study is conducted, with two focal points: the cost of acquiring a material unit C_m and the processability of this material unit to the desired form. Machining, casting, forming and welding are used as potential processes, given their affinity with metallic materials. Once again, the CES EduPack software [47] is used to obtain a reference score for each material and process, aiming to confirm or disprove the material candidates proposed by the previous trade-offs.

Table 4.8 provides ratings per material per process, ranging from 1 to 5 and from worst to best. The overall distribution of ratings concludes to similar arguments with the results discussed in [46]. The advantage of aluminum alloys can be accredited to its versatile manipulation with different processes, though welding is a more tedious procedure, as it involves additional material treatment to restore strength in weld zones. Comparison between the nickel-based superalloy and stainless steel is essentially an exchange of performance for cost and vice-versa. Ultimately, accounting for the inherent constraint of this study, which is constructing the assembly based on university-level capabilities, the choice of using a stainless steel wire to create the spring and its endplate is a reasonable compromise.

Table 4.8: Manufacturing feasibility of qualified materials

Material	Machining	Casting	Forming	Welding	Cost [€/kg]
Al alloys WA[a]	4 - 5	4 - 5	3 - 4	4 - 5	1.68 - 1.8
Ni superalloys	3	3	3 - 4	4 - 5	13.4 - 16.1
Stainless steel	2 - 3	3 - 4	2 - 3	5	4.8 - 5.03
Ti alloys	1 - 3	3	2 - 4	4 - 5	17.7 - 18.2

[a] WA: wrought, age hardened (2xxx, 6xxx and 7xxx alloys)

Other Considerations

The general selection process is concluded with a set of material candidates that can meet the expectations for the tank assembly. Nonetheless, there might be arguments against its completeness, stemming from less obvious considerations. In an attempt to solidify the options made, the reasoning behind ignoring some considerations is explained.

Operating Temperature: All material properties are considered temperature-dependent to a certain degree, and more importantly have a minimum operating temperature before becoming unusable in space. Metals are quite convenient in that aspect, for a number of reasons: they do not suffer transition to brittleness like ceramics, have moderate expansion capabilities that could be exploited for further pressurization and can be easily adapted to complex shapes with minimal tooling effort. All these traits are essential for prevention of unforeseen circumstances that cancel the mission, especially failures. Under normal operation, minimum temperatures are expected to be within the range of operation of metals, ceramics, polymers etc. Potential failure though of the thermal control system or trajectory mishaps may bring the module's temperature to cryogenic levels. Freezing of the propellant may be unavoidable, but as long as it can be contained within the tank, the satellite integrity should be unaffected. To that end, tolerant to low temperature materials are a priority, leading to exclusion of brittle ceramics and metals. Common materials such as aluminum and titanium alloys can be ductile down to $1 - 2\ K$, effectively countering temperature issues.

Galvanic Corrosion: A sound argument against the use of metals for both components of the tank assembly is the emergence of phenomena like *galvanic corrosion*. Put in simple terms, when two metals with different galvanic potential are in close contact or friction, and under the presence of an electrolyte, a closed circuit is formed. The resulting flow of electrons oxidizes the anode and causes wear in the surface layers, essentially corroding the material. The risk is apparent, as the spring endplate and the tank walls are almost constantly subject to friction when the thrust phase is active. Two crucial assumptions are to be taken for granted for the continuation of this preliminary stage: first, the problem can be assumed to be quasi-static, since the thrust time duration is small compared to the orbit period, hence the displacement of the spring should not cause noticeable friction forces. Second, the materials selected are assumed to be galvanically compatible based on the guidelines of [39] and [47], minimizing the risks. As a last resort, the components can also be passivated or coated to fully tackle the issue.

Volume over Mass: In the spring material section, the resilience metric is measured as energy per unit volume. While it would make more sense to measure resilience per unit mass, promoting lighter materials and making the trade-off more unambiguous, the volumetric efficiency of the spring is prioritized. As already mentioned in [46], a small change in propellant capacity entails a greater change in Δv against the equivalent change in dry weight. It can be inferred that reducing the volume occupied by the spring will indeed benefit the utilizable propellant volume, leading to the decision made. For this argument to be sound, one can also check the budgets imposed at Requirements 1.1 and 1.2, highlighting the restricted volume.

Material Designation

The abundance of aluminum alloy and stainless steel varieties poses a minor challenge in designating a specific material and can be overcome either by another trade-off procedure, leading to unnecessary time consumption only to observe minute differences, or by selecting a variant that has widespread application in space components. Following the guidelines about flight qualification in [39], as well as the material databases of [10] and [47], the ***Al-6061-T652*** aluminum alloy is chosen for the pressure vessel walls and the ***A301-3/4H*** stainless steel for the coil spring mechanism. Both variants resulted from a sequential research of space-qualified materials (Requirement 3.1), materials with high resistance to cryogenic temperatures, stress corrosion cracking and galvanic corrosion (Requirements 3.3 and 3.4) resistance on [39] and [10], and materials with the highest possible yield strength within the respective alloy categories on [47]. Values of individual materials are given in Table 4.9.

4.5.2. Shape Selection

Exploring the geometrical aspect of the tank, special attention must be given to the overall shape, it affecting the volume capacity, the total mass, the manufacturing as well as the integration process. Both prismatic and axisymmetric elementary shapes are assessed at this stage, with more complex geometries being excluded because of the complications involved in the manufacturing process. Figure 4.14 shows the shapes considered, with a color-coded to scheme to indicate the choices made. Green stands for the preferred option, blue for the alternative candidate, while red indicates the discarded shapes, each displaying its own shortcomings.

Polygon: The additional folding zones needed to reproduce a polygon create more stress

Table 4.9: Material property table

	Symbol	Units	Al-6061-T652	A301-3/4H
Cost	C_m	€/kg	1.71 - 1.84	1.78 - 2.07
C.T.E.	α_τ	$\frac{\mu}{m^oC}$	23.4 - 24.6	16.5 - 17.3
Min. Temperature	T_{min}	^oC	-273	-150
Density	ρ	$\frac{kg}{m^3}$	2690 - 2730	7880 - 7960
Yield Strength	σ_y	MPa	241 - 281	856 - 1010
Young's Modulus	E	GPa	66.6 - 70.0	179 - 193
Frac. Toughness	K_{1c}	$MPa \cdot m^{0.5}$	30 - 36	72 - 81
Yield. Resistance	$Y.R$	$m^{0.5}$	0.113 - 0.143	0.07 - 0.09
Specific Strength	$S.St$	$\frac{kJ}{kg}$	88.8 - 104	98.4 - 118
Toughness	G_c	$\frac{kJ}{m^2}$	13.3 - 18.9	27.8 - 35.4
Resilience	R_v	$\frac{kJ}{m^3}$	427 - 576	2010 - 2970

concentration zones, add unnecessary manufacturing steps and reduce the available cross-section, effectively compromising volume capacity.

Sphere: The most common shape for fluid containment, optimal in terms of pressure handling. However, it suffers from integration and production issues. Its incompatibility with the spring-based pressurization, the negative effects on structural performance due to splitting and rejoining the envelope and the difficulty in generating strong mounting points for the tank to be installed in the propulsion module render it unfeasible.

Freeform: A freeform shape would be ideal from a compromise perspective, in that structural performance and integration capabilities can coexist. The greatest disadvantage stems from the design complexity associated with custom shapes which cannot ensure performance gains in the budgeting aspect.

Prism: The simplest of all prisms is a rectangular envelope, providing ample volume for the propellant and the mechanism to reside. Contrary to the result seen in [46], which proclaimed the cubic as first choice, it comes as an alternative in this study, particularly due to additional envelope mass with respect to a cylindrical object of the same dimensions and lower structural performance.

Cylinder: An axisymmetric shape that offers a good balance between pressure handling, propellant capacity, dry mass and manufacturing capabilities. A disadvantage may be found in the integration procedure, since the round surface of the cylinder lacks in strength, but it can be circumvented with an appropriate design.

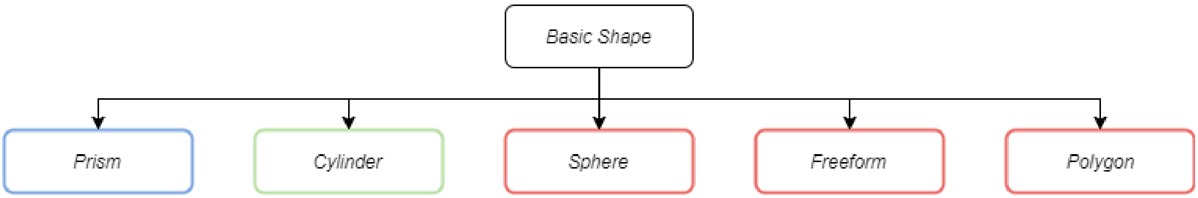

Figure 4.14: Shape alternatives for the tank envelope.

4.5.3. Configuration Features

The arrangement of various functional features, encapsulated by the term 'configuration', is concerned with maximizing the assembly's functionality, it being integration (see Requirements 5.x), servicing, performance and so forth. Design-wise, the tank assembly can incorporate features that pertain to 4+2 unique axes, presented in the following list. A distinction is made based on whether the features can be qualitatively studied or have to be verified by a thorough analytical/numerical study, essentially discerning *integration features* from *performance features*, shown in the following list.

1. *Lid Formation (L)*

   L1: A single lid, placed at the base closest to the connectors. It is the side from which both the spring and the propellant are inserted.

   L2: Two lids, placed at the two cylinder bases. For modularity purposes, one is assigned to the various sensors and ports and one will accommodate the spring mechanism.

2. *Spring-to-Tank Interface (ST)*

   ST-B: A bolted connection between the spring plate and the tank base. Bolt orientation has not any effect on the connection.

   ST-C: One of the spring ends is locked into position by multiple clamps extending up to the first active coil.

   ST-PF: The spring is press-fitted into a groove/slot, sized by the spring dimensions.

   ST-WAR: The spring end is attached to the tank base by welding, rivets or adhesive.

3. *Lid-to-Tank Interface (LT)*

   LT-B: A bolted connection between the lid and the tank base. The bolt orientation has an immediate effect on propellant capacity and overall tank dimensions.

   LT-S: The lid is held into contact with the tank by a sealant, such as an elastic ring.

   LT-P: A secure connection between the lid and the tank is achieved by the internal pressure.

   LT-Sc: A screw cap lid is considered, enclosing the propellant side of the tank.

   LT-WAR: Welds, adhesives and rivets are used to join the lid and the tank.

4. *Tank-to-Module Interface (TM)*

TM-D-S: The tank assembly is slid into the structure bars through mounting holes, while is separated from other components by spacers.

TM-P-B: A bolted connection between the tank and the module, passing through the PCB and terminating onto a metallic backplate.

TM-P-C: Clamps or braces running around the tank create the connection to the PCB.

TM-P-AR: Adhesives or rivets are employed to connect the tank and the PCB.

5. *Spring Formation (SF)*: the spring mechanism is introduced as a stand-alone component, allowing for better fine-tuning of the tank's behaviour depending on system requirements. The number and combination of springs affects the overall stiffness, deflection and hence pressure evolution over time in the tank.

SF1: A single spring is inserted to the tank, with one base capped off for the pressurization.

SF2N: A nested, double spring system, with both bases capped off for pressurization and alignment purposes.

SFX: The pressure load is distributed in a spring multiplicity, again capped off at both bases. The exact number X is yet unknown, but reliant on manufacturing capabilities.

6. *Chamber Formation (CF)*: describes the spatial arrangement of the spring and the propellant chambers, both dependent on the SF options and the system requirements.

CFU: A cylindrical tank with a uniform diameter along the main axis. Assumes a spring of similar diameter.

CFS: A two-level cylindrical tank. The larger diameter chamber is occupied by the propellant and the smaller diameter chamber snugly accommodates the spring system.

From an efficiency standpoint, the numerous configurations that may arise from a mix-and-match approach is quite problematic, greatly emphasized by the fact that no performance features are fixed. In overcoming the issue, a slightly differentiated trade-off method is followed. The previous trade-offs relied on the comparative performance of design options with respect to criteria, but the features listed above are not directly comparable to each other, as there is no reference point for individual scores. In this current variation, a pro-con screening process is used to eliminate features with insurmountable drawbacks and qualify fitting alternatives, as seen in Figure 4.15. Driven and biased configurations that may underperform are avoided by allowing secondary alternatives where needed, each associated with a preference order. This latter is determined by the extent of simplicity associated with the feature employed. For instance, a press-fit interface between the spring and the tank envelope is much easier to implement than threading and bolting the two components, it being a single step during the initial boring of the aluminum block and offering a similar structural integrity with no additional mass.

4.6. Preliminary Design

Setting the foundation for the next chapters, them being focused on analytical and numerical studies, a preliminary design must be generated. Table 4.10 summarizes the major choices made, but a discussion can also be made about minor aspects of the design, such as the PMD. While the system is expected to be leak-proof, the insertion of a bladder is beneficial, yet not

Category	Feature	Design				Manufacturing / Assembly		Performance		Verdict	Order
		Mass	Volume	Simplicity	Feature Compatibility	Feasibility	Accessibility	Structural Integrity	Tightness		
Lid Formation	L1						🟨 Placement of connectors			Accepted	First
	L2			🟨 Added complexity, lid on spring side			🟩 Improved	🟨 Compromised by second lid	🟥 Higher leakage risks if backflow occurs	Accepted	Second
Lid-to-Tank Interface	LT-B	🟥 Increased			Compatible w. LT-S			🟩 High, strong link with tank envelope		Discarded	First
	LT-S				Compatible w. LT-P, LT-B				🟥 Not enough grip from sealant	Discarded	-
	LT-P	🟩 No additional components			Only applicable to L2, compatible w. LT-S				🟨 Compromised at low pressure levels	Accepted	Second
	LT-Sc	🟥 Increased		🟨 Requires separate study	Only applicable to L1	🟥 Threading issues, may break cap			🟩 Good leak protection	Discarded	-
	LT-WAR						🟥 Permanent joint	🟥 High stresses		Discarded	-
Spring-to-Tank Interface	ST-B	🟥 Increased				🟥 Low, threading on spring endplate		🟩 High, strong link with tank envelope		Accepted	Second
	ST-C				Only applicable to L2	🟥 Low	🟥 Requires disassembly			Discarded	-
	ST-PF			🟩 High, during initial boring			🟩 Slide-in			Accepted	First
	ST-WAR						🟥 Permanent joint	🟥 High stresses		Discarded	-
Tank-to-Module Interface	TM-D-S			🟩 Slide-in, Heritage		🟩 High		🟩 High, strong link with module frame		Accepted	First
	TM-P-B	🟥 Increased		🟥 Requires Backplate		🟥 Low, incompatible shape				Discarded	-
	TM-P-C	🟥 Increased		🟥 Complex joint				🟨 Stresses on PCB		Discarded	-
	TM-P-AR						🟥 Permanent joint	🟥 High stresses		Discarded	-
Spring Formation	SF1									TBD	First
	SF2N	🟥 Increased		🟥 Alignment issues	Conflict with ST-PF			🟥 Buckling and vibration risks		Discarded	-
	SFX	🟥 Increased	🟩 Optimal volume usage	🟨 Requires separate study	Conflict with ST-PF					TBD	Second
Chamber Formation	CFU		🟨 Wasted internal volume							TBD	First
	CFS			🟨 Added complexity, section change				🟨 Weak structural zones	🟩 Better protection against backflow	TBD	Second

🟩 Benefit
🟨 Minor drawback
🟥 Major drawback

Figure 4.15: Trade-off table for the proposed feature alternatives.

interfering with the spring operation. Further, should a sealant be included, the practice described in [46] seems sound. Being a small scale assembly, the tank walls are expected to be thin leaving minimal surface for a sealant groove, so a lid groove is preferred. The lid is also required to provide space for the sensors and the propellant ports, the dimensions of which are not available to date and are instead approximated by small holes.

Table 4.10: Preliminary design features

Components	Envelope	Lid	Spring
Material	Al-6061-T652	Al-6061-T652	A301-3/4H
Shape	Cylindrical	-	Helical
Formation	CFU	L1	SF1
Interface	TM-D-S	LT-B + LT-S	ST-PF

Aside from the description, a visual representation of the assembly and the constituent parts is provided for a better understanding of the configuration choices made. To begin with, a half-section view of the envelope is displayed in Figure 4.16c, revealing the spring interface ST-PF marked in red. Its form will allow the housing of the helical spring while preserving a certain alignment accuracy. Additionally, the internal groove can be extended (if needed) to provide structural support to the spring endplate when the system is loaded down to its solid length. Speaking of the spring, a depiction of the SF-1 configuration is available in Figure 4.16b. From a manufacturing perspective, it is convenient for the helix and the endplate to be made out of the same material, it being exceptionally weldable, but with no particular information on the manufacturing accuracy required to achieve such a welding, this specific point is open to discussion, once a more finalized design is achieved. The L1-type lid is shown in Figure 4.16a. The four holes marked with red are intended for pressure and temperature sensors (2), a fill/drain port (1) and a connection to the control valve (1). A white groove has been included for the insertion of a sealant ring, according to the LT-S interface. Figures 4.16d and 4.16e show the author's impression of the tank assembly as defined at this preliminary stage. The tank envelope (in white) has mounting points for interfaces TM-D-S in the outermost holes, while interface LT-B is enabled through the innermost holes.

A small remark on the TM-D-S extrusions has to be made: following the volume requirements, all dimensions pertaining to the tank itself were constrained to less than $3\ cm$, also accounting for tolerances and insertion procedure. However, the tank-module interface is not a structural part of the pressurizing tank, and can be omitted from the requirements. Then, the sizing of the interface must be derived from other geometric constraints, in this case the attachment procedure. In particular, the propulsion module must comply with the *PQ60 standard* [38], so the structure bars present in the frame have a specific dimension to be respected, leading to the diameter difference between the tank envelope and the supporting interface holes. This necessity also comes with the advantage of space for the external placement of the lid interface, maximizing the frontal cross-section of the envelope and thus the propellant capacity.

4.7. Conclusion and Remarks on the Chapter

Summarizing on the actions taken towards a preliminary concept design, a series of trade-off analyses was executed. The lacking knowledge on compliant mechanisms as a liquid storage device necessitated a modified trade-off strategy. Starting from the generation of plausible, as well as far-fetched, design concepts, a two-stage trade-off method has been applied to progressively reduce the candidates. First, qualitative aspects were used to compare all designs, out of which the four best advanced to the second stage. Counteracting any bias towards certain solutions, a sensitivity analysis was conducted, giving the advantage to concepts having a balance between innovation, performance and simplicity. The process is repeated but with more tangible data, ultimately concluding that a design based on a helical spring offers the best starting point for a passive propulsion storage and expulsion module. Remarkable is the fact that flexure-based compliant mechanisms appear to be less performing, but this is not the case. Instead, crucial to the final decision is the factor of complexity associated with flexure-based analytic and simulation models compared to a well-established elastic element such as the spring. Aside from a selecting a design concept, the material, shape and configuration choices are confronted with additional trade-offs, resulting in a complete, fully contained propulsion storage design, seen in Table 4.10. Chapters 5 and 6 will handle the measurable performance aspects in a higher level of detail and compare them with the system requirements of Chapter 3.

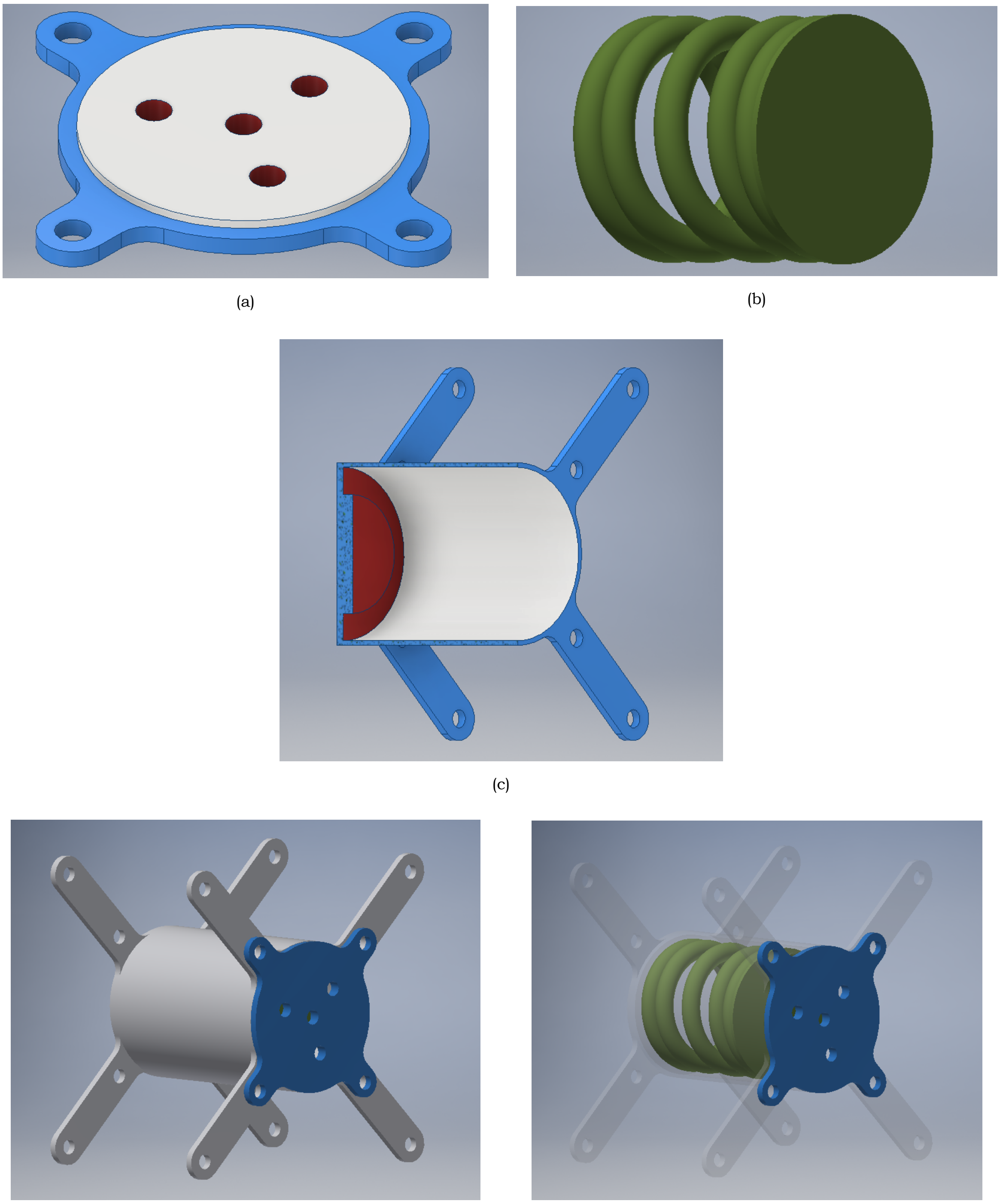

(a) (b)

(c)

(d) (e)

Figure 4.16: Impression of the preliminary tank assembly.

5

Analytical Study

5.1. Introduction

In this chapter, the conceptual decisions made so far are converted into tangible results, with the aid of analytic modeling. More specifically, the module is split to its constituent parts and evaluated under a series of load cases, static and dynamic. For the more important of these cases, the appropriate requirements from Chapter 3 are isolated and used as the bare minimum standard for which the parts must be sized. Simple analytic models and graphical representations are used to derive the optimal numerical values for the parts' key parameters, once identified, in order to produce a viable system. A second design cycle is also implemented for the underperforming components, ultimately concluding to a detailed design proposal that represents what can be done with just theoretical models.

5.2. Model Introduction

A simple representation of the tank assembly is shown in Figure 5.1. The tank assembly is seen in a half-section view, revealing the spring and the fluid volume, also referencing the dimension variables to be used throughout the chapter. Capital letters have been purposefully placed to indicate the load cases studied for the tank assembly, namely:

A. Structural response of the tank envelope when fully loaded, at static conditions.
B. Structural response of the lid and bolt sub-assembly when fully loaded, at static conditions.
C. Structural response of the spring during fluid injection and pressurization.
D. Structural response of tank assembly when accelerated.
E. Dynamic response of spring and fluid during thrust time.

Answering to the problem of structural interaction between the components and requirement limitations, Cases A to E are solved in the order displayed. Cases A and B define the available space for the spring and fluid to reside, owing to the external mass and volume restrictions imposed and the priority given to safety. Case C produces a feasible spring model

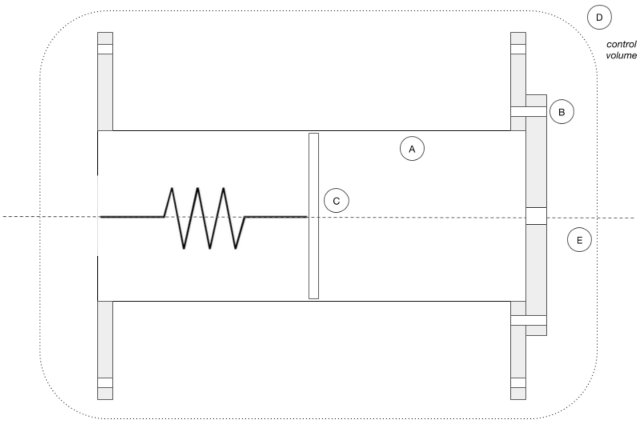

Figure 5.1: Visual representation of the tank assembly.

and the maximum propellant capacity for this specific spring, while Case D deepens the analysis with non-permanent loads and defines the structural interface TM-D-S (see List 4.5.3). Lastly, Case E assumes a finalized assembly and predicts its time-dependent behaviour over a single thrust cycle in terms of distinguishable performance figures.

5.3. Case A: Structural Response of Tank Envelope

The component in discussion is bound by requirements that in the author's view serve different objectives and thus are conflicting. The reader is reminded of these requirements:

- PROP-TNK-1.2: *The total (footprint) volume of the tank shall be less than* $10.584\ cm^3$.
- PROP-TNK-1.5: *The tank design shall maximize the availability of* Δv.
- PROP-TNK-4.1: *The tank shall be able to withstand a Maximum Expected Operating Pressure (MEOP) of 5.5 bar.*

Balancing the three requirements is crucial to the design optimality: Requirements 1.2 and 1.5 promote a tank design with thin envelopes to maximize propellant capacity, while Requirement 4.1 is steering the design towards thick envelopes, at the cost of capacity and total mass. Fulfilment of both objectives is attempted in this section with an iterative algorithm explained below:

Trial dimensions L_0 and h_0 are selected for the external tank length L and the wall thickness h, according to the space available in the propulsion module from Requirement 1.2. Assuming that the envelope is a hollow and capped cylindrical volume (as envisioned in Figure 5.2), the tank radius R is determined via Equation 5.3.1a, with $V_{tank} = 10584\ [mm^3]$, as per Requirement 1.2. With the tank geometrically defined, circumferential and longitudinal stresses can be estimated with Equation 5.3.1b on cylindrical pressure vessels. According to [44], the highest stress encountered in a cylindrical vessel is of radial nature, so the tank is sized for a circumferential stress equivalent to a maximum pressure of $MEOP = 5.5\ bar$, as stated in Requirement 4.1. They however only conclude whether the selected thickness is acceptable or not, leaving the designer to blindly search for another value. Instead, the equations are solved for the minimum required thickness to withstand the pressure load, which is compared to the previous iteration. Should the difference between iterations be smaller than 1%, the thickness is then compared to the manufacturing limit (the greater of which

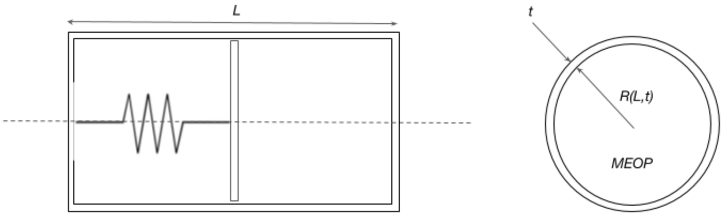

Figure 5.2: Impression of the cylindrical tank assembly, along with the dimension triplet L, h, R.

is selected), otherwise the algorithm executes another iteration. Finally, the correspondent radius is calculated to output a dimension triplet L, R, h.

$$V_{tank} = \pi \cdot (R+h)^2 \cdot L \rightarrow R(L,h) = \sqrt{\frac{V_{tank}}{\pi \cdot L}} - h, \ [mm] \tag{5.3.1a}$$

$$h_{min}(R) = \frac{MEOP \ [10^5 \ Pa]}{\sigma_y \ [10^6 \ Pa]} \cdot R \tag{5.3.1b}$$

$$h = max(h_{min}, h_0) \tag{5.3.1c}$$

Aiming to be consistent with other aspects of this analytical study, the tank length itself is a variable dependent on the outputs of Case C, discussed in Section 5.5. The author is aided by a *MATLAB* script, found in Appendix B and named *SizeTank*. Its main purpose is to expand upon the approach discussed by iterating over different tank lengths and provide a graphical means of understanding the effects of the dimension triplet. In short, they are expressed through the volume capacity V_{in} and the envelope mass m_{shell}. Both are easily calculated, as seen below:

$$V_{in} = \pi R^2 \cdot L_{in} = \pi R^2 \cdot (L - 2h) \tag{5.3.2}$$

$$m_{shell} = \rho \cdot V_{shell} = \rho_{al}(10584 - V_{in} \ [mm^3]) \tag{5.3.3}$$

Figure 5.3 displays the correlation of the various outputs as the length L changes, limited to $3.5 \ cm$ to account for tolerances and limitations of the structure frame. The effect of the wall thickness h is in accordance with the requirement tendencies, with thinner walls offering a higher capacity. Surprisingly, the thickness remained unvaried with multiple initial values, implying that the pressure load exerted onto the thinnest walls producible from a manufacturing perspective is small and can be safely contained. Settling on extremely thin

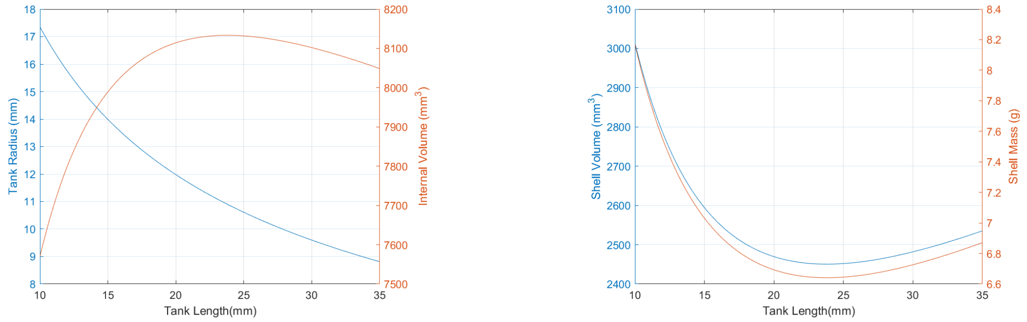

(a) Tank dimensions at $h = 1\ mm$

(c) Shell properties at $h = 1\ mm$

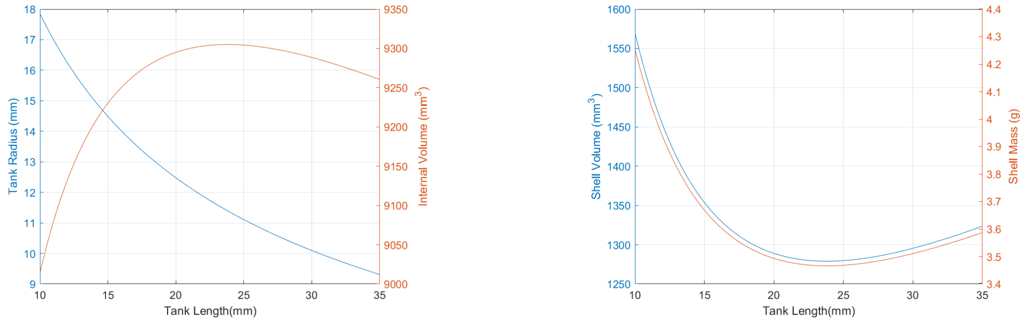

(b) Tank dimensions at $h = 0.5\ mm$

(d) Shell properties at $h = 0.5\ mm$

Figure 5.3: Tank envelope properties as a function of tank length L.

walls is not advised, given the crude stress estimation that does not consider point-to-point stress variation, a striking example of which is the time-dependent section change between fluid and spring, most probably entailing shearing. Considering this and the safety-oriented thesis approach, a thickness of $h = 1\ mm$ is selected. Using Equation 5.3.1b, a maximum tensile stress of $6.583\ MPa$ is calculated, leaving ample room for optimization. Another characteristic of the graphs is the existence of an optimal area with respect to volume capacity and shell mass, which however brings marginal benefits for the mass footprint, making the selection of an ideal length unjustified.

5.4. Case B: Structural Response of Lid and Bolts

The tank design proposed in Chapter 4 includes at least one lid, rigidly attached to the main enclosure with bolts. Subject to the internal pressure load, the complex shape of the lid would require an in-depth study of its deflection, possibly through Finite Element Analysis (FEA). An analytical model is instead explored, in the form of simple force balance that relies on rigid-body mechanics. The principal assumption to make is the direct transfer of the entire load onto the bolts, while the lid remains unaffected. Any non-longitudinal loads are removed from the calculation process, leaving only the pressure acting on the interior surface of the lid, the pre-tension load and the reaction forces. In fact, this method has also been applied in [46] for a similar condition, with two key difference: first, that particular lid included fastener holes on the tank enclosure walls, whereas the lid of Figure 4.16a will be attached on the TM-D-S interface supports, implying the existence of protrusions from the main lid structure and hence some beam deflection theory (see Figure 5.8). Second, the model in [46] is somewhat incomplete, lacking the pre-tension load that is a necessity for every bolted connection. Covering for that setback, this study includes pre-tension so as to better predict the stresses exerted onto the lid. The method reported in [32] is implemented, consisting in a single equation that combines material and geometrical properties of the lid-bolt assembly, as follows:

$$\sigma_{bolt} = \frac{F_i + C \cdot F_{ext}}{A_t} \tag{5.4.1}$$

In the equation, the reader can discern the main components:

1. A_t: the *tensile stress area* of the bolt, is the fraction of the bolt thread assumed to receive the load. Related to the bolt's mean diameter and pitch, it is a standardized function and taken as-is from tabulated data in [32].
2. F_i: the pre-tension load, used to increase the bolt stress such that perfect contact is ensured when external loads are applied. Correlated to both A_t and the *proof strength* of a material σ_p, it can be approximated by $F_i = 0.75\sigma_p A_t$.
3. C: the bolt loading factor is associated with elastic material theory, although it is summarized as a measure of how much of the load is received by the bolts. Its complement, $1-C$ is the fraction of load received by the members fastened, in this case the lid and the interface support. Normally, the designer of the bolt connection would go through the process of evaluating C, but according to [32], the value $C = 0.25$ can be used without much effect on the results.
4. F_{ext}: this term represent the internal pressure load applied to the bolts, divided by the number of bolts (4). Its magnitude can be easily derived from Figure 5.5, as $F_{ext} = 0.25 P_{max} \pi R^2$.

Equation 5.4.1 is reformatted to accommodate the previous remarks, and the result is a sum of distinct material and geometry contributions.

$$\sigma_{bolt} = \underset{\text{Material}}{\overbrace{0.75\sigma_p}} + \overbrace{0.25 \cdot \frac{\pi}{4} \frac{R^2}{A_t} P_{max}}^{\text{Geometry}} \tag{5.4.2}$$

The material-dependent term spreads over a too wide range of materials for the author to conduct a full research, due to time constraints and associated data gathering and comparison. Instead, opting for a material group comparison based on the order of magnitude for various properties has been proven more time-efficient and validated in Chapter 4. Characterization of the material group suitability is achieved through the *Property Class*, a two-digit number ($x.y$) summarizing a material's yield and tensile strength [12]. During a brief literature survey, aluminum and steel bolts seem to be the first choice of manufacturers, most likely because of being inexpensive and versatile. The crucial difference between these material groups is strength, which as shown in the previous chapter promotes the use of steel, along with the higher corrosion resistance. Consequently, this section is focused on steel bolts with ranging property class. Table 5.1 imports data from [12], [11] and [24], also including the available metric sizes of carbon steel bolts, while Table 5.2 is focused on stainless steel bolts [13], defined by the *Steel Grade*.

Table 5.1: Material and Geometry properties of carbon steel bolts

Property class	Proof Strength σ_p $[MPa]$	Yield Strength σ_y $[MPa]$	Tens. Strength σ_u $[MPa]$	Sizes available
3.6	180	180	300	Unknown
4.6	225	240	400	M5 - M36
4.8	310	340	420	M1.6 - M16
5.6	280	300	500	Unknown
5.8	380	400	520	M5 - M24
6.8	440	480	600	Unknown
8.8	580	640	800	M1.6 - M16
8.8	600	660	830	M16 - M36
9.8	650	720	900	M1.6 - M16
10.9	830	900	1040	M5 - M36
12.9	970	1080	1200	M1.6 - M36

Table 5.2: Material and Geometry properties of stainless steel bolts

Steel Grade	Property Class	Proof Strength 85% $\sigma_y[MPa]$	Yield Strength σ_y $[MPa]$	Tensile Strength σ_u $[MPa]$	Sizes available
A1 - A5	50	178.5	210	500	$\leq$ M39
	70	382.5	450	700	$\leq$ M24
	80	510	600	800	$\leq$ M24
C1	50	212.5	250	500	Unknown
	70	348.5	410	700	Unknown
	110	697	820	1100	Unknown
C3	80	544	640	800	Unknown
C4	50	212.5	250	500	Unknown
	70	348.5	410	700	Unknown
F1	45	212.5	250	450	$\leq$ M24
	60	348.5	410	600	$\leq$ M24

The last column of both tables is used to limit the material selection, based on a simple assumption: the TM-D-S interface supports are not wider than $10\ mm$. With a thinner support and ample surface for the bolt head to rest, the allowed bolt diameter is reduced to the sub-M5 range. As far as stainless steel bolts are concerned, lack of information on sizes promotes the inclusion of more common steels, such as the A2/A4-70. Having determined a reasonable set of options, a *MATLAB* script called *BoltStress* has been quickly written to plot the effects of material and geometry on the developed stress, the results of which are seen in Figure 5.4.

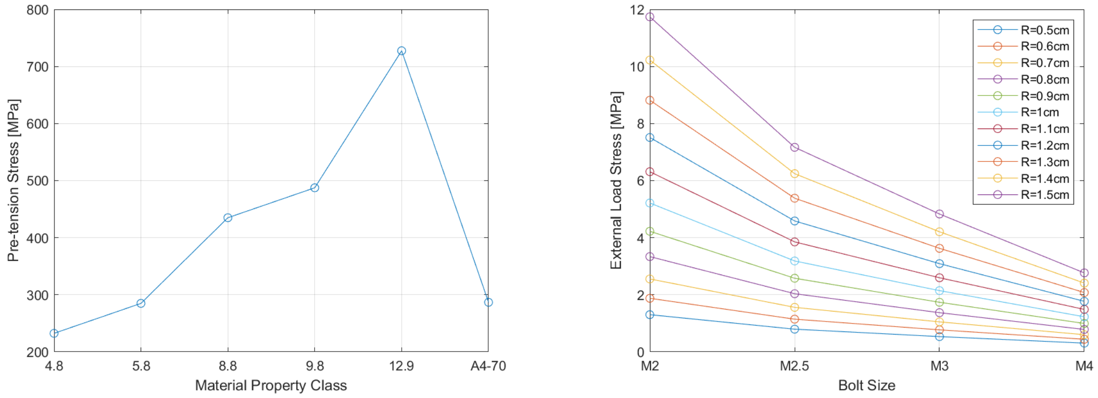

(a) Material-dependent pretension stress

(b) Geometry-dependent ext. load stress

Figure 5.4: Maximum bolt stress experienced during pressurization

The results are predictable. For such a low pressure developed in the tank, the stress experienced by each bolt is hardly noticeable compared to the pretension stresses, even at the smallest size considered. This observation enables the author to select any combination of material and size, provided a last calculation: the summation of both contributors as seen in Equation 5.4.2 is compared with the yield strength σ_y and reversed, to produce a safety factor. The outcome has given a minimum safety factor above 1.3, a safe value for bolts. Nonetheless, accounting for any unrealistic assumptions made, an $A4 - 70$, $M2.5$ set of 4 bolts is selected to attach the lid. The expected mass impact can be quickly estimated by a cylindrical volume approximation augmented by a factor for the bolt head, seen below:

$$m_{bolt} = 4 \cdot (1.5 \cdot \rho_{steel} \cdot (0.25\pi d_{bolt}^2) \cdot l_{bolt}) \xrightarrow{M2.5\ x\ 5} m_{bolt} \simeq 1.2\ g$$

5.5. Case C: Structural Response of Spring

In accordance with the conclusions of Chapter 4, a helical spring has been opted for a pressurizing fluid mechanism. Sizing of said part is paramount not only to the structural stability of the tank design, but also the performance expected from a moving device. The more affine of requirements discovered in Chapter 3 are reinstated:

- *PROP-TNK-1.2*: *The total (footprint) volume of the tank shall be less than* $10.584\ cm^3$.
- *PROP-TNK-1.5*: *The tank design shall maximize the availability of* Δv, *within the constraints of Requirement PROP-TNK-1.2*
- *PROP-TNK-4.1*: *The tank shall be able to withstand a Maximum Expected Operating Pressure (MEOP) of* $5.5\ bar$.

- *PROP-TNK-6.3*: *The tank shall display a stiffness ratio higher than TBD, in all off-axis directions.*
- *PROP-TNK-6.4*: *The tank design shall have a yield safety factor greater than 1.6.*
- *PROP-TNK-6.5*: *The tank design shall have an ultimate safety factor greater than 2.0.*

5.5.1. Physical Problem and Assumptions

Figure 5.5 shows a free-body diagram of the loaded spring. During the injection phase, the fluid is exerting a pressure force $F_p(x)$, where x represents the fluid displacement in the tank. The spring is exerting a reaction force $F_s(x_s)$, at the contact point between the helix and the plate. On the basis of a rigid plate, some assumptions can be made to simplify the problem:

1. The propellant is in contact with the spring plate at all times. According to reports on spring-loaded fluid dispensers such as [114], the injection process causes an air bubble to form between the interface plate and the fluid. If one assumes a very slow fluid injection, it is possible to avoid the formation of said bubble and acknowledge the plate-fluid contact. Then, the spring displacement x_s and fluid displacement x are equal, hereafter represented by δ to comply with notation of previous chapters.
2. The spring is elastically deformed with a constant stiffness k, obeying *Hooke's Law*. This accompanies the assumption of a constant-property helical spring. Variable-property alternatives would require more advanced calculations of the spring geometry. For instance, delving into variable-property calculations would at the very least require the designer to treat the spring as a concatenation of individual lesser springs, each with their own geometric properties and response, then resort to differential and integral equations to merge the components into a single entity and calculate an effective stiffness to better fit the format used so far in this chapter. Designs with variable properties are indeed beneficial for the problem and have found real-world applications, yet the line of thought discussed in Chapter 4 has focused on the simplest of springs with a number of proposed configurations, keeping the study to a proof-of-concept level. Other design avenues are to be explored depending on the system's response.
3. The non-linear stiffness behaviour found at solid length deflection is disregarded to achieve maximum propellant capacity. This is an impossible situation from a physical standpoint, as the coils come into contact when fully compressed and form a solid substructure. In turn, a stiffness gradient between the spring ends is created, increasing the overall complexity. For sizing a spring, it is sufficient to observe the load-bearing capacity of the coils. This being the case, the coils are allowed to edge-to-edge contact, crudely forming a hollow beam. The linear load-deflection curve is then extended up to the solid length compression.
4. Pressure distribution over the plate surface is uniform, hereafter expressed with P. For sizing the spring, the maximum pressure P_{max} is used as the worst-case scenario.

Application of a force balance onto the rigid spring plate gives rise to Equation 5.5.1, the basis for all subsequent actions. The reader should realize that the pressure-deflection curve is strongly dependent on the tank internal radius R and the spring stiffness k. Noteworthy is the fact that Requirement 1.2 has been created according to a preset dimension, in particular $L \leq 20\ mm$, implying that R is a fixed value. For the sake of completeness and consistency

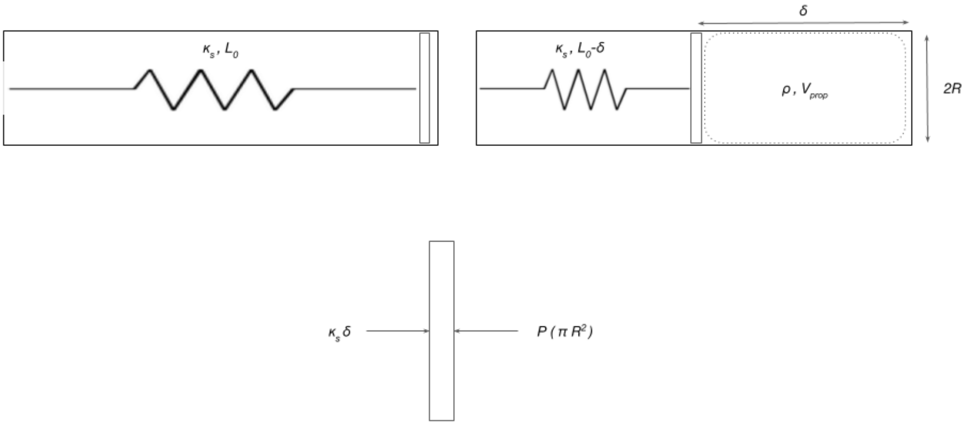

Figure 5.5: Free body diagram of spring deflection.

with Section 5.3, a parametric study of the dimension pair L, R is included to draw more solid conclusions on the spring properties.

$$\delta = P \cdot \frac{\pi R^2}{k} \rightarrow V_{prop} = P \cdot \pi^2 \frac{R^4}{k} \tag{5.5.1}$$

5.5.2. Optimization study

The content of Requirement 1.5 on ”maximization” implies that multiple solutions can be accepted as long as they are viable, one of which is the absolute best. This latter can be obtained by what is called an optimization study. Broadly speaking, an optimization process attempts to improve a specific property, called objective, through variation of a predetermined set of independent variables, all within a design space controlled by external limitations. These latter can be split into bounds, limiting the range of values an independent variable can have, and constraints that apply on dependent or interim properties.

From a computational standpoint, engineering optimization studies are usually associated with minimizing a property, for a specific reason: physics. Dealing with real-world entities automatically creates a lower limit which the solver cannot violate, as it would not produce a meaningful result, for instance negative time or mass. On the other hand, maximization objectives are often uncapped, leading to infinity value overflows, NaN results and other types of numerical errors. In light of this, two design options are possible for improving the spring: either follow Equation 5.5.1 and minimize the spring stiffness k, or maximize the propellant capacity through a sign inversion process. Both options can be reformulated as minimization problem, available in *MATLAB* through the *fmincon* solver, a constrained minimization algorithm the details of which are extensively discussed in the software documentation [106]. That said, the propellant capacity is a more tangible property and a direct requirement, whereas the spring stiffness is a more underlying property of the system, promoting the second design option as the focus of the optimization study. Based on the software documentation‘, a proper setup includes an objective function, a number of constraint functions and an initial design vector along with its upper and lower bounds.

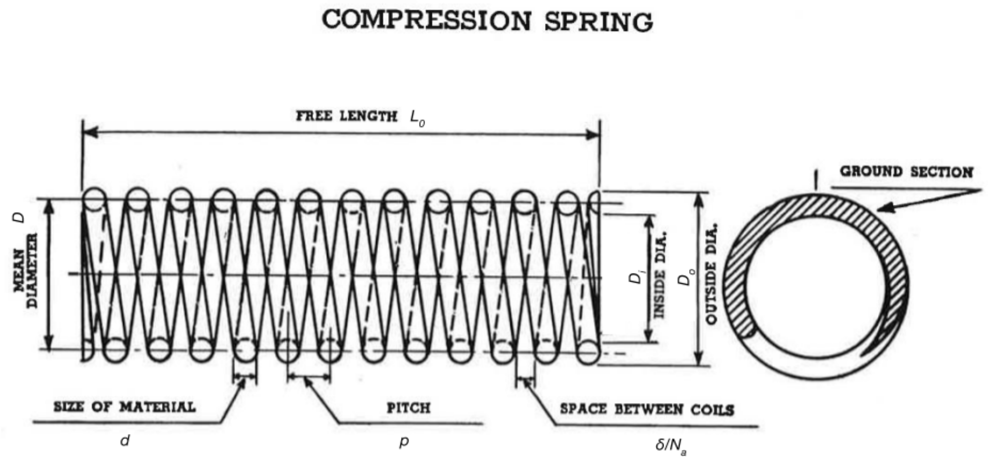

Figure 5.6: Typical parameters of a helical compression spring. Source: [15]. Notation derived from [21, 24, 105]

5.5.3. Design Variables

In generating an appropriate design variable vector and the relevant spring equations, a design guide must be sourced. A major challenge presented to the author was the multitude and variety of helical spring design guides available in either software forms or in scientific articles and books, with troublesome mathematical inconsistency. As a matter of fact, during the first runs of research, noticeable conflicts arose between different equation sources that obstructed the progress of the analysis. The only workaround to this issue was the generation of a new consistent equation set for the spring optimization framework, merging elements from three independent sources: the design guide of [24], the numerical study of [105] and the *Autodesk Inventor* suite [21]. This new equation set applies to all theories with no quality or accuracy penalty, based on a common notation presented below.

Figure 5.6 illustrates the basic design parameters of a helical compression spring, for a squared and ground end configuration. Namely, the reader can recognize the wire diameter d, the mean spring diameter D, the number of actively deforming coils N_a, the spring pitch p and the free length L_0. Manipulation of aforementioned variables results in a secondary set of spring parameters, shown in Equation 5.5.2:

$$\textit{Solid length}: \ L_s = (N_a + 2)d \tag{5.5.2a}$$

$$\textit{Free length}: \ L_0 = pN_a + 2d \tag{5.5.2b}$$

$$\textit{Spring index}: \ C = D/d \tag{5.5.2c}$$

As seen in Equation 5.5.1, the spring stiffness is crucial for the design optimization. Following the design guides, the spring stiffness can be expressed in terms of the predefined variables N_a, C and d and the shear modulus G, the effect of which has been pointed out in Section 4.5.1.

$$k = \frac{Gd^4}{8D^3N_a} \xrightarrow{Equation\ 5.5.2c} k = \frac{Gd}{8C^3N_a} \tag{5.5.3}$$

By now, the reader should recognize the design vector for the optimization study being $X = [d\ D\ N_a\ p]$, however its dimensionless variant is preferred, serving two purposes: first, better convergence is achieved from random initial conditions, and second, better consistency of the upper and lower variable bounds. This latter stems from the physical limitations each design variables may have. For instance, the wire diameter cannot be of the same order of magnitude as the mean spring diameter due to the effect it would have on the generated product. In creating this dimensionless vector, each variable is divided by its respective upper bound (see next paragraph), such that the new upper limit is always unity. The lower bound follows suit, being a finite value greater than zero, for obvious reasons. All the above considered, the design variable vector is presented:

Table 5.3: Design vector for the optimization study

Variable	Description	Bounds
d^*	Norm. Wire diameter	$0.1 \leq d^* \leq 1$
D^*	Norm. Mean spr. diameter	$0.1 \leq D^* \leq 1$
N_a^*	Norm. Active coil no.	$0.125 \leq N_a^* \leq 1$
p^*	Norm. Coil distance (pitch)	$0.1 \leq p^* \leq 1$

Naturally, the absolute values are derived by multiplying the dimensionless vector with a maximum limit value, X_{ABS}. This latter can be roughly estimated based on guidelines or realistic dimension assumptions. A plausible vector employed in this study is $X_{ABS} = [5\ 2R\ 16\ 10]$. The $2R$ limit is implicitly enforced by the size of the tank, whereas the N_a limit is obtained from [21], which is slightly more relaxed than the limit of [24]. The limit for the pitch is set to such a value that is consistently greater than the wire diameter, otherwise spring physics would be violated.

5.5.4. Objectives

The propellant capacity $m_p = \rho_{H_2O} V_{prop}$ is to be maximized, but the nature of the solver enforces a sign inversion of the objective, such that the minimization of a negative value would be equivalent to the maximization of a positive value, avoiding infinity overflows. That said, Equation 5.5.1 is employed and sign inverted to produce the first objective function:

$$f : m_p = -\rho_{H_2O} V_{prop} = -\rho_{H_2O} \cdot \pi^2 \frac{R^4}{k} \cdot P \tag{5.5.4}$$

A second objective can also be evaluated. According to Requirement 1.1, the total system mass is bound to a finite value. The results of 4.5.1 show that the steel spring is probably the heaviest component and its mass should be minimized to stay within budget, also improving the load response. Mass evaluation is facilitated by treating the helical spring as a cylindrical wire with dimensions d and l. This latter stems from common manufacturing practices, i.e. twisting the wire such that it acquires the parameters seen in Figure 5.6. Some rudimentary geometry calculations prove that:

$$l = (N_a + 2) \cdot \sqrt{(\pi D)^2 + p^2}$$

To that, a $0.5\ mm$ thick plate is added to interact with the fluid and perform the pushing function. Then, the spring-and-plate mass function is formed:

$$g : m_{spring} = \rho_s \cdot V_s = \rho_s \cdot \Big(\frac{\pi d^2}{4} l + \pi R^2 \cdot 0.5\ [mm]\Big) \tag{5.5.5}$$

Linear interpolation of the two objectives is possible with a tuning factor ω, which allows the designer to write a single objective function and actively compare the impact of spring and fluid masses on the budget. As a first iteration, the ω factor is set to 1, fully prioritizing Requirement 1.5 on propellant capacity. Should the results produce a prohibitive spring mass, the tuning factor can be altered to compensate, unavoidably sacrificing propellant capacity.

$$h : min\Big(\omega \cdot f + (1 - \omega) \cdot g\Big) \tag{5.5.6}$$

5.5.5. Constraints

The solution space available for conducting the optimization study is vast, and exponentially increased according to the number of independent design variables. Aiming to meet the problem's objectives and the system requirements mentioned, a set of design constraints must be generated to steer the optimization scheme towards feasible solutions. Among the various model sources used for the problem, frequency and fatigue-related constraints have been discarded for two reasons. First, the fully loaded tank is assumed to operate as a single entity, so internal spring vibrations - or propellant sloshing for all that matters - is recoverable within the assembly and thus ignored. Second, the majority of constraints related to fatigue are applicable under the premise of cyclic loading, which is not valid for the current mode. Indeed, the spring is subject to a single load cycle, with a decreasing load trend. As such, only geometric, structural and dynamic constraints following from system requirements and basic operation principles.

For starters, the spring is geometrically limited by Requirement 1.2 and its dependencies. As seen in Section 5.3, the tank dimensions are correlated and compacted into a triplet L, R, h, hence the spring length and diameter are physically limited by said triplet. The notation of Figure 5.6 is used to create the mathematical context, in the following fashion, with L_{in} representing the free internal length once the tank lids and the spring plate are accounted for:

$$c1 : \ \frac{D + d}{2R} \leq 1 \xrightarrow{D=Cd} (C + 1)\frac{d}{2R} - 1 \leq 0$$

$$c2 : \ L_0 \leq L_{in} \xrightarrow[L_in=L-2.5\ mm]{L_0=pN_a+2d} \frac{pN_a + 2d}{L_{in}} \leq 0$$

Another geometric constraint is derived from the spring operation, where the distance between active turns is shortened until they come into contact and cannot deflect any further. Despite it being a physical reality, an explicit constraint must be added to the solver and prevent a numerical coil overlap. An equality constraint for the overlap would be too strict, as there is the possibility of lesser compression, so an inequality constraint is preferred. In this next equation, the level of displacement is controlled by the second additive (i.e. 1.15 corresponds to $1/1.15 \simeq 87\%$ of solid length deflection).

$$c3:\ \delta \leq L_0 - L_s \xrightarrow[L_s=(N_a+2)d]{L_0=pN_a+2d} \frac{N_a(d-p)}{\delta} + 1 \leq 0$$

The spring index C is yet another geometric constraint to acknowledge, it being relevant to manufacturing practices. According to [24], springs with too thick a wire diameter tend to be unnecessarily heavy and stiff, whereas spring with too thin wires are structurally prone to failure, justifying the existence of a spring index to quickly assess a spring. Numerical values have been reported in that source to range between 4 and 12, allowing for two additional constraints to be implemented:

$$c4:\ C \geq 4 \rightarrow -\frac{C}{4} + 1 \leq 0$$

$$c5:\ C \leq 12 \rightarrow \frac{C}{12} - 1 \leq 0$$

Structural constraints are primarily driven by the material properties and Requirement 4.1, complemented by Requirements 6.4 and 6.5. A helical spring is subject to shearing caused by the internal twisting motion of each wire element. Using Castigliano's theorem as seen in [24], the shear stress of Equation 5.5.7 holds true.

$$\tau = \frac{8FD}{\pi d^3} = \frac{8C}{\pi}\frac{F}{d^2} \xrightarrow{F=P\pi R^2} \tau = \frac{8C}{\pi}\left(\frac{R}{d}\right)^2 \cdot P \tag{5.5.7}$$

A correction factor must be inserted to the equation as this latter provides an average value based on the mean spring diameter and does not express the maximum stresses experienced by the coil extremities. This correction factor is a point of (contempt?) between the design guides considered so far. In [24] and [21], the *Bergstrasser factor* K_B is employed and given in Equation 5.5.8, while the authors of [105] propose a factor of $1.66C^{-0.16}$, following the practices of [95]. Both numbers originate from the Wahl correction factor K_W with different assumptions, which unavoidably leads to unique profiles, as seen in Figure 5.7. The results are clear and promote the use of the K_B, so Equation 5.5.7 is augmented with this factor.

$$K_B = 1 + \frac{5}{4C-3} \tag{5.5.8}$$

In order to materialize the stress constraint, auxiliary information must be provided. For starters, the shear stress is compared to a limit discussed in [24], it pertaining to the manufacturing process and selected material(s). Assuming an ideally manufactured spring, the allowable shear stress can be calculated as $60\ \%$ of the material's ultimate strength σ_u. A safety factor of $20\ \%$ is also imposed such that survival of the spring is ensured. The value is in contrast with Requirement 6.4 ($20\ \%$ vs. $60\ \%$), but is preferred as a dedicated guide should have closer relation to real-world objects than an arbitrary requirement. Then, one can interpret the constraint as:

$$c6:\ \frac{0.6\sigma_u}{\tau} - 1.2 \geq 0 \rightarrow \frac{2\tau}{\sigma_u} - 1 \leq 0$$

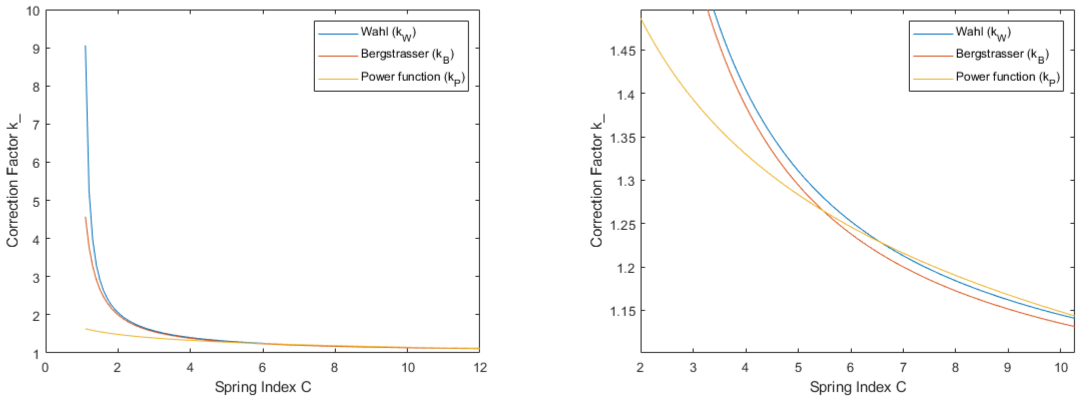

(a) Full range

(b) Zoomed

Figure 5.7: Comparison of stress-correction factors

5.5.6. Optimization Results

Table 5.4 concentrates the parametric optimization study as defined throughout the section, owing to a dedicated *MATLAB* script found in Appendix B called *CoilOpt*, for a tank with lengths $L_{tank} = 20,\ 25,\ 30$ and 35 mm. With a slight deviation observed in the $20\ mm$ case, the design vector (d, D, N_a, p) follows a pattern, with the spring index C and its dependencies being constant. The reason is quite simple: the optimized spring design should try and minimize its stiffness. From both Equation 5.5.1 and 5.5.3, the element in the highest power is the spring index, thus having the strongest impact. That said, the shear stress constraint $c6$ is always capped, which again can be traced back to C. The reader can also notice that for an increasing spring length and a constant spring index, the problem is shifted towards a thinner wire and a tighter coil distribution, effectively decreasing the stiffness k and increasing the overall deflection δ. Further, the correlation between geometry and pressure load is advantageous for the total mass budget discussed in this specific load case. As a matter of fact, opting for a longer spring increases the propellant capacity and simultaneously decreases the spring mass, owing to the thinner wires used.

Regarding the deviation present in the $20\ mm$ case, a brief troubleshooting session was conducted. By acknowledging the patterns in the design variables, it is logical to deduce that for a $20\ mm$ spring, the optimal number of coils should have been 1.75. This would have violated the lower bound imposed by the guidelines, so the system locked into the lowest value, affecting in turn all spring parameters. Insofar as the spring is a viable option for the tank assembly and the designer of the finalized product is more adept with the component, the optimal value can be utilized. The author however is obliged to deem the results of this model valid, given the theoretical approach employed and the table reflects what can be obtained without violating any bounds or constraints imposed in this fashion.

Speaking of constraints, one should remember of Requirement 1.2. The tank shall be sized to fit within a predetermined volume, but as it must be compatible with the PocketQube frame, the maximum allowable length is $20\ mm$. Consequently, a tank length of $L = 20\ mm$ and all correlated values will be used for subsequent calculations throughout the analysis.

Table 5.4: Spring optimization results

Variable	Units	Values (rounded to max. 3 digits)			
L	mm	20	25	30	35
R	mm	11.97	10.61	9.6	8.81
d^*	1	0.586	0.527	0.477	0.438
D^*	1	0.830	0.876	0.876	0.876
N_a^*	1	0.125	0.197	0.287	0.387
p^*	1	0.583	0.547	0.497	0.455
d	mm	2.92	2.635	2.384	2.189
D	mm	19.88	18.584	16.81	15.431
N_a	1	2	3.152	4.597	6.195
p	mm	5.83	5.473	4.951	4.545
C	1	6.8	7.051	7.051	7.051
K_B	1	1.207	1.198	1.198	1.198
k	N/mm	42.652	21.748	13.487	9.138
τ	MPa	602.5	602.5	602.5	602.5
δ	mm	5.804	8.944	11.8	14.6
L_0	mm	17.5	22.62	27.53	32.53
m_p	gr	2.613	3.163	3.414	3.56
m_{shell}	gr	6.69	6.645	6.726	6.871
m_s	gr	15.166	14.455	13.517	12.854

5.6. Case D: Structural Response of Accelerated Assembly

One of the secondary cases to be considered are the acceleration forces experienced during launch and sudden manoeuvres. Sloshing caused by the acceleration forces is not included in the study, it encompassing complex fluid dynamics analysis, but the structural aspect is of paramount importance to the tank's position and performance stability throughout the mission lifetime. As in all cases encountered so far, the analytical models explained rely on certain simplifying assumptions:

1. The supports and the lid are thin beams, lending for the *Euler-Bernoulli* equations.
2. The lid is not deflected, transferring the acceleration to the supports.
3. The support is strongly attached to the lid by the bolts, impeding any relative motion. Combined with the previous assumption, the lid-side end of the support is not allowed to rotate.
4. The structure-side of the support is fixed to the frame, so it cannot move or rotate. In more practical cases, a minuscule gap should be allowed to account for tolerances, but for a simplified model it is efficient.
5. The spring cannot be accelerated and bent sideways, due to the form and size acquired at Section 5.5.

The acceleration load is obtained from Requirement 4.2. The entire satellite is accelerated, and since all components are structurally connected with clamping, the satellite's mass is most appropriate for the calculations. Taking the worst-case scenario, the acting load is obtained:

$$F_{accel} = m_{SC} \cdot 5 \cdot g_0 = 0.45\ kg \cdot 5 \cdot 9.80665\ \frac{m}{s^2} \simeq 22.06\ N \rightarrow \tag{5.6.1}$$

$$q = \frac{F_{accel}}{L} = \frac{22.06\ N}{0.036\sqrt{(2)}\ m} = 433.4\ N/m \tag{5.6.2}$$

5.6.1. Accelerated Supports

Figure 5.8 shows the free-body diagram considered for the model setup. Point A is fixed, whereas section BC is only allowed to translate. The physical interpretation follows from the acceleration pushing the assembly, and the lid acting as a stoppage to the central section, mapped between points B and C. Since BC is an overhang to point B, it can be replaced by a shear force and an associated moment, effectively reducing the problem to a single-section beam with two boundary conditions: a fixed constraint on point A and a no-rotation constraint on point B. The two load types (distributed - overhang) are incompatible due to these boundary conditions, thus requiring to solve the problem twice, once for the distributed load, and another for the total load case. The effects are shown in comparative charts.

Section BC

Section BC can be treated as a beam moving relative to point B. On a local coordinate system, the deflection profile can be tackled as a fixed-free beam problem, with forces and moments

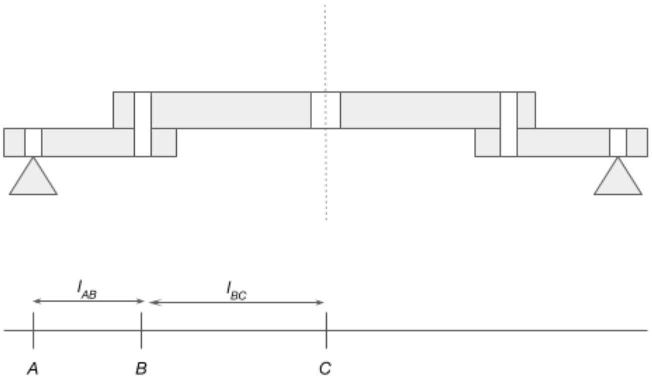

Figure 5.8: Free body diagram of accelerated assembly: lid view.

being derived by balance on B, shown below. For the sake of simplicity, the bolt and support beam hole diameters are omitted and the calculations are performed on a point-to-point basis. In addition, the beam length ratio $\bar{l}$ is introduced:

$$\bar{l} = \frac{l_{BC}}{l_{AB}} = \frac{l_{BC}}{l}$$

Then, the boundary conditions for point B, essentially the shear reaction force R_B takes the form:

$$\sum V = 0 \longrightarrow R_B = q \cdot l_{BC} = q \cdot l \cdot \bar{l}$$

Section AB

Caused by the satellite acceleration, the beam is subject to a distributed load q, spanning over its length and a concentrated overhang load, determined from the previous section. The deflection, stress and moment profiles are obtained by using polynomial integration and the *Euler-Bernoulli* thin beam equations, as reported in [44]. The load q is given:

$$w'''' = -\frac{q}{EI}$$

Since q is uniform along the section, $w'''' = a$, a constant. Integrating multiple times over the local length x, or its normalized form u, leads to the equation set provided in Table 5.5. The second, normalized form is used hereafter for calculations. Then, according to the boundary conditions suited for each load case, the problem is solved twice and a unique set of polynomial coefficients is determined per case. The boundary conditions and the respective coefficients are reported in Table 5.6.

Insertion of the coefficients back to the contents of Table 5.5 gives rise to the analytical model for the accelerated supports presented in Table 5.7. It is possible to discern the effect of the overhang load on the behaviour of a fixed-free beam by looking at the various equation coefficients or at Figure 5.9.

The general behaviour of the support is now available, but stresses developed under the acceleration have yet to be defined, needing a sizing study of the beam's cross-section. A rectangular beam is considered sufficient for this predictive model, composed by a width b

Table 5.5: Polynomials for section AB

	Equation Name	$x,\ 0 \leq x \leq l$	$u = x/l,\ 0 \leq u \leq 1$
w''''	Load	a	a
w'''	Shear	$ax + b$	$l\left(au + \frac{b}{l}\right)$
w''	Curvature	$\frac{a}{2}x^2 + bx + c$	$l^2\left(\frac{a}{2}u^2 + \frac{b}{l}u + \frac{c}{l^2}\right)$
w'	Slope	$\frac{a}{6}x^3 + \frac{b}{2}x^2 + cx + d$	$l^3\left(\frac{a}{6}u^3 + \frac{b}{2l}u^2 + \frac{c}{l^2}u + \frac{d}{l^3}\right)$
w	Deflection	$\frac{a}{6}x^3 + \frac{b}{2}x^2 + cx + dx + e$	$l^4\left(\frac{a}{24}u^4 + \frac{b}{6l}u^3 + \frac{c}{2l^2}u^2 + \frac{d}{l^3}u + \frac{e}{l^4}\right)$

Table 5.6: Boundary conditions for section AB

Distributed load		Total load	
Boundary Condition	Solution	Boundary Condition	Solution
$w'''(1) = 0$	$b = -al$	$w'''(1) = -\frac{R_B}{EI}$	$b = -(1 + \bar{l})al$
$w'(0) = 0$	$d = 0$	$w'(0) = 0$	$d = 0$
$w'(1) = 0$	$c = \frac{al^2}{3}$	$w'(1) = 0$	$c = \frac{al^2}{6}(2 + 3\bar{l})$
$w(0) = 0$	$e = 0$	$w(0) = 0$	$e = 0$

Table 5.7: Model Equations

	Magnitude	Profile (Distributed load)	Profile (Total load, $\bar{l} = 1$)
w'''	$\frac{-ql}{EI}$	$u - 1$	$u - 2$
w''	$\frac{-ql^2}{6EI}$	$3u^2 - 6u + 2$	$3u^2 - 12u + 5$
w'	$\frac{-ql^3}{6EI}$	$u(u-1)(u-2)$	$u(u-1)(u-5)$
w	$\frac{-ql^4}{24EI}$	$u^2(u-2)^2$	$u^2\left(u^2 - 8u + 10\right)$

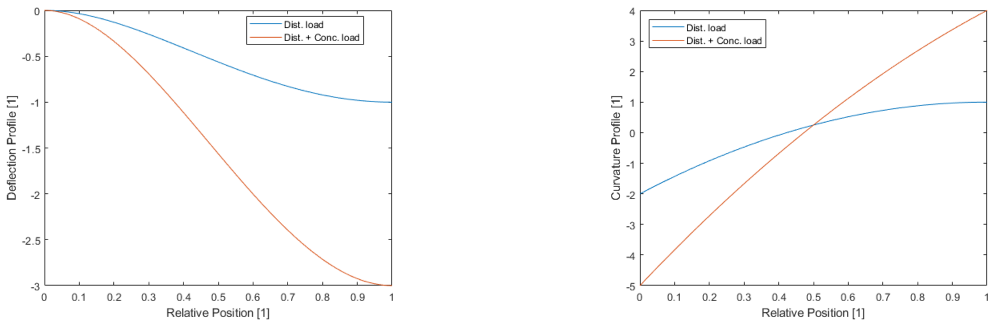

(a) Deflection $w(u)$

(c) $w''(u)$

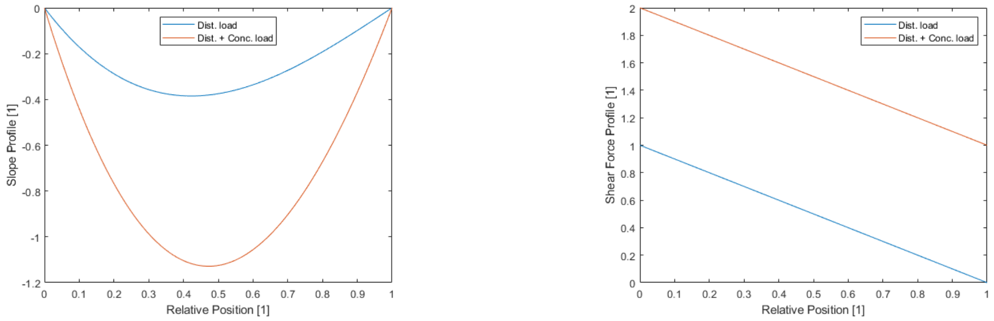

(b) Slope $w'(u)$

(d) $w'''(u)$

Figure 5.9: Structural response of the accelerated supports (dimensionless)

and a height h. The length l_{AB} is assumed equal to $9\ mm$ and $\bar{l} = 1$, while width and height can be modified based on the bolts selected in Case B.

For the remaining calculations, the analysis made earlier can be useful. From [44], $M = EIw''$, with the curvature w'' being defined by both magnitude and relative position on the beam. In addition, the bending stress can be modelled as $\sigma = \dfrac{Mc_y}{I}$, where c_y is the max distance from the beam's neutral axis and I the cross-section. Both can be found in various engineering books, hereby presented:

$$I = \frac{1}{12}bh^3, \quad c_y = \frac{h}{2}$$

After refactoring, and the stress level can be correlated to the relative position u, the beam height h and the beam width b as follows:

$$\sigma(u) = \frac{Eh}{2}w''(u) = -\frac{q}{b}\left(\frac{l}{h}\right)^2 \cdot \left(3u^2 - 12u + 5\right) \tag{5.6.3}$$

Judging from the curvature profile in Figure 5.9c, the beam extremities will sustain the highest stresses, reducing Equation 5.6.3 to a two-argument function. For a number of width and height combinations, the beam structural response is recorded in Table 5.8. Even at the worst case considered, it being the thinnest beam possible loaded by the entire satellite mass, the effects of acceleration are minimal and need not be further discussed. A side advantage of such observation is that positioning of these supports can be varied to facilitate integration of the tank with other components, such as the control valve. This however must be tackled once detailed product dimensions are available. As far as mass is concerned, a parallelepiped beam can be used as a first approximation, hence

$$m_{support} = 8 \cdot \rho_{al} \cdot b \cdot h \cdot (l_{AC} - (R+h)_{shell}) \xrightarrow[b=5\ mm, h=3\ mm]{l_{AC}=18\sqrt{2}\ mm} M_{support} \simeq 4.0\ g$$

Table 5.8: Structural response of the beam for various width and height values

b $[mm]$	h $[mm]$	$\sigma_{max,A}$ $[MPa]$	$\sigma_{max,B}$ $[MPa]$	$\delta_{_B}$ $[\mu m]$
1	3	−34.051	27.24	6.48
1	5	−12.26	9.8	1.40
2	3	−17.025	13.62	3.24
2	5	−6.13	4.9	0.7
2	7	−3.12	2.5	0.25

5.6.2. Accelerated Spring

Under normal, idle conditions, the spring and the propellant are balanced in a position determined by the available propellant mass. Moreover, the propellant being incompressible, full contact is ensured at all times, so the tank interior is considered to be accelerated and moving uniformly. Acknowledging this and still operating under the premise of *Hooke's Law*, the spring deflection due to this load can be calculated:

$$\delta_{accel} = \frac{F_{accel}}{k} \xrightarrow{Table\ 5.4} \delta_{accel} \simeq 2 - 0.5\ [mm] \tag{5.6.4}$$

The spring deflection is large enough to assume that the spring will be overloaded with acceleration-related stress. Two sub-cases can be identified: in compression, the spring receives additional shear stress at the coils, because of the added deflection. For the springs provided in Case C, additional stress can only be converted to axial load due to their solid-length state at full propellant capacity. In tension, the acceleration force is subtracted from the pressure load, causing spring deflection towards the undeformed state. However, the fluid cannot be compressed, so the additional load is exerted onto the tank walls. With that said, the design choices made during Case A and Case C calculations are able to compensate for the lack of specific analytical models, hence no further discussion is required.

5.7. Case E: Dynamic Response of System

The entire assembly has been sized for a good static response with reasonable margins of safety, but its functionality is still under question, requiring a time-dependent analysis of the system. Contrary to the previous sections, where analytical models were employed for an isolated tank, the dynamic response of the spring and the fluid must be evaluated as a part of the entire propulsion module. This decision comes as a natural consequence of the tank's purpose, which is to provide a specific mass flow determined by the thruster working conditions, and as a by-product of a preliminary attempt to conduct an individual transient study of the tank. Under this premise, the operational principle of the module is discussed as a series of concatenated actions of the individual components:

1. From an idle state, the thruster is pre-heated to its optimal thermodynamic conditions P_c, T_c to fully vaporize any propellant reaching the main chamber section.
2. Once that procedure is complete, the gate valve opens and joins the tank assembly with the thruster.
3. The pressure difference between the thruster pressure P_c and the tank pressure P causes an impulsive movement of fluid, towards the chamber.
4. The volume lost from the tank causes a force imbalance between the spring and the fluid pressure load, enabling the spring to move to its undeflected position.
5. While the valve is open, the spring momentum ejects more fluid into the system, keeping the cycle active. Simultaneously, the spring loses momentum as the tank pressure P decreases.
6. Upon termination of the thrust manoeuvre or pressure balance between chamber and tank, the valve closes. Depending on the valve response, a sudden pressure rise is encountered at the tank due to the water hammer effect.
7. The spring balances to a new position, ending the pressure-displacement loop.

Based on the above explanation, an analytical model that considers the three main components, namely the tank, valve and thruster, must be implemented. Retaining a motif consistency with previous sections, some assumptions are much needed to reduce the impact of additional complexity due to the multiple components.

- Time starts counting from Step 2, meaning the thruster is already set to its optimal thermodynamic conditions. Attempting to model the transient behaviour of pre-heating the chamber would require additional information about its material properties, electronic control and so on, which is irrelevant to the process of characterizing the tank. While analytical models for both the transient and the steady state response have been presented in Chapter 1, they are not fundamental to the process discussed in this section.
- The system is expected to operate with a mass flow output equal to the critical mass $\dot{m}^*$, preventing choked flow situations.
- Pressure losses across any piping are considered negligible, given the length and working pressure of the system. Instead, pressure losses due to components themselves or their transitions are included when available, or adjusted by correction factors.
- The valve has a finite reaction time t_v, meeting two objectives: enable the overall use of time-dependent models and introduce a smooth pressure transition model. An immediate valve response causes strong pressure drops and spikes, which may lead to numerical instabilities during the simulation, so a time-delay factor such as t_v can bypass this impact.

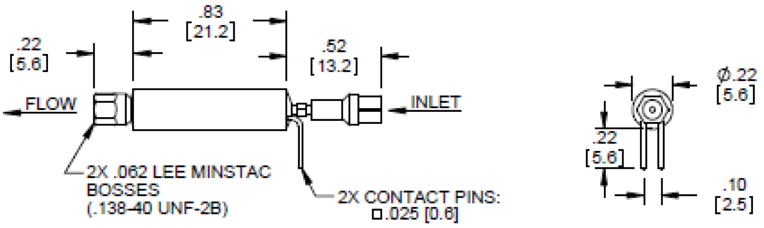

Figure 5.10: The INKX0511400AA5 VHS Solenoid Lee Valve (mm in brackets). Source: [61].

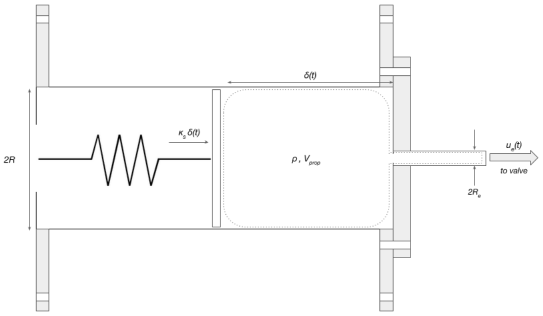

Figure 5.11: Visual representation of time-dependent model.

- As far as the fluid movement is concerned, no-slip conditions at the tank walls are not needed, since the spring enforces movement of the entire surface A. This behaviour is better approximated by slip conditions that nullify radial gradient of the fluid velocity.
- The spring mass is transferred onto the plate, allowing the use of simple oscillatory models. This is unrealistic in terms of the object's behaviour, being also subject to inertia effects, but the movement expected during each cycle is small enough to treat the spring as a quasi-static object, hence the mass concentration should not have an impact on the model's accuracy.
- The fluid port of the tank lid has a radius R_{exit} equal to the valve inlet radius R_v. A reasonable assumption for the valve model is the *INKX0511400AA5 VHS Solenoid Lee Valve*, seen in Figure 5.10. According to the report of [61], this specific valve can contain $35\ \mu L$ of propellant within its main cylindrical volume. By simple combination of all available dimensions, the radius R_v turns out to be $0.725\ mm$, used in subsequent calculations.

A preliminary dynamic model is constructed according to a *fluid-structural interaction* problem. This entails a two-way coupling between the fluid and the solid domain, such that the forces and displacement properties are common or analogous. For the object at hand, the solid domain is represented by the spring and the fluid domain is represented by the expelled fluid leaving the tank. The reader can visually understand this in Figure 5.11.

5.7.1. Transient Behaviour of Helical Spring

The time-dependent response of the spring is a well known problem in the engineering world, so the physical interpretation is only given as a reminder. This flexible element is described by a stiffness constant (already seen as k) and a damping constant c that corresponds to friction losses, if assumed to exist. At any point in time, the pressure force $P(t)A$ causes an acceleration of the spring towards a deflected position and the internal reaction forces $k\delta(t)$ and $c\dot{\delta}$. The total acceleration of the spring is determined by simple summation of the forces exerted, per mass unit m, here equivalent to the spring and plate mass m_s :

$$\ddot{\delta} = -\frac{k}{m}\delta - \frac{c}{m}\dot{\delta} + \frac{A}{m}P(t) \tag{5.7.1}$$

The natural response of a spring affected by external forces is an oscillatory behaviour around an equilibrium point, determined by the force magnitude and excitation frequency and the damping constant. However, the time-varying pressure force is dependent on the fluid present in the tank at all times, hence the common analytical solutions found in various literature sources cannot be used yet. Another difficulty found in the spring model is the selection of an appropriate damping constant. Throughout the chapter, friction forces have been neglected and thus all structural models are idealized, but the spring is expected to develop friction with the tank walls due to its outer diameter D_o. To resolve this issue, another assumption is made: according to Requirement 6.2, the 6000 cycles estimated over an Earth year can be translated to a single per-orbit thrust maneuver. Such a small event frequency means the thrust duration is small compared to the idle state, proven in Chapter 1. A direct implication is the quasi-static format of the problem, allowing the author to ignore friction. With this in mind c is only determined by the internal damping of the spring coils as follows:

$$c = 2\sqrt{k \cdot m_{spring}}$$

5.7.2. Transient Behaviour of Fluid Flow

Predicting the fluid domain evolution is an intricate process that relies on two main contributions: fluid compression, a property-dependent occurrence, and fluid ejection, a flow-dependent occurrence. A textbook method to predict fluid flow is the employment of the *Navier-Stokes* equations, with all relevant assumptions. Nonetheless, the amount of complexity involved with partial differential equations, time-dependent derivatives and varying force input outweighs the detail and accuracy obtained from the solution, not to mention that spatial flow gradients are negligible.

A more crude prediction of the flow development can be made through the fundamental principle of fluid compressibility. Fluids, and all materials for that matter, are characterized by a property called *Bulk Modulus* (β), describing the equivalent compression and expansion capabilities of a material. In mathematical terms, Equation 5.7.2 correlates the relative volumetric expansion $\Delta V/V$ to the pressure load differential ΔP:

$$\beta = \frac{\Delta P}{\frac{\Delta V}{V}} \rightarrow \Delta P = \beta\frac{\Delta V}{V} \xrightarrow{\frac{\partial}{\partial t}} \dot{P} = \beta\frac{\dot{V}}{V} \tag{5.7.2}$$

Finding the fluid volume V is straightforward. The control volume designated by the dashed line in Figure 5.11 contains fluid equal to $A\delta$, which at the start of each thrust manoeuvre, is equal to V. The volume change rate $\dot{V}$ on the other hand is more complex. As already explained, the fluid volume V is reduced twice: one is associated with the physical reduction of the control volume and determined by the spring velocity $\dot{\delta}$, and the other is related to fluid mass leaving the control volume, hence a volumetric loss. This latter is in turn caused by the pressure gradient developed between the tank and the feed system, and determined by the exit velocity u_v.

A critical element in simulating the fluid response and in particular the velocity u_v is the valve actuation model. Despite the lack of information about the physical component, it is possible to replicate its function with a transient Bernoulli equation, an implementation of which is found in [80]. This formulation offers a good starting point, presenting a few similarities with the current problem. For instance, both systems start from a resting position, irrespective of the cause. In this study, the valve isolates the tank and creates an idling standalone component. Moreover, the model found in the source example concludes with a velocity equation that can be split into a magnitude - derived from the steady-state Bernoulli equation - and a time-dependent factor reflecting the system's *response time*, t_v. Being a mechanical component, the valve is also characterized by a response time for its full actuation, enabling the use of a hyperbolic tangent function to simulate the opening and closing process. In mathematical terms, the transition can be seen in Equation 5.7.3, where t_{thr} denominates the thrust time:

$$A_v(t) = A_{v,max} \cdot \begin{cases} \tanh\left(\frac{t}{t_v}\right), & \text{if } 0 \leq t \leq 4t_v \\ 1 - \tanh\left(\frac{t-t_{thr}}{t_v}\right), & \text{if } t_{thr} \leq t \leq 4t_v + t_{thr} \end{cases} \tag{5.7.3}$$

In determining the magnitude, the steady-state Bernoulli formulation is employed at the lid exit point, assuming there is no significant pipe length between the tank and the valve inlet:

$$P(t) + \frac{1}{2}\rho u^2 = P_{v,in} + \frac{1}{2}\rho u_v^2 + \Delta P_{loss} \rightarrow u_v^2 - u^2 = \frac{2}{\rho}(P(t) - P_{v,in}) - \Delta P_{loss} \tag{5.7.4}$$

Correlation of the fluid velocities u and u_v is apparent via the continuity equation:

$$\dot{m} = const. \rightarrow u \cdot A = u_v \cdot A_v \xrightarrow{\alpha=\frac{R_v}{R}} u = \alpha^2 \cdot u_v \tag{5.7.5}$$

Then, the fluid velocity magnitude can be estimated for a real-world case as follows:

$$u_v = \sqrt{\frac{2}{\rho}(P(t) - P_{v,in}) - \Delta P_{loss}} \cdot \sqrt{\frac{1}{1-\alpha^4}} \tag{5.7.6}$$

The accuracy of Equation 5.7.6 is limited by the approximation of total pressure losses ΔP_{loss} caused by the lid entrance geometry and the subsequent *vena contracta* effect, the localized acceleration of the fluid, other components downstream of the exit and so forth. Without any concise information, the search for analytical models is impractical and time-consuming. Instead, the effect of non-ideal conditions and associated pressure losses can be compacted into a single value called *Discharge Coefficient*, or C_d [84]. The structural resemblance between the lid and a cornered tap orifice allows for the coefficient to be evaluated according to orifice design properties. The schematic found in [84] shows an empirical approximation of the discharge coefficient as a function of both the radius ratio α and the diameter Reynolds number Re_d. Taking a worst-case scenario, Table 5.4 gives a value of $R = 11.97\ mm$, whereas the orifice radius is $R_v = 0.725\ mm$, as per previous assumptions,

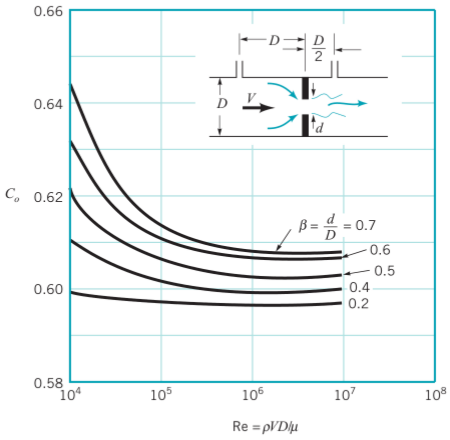

Figure 5.12: Orifice meter discharge coefficient. Source: [84]

outputting a ratio equal to 0.0605. The latter is much lower that the lowest value present in the chart, seen in Figure 5.12, but the overall profile of C_d across a range of Reynolds numbers shows that for small radius ratios the coefficient is invariable. For practical purposes, a value of $C_d = 0.6$ is selected and pressure losses are omitted from Equation 5.7.6.

Integrating all discussed parts gives rise to the volume change rate $\dot{V}$, and ultimately in Equation 5.7.8, closing the loop for the fluid-structure interaction problem.

$$\begin{cases} \dot{V} = \dot{V}_s + \dot{V}_{ej} = A\dot{\delta} + A_v(t)u_v \\ u_v = C_d\sqrt{\frac{2}{\rho}(P(t) - P_{v,in})} \cdot \sqrt{\frac{1}{1-\alpha^4}} \end{cases} \tag{5.7.7}$$

$$\dot{P} = \beta\left(\frac{\dot{\delta}}{\delta} + \alpha^2\frac{u_v}{\delta}\right) \tag{5.7.8}$$

At this point, the basic tank model is formulated within a closed loop but it is incomplete, due to a major unknown: the valve pressure $P_{v,in}$. Having considered an idealized thruster performance, no gaseous propellant is left downstream of the valve, meaning that the correspondent pressure $P_{v,out}$ drops back to the nozzle exit pressure and consequently the valve pressure $P_{v,in}$ is subject to variations over time. A reasonable method to estimate the valve inlet pressure is a backtrack calculation of all interim stages, starting from the chamber. Involving the nozzle does not contribute much, as its pressure value can be derived as a function of the main chamber pressure P_c and the nozzle geometry, seen in Equation 1.1.15. Accounting for the assumption of immediate vaporization, the time required for the propellant to reach the main chamber section and become a gas is sufficiently small to consider a steady-state operation of the thruster, thus $P_c = P_{c,max}$ and $\dot{m} = \dot{m}^*$. Propellant flow through the chamber inlet towards the main chamber section is summarized to a flow expansion process, so a reverse orifice model can be utilized to calculate the inlet pressure $P_{c,in}$ with a low level of confidence. Once again, the Bernoulli equation and continuity equations are employed, although modified to exploit technical data on the critical mass flow $\dot{m}^*$. The α_{ci} factor represents the diameter ratio between the inlet and the main chamber, in a similar fashion to α.

$$P_{c,in} = P_c + \frac{1}{2\rho C_d^2} \cdot \left(\frac{\dot{m}}{A_c}\right)^2 \cdot \frac{1-\alpha_{ci}^4}{\alpha_{ci}^4}$$

Another flow constriction is assumed to exist between the valve outlet and the chamber inlet, with no significant feed line length. The orifice model holds true in this instance, with α_{vi} corresponding to the area ratio between the valve and the chamber inlet.

$$P_{v,out} = P_{c,in} + \frac{1}{2\rho C_d^2} \cdot \left(\frac{\dot{m}}{A_v}\right)^2 \cdot \frac{1-\alpha_{vi}^4}{\alpha_{vi}^4}$$

Lastly, the valve is known to cause a pressure drop of $0,433\ Pa$ according to [93] due to internal characteristics. The drop is tremendously small compared to the working pressure of the system, but aids the completeness and accuracy of the model. Once all interim calculations are complete, the valve inlet pressure $P_{v,in}$ can be calculated and inserted in Equation 5.7.6, marking the completion of this rudimentary FSI model.

5.7.3. *SIMULINK* Model

Following from the analytical model description the iterative aspect of the model becomes apparent, with spring and fluid variables being strongly coupled. Among the plentiful software available for solving a problem of this type, the *SIMULINK* graphical programming environment offered by MathWorks [106] has been selected for its intuitive block-based approach and the ease of use. There is a certain learning curve for the non-acquainted, but the included OnRamp course provided by the company was more than sufficient to familiarize the author with the software.

Figure 5.13 illustrates a schematic of the *SIMULINK* model that has been set up, solving the *fluid-structure interaction* problem, while in Appendix B detailed schematics of the individual components are presented. The reader can discern three subsystems in addition to the basic integration blocks: the valve controller, which as the name implies, defines the valve openness based on the hyperbolic tangent approach described in [80], the spring solver that calculates the spring acceleration from Equation 5.7.1 and subsequently the new position and velocity, and the fluid solver that estimates the pressure change rate from Equation 5.7.8 and in turn the new pressure.

Implementation of the model also requires certain design parameters, that can either be derived from the preluding literature study or approximated through reasonable assumptions. Table 5.9 collects all necessary design parameters, followed by an appropriate rationale. These values are not intended to fully cover the real-world problem, but the general behaviour should still be sufficient to draw productive conclusions on the design concept and its peculiarities.

Calculation of the valve inlet pressure $P_{v,in}$ was halted due to a total pressure drop along the transitions of $2.04\ Pa$, raising doubts on the accuracy of this proposed method. Upon further literature inspection, primarily on the sources from which parameters where taken, the analyses conducted on just the heater chamber section revealed a pressure drop of $1.28\ bar$ on behalf of [93], whereas [50] argues said result with a series of alternative values, based each time on a different pressure drop model. In the simplest of cases, a pressure drop along the chamber of $3.1\ Pa$, greatly amplified to $238\ Pa$ if the internal heater pillars of the thruster are included. In all cases, the value calculated in this study seems small to be realistic.

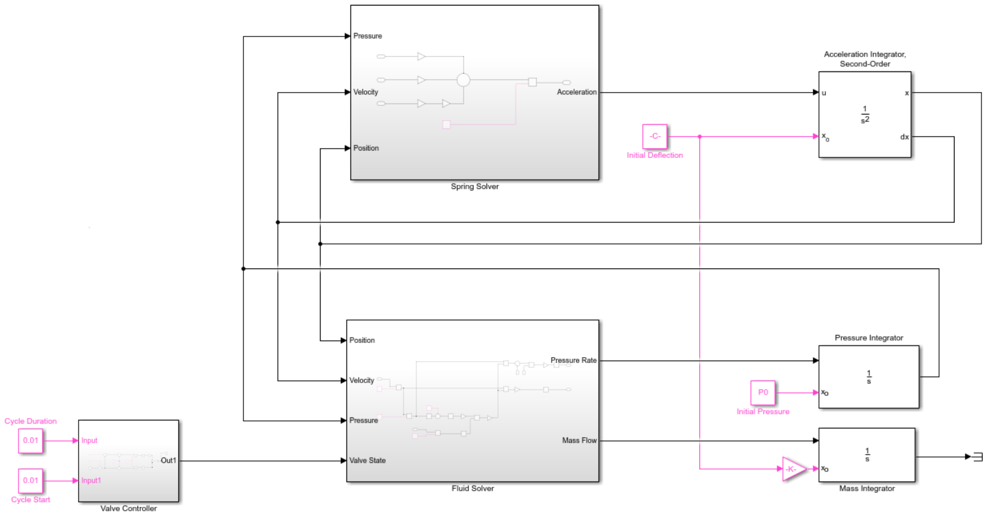

Figure 5.13: *SIMULINK* model schematic for the fluid-structure interaction problem.

Table 5.9: Simulation parameters for transient model

Parameter	Description	Units	Value	Rationale
		Valve Controller		
t_v	Response time	ms	0.25	Valve response time [61]
t_{thr}	Thrust duration	ms	10	-
R_v	Valve inlet radius	mm	0.725	Microvalve inlet port area [61]
ΔP_v	Pressure drop across valve	Pa	0.433	Data from [93]
		Spring Solver		
k	Spring stiffness	N/mm	42.75	Section 5.5, 20 mm tank length
c	Damping constant	Ns/mm	0.0532	Oscillation stability
m_s	Spring mass	gr	16.17	Section 5.5, 20 mm tank length
R	Plate radius	mm	11.97	Section 5.3, 20 mm tank length
		Aux.Thruster Data		
P_c	Thruster pressure	bar	5.44	Requirement 6.1
T_c	Thruster temperature	K	550	Data from Chapter 1
A_c	Main chamber cross-section	mm^2	0.45	Data from [50]
A_{ci}	Inlet cross-section	mm^2	0.06	Data from [50]
A^*	Nozzle throat cross-section	mm^2	0.0019	Data from Chapter 1
γ	Specific heat ratio	1	1.33	-
		Initial Conditions, $t = 0$		
P	Tank pressure	bar	5.5	Requirement 6.1, Sizing target
δ	Initial spring deflection	mm	5.659	Section 5.5, 20 mm tank length

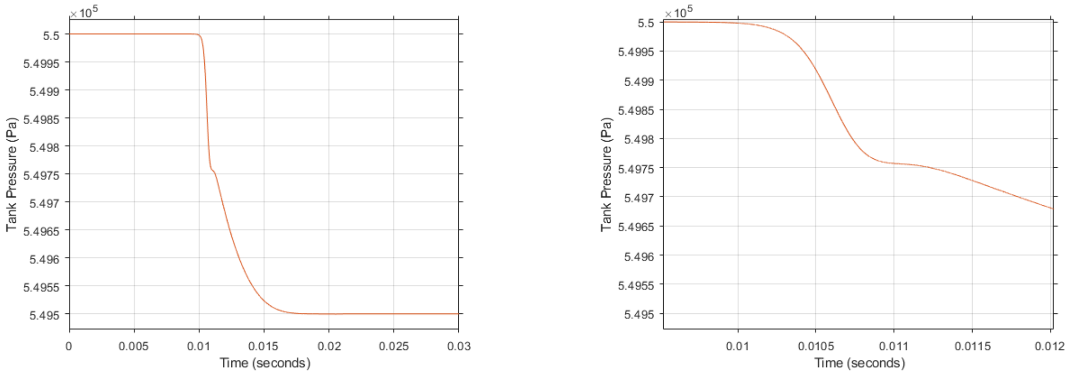

(a) (b)

Figure 5.14: Pressure evolution during thrust cycle for the SF1 configuration.

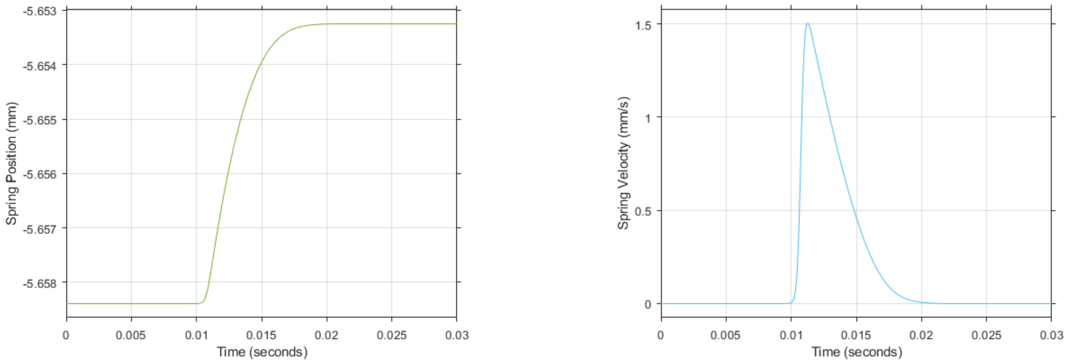

(a) Position, in absolute displacement (b) Velocity

Figure 5.15: Spring movement during thrust cycle.

As a result, a more reasonable approach would be to apply a total pressure drop from the valve to the nozzle, with any consequences this has on the confidence level of this analysis. On the bright side, this preliminary result can be corrected once more advanced models are introduced in numerical simulations. That said, a total pressure drop of $5500\ Pa$ is proposed, meaning that for a chamber pressure $P_c = 544000\ Pa$, the valve pressure $P_{v,in}$ amounts to $549500\ Pa$. This is in a better accordance with the analysis of [50] insofar as complex models regard, where a chamber pressure drop of approximately $1\ \%$ of the inlet pressure has been reported.

5.7.4. Results

Figures 5.14 through 5.16a summarize the performance of the spring-fluid system in a single thrust cycle, under the setup of Table 5.9. The results are within theoretical expectations, with small initial oscillations until the valve reaches a fully open state. In addition, the lack of a pressure spike at the cycle end indicates a smooth and linear mass outflow down to the point of pressure equalization. Going by the values of Figure 5.16b a total of $2.31\ mg$ has been expended in the time interval of $10 + 3 \cdot 0.25 + 3 \cdot 0.25 = 11.5\ ms$, averaging a $201\ mg/s$ mass flowrate. The latter is way in excess of results from similar projects worked on by [93], [61], [50] and [59], in which values range from $0.3 - 3\ mg/s$, which is a discouraging point for the application of this specific spring contraption.

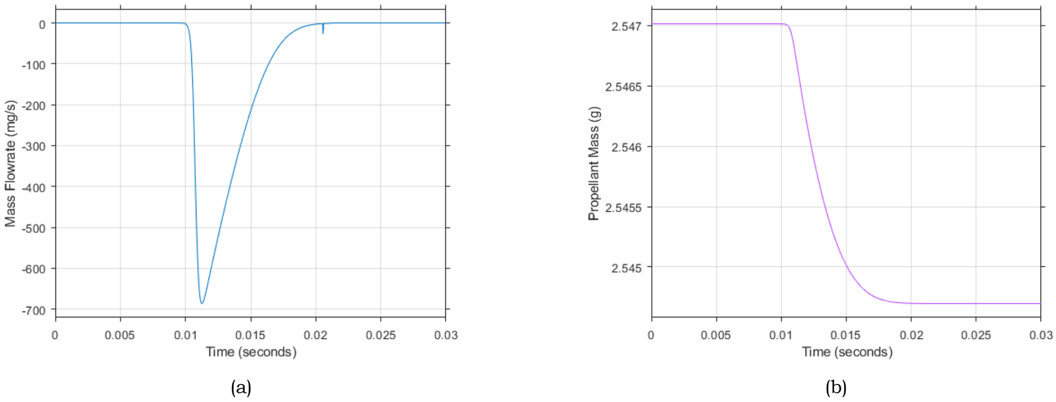

(a) (b)

Figure 5.16: Propellant mass evolution during thrust cycle for the SF1 configuration. The negative value expresses fluid leaving the tank.

Among the sheer number of assumptions, approximations and crude methods applied in this transient analytical model, the author discerns two main contributors to such a high mass flowrate:

1. The mechanical properties of the spring, in particular the high stiffness k. As far as the optimization is concerned, not much can be done, due to the results of Table 5.4. Even at the most optimistic case of a $33\ mm$ long spring, the stiffness is reduced by a mere factor of 4.66, a far cry of the 200 required to reach a mass flowrate within the established range of literature sources. The only solution to obtaining a better, softer spring is a change in either the configuration (see List 4.5.3 and Figure 4.15) or the form, moving to telescopic variants.
2. The pressure difference $P - P_{v,in}$. The form of the fluid velocity in 5.7.6, and by consequence the mass flowrate $\dot{m}$, is strongly affected by the difference in pressure between the tank and the valve inlet. It seems that the assumptions made for the pressure $P_{v,in}$ are erroneous and do not provide a high enough resistance to the flow. As a matter of fact, by expanding 5.7.6 and solving for the pressure difference under the premise of a choked flow, the following statement holds:

$$P - P_{v,in} = \frac{1}{2\rho C_d^2} \cdot \left(\frac{\dot{m}}{A}\right)^2 \cdot \frac{1-\alpha^4}{\alpha^4} \rightarrow P - P_{v,in} = 1.1 \cdot 10^{-3}\ Pa$$

   With such a small value of pressure drop across the tank-valve point, the model could only run for sub-millisecond times, which are too close to the valve reaction time t_v and imply that as soon as the valve opens, the entire thrust manoeuvre is completed.

5.8. Troubleshooting: configuration change

In dealing with the issues of Section 5.7, a new configuration can be explored within the scope of this chapter, as the core model treats the pressurization assembly as a single unit. The *SFX* formation found in List 4.5.3 and Figure 4.15 seems promising, as it will minimize wasted space due to the single spring by accommodating smaller springs. Ideally, this will spread the load in softer springs and improve deflection levels. This can be achieved in two methods: either by following the list description, hereafter called Option A or Real SFX, or by subdividing the tank in multiple equal compartments and running the optimization, thus artificially replicating the configuration under the name of Option B/ Pseudo-SFX. Both designs are characterized by benefits and drawbacks pertaining to manufacturing, operation and part feasibility, but they are temporarily ignored for the sake of a performance study. For instance, the optimization results are not rounded to manufacturing dimensions as previously without and serious performance penalty.

Option A: SFX

The configuration proposed relies on fitting a number of equal springs behind the piston plate such that the pressure load is split in a wider area, aiming to reduce the total spring stiffness and improve the propellant ejection rate along with the propellant capacity. The size and number of springs required can be determined by solving a well-known *circle packing problem*, which is introduced to the core optimization process as a design constraint known as *packing factor,* f. First, each spring is treated as a circle with diameter $D + d = (C + 1)d$. It follows that the area footprint of all participating springs is

$$A_s = N_s \cdot \frac{\pi}{4}(C+1)^2 \cdot d^2$$

where N_s is the number of circles. Naturally, the area of the piston plate is $A = \pi R^2$ according to the calculations of 5.3. The packing factor f is defined as the ratio between the two:

$$f = \frac{A_s}{A} = \frac{N}{4}(C+1)^2 \cdot \left(\frac{d}{R}\right)^2 \tag{5.8.1}$$

Since no manufacturing dimensions are regarded, it is safe to leave an error margin of 5% to account for any subsequent adaptations, hence the packing constraint can be stated as the spring area not exceeding 95% of the maximum packing factor known for the number of circles N_s, f_{lim}. This value has been identified in literature for a broad range of circle packings as shown in [14]. The design constraint then obtains the usual form seen in 5.5:

$$c7: \; \frac{N_s}{4}(C+1)^2 \cdot \left(\frac{d}{R}\right)^2 - 0.95 f_{lim} \leq 0$$

Option B: Pseudo-SFX

This artificial multi-spring formation is much easier to implement, as the core optimization model is not changed. Instead, solving for a single compartment only requires the division of the total tank volume by the number of compartments N_c and then applying the usual script, for a single-spring pressurization tank. Total propellant capacity and spring mass is obviously calculated by multiplication with N_c.

Optimization results

Figures 5.17 and 5.18 illustrate the variation of the optimization objectives m_p and m_s and the spring stiffness k as a function of the number N_s or N_c depending on the model. In this instance, numbers 1 to 10 were examined, though the model can be greatly expanded as long as a physical model is still achievable. The graphical charts are aided by tabulated data regarding the spring characteristics, also introducing a propellant-to-spring mass ratio m^* to better assess the effect of N. More detailed information on the springs are provided in Appendix C.

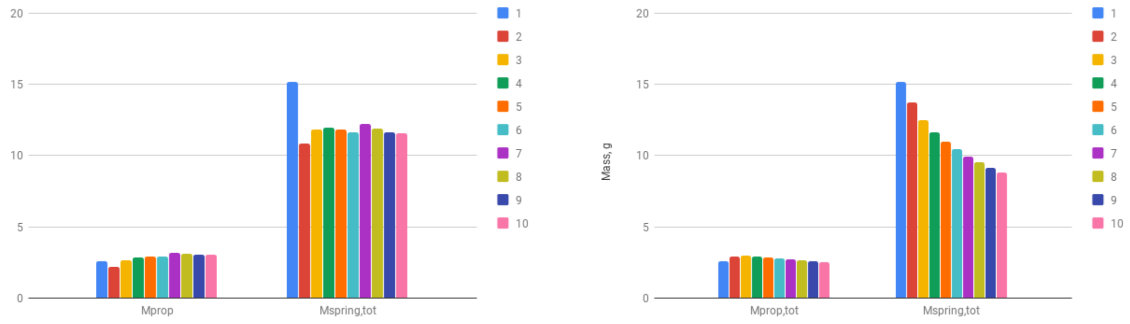

(a) Real SFX

(b) Pseudo-SFX

Figure 5.17: Propellant and spring mass variation for the SFX configurations 1 through 10.

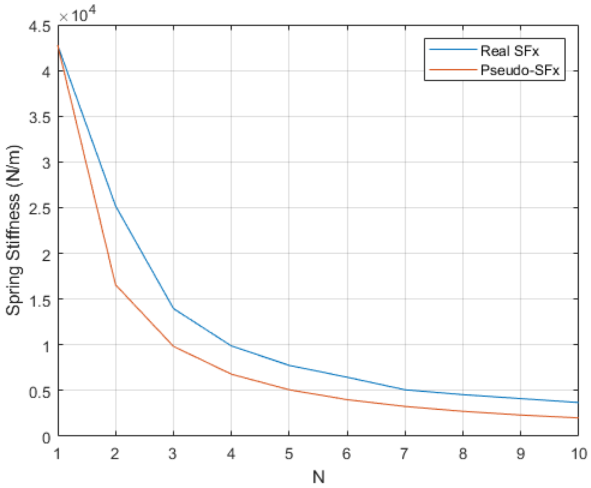

Figure 5.18: Spring stiffness variation for the SFX configurations 1 through 10.

The improvement of the spring properties with either option is apparent, as seen in the gradual reduction of the stiffness, while the mass footprints reveal that an optimal point exists for each objective, allowing the designer to opt for different formations according to the limits imposed by requirements, budgets etc. For the primary objective of this study, a high-capacity tank, the optimal points within the described number range N_s and N_c are 7 and 3 respectively. Between the two, Option A is superior in terms of propellant volume ($+200\ mg$), also confirmed by the lower individual spring stiffness k, hence the time-dependent model is

Table 5.10: N-dependent mass budget of propellant and springs

	Option A		Option B	
N	m_p $[gr]$	m_s $[gr]$	m_p $[gr]$	m_s $[gr]$
1	2.61	15.18	2.61	15.18
2	2.2185	10.8632	2.9308	13.7046
3	2.6682	11.8363	2.9442	12.4929
4	2.8292	11.9514	2.9064	11.6388
5	2.8836	11.8319	2.8440	10.9695
6	2.8853	11.6309	2.7774	10.4148
7	3.1403	12.2156	2.7090	9.9379
8	3.0817	11.9063	2.6408	9.5176
9	3.0140	11.6123	2.5731	9.1413
10	3.0286	11.5656	2.5070	8.8
N	m^*	Δm^* (%)	m^*	Δm^* (%)
1	0.1719	-	0.1719	-
2	0.2042	18.78	0.2139	24.38
3	0.2254	10.38	0.2357	10.20
4	0.2367	5.01	0.2497	5.96
5	0.2437	2.95	0.2593	3.82
6	0.2481	1.79	0.2667	2.86
7	0.2571	3.63	0.2726	2.22
8	0.2588	0.68	0.2775	1.79
9	0.2596	0.28	0.2815	1.45
10	0.2619	0.89	0.2849	1.21

executed with this new proposition to seek any meaningful performance gains.

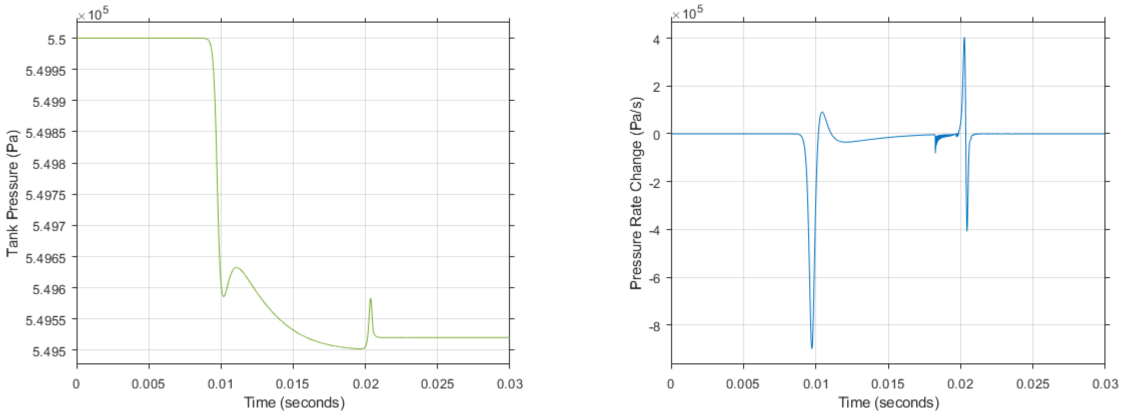

(a)

(b)

Figure 5.19: Pressure evolution during thrust cycle for the SFX configuration, at $\Delta P = 500\ Pa$.

Figures 5.19 through 5.21 mark the absolute improvement of the tank behaviour, primarily in the departments of mass capacity and management. More specifically, the lighter, softer springs seem to offer a lower mass flowrate $\dot{m}$ for a prolonged period of time compared to the SF1 configuration, proven by the pressure spike at the predefined valve shut-off event. This latter also confirms the existence of a water hammer effect in such high-speed valves. Further, the final value of tank pressure indicates that the cycle duration can be extended for the same pressure drop across the tank lid without significant impact on the mass expenditure, as the overall capacity is vastly increased. On the downside, the SFX configuration does not manage to reach satisfactory results with respect to the desired values found in literature. Once again, the mass flowrate is incredibly high for such a minuscule cycle duration ($10\ ms$ vs. $54\ s$) and the pressure change at the valve opening sequence is steeper and greater, due to the reduced spring mass. Even by limiting the pressure difference at $P_0 - P_{v,in} = 50\ Pa$, the results are still way off the target values, as shown in Figure 5.22.

Regardless of the cause and despite the aforementioned attempts of improving upon the original design, the model does not respond appropriately to the requirements and the common analytical models provided in literature and this leads to a single conclusion: a constant-

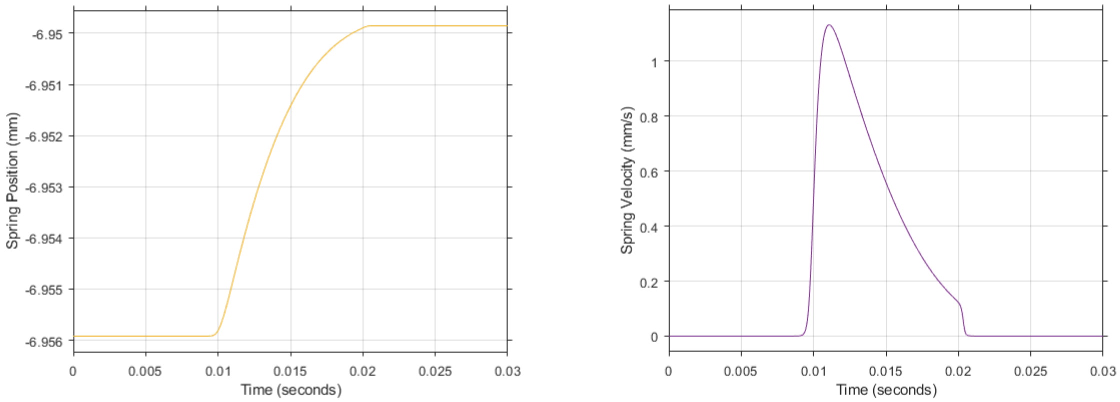

(a) Position, in absolute displacement

(b) Velocity

Figure 5.20: Spring movement during thrust cycle.

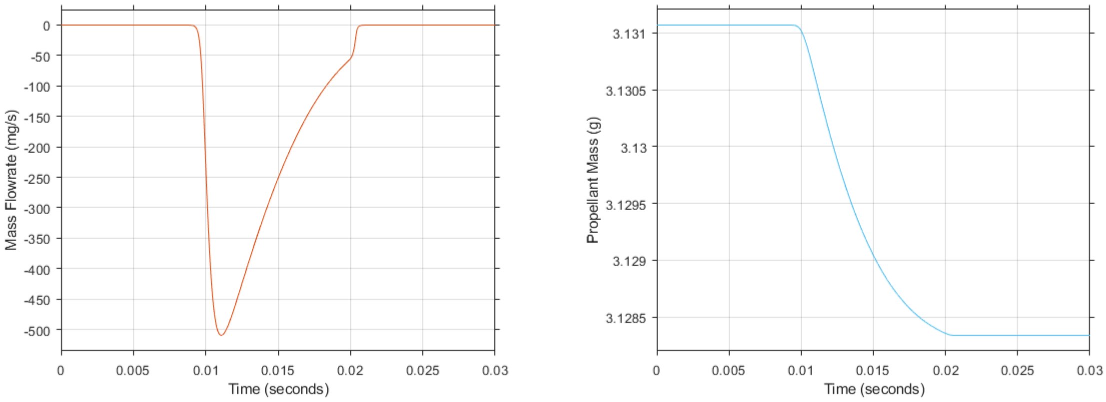

(a) (b)

Figure 5.21: Propellant mass evolution during thrust cycle for the SFX configuration. The negative value expresses fluid leaving the tank.

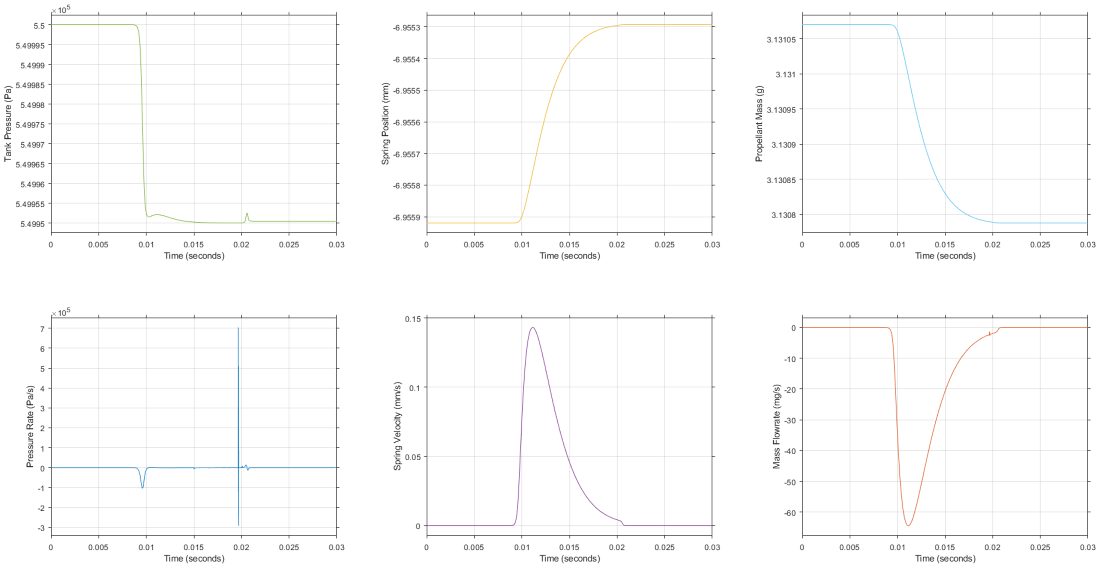

Figure 5.22: System behaviour in a single cycle, at $\Delta P = 50\ Pa$.

stiffness spring, which by default acts as a force multiplier for the deflection and hence the propellant volume/mass, can optimistically be used in subtle attitude correction manoeuvres, where short and strong thrust bursts are required. From a first inspection, a spring-powered tank does not look promising in its current form. The statement will be reinspected upon entering the next chapter, where more advanced models and better defined geometries will give more insight on the processes involved with Fluid-Structure Interactions.

5.9. Detailed Design Proposal (DDP)

The analysis conducted in Load Cases A through E draws productive conclusions on the structural and dynamic response of the spring-loaded assembly from a concept viewpoint, with some design choices being already available from Chapter 4. Nonetheless, proceeding onto the design phase requires the acquisition of a fixed parameter set for all constituent parts, namely the *SF-x* spring, the *LT-B/S* lid, the *CFU* envelope and the *TM-D-S* support beams, which in turn requires the compliance of said concept with system requirements and common manufacturing practices.

For starters, Requirement 1.2 mandates the assembly to reside within the structure frame of the *PocketQube* standard, shown in Figure 1.2 (Page 3), with a maximum total length of $20\ mm$ due to higher-level requirements provided by the PocketQube team. This immediately enforces data from Table 5.4 to be used for the tank envelope and consequently the lid, while data on the support beams can be directly extracted from the aforementioned figure. On the topic of geometric constraints, a correction to the internal tank length must be applied. The analytical model provided in Cases A and C takes for granted a purely cylindrical tank, defined by the walls. However, the inclusion of the lid introduces an alignment groove, with consequences on the internal tank length, L_{in}. Despite the lack of an exact method to determine them, an estimate of $0.5\ mm$ is made to account for future application of a sealant, should it be required. The strong impact of such a change is reflected in the free length L_0 and the spring pitch p.

Other, more technical constraints are found in the actual spring design, mostly pertaining to manufacturing guidelines. First, and regardless of the SF1 or SF-x arrangement, the spring wire diameter d is not of arbitrary size, thus not necessarily matching the optimized values found previously. Instead, the Spring Wire Gauge (SWG) catalog from [16] seems applicable for stainless steel wires, hence the A301-3/4H steel selected. Based on a broader research, wire gauge standards differ vastly among manufacturers and materials, so the choice is purely justified by affinity of materials and size decimation. Second, according to the spring design guide of [24], the active coil number N_a is often rounded to half-turns or quarter-turns to facilitate the production of accurate springs. In this instance, a quarter-turn approximation is closer to the results obtained so far and utilized to alleviate the effects of said change, primarily on the spring pitch p. However, the same cannot be said about the wire diameter, as the entire spring arrangement is highly dependent on a derived value, the spring index C. Unfortunately, the optimization script *CoilOpt* was not intended to run with set design variables, so recalculation of the design vector X is done manually: the spring wire diameter d is replaced by its next smaller value in the SWG catalog, and the packing constraint $c7$ is solved for the required spring index C under the premise of a 95% packing factor efficiency. A 98% efficiency can be attempted with marginal increase of the spring index, but keeping the same packing factor will better highlight the changes posed by the constraints. The index is validated with another C value that is derived from stress constraint $c4$. Naturally, the smallest of the two is selected, promoting safer designs. Further, the new

N_a is once again found by the closest approximation of the previously obtained result, then used to calculate the spring stiffness k, as well as the spring pitch p by means of the length constraint $c2$ and the overlap constraint $c3$.

Table 5.11: Effect of practical constraints on spring design

	Units	Concept	Practical	Difference (%)
d	mm	1.0722	1.067	-0.484
C	1	6.2592	6.1818	-1.236
N_a	1	7.8408	7.5	-4.346
p	mm	1.9607	1.93	-1.565
k	N/mm	5.0845	5.4908	+7.99
f	1	0.7388	0.7173	-2.99
m_p	gr	3.1404	2.9079	-7.4
m_s	gr	12.2156	11.5862	-5.15

Table 5.11 presents the changes done to the vector X and its effects on mechanism-related properties. Given the introduction of new constraints, an inevitable decrease in performance is observed, due to the cascading effect of the wire diameter d alteration, modifying the spring index such as to fit the configuration and resist the load, resulting in a new minimum spring pitch for solid length compression and ultimately a new coil count to fit the reduced length. Indeed, despite the 5.15% lighter mechanism assembly, the propellant capacity has been reduced by 7.4%, while the individual spring stiffness has increased by almost 8% with obvious negative impact on the dynamic response of this system. This unfortunate situation could not be improved by increasing the wire diameter d. The spring index needed for the configuration to still meet constraints $c4$ and $c7$ would either result in spring underloading, hence wasted internal displacement and prop. capacity, or coil intermingling due to exceeding the packing factor f_{lim}.

In light of this discussion, Table 5.12 summarizes the necessary dimensions and parameters for the detailed design. Values for segments that have been omitted during this analysis will be reintroduced in the next chapter, either with implicit calculations or through numerical validation. Potential confusions with the definition of 'length' are avoided by treating each part as shown in the various figures placed in alloted sections.

The principal conclusion that can be drawn from the tabulated values is the high mass footprint, meeting Requirement 1.1 by about 14.38%. The compromise made between space and mass requirements led to a small propellant fraction (10.61% of total mass) and an anticipated high spring mass percentage (42.3%) accredited to the high density of steel. Under the current set of values, the efficiency of a steel helical spring as a pressurizing device is arguable and impractical, yet the design itself is viable and compliant with all affine requirements. Conclusive evidence will be acquired in the next chapter with the implementation of software models, ultimately confirming or disproving the validity of mentioned analytic models and in turn the proposed design parameters. Much in the same fashion as Chapter 4, a visual illustration of the design proposal is presented in Figure 5.23, highlighting the properties of the system. The *ST-PF* grooves are visible in both the envelope and the interface plate

Table 5.12: Detailed design proposal (DDP) for the tank assembly

Parameter	Description	Units	Value (approx.)
	CFU Envelope Shell		
L	Tank length	mm	20
h	Wall thickness	mm	1
R	Int. Tank radius	mm	11.97
	TM-D-S Supports		
L_{AC}	Beam length	mm	21
w	Beam width	mm	6
h	Beam height	mm	2
	LT-B + LT-S Lid		
R_{lid}	Lid radius	mm	12.97
D_b	Bolt diameter	mm	2.5
L_b	Bolt length	mm	TBD
L_s	Lid support length	mm	TBD
L_g	Lid groove length	mm	0.5
	ST-PF Groove and SFX Springs		
N_s	Number of springs	1	7
W	Man. tolerance	mm	TBD
N_a	No. active coils	1	7.5
d	Wire diameter	mm	1.067
D	Mean diameter	mm	6.595
p	Pitch spacing	mm	1.93
L_{sg}	Groove length	mm	1
L_{sp}	Spring plate length	mm	0.5
	Mass Budgets		
m_p	Propellant mass	gr	2.908
m_{shell}	Shell mass	gr	6.693
m_s	Spring & plate mass	gr	11.59
m_{lid}	Lid mass	gr	0.7
m_{bolt}	Bolt mass	gr	1.5
m_{beam}	Support mass	gr	4.0
m_{Sys}	Expected tot. mass	gr	27.4

(shown in red), while minor modifications in terms of placement and sizing can be observed in the *TM-D-S* beams, to better accommodate the *LT-B* lid.

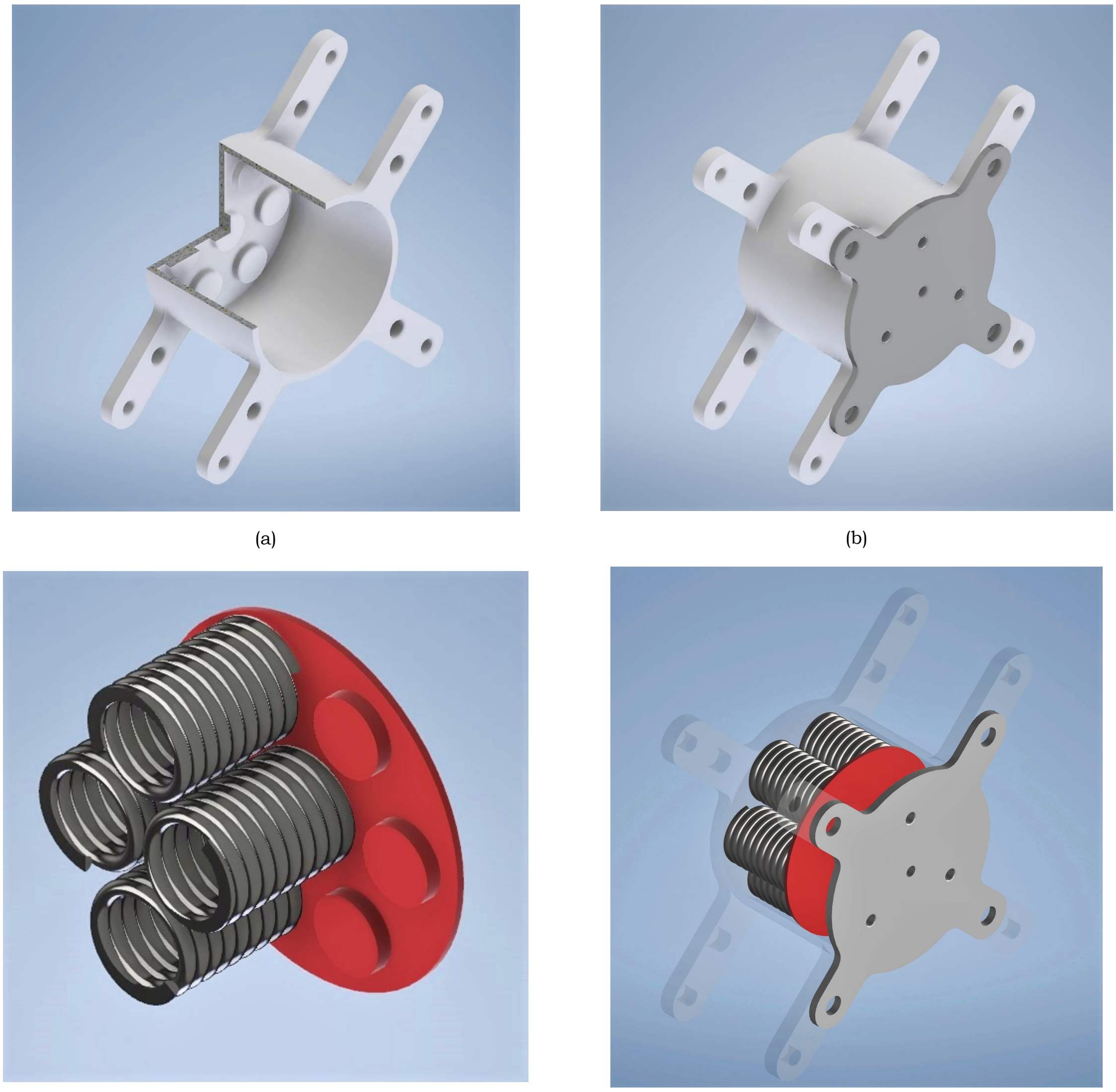

(a)

(b)

(c)

(d)

Figure 5.23: Impression of the DDP tank assembly.

5.10. Conclusion and Remarks on the Chapter

The propulsion storage assembly progressed from the conceptual design of Chapter 4 to a detailed set of dimensions and properties of Table 5.12. The transition is achieved by a combination of analytic models, system requirements and optimization studies for a number of static and dynamic load cases. Disassembling the system into three main components - namely the envelope sub-assembly, the spring sub-assembly and the fluid domain - has allowed for analytic models to stay relatively simple in terms of theoretical formulation and calculations, but segmented the problem of sizing into smaller sub-problems that share some properties. Care has been taken in the order of placement within the chapter, moving from the exterior towards the interior components and after all structural calculations, the dynamic response of the module.

The outcome is contradictory, or rather two-faceted: there is the positive outcome of excellent static response of all components, meaning that the individual components and the whole tank module can survive a sustained launch and operation in space, but there is also the negative output produced by the dynamic response analysis. Despite the derivation of a fluid-structure interface (FSI) problem that is tied to real-world accumulator models, and regardless of the achievements made in the spring optimization study, the output is unsatisfactory. Replacing the SF1 spring configuration with a SFX, seven-spring variant did improve the propellant capacity quite notably, but the overall impression is similar. Because of the contradiction, the analytic models themselves are put into question in the next chapter with computer-aided engineering software and more complex structural and fluid theory.

6

Finite Element Modeling

A validation study is executed to confirm or disprove the results obtained so far in terms of the static and dynamic response of the tank assembly to the load cases considered. The outcome of this study will provide conclusive evidence on the design' suitability as a propellant storage and expulsion device. The chapter revolves around the process of bringing the study into fruition, starting from the selection of appropriate tools, then reinstating the load cases for which the validation is needed, making the necessary assumptions for the models between chapter to be comparable and finally comparing the numerical output produced. Based on the outcome, the analytic models of Chapter 5 are confirmed or disproved, while the consequences of this verdict on the design success are discussed.

6.1. Software Selection

A basic requirement for conducting a finite element study is, aside from the envisioned object(s), the use of appropriate software that can handle a number of case scenarios, like the ones presented in Chapter 5. Numerous products are available in the market, with different classifications according to their field of application and more often than not, commercial products are also licensed for academic use, which is necessary from a legal standpoint for a student thesis. Among the different choices, the finite element study will be conducted with two software products, each serving its own purpose. First, the *AUTODESK INVENTOR* suite is used to materialize the proposed design found in Section 5.9, with an specific feature being particularly useful: the software comes with an in-built spring design module called *Design Accelerator*, allowing the author to verify the feasibility of the SFx springs through both analytic and empirical formulas. That said, the items are indeed generated manually for better control of the geometry intricacies, chief among which are the ground ends. The second piece of software, more oriented towards the actual simulation study, is the popular FE and FV modeler *ANSYS MULTIPHYSICS* suite, version 19.2. The workflow interface, the individual modeling and solving packages as well as the detailed user and theory manuals are much desired features for a student with little experience on the field. Cross-compatibility between the two programs is by default enabled and utilized for transferring geometries, further facilitating the workflow.

6.2. Simulation Strategy

Finite element analyses often pose to the designer a dilemma between rapid generation of low to medium accuracy results and high accuracy but time and resource-expensive models. Among the contributing factors, the geometry and mesh setup have a leading role in defining the model accuracy, load-stress behaviour, load-deflection behaviour and so on. Various techniques are available for the designer to control the mesh quality or element count, affecting the simulation time and results, but a complex geometry will under all circumstances require a complex (and high count) mesh, thus prolonging the analysis and consuming more computer resources. A practical countermeasure would be the simulation of sub-assemblies, entities forming part of the total assembly, yet able to stand on their own. On the condition that they are not structurally coupled by a certain load case, this is possible with the tank design offered in Chapter 4, as a consequence of the modular approach. For the intended purposes of this chapter, which is the validation of analytic models provided in Chapter 5, two sub-assemblies have been identified for the load cases discussed, shown in Figure 6.1.

- *Envelope sub-assembly*: includes the main tank body, the lid and the interface support beams. The *ST-PF* interface, the internal groove formation used to connect the spring to the outer tank parts, has been omitted from the design as it offers no advantage in terms of structural rigidity of the envelope and only serves the purpose of maintaining the alignment of the springs parallel to the propellant ejection axis. Further, the envelope design itself assumes a compartmentalized system, with the propellant-filled side being subject to pressure loads and the spring-filled side being practically unloaded, even if the generic model of Section 5.3 did affect the tank wall thickness in the same way. That said, the *ST-PF* interface is not important for the envelope's rigidity. The lid bolts are not needed as they have been over-engineered in Section 5.4 and can be replaced by equivalent boundary conditions. The sub-assembly is subject to load cases A and D, and due to its two-plane symmetry, a quarter-model is used to represent the geometry and exploit the symmetries to perform a computationally efficient analysis.

- *Spring sub-assembly*: includes the *SF-x* spring group, the piston plate and a substitute plate for the *ST-PF* interface to form a closed body. The latter is a virtual replacement of the interface that will be integrated onto the bottom tank wall in the final product, but insofar as the springs' capability is concerned, the plate enables isolation of the pressurization mechanism from the remaining container and allows the author to perform a finite element analysis with a much smaller, yet detailed mesh. This is a physically acceptable condition as long as the results of load case A do not show significant deformation of the wall due to pressure. Going by the theoretical analysis of Section 5.3, this stands to reason and therefore kept as-is for this section. Another benefit for the inclusion of this plate is the better measurement of the spring longitudinal deformation. If a spring end is left free, transverse deformations will occur and the overall expulsion performance is lowered. By careful placement of the interface and the springs, these deformations can be minimized, contributing to a better-performing design. The sub-assembly is only subject to load case C, which is focused on the static performance of springs.

- The *fluid-structure interface* (FSI) model presented in Section 5.7 requires the use of both the envelope and the spring sub-assemblies to define the active fluid domain, increasing the model complexity and thus the computer workload. In addition, the theoretical formulation developed cannot be replicated in the software without a vastly deeper

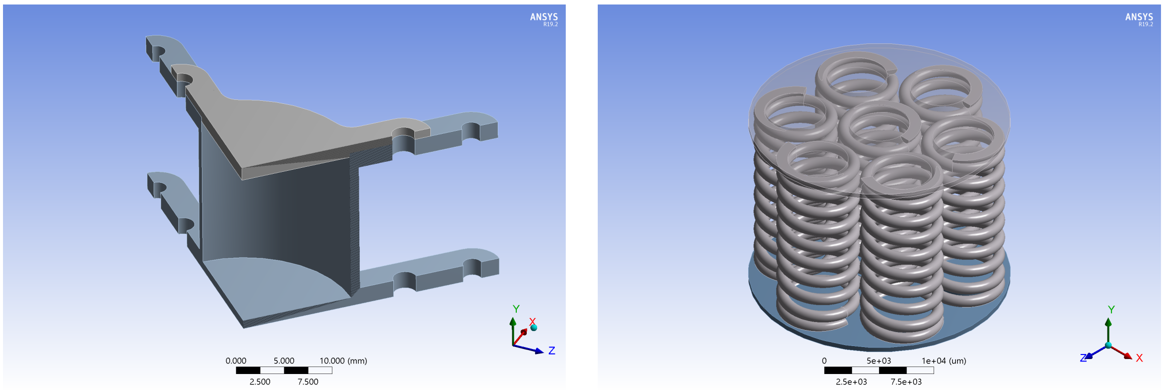

(a) The envelope sub-assembly model

(b) The spring sub-assembly model

Figure 6.1: Proposed sub-assemblies for the FEA simulations

knowledge of the latter, especially *user-defined functions* that couple the solid and fluid interfaces if deemed necessary. The issue is revisited in Section 6.6.

The mesh-dependent result convergence is verified by means of progressive refinement until simulation results show little to no variation, in the order of $2-5$ %. Different techniques are used to control specific meshing regions such as contact faces and small areas, but the marking difference between the two geometries does not allow for a universal methodology or even a comparison of the techniques, so the individual measures taken to refine the mesh will not be mentioned. Instead, emphasis is given to the primary metrics often used to characterize a mesh, compactly shown in Table 6.1 and in order of appearance: element type, mean and standard deviation of mesh quality ($\overline{Q}/Q_{sd}$) ranging from low to high and from 0 to 1, and number of elements and nodes (E/N). Without any previous knowledge on the mesh accuracy, three (3) levels of refinement are implemented as a starting point, then evaluated based on the results achieved. In particular, the meshing procedure should ideally reach converged points that match the theoretical predictions discussed in Chapter 5. On the other hand, constant-trend or diverging metrics would imply a disagreement between analytic and FE models that must be resolved.

Table 6.1: Mesh parameters for the sub-assemblies

Envelope sub-assembly (Type: Hexa/Prism)				
	Nominal	1^{st}	2^{nd}	3^{rd}
$\overline{Q}$	0.856	0.95	0.967	0.975
Q_{sd}	0.114	0.083	0.072	0.056
N_e	1574	9842	69686	129411
N_n	10242	53327	331575	597713

Spring sub-assembly (Type: Hexa/Tetra)				
	Nominal	1^{st}	2^{nd}	3^{rd}
$\overline{Q}$	0.853	0.853	0.882	0.87
Q_{sd}	0.102	0.102	0.093	0.101
N_e	82847	84997	167625	201167
N_n	270286	273266	622417	668817

6.3. Case A: Structural Response of Envelope Sub-assembly

6.3.1. Model Setup

The simplistic equations discussed in Section 5.3 for the determination of a minimum wall thickness across the entire object showed that even sub-millimeter values are sufficient for the low levels of pressure buildup found in the system, with a more conservative approach of $1\ mm$ being more useful at this stage of development. In terms of numerical output, the model had not accounted for deflection of less loaded components, so as a reference point the author can only rely on the maximum stress obtained by Equation 5.3.1b, or equivalently the safety margin of Requirement 6.4. This section attempts to confirm said outputs with a more complex and refined model, consisting of the following boundary and load conditions:

1. *Bonded contact region*: the envelope and lid are treated as a single enclosed unit, matching the original speculations of Chapter 5. The physical existence of bolts in this particular case is not crucial for the structural behaviour to be observed, while sizing the *LT-B/LT-S* groove appropriately should lock the components together as if they were indeed bonded.
2. *Two-plane symmetry*: the existence of a two-plane symmetry allows for great reduction in the mesh complexity, and therefore the model itself, but requires careful meshing methods due to the plane orientation between the two individual symmetries. This is covered for the model in discussion by means of a fully mapped meshing and a manually controlled mesh distribution across the various edges. A representation of the mesh is shown in Figure 6.2a, for the nominal reference point.
3. *Fixed support*: the equation-based model only focuses on the enclosure and does not consider the *TM-D-S* supports, perhaps affecting stress levels at these junctions. Inclusion of a proper fixed support condition in this model will produce higher quantity and higher quality outputs.

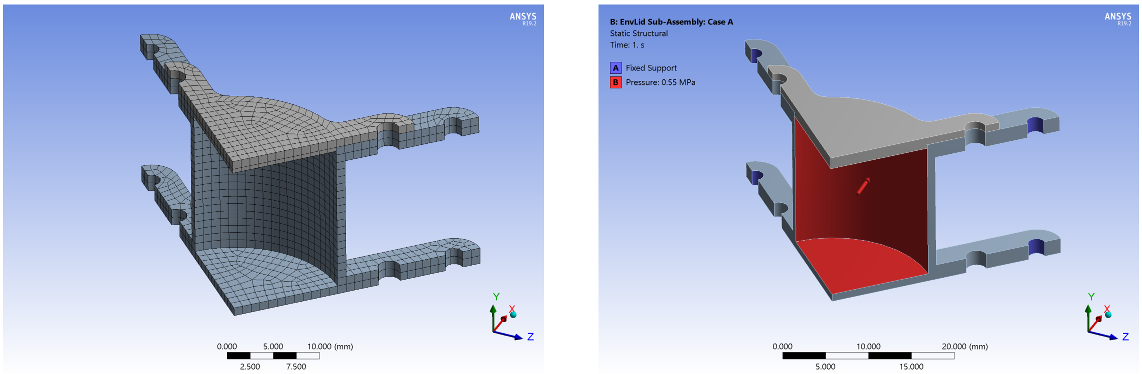

(a) Nominal mesh diagram

(b) Load/Boundary conditions

Figure 6.2: Model setup for the envelope sub-assembly

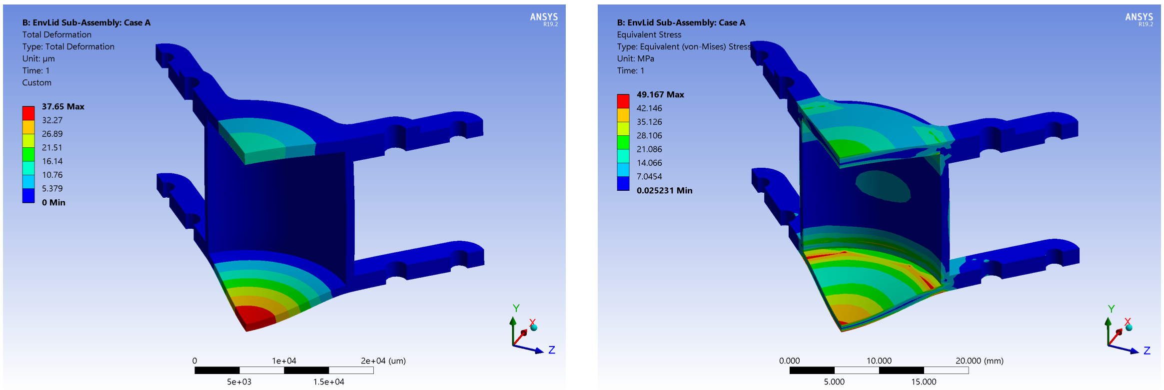

(a) Total deformation

(b) Von-Mises stresses

Figure 6.3: Simulation results for the envelope sub-assembly (nominal mesh).

4. *Omni-directional pressure load*: a pressure force is applied onto all internal faces of the enclosure, casting aside the absence of the SFx springs. It contrasts the reality of the problem, where the bottom does not participate in the fluid volume, but it serves the purpose of demonstrating the structural performance of the tank design. All of the above are shown in Figure 6.2b.

6.3.2. Results and Discussion

Figure 6.3 illustrates the simulation results by means of the element *total deformation* (δ) and *Von-Mises* stress values (σ). The first relates to how much an element is displaced in the three-dimensional space, taking into account all contributions, whereas the second does the same thing for stresses, also including shearing phenomena. Simple observation of the subfigures indicates a normal deflection behaviour, with the *TM-D-S* supports remaining affixed to their original position and the lid experiencing a small deflection that does not affect the tank's integrity. As a matter of fact, the actual lid design is intended to have a propellant port connected to the control valve, this latter being the recipient of any pressure buildup, so the lid is unaffected by the internal loads. Even at this exaggerated case of loading the tank's bottom wall, no signs of excessive deformation appear, while reading the respective subfigure legends and logged data of Table 6.2 safely leads to the conclusion that the system responds appropriately to the pressure load within vast safety margins.

Table 6.2: Case A comparison study

	Nominal	1^{st}	2^{nd}	3^{rd}	Sec. 5.3
δ_{max} (μm)	37.65	38.37	38.66	38.72	-
$\overline{\delta}$ (μm)	2.57	2.75	2.98	3.04	-
$\overline{\delta}_r$ (μm)	0.145	0.158	0.152	0.162	-
$\sigma_{_{VM,max}}$ (MPa)	49.17	54.25	63.51	70.68	-
$\overline{\sigma}_{_{VM}}$ (MPa)	8.28	7.47	7.05	7.02	6.583

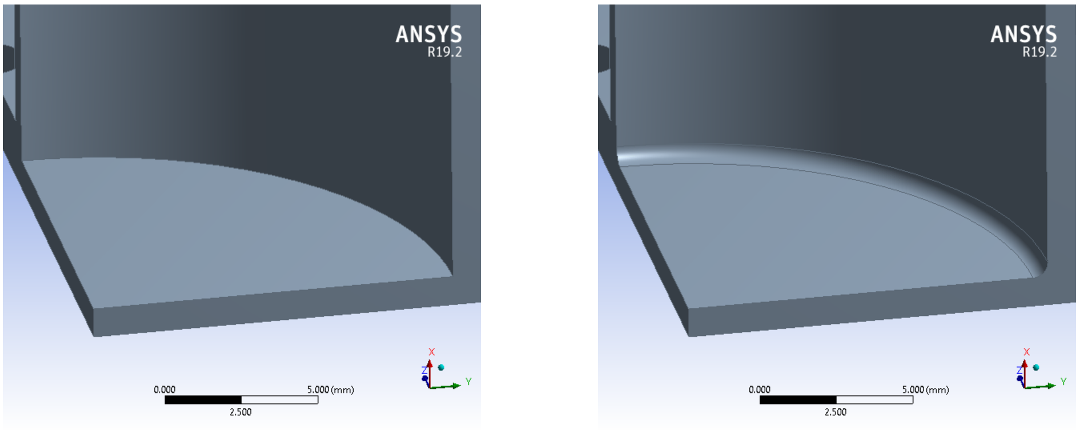

(a) Before fillet (b) After fillet

Figure 6.4: The singularity edge, before and after the fillet

Convergence study

According to the findings shown in Table 6.2, convergence has been only achieved with respect to deformation, whereas stresses show a non-uniform behaviour. More specifically, the average stress level $\overline{\sigma}_{_{VM}}$ follows a converging trend, but the peak stress value $\sigma_{_{VM,max}}$ has increased after three refinements. This is traced back to a phenomenon called singularity. Broadly speaking, when meshing an abrupt geometry change such as 90^o corners, the connecting edge experiences higher stresses, which are further increased by the no-displacement imposition. The problem is easily fixed by introducing a small fillet at that edge, shown in Figure 6.4. A convergence study is now possible for those max. stress, although a peculiarity of ANSYS Meshing requires a slightly different setup that relies on *Tetra* mesh rather than the previously employed *Hexa* and automatic mesh refinement. The results of Figure 6.5 clearly mark the convergence of these stresses and prove that the tank envelope never suffers enough damage to violate the 1.6 safety factor dictated by Requirement 4.2, confirming the suitability of the design proposal in terms of this component.

6.4. Case D: Structural Response of Accelerated Assembly

6.4.1. Model Setup

Already seen in Section 5.6, the longitudinal and lateral acceleration loads dictated by Requirements 4.4 and 4.5 are not expected to cause any significant deformation of the system,

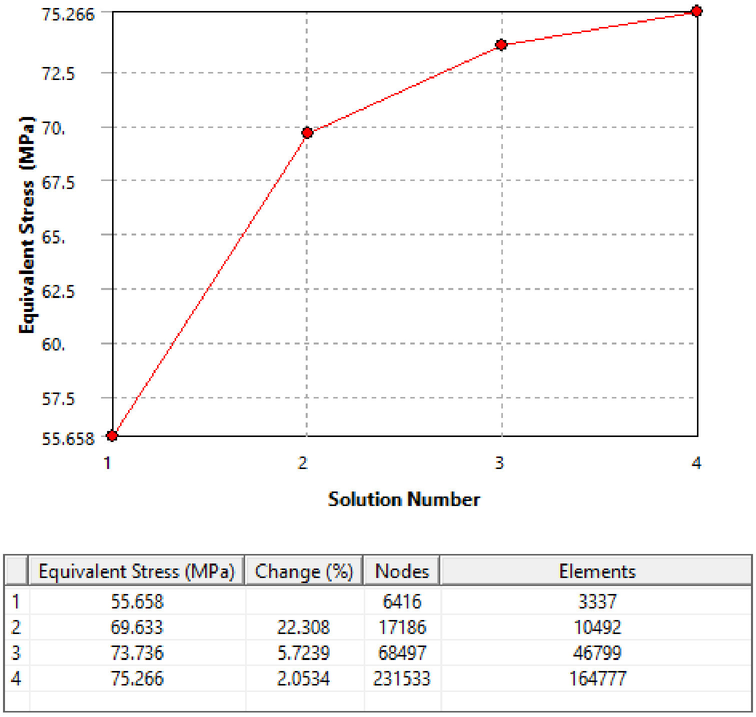

	Equivalent Stress (MPa)	Change (%)	Nodes	Elements
1	55.658		6416	3337
2	69.633	22.308	17186	10492
3	73.736	5.7239	68497	46799
4	75.266	2.0534	231533	164777

Figure 6.5: Convergence study results for the filleted edge of Case A

hence the implementation of a finite element model serves the purpose of confirming the efficiency of the analytic model from an accuracy standpoint. The model follows from the previous section, with the subject geometry expanding upon the theoretical part used for the calculations, but different boundary conditions that cater to this specific load case. While the fixed support condition is still valid, the intricacy associated with a ”rigid lid” did initially cause an issue. Based on the *ANSYS Mechanical* software, it is possible to treat a body as fully rigid, at the cost of the ability to mesh said body, with all consequences that stem from such a move regarding its stresses and movement. Straying from this assumption made in the previous chapter, the lid is treated as a flexible medium and its boundary conditions are modified to comply with the expected outcome, or in other words, for it to behave like a rigid lid and not bend or move other than parallel to the acceleration vector. That said, a *displacement* condition is imposed according to the aforementioned. Application of the acceleration load also required some investigation. According to Requirement 4.4, the tank must withstand accelerations of $5g_0$, but in reality the beam supports experience much higher levels attributed to the spacecraft's inertial weight, which is $5g_0 \cdot 0.45[kg] \simeq 22.065\ N$. WIth a full tank weight of $27.4\ gr$, the equivalent acceleration is $805\ m/s^2$. Staying in line with the analytic model, a force vector of $F = 22.065\ N$ is applied to the system. The boundary and load conditions are depicted in Figure 6.6, color-coded and labeled.

6.4.2. Results and Discussion

Simulation results for a nominal mesh resolution are illustrated in Figure 6.7, expressed in terms of *total deformation* and *normal stress* with respect to the X axis. The first is used to prove the argument of a minor load case, whereas the second comes as an alternative to the more common *bending stress*, which however is incompatible with the element types

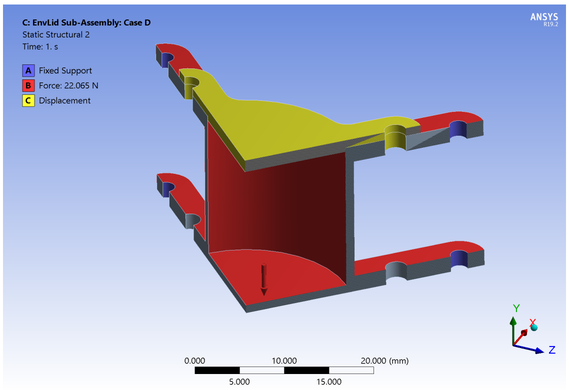

Figure 6.6: Model setup for the accelerated sub-assembly

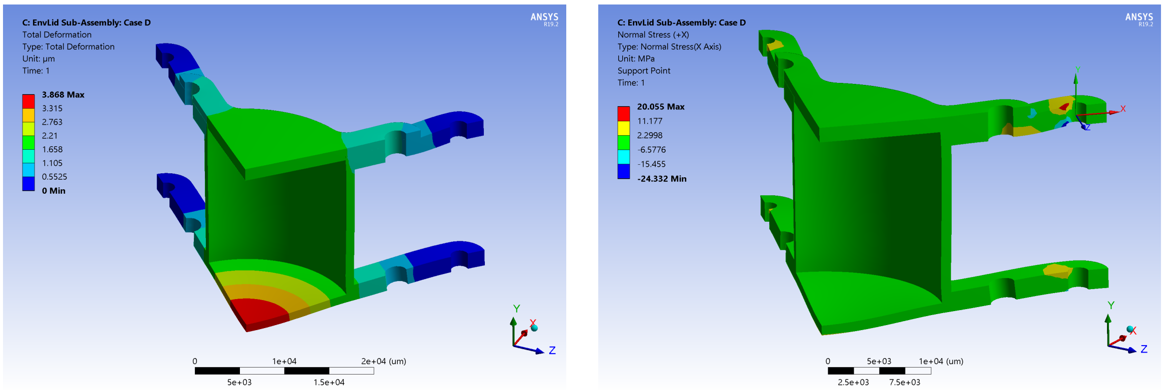

(a) Total deformation

(b) Normal stress on the X axis

Figure 6.7: Simulation results for the accelerated sub-assembly (nominal mesh)

employed in this model. For the bending stress to be used, the model would have to be redefined as a construct of beams and shells, which in turn would require sufficiently thin parts. Given the design parameters of Section 5.9, the support beams cannot be seen as thin structures and the simpler element model was preferred. Accuracy issues from this change are prevented by creating a local coordinate system that is aligned with the beam's neutral axis and whose origin is placed on the center of the fixed support hole, matching the coordinate system of the analytic model. Normal stresses are then calculated using this new coordinate system and simultaneously following the notation of Section 5.6 for distinguishing the two stress loci of importance.

Table 6.3 highlights the disagreement between FE and theory, while the refinement process shown in the respective columns shifts the attention towards the analytic model of Section 5.6. The deformation data clearly follow a converging pattern for the whole range $u = 0 \rightarrow u = 1$, but do not match the calculations of Section 5.6. The conclusions drawn on the analytic model were based on some theoretical values, but once the actual values of Section 5.9 are plugged in the formulas of Table 5.7, the resulting deflection for the $u = 1$ - bolt point is much higher and the model reverts to a fixed-free cantilever beam, which of course does not represent the current situation. Perhaps a more engineering-based approach with free body diagrams (FBD) and multi-body force/moment analysis might prove more accurate, at the expense of higher complexity.

The shortcomings of the analytic model also appear in the stress department, with striking value difference between theory and ”practice”. A converging pattern is not as apparent and the max./min. stress values are well in excess of the analytic reference for both locations, meaning that either the simulation model is wrong or that the analytic model is badly constructed. If the premise of the deflection convergence pattern is sound, then the stresses must also follow the pattern, therefore directing the attention towards any omissions or mistakes in the theoretical model. As a matter of fact, one of the key issues with the equation-based model is the condensation of a three-dimensional problem into a point-to-point polynomial equation, leading to severe loss of information. For instance, the single-point hole approximation is proven to have caused the loss of information regarding an important stress concentration factor mentioned in [44],[24] and [119], used explicitly for hole features in out-of-plane beam bending conditions, such as the current situation. The approximate equations are incompatible with the ratio d_{bolt}/b_{beam} (with d_{bolt} the bolt hole diameter and b_{beam} the beam width) and cannot be used to obtain a concentration factor, so for the sake of calculations a sample value of 2 is taken, which plugged into Equation 5.6.3 should rectify the issue. However, agreement is still not reached and the second issue emerges, at the second important location ($u = 1$). The theoretical model fails to capture any of the intricacies related to the existence of the lid, such as the geometry change, the load concentration at the bolt hole and the deflection of the lid itself, due to the ”rigid lid” assumption. The same solution to the deformation problem is proposed, that is applying a free body diagram of the lid, the beam and the part of the tank envelope in contact with the two items, then applying the acceleration load to each and deriving the coupling factors for which the beam would acquire the correct deflection profile, which is expected to be in stark contrast with the overhang load profiles developed in Section 5.6.

On the face of the deformation and stress magnitudes, the system can be said to respond well to the predefined acceleration load with reasonable safety margins, and need not be revisited as such for the next design phases. However, the result validation through simulation models has proven its significance with regards to testing hypothesis, theory accuracy and overall thought process of a physical phenomenon. Should a next design cycle be required, a multibody analysis seems to be the fundamental approach to follow, with or without the polynomial simplifications proposed.

Table 6.3: Case D comparison study

	Nominal	1^{st}	2^{nd}	3^{rd}	Section 5.6
$\bar{\delta}_{body}$ (μm)	1.529	1.539	1.546	1.558	-
$\delta_{body,max}$ (μm)	3.87	3.952	3.978	3.98	-
$\delta\mid_{u=1}$ (μm)	1.045	1.075	1.084	1.088	5.47

$\sigma_{max}\mid_{u=0}$ (MPa)	20.07	26.09	32.33	34.67	15.375
$\sigma_{min}\mid_{u=0}$ (MPa)	-24.34	-30.51	-37.44	-40.16	-15.375
$\sigma_{max}\mid_{u=1}$ (MPa)	10.44	11.55	14.15	16.01	3.85
$\sigma_{min}\mid_{u=1}$ (MPa)	-12.3	-21.2	-31.25	-36.04	-3.85

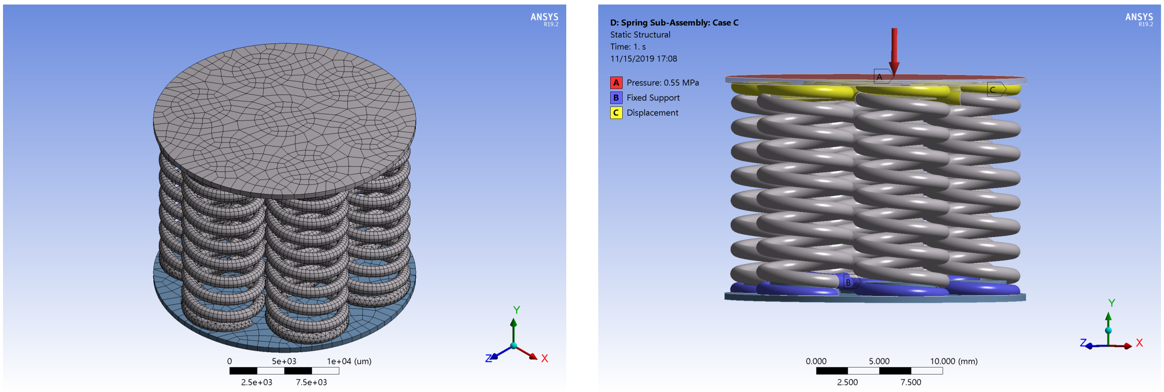

(a) Nominal mesh diagram

(b) Load/Boundary conditions

Figure 6.8: Model setup for the spring sub-assembly

6.5. Case C: Structural Response of SFx Spring Sub-Assembly

The theoretical study of Sections 5.5 and 5.7 demonstrated the capabilities of a multiple-spring configuration with regards to withstanding a pressure load designated by requirements on Chapter 3. However, the assumption of non-transverse deformation and the sole use of parameters raise questions on the actual performance produced by the configuration. A finite element approach that encompasses a practical design and arrangement of the springs should, under the same pressure load, either confirm the analytic model, or highlight any performance losses caused by various assumptions made along the way.

6.5.1. Model Setup

A model setup is shown in Figure 6.8b. The 6 outer springs are positioned in a circular pattern, forming three pairs of opposite-oriented spring ends, all towards minimizing geometrical asymmetries that may inflict upon the compression output. The seventh, central spring, which obviously does not have a counterpart, will create some inconsequential asymmetry in the design. Paramount to the correct setup of the model are the inactive coils, formulated by a *fixed support* condition for the bottom plate and a constrained *axial displacement* for the top side, aided by a *bonded contact region* with each respective plate to complete the boundary condition set. The load on the other hand is simply applied by means of a pressure load normal to the piston plate.

6.5.2. Results and Discussion

Representative simulation results are depicted in Figure 6.9, mainly focusing on three tangible criteria, namely the *total deformation* δ_{tot}, the *transverse deformation along the X and Z axes* and the *max. shear stress* τ, while logged values are found in Table 6.4. The selection of aforementioned metrics stems from both the theoretical background of Section 5.5 and Requirement 4.4 regarding safety factors. Even at a first glance, the simulation reveals some conflicts with the analytic model, with a non-zero transverse deflection of the springs being the predominant discrepancy. This is a realistic behaviour accredited to the manufacturing method of the spring ends. For a squared-and-ground spring, the wire helix is drawn in N_a+2 coil turns and ground at half the wire diameter to create flat surfaces. The asymmetric distribution of material is responsible for converting the axial load received by the piston plate into off-axis moments, in turn causing the transverse displacement of active coils. However, the legend of Figure 6.9b reveals a symmetric range of values which can be extrapolated to all pairs of opposite springs, implying that correct placement of these springs in the assembly should for the most part control the individual deflections and allow the system to move only parallel to the load axis. This is also true to some extent for the Z-axis deformation, although the placement of the springs does increase deflection, once again because of the spring end formation. Contrarily, the central spring does not have a counterpart and leads to a non-zero net deformation along either of the transverse axes, as shown in Table 6.4. In summary, the values are small and hence the system is treated as if it deflects axially. Another point of discussion is the remarkable proximity in total deformation values between the prediction and the simulation. The off-axis deflections may be responsible for subtracting some of the elastic energy used to compress the spring, but their contribution is small and should not be associated to the performance loss. Even accounting for this phenomenon, the total deformation is within $1\ \%$ of error compared to the theoretical value, and more astounding is the fact that deformation levels are nearly constant in all refinement stages, proving a mesh-independent behaviour. Minor variations in the transverse axes' values may stem from the averaging techniques used from the solver and the element-based deformation values, but again, they are too small to be considered as a flaw of the model.

Table 6.4: Case C comparison study

	Nominal	1^{st}	2^{nd}	3^{rd}	Sec. 5.5
δ_{tot} (mm)	6.416	6.416	6.41	6.41	6.441
$\bar{\delta}_y$ (mm)	3.3	3.3	3.2	3.2	-
$\bar{\delta}_x$ (μm)	0.3	0.3	-0.14	-0.14	0
$\bar{\delta}_z$ (μm)	10.1	10.0	12.2	11.4	0
τ_{max} (MPa)	952.45	951.84	906.27	897.78	602.5
$\bar{\tau}$ (MPa)	236.71	234.12	268.36	249.87	-
$FoSy_{min}$	0.63	0.633	0.665	0.671	1
$FoSy_{avg}$	6.53	6.63	4.75	5.46	1

Noteworthy is the inconsistency between software and theory as far as shear stress is concerned in both absolute magnitude and location of their appearance. Figure 6.9d reveals that high-stress locations are not found at the coil external side, as expected from Section 5.5, but rather at the coil's internal side and at a particular point between the topmost and second topmost coil turn. While the latter can be purely seen as an artifact caused by the virtual contact between the two turns, the internal side of the coils should not be stressed that much and raises questions on the model's validity. The plausibility of a stress concentration factor is low, as its existence would go against the principles of a *distributed* compliant mechanism which have been discussed in Chapter 2. Even if it did exist from a numerical standpoint, the spring design methodology employed (see [24]) is quite vehement on not using a stress-concentration factor, but rather relying on stress-correction factors. With no further information other than the stress diagram available, two scenarios appear to contribute in the excessive stress: first, the geometrical asymmetry caused by the non-integer coil number N_a which slightly overextends the internal coil surface, and second, the

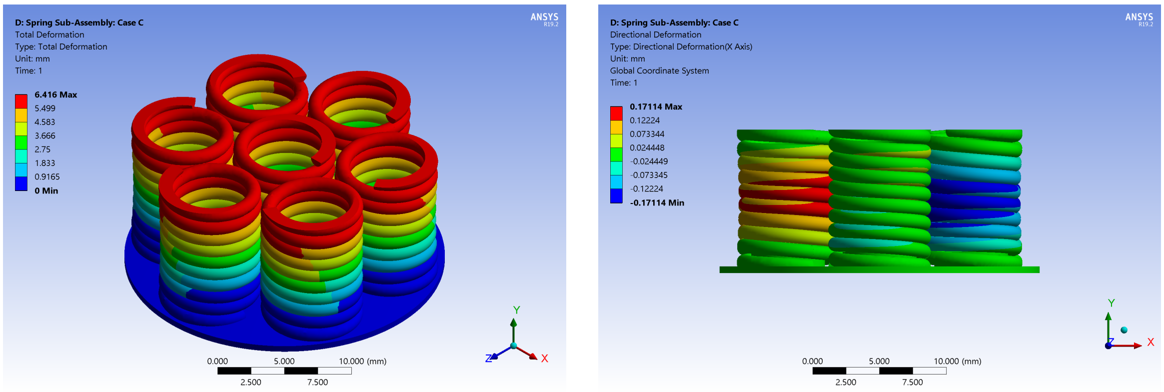

(a) Total deformation

(b) Transverse deformation (+X)

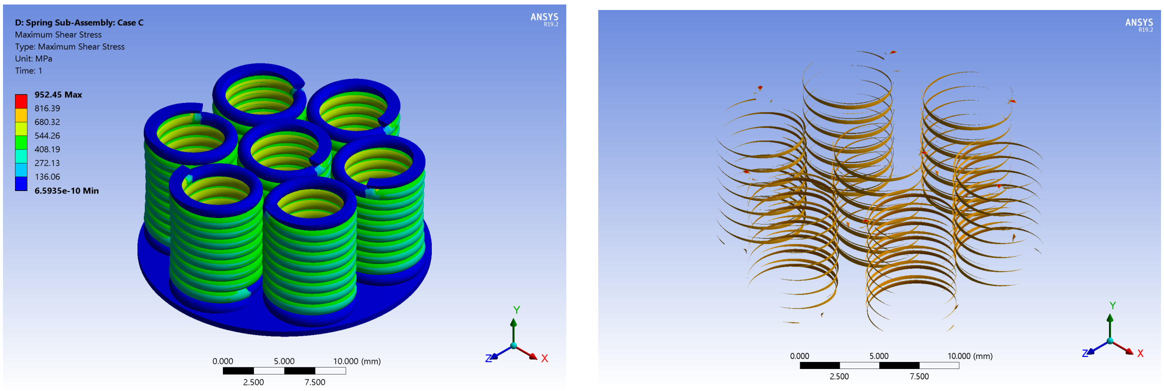

(c) Max. Shear Stress

(d) High-stress elements

Figure 6.9: Simulation results for the spring sub-assembly (nominal mesh)

imposition of solid length compression which creates an off-axis torque to the coil side where no flat ends exist, hence the transverse deflection. Both can be verified by overlapping Figure 6.9d to Figure 6.9a, noticing that the higher stresses do indeed match the locations of high transverse deflection of the springs.

Casting aside this peculiarity, the system responds appropriately with reasonable safety factors. Speaking of safety factors, the original lower limit of 1.2 has been replaced with unity in the tabulated data, considering as a new reference point the limit shear stress provided in Section 5.6 that already incorporates Requirement 4.4 and all the necessary conversions.

6.6. Case E: Dynamic Response of Tank Assembly

The time-dependent response of the tank system during an arbitrary thrust cycle has been largely determined by a very simple equation set, loaned by a spring-loaded accumulator model, with unsatisfactory results as far as absolute values are concerned. Being aware of the limited accuracy of such a reduced complexity model, a validation study by means of FEM is imperative, not without any challenges to overcome, chief among which is the design strategy selected for a computationally efficient, yet numerically accurate FSI model. The options are finite, as follows:

- *Multi-body study*: the spring sub-assembly, the fluid domain and the valve plunger are designed and simulated via full two-way FSI coupling, which naturally is heavy on computer resources, but it should give the optimal image of both fluid movement and spring deflection.

- *Single-body study*: focusing on the fluid domain, interacting bodies are approximated by mathematical equivalents, being forces or displacements. Accuracy in this case is lower, traded for faster and efficient simulations.

Following the motif presented so far, going for a single-body simulation is preferred, but must be accompanied by a number of conditions in order to retain physical accuracy. First, the problem is focused to fluid movement to such an extent that the individual springs deformation seen in Case C is largely covered by the plate displacement, ignoring the stress levels. Second, the assumptions mentioned in Section 5.7 about the basic physics must be carried over in the setup, including the free slip boundary conditions where applicable, the laminar flow etc. Third, any method used to compensate the lack of non-fluid bodies must result in an equivalent system.

This latter is achievable by using the *ANSYS CFX* environment. Comprised of a model setup interface, a finite volume solver and a post-processing result viewer, the CFX environment offers all tools required to perform the aforementioned single-body study, the most powerful of which is the *CFX Expression Language*(CEL). Not a language in the literal sense, the CEL makes any physics-related field accessible to the user such that the program's capabilities can be expanded with custom expressions, variables, field profiles and so on. For instance, one can request a specific velocity profile along a boundary at a specific time and under a boolean trigger, should they choose to. The software also comes with a built-in Rigid Body solver, feature that is well aligned with the design strategy proposed, due to its capability of solving linear springs mathematically.

Geometry and Mesh

Figure 6.10 illustrates the fluid domain used as the active geometry for the study. The domain extracted from the tank assembly is cylindrical, however a more efficient form can be obtained by exploiting the rotational symmetry inherent to all revolute primitives and reduce the overall domain footprint. Naturally, this is only possible under the premise of a non-perpendicular flow, so no fluid moves across the boundaries defined by the slice. For the premise to be true, a number of requirements must be satisfied:

1. The spring must move slow enough or push fluid slow enough so as to not cause vortices and hence tangential or circumferential flow.
2. The spring must move along one axis, such that torsional and bending moments due to structural asymmetry cannot exist, eliminating the risk for fluid to move in other directions. This is a similar requirement to 6.3, but more focused on the fluid aspect.

Both requirements can be satisfied by the results of Chapter 5. More specifically, in Section 5.5 the unidirectionality of the SFx assembly is proven, with any sideways deflection being always counteracted with a symmetrical spring. Simultaneously, Section 5.7 proves that, rounded to the nearest order of magnitude, the maximum Reynolds number is clearly in the region of laminar flows, as shown below:

$$Re_{max} = \frac{4\dot{m}_{max}}{\mu\pi^2 \cdot R_v} \simeq \frac{\cdot 10^{-3}}{10^{-3} \cdot 1 \cdot 10^{-3}} = 1000 \tag{6.6.1}$$

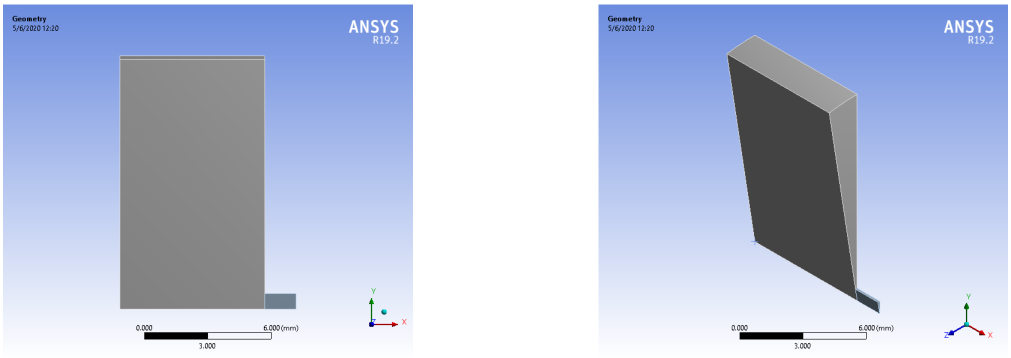

(a) Side View

(b) Isometric view

Figure 6.10: The fluid domain geometry, sliced at an 9^o angle (2.5% of circle)

Based on purely mathematical terms, the non-perpendicular flow premise is valid and the rotational symmetry can be safely applied to slice the domain. Selection of the slicing angle is instead related to the CFX software. Based on the user's guide [19], angles in the range of $2-5^o$ are assumed to create 2D geometries, which meshing-wise would be challenging, with thin regions producing low-quality mesh. On the other hand, too large of an angle would cause either low mesh resolution or low simulation speed. Neither of the two outcomes are desired as the analysis is already intensive being transient. In addition, angles that don't scale well with 360^o would add inaccuracies when estimating cross-section areas. One of the possible options is a slice angle of 9^o, or in terms of circle fraction, 2.5%. The reader can discern the fluid volume enclosed in the tank assembly, as well as the respective volume filling the lid port. While the latter is not accounted for propellant capacity, it has a dramatic effect in terms of flow characterization and is equally important for the analysis.

Meshing this geometry does not stray much from what has been mentioned about the other sub-assemblies, primarily in the aspect of using techniques that apply to this sliced geometry to improve upon the mesh quality even under the nominal resolution. One minor difference is the use of two refinement levels instead of three, as the computational savings achieved by the axisymmetric exploit have diminished returns from the 3^{rd} refinement onward, according to the data of Table 6.5. The corresponding mesh distribution at the nominal resolution is found in Figure 6.11a. The reader can discern the higher mesh density in the piston region and the lid port region, where significant flow deformation is expected.

Table 6.5: Mesh parameters for the fluid domain

Fluid domain (Type: Tetra)				
	Nominal	1^{st}	2^{nd}	3^{rd}
$\overline{Q}$	0.812	0.827	0.831	0.837
Q_{sd}	0.124	0.108	0.104	0.098
N_e	23079	65260	144283	672084
N_n	5308	13642	29452	128283

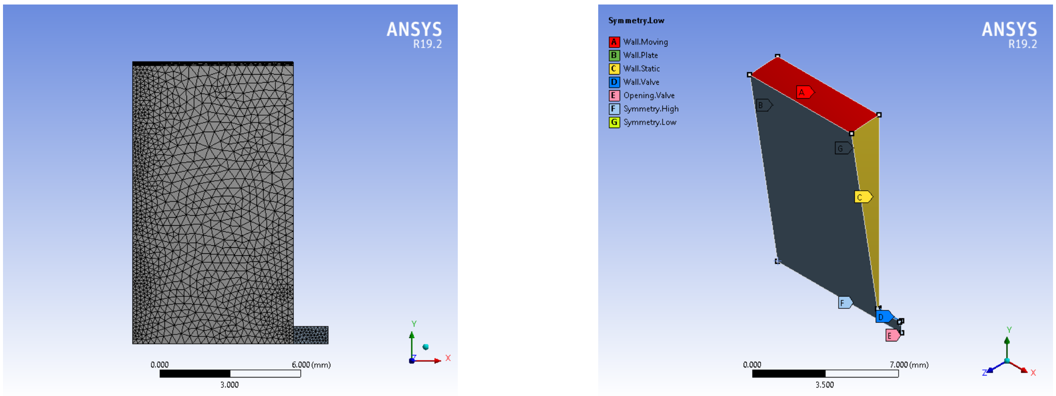

(a) Mesh diagram for the fluid domain

(b) Boundary conditions for the fluid domain

Figure 6.11: The fluid domain mesh, at nominal resolution

6.6.1. Model Setup: Theory

The analytic model discussed in Section 5.7 relies on the premise of a single uniform domain and calculates flow properties at the control volume exit, which is the valve opening, on a macroscopic scale. Despite being sufficient to get a first estimate of the occurring events, the model is quite simplistic in its formulation and unable to describe the fluid domain in its entirety. On the other hand, FEM solvers go much deeper into analyzing flow fields by locally solving the general *Continuity* and *Navier-Stokes* momentum equations, seen in Chapter 1 and reminded in Equation 1.1.6 and obtaining point-to-point pressure and velocity variations. Noteworthy is to mention that, while the analytic model uses the fluid's bulk modulus β to calculate the pressure change rate $\dot{P}$, the CFX solver treats liquids as incompressible fluids, unless otherwise specified. This is not excepted to influence the flow during the opening and closing sequences, since β is comparable to moduli of solids and essentially incompressible.

$$\begin{aligned}
\textit{Continuity Equation}: &\ \frac{\partial \rho}{\partial t} + \nabla \cdot (\rho \mathbf{u}) = 0 \\
\textit{Momentum Balance}: &\ \frac{\partial}{\partial t}(\rho \mathbf{u}) + \nabla \cdot (\rho \mathbf{u}\mathbf{u}) = -\nabla p + \nabla \cdot \overline{\tau} + \rho g
\end{aligned}$$

Much simpler is the treatment of the spring assembly, using a linear momentum solver that implements Newton's 2^{nd} Law of Motion. The position, velocity and acceleration vectors of the rigid body are derived from the *Newmark* integration scheme, a model widely used in structural dynamics [19] and based on the CFX setup has second-order accuracy. Two disadvantages observed with the stock solver are the high sensitivity to timestep selection, relying on second-order differentials, and the omission of a damping that may accelerate convergence. The latter may be of lesser importance for slow moving objects and can be solved manually by introducing an external force, but the sensitivity to time is troubling. Dealing with a fluid-structure interface problem requires small timesteps to capture flow changes, yet large enough to properly account for the acceleration of the rigid body.

6.6.2. Model Setup: Solver

The focus of a time-dependent analysis heavily tends towards accuracy, since fluid flow phenomena can occur during sudden events and must be captured with an appropriate timescale. On the other hand, computer resource management is difficult in excessively small timesteps, considering the numerical advancement of flow properties with either first-order integration or second-order interpolation methods. Among the timescale selection options offered by CFX, the *Adaptive* methodology seemed promising, being able to vary the timescale until sufficient accuracy is reached by the solver for each timestep, but unfortunately did not function at all. Besides mesh refinement and coarsening, the solution of switching the model to a fully closed domain by replacing the valve opening with a wall, was attempted. Ideally this would have caused fluid to stall, the spring to decelerate and then accelerate in a reverse flow situation, all with strong timescale reduction. None of the solutions worked, because of how time adaptation works in CFX. For the solver to perform time adaptation, two conditions must be violated: either the number of iterations within a timestep fails to stay within predefined target values, or the *Courant number*, a fundamental stabilization factor in second-order numerical integration schemes, fails to stay below a target value. Upon inspection, the solutions proposed never manage to violate convergence, so time never scaled up or down.

The benefit of having custom expressions is becoming clear. Since every type of user accessible field can be tailor-made, an adaptive timescale was written manually exploiting the a priori knowledge of the time and duration of all the flow events that occur during the thrust cycle. The timestep has the form of a conditional and is expressed as follows, in notation compatible with the CFX software:

$$\text{if } t \leq tClose - 4 \cdot tValve,\ 0.005\ [ms],\ 0.01\ [ms]$$

In the above, $tClose$ stands for the valve closing event instant and $tValve$ is the already known valve reaction time, t_v, while the values have been selected based on convergence stability. The multiplication factor of 4 is selected based on Equation 5.7.3. The hyperbolic tangent used to approximate the closure of the valve gate offers a good proximity to a step function, but being an exponential it requires at the very least 3.6 periods (which are determined by the reaction time $tValve$) to reach unity. In physical terms, the expression allows enough delay for the solver to have reached a steady closed state before rescaling the timesteps.

The argument of having a timescale reduction at the opening sequence as well is sound and has been explored, but starting from a resting position, the interpolation methods used to propagate the system in a smaller timescale caused quite a few numerical oscillations around the point of opening without accuracy gains and was thus discarded. The closing event is on the contrary one of the critical events as it may or may not cause a water hammer event, already predicted at 5.7.

The solver is also tuned manually with respect to the FSI coupling degree. In a default scenario, the fluid and rigid body solvers in CFX work in a staggered fashion, in a 1:1 ratio, meaning that data is exchanged once per solver per timestep before the next iteration starts. However, the strong coupling present in the piston interface, as well as the sole fact of having a pressure load dictate the spring dynamics requires more effort in reaching a converged state for each iteration. In CFX, this is achieved by accessing the rigid body solver and enabling the option *Rigid Body Control* → *Update Frequency* → *General Coupling Control*. Setting an interval between 3 and 8 iterations translates into solving the spring model 3 to 8 times before transferring the displacement data to the fluid solver. Speaking of the latter, it is also tuned to perform a convergence loop from 2 to 5 iterations before advancing to the next timestep. Both measures ensure a better stability during steep flow changes, particularly at the start of the simulation, where initial conditions have not propagated to the entire flow field.

Another intervention is done to the solver in order to generate a validation study under equal terms between analytic and FEM models. Recalling upon the schematic of Figure 5.13, the simulation is assumed to stop on either the prescribed runtime or if the exiting mass flow reduces to 0 (or a close proximity). This same interrupt condition is applied to the solver as a means to measure the limit duration of a single thrust cycle over a given pressure drop, with a minor trick: since the first timesteps are often accompanied by numerical oscillations as the solver tries to pinpoint the exact initial conditions, the possibility of overshooting fluid velocity and hence mass flow values into the positive region exists, causing a premature termination of the analysis. Preventing that is as simple as allowing the solver to stop only after the valve has been opened. This logical AND condition is summarized below:

$$\text{if } t > tOpen \;\&\&\; massFlow()@Opening > 0 \; [kgs^{-1}]$$

Once again following CFX-compatible notation, $tOpen$ is the instant when the valve opens, $massFlow()@Opening$ is the calculated mass flow across the *Opening* boundary.

6.6.3. Model Setup: Spring

As part of the FSI design strategy, a linear spring formation must be approximated with the current geometry that is comprised of fluid boundaries. This is possible in CFX by first associating one of the boundaries, in this case the fluid-solid interface found at the piston side, with a rigid body entity and then construct the spring formation via its physical properties and acting forces. Due to the geometry used and some software peculiarities, a number of tricks were applied to obtain the proper equivalent for the spring sub-assembly:

1. A spring stiffness scaling factor is used to account for the reduced geometry area, determined by the angle ratio between the slicing angle and the full circle angle, that is 2π. Judging by the results of Section 6.5, the pressure and spring forces are distributed equally to the plate geometry and the assembly moves along one axis. Thus, a virtual spring with a scaled stiffness can be safely used to approximate the sub-assembly, with rotational symmetry handling the extrapolation to the full cylindrical domain values. Contrarily, the mass property must represent the entire assembly, once again due to the rotational symmetry, otherwise the solver would treat the model as if it only contained one spring instead of the seven physical springs.

2. A damping force is manually added to the system as an external force to correct the undamped linear spring model used by the CFX rigid body solver. This is done through a CEL custom expression called $ForceDamping$ and an internal function called *rbstate* which calls the position, velocity and acceleration components of the rigid body. Despite the low contribution expected for slow moving objects, it is an easy modification that should be adopted in the future. The formulation is shown below in CFX notation, where $SpringC$ is the internal damping constant c used in the previous chapter.

$$ForceDamping: \; -SpringC \cdot \; rbstate(Linear\ Velocity\ X)@\text{Name of Rigid Body}$$

6.6.4. Model Setup: Fluid

Shifting the attention towards the fluid model, an abundance of settings and property fields are accessible to the user for manual tuning, the explanation of which would expand to many pages. A summary of the choices made are cataloged in Tables 6.6 and 6.7 with supporting arguments following it, while the reader is strongly encouraged to consult the CFX User's Guide [19] for a detailed explanation. Settings not mentioned should be assumed to have the default value.

Table 6.6: Fluid domain settings

Domain Settings		
Name	Option	Argument
Ref. Pressure	$0\ [Pa]$	Not included in pressure force calculations
Mesh Deformation	Regions of Motion	Required for moving and deforming bodies
Heat Transfer	None	Unrelated to current analysis
Turbulence	None	Equation 6.6.1

Special emphasis must be given to the *Opening* boundary condition, for it implements a series of mathematical workarounds to the universal limitation of fluid solvers, the inability to switch boundary conditions while simulating. This opening is assumed to replace the valve gate, which by definition opens and closes, to simulate flow starting and halting during a thrust cycle. A partially open gate for instance translates to the solver as a condition between a wall and an opening, an impossible situation. In order to achieve this condition as closely as possible, a prescribed, time-dependent pressure level equation is proposed, shown in Equation 6.6.2:

$$P(t)|_{opening} = P_0|_{tank} - \Delta P \cdot GateOpen(t) + P_{jump}(t) \tag{6.6.2}$$

This complex expression is segmented based on the events occurring the simulation. The opening pressure P is equal to the initial tank pressure P_0 while the system is disconnected from the thruster. At the beginning of the thrust cycle, a pressure drop ΔP is gradually applied, following the valve openness state $GateOpen$ seen in Equation 5.7.3, and this holds for the entire thrust duration. In the event of a timed or sudden valve closure, the tank assembly experiences a pressure jump strongly dependent on the fluid momentum at that point in time and the valve openness state. Once again, the jump is not applied instantly, but instead follows the transition between opening and wall and is expressed as follows:

$$P_{jump}(t) = \frac{1}{2}\rho \left(\frac{massFlow()@Opening}{\rho \cdot area()@Opening \cdot GateClosed(t)} \right)^2$$

$$GateClosed(t) = \frac{(1 + 0.1\%) - tanh(\frac{t - tClose}{tValve})}{2 + 0.1\%}$$

Critical to the successful implementation of the jump is the denominator $GateClosed(t)$. Despite being similar to the approximation of 5.7.3, it is limited to closing the valve gate to a finite percentage of its fully open cross-section $area()@Opening$, as division by zero is deemed a fatal solver error. In order to prove the point of a water hammer effect, a tentative value of 0.1% is used. For a sufficiently small timestep, this limit can be pushed to lower values, but has negative impact on the simulation time. This entire implementation is clever enough to avoid circular dependencies between solver variables, in that two different fluid velocity values are utilized to generate the jump, and has the physical meaning of slight flow acceleration when the closing sequence begins. The first is hidden within the $massFlow$ variable and is the solution to the momentum transport equations of the previous timestep, whereas the second is calculated based on the cross-section area at the current timestep. The major caveat is of course that it does not fully reflect a real situation, due to the inherent flaw of boundary condition switching, but is close enough from a physics standpoint to be considered valid as a pressure model.

Table 6.7: Fluid boundary conditions

Name (Figure 6.11b)	Type	Mesh Motion	Mass and Momentum	Argument
D (Wall.Static)	Wall	Stationary	Free Slip	Forced displacement
C (Wall.Moving)	Wall	Unspecified	Free Slip	Wall follows fluid motion
F (Opening.Valve)	Opening	Stationary	Entrainment	Equation 6.6.4
G (Wall.Piston)	Wall	Rigid Body Solution	No Slip	Fluid-Solid Interface
E (Wall.Valve)	Wall	Stationary	No Slip	Non-deforming fluid volume
A/B (Symmetry)	Interface	Cons. Flux	Cons. Flux	Rot. periodicity

6.6.5. Results and Discussion

Representative FEM results are shown in Figure 6.12 for a single thrust cycle where the tank is left to expand until the pressure drop ΔP become zero. The overall behaviour seems normal in terms of pressure and mass flow development, as well as of spring displacement. An inconsequential numerical instability is observed at the initial timesteps due to the integration methods used by the solver and the fact of having a transient system converge to a steady state. After the valve opening sequence though, the system displays a gradual expulsion process that is compliant with the analytic model results of Section 5.7. As a matter of fact, any assumptions made for the fluid are confirmed, with an average Reynolds number of 18, value that corresponds to low-speed laminar flows.

Results have also been produced for a sudden cut-off of the same thrust cycle, illustrated in Figure 6.13. The system has a good transient response to this sudden event, capturing the pressure jump and displaying the same time lag between opening and tank pressure, while even more promising is the observed pressure recovery that was predicted by the analytic

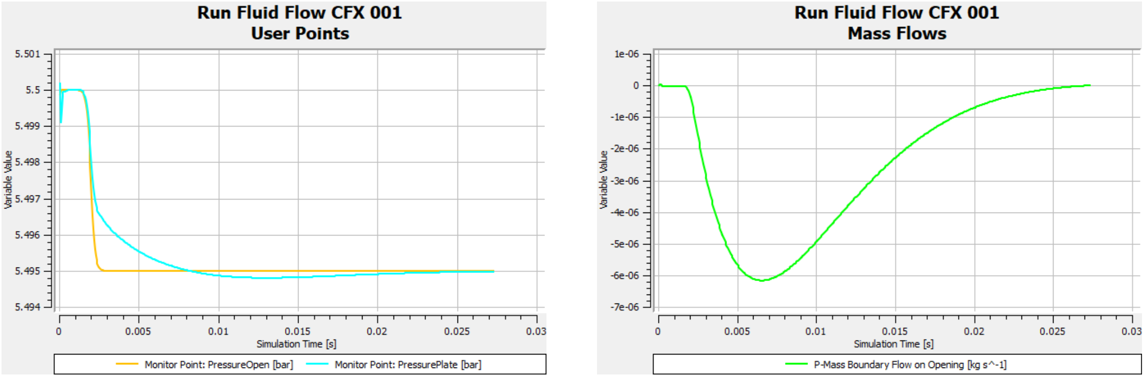

(a) Pressure: Opening (Cyan), Inner (Yellow)

(b) Mass flow at opening, in kg/s

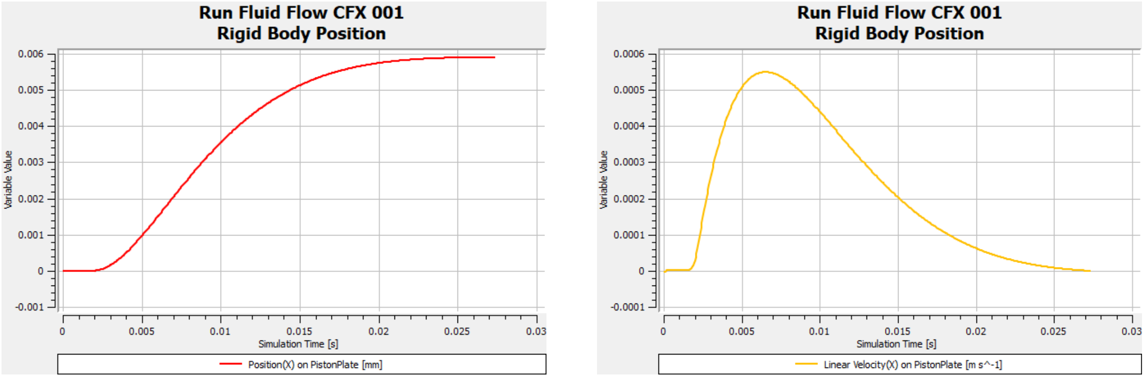

(c) Spring position in mm

(d) Spring Velocity in m/s

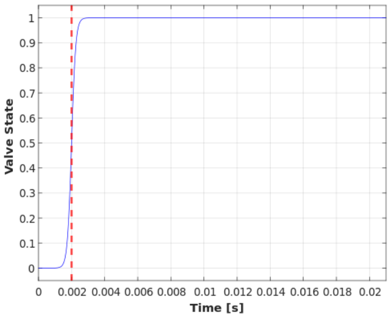

(e) Valve state for the free flow: Opens at red line

Figure 6.12: Flow development for uninterrupted thrust cycle, for a pressure drop $\Delta P = 500\ Pa$

model, showing good agreement between the two. The claim is reinforced by the spring halting to its new position without oscillatory behaviour.

Peculiarities however are noticeable in both qualitative and measurable aspects. For starters, the pressure profiles of Figure 6.12a indicate that the tank inner pressure (yellow line) lags behind the valve opening pressure level (cyan line) set by Equation 6.6.2, and this is an expected situation due to the spring-driven pressurization and the flow restriction. Unexpected though is the fact of the tank pressure being slightly lower than the opening pressure, contrary to predictions made by the theoretical background of Chapter 5 and its associated analytic model. Potential explanations include a larger timestep that overshot the fluid solver outputs and disguised pressure losses not taken into account. The first is disproved by the other performance metrics that show no sign of overshoot or discontinuity such as reverse flow, whereas the second may be accurate if fluid is impulsively moving faster than the spring and based on Equation 5.7.8 the actual pressure drop at the fluid-solid interface is augmented. Considering the minimal effect this has on the mass flow output, no further inspection is needed.

Greater emphasis is given to the comparison of analytic and FEM values for the mass flow, thrust duration and spring displacement in Table 6.8. Values from he FEM model are multiplied by the number of slices to obtain output for the full domain. In addition, a gross estimate of the maximum number of orbits and the maximum thrust time for the system is made, based on the assumption of identical thrust cycles until the SFx assembly is fully unloaded. The outcome is quite contradictory, indicating only partial agreement between the two counterparts. Despite both measuring a similar spring displacement, the FEM model outperforms the analytic equivalent in terms of mass flow and thrust duration. This can be traced back to the fundamental theory employed for each model, more specifically the fluid solver. The first-order approximation of Equation 5.7.6 cannot compare to the second-order accurate *Navier-Stokes* equations used in CFX, lacks significant details on fluid acceleration and has the inability to let the flow develop below the valve opening pressure, with a negative square root error halting the simulation.

Based on this brief analysis, the outputs of this validation study can be interpreted in two manners. First, the validation study disproved the analytic model of Chapter 5 with absolute values of important metrics corresponding to a better performing tank than anticipated. Second, and most unfortunate, the system is still unable to match the target value of $54\ s$ set in Chapter 1 or the 6000 orbits specified by Requirement 6.2, under the current pressure drop. Seeking improvement over the current status, the process was repeated with a pressure drop of $\Delta P = 50\ Pa$, the results of which are also shown in Table 6.8. This variant highlights even more the quality difference between a simplified analytic model and a finite element solver, with the latter showing far better results in terms of propellant management (lower mass flow) and thrust duration. On the other hand, and despite meeting the 6000 orbit requirement, the mass flow is still too high to reach the $54\ s$ thrust duration, safely concluding that the SFx spring-loaded tank is not suitable for the mission specifications of Chapter 1. This is not a dead end for the propulsion system itself, as it meets the majority of requirements of Groups 4 and 6, but there is now solid evidence to denote the incompatibility of the given mission with the proposed solution.

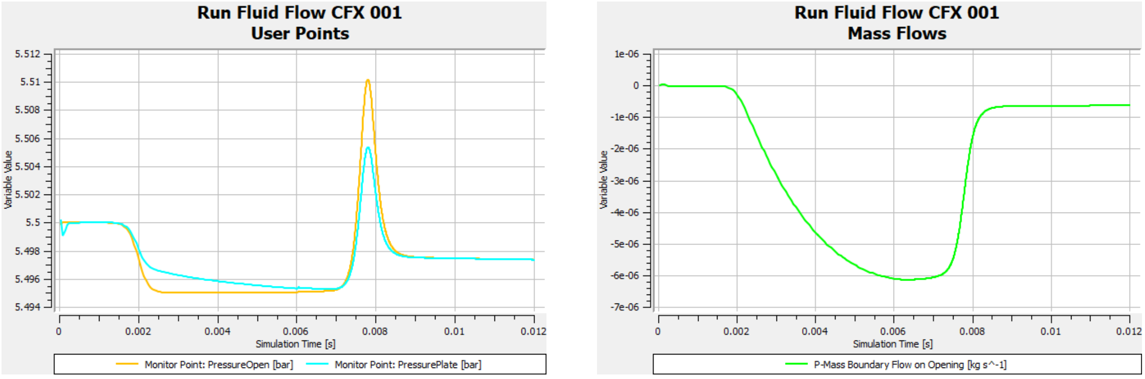

(a) Pressure: Opening (Yellow), Inner (Cyan)

(b) Mass flow at opening, in kg/s

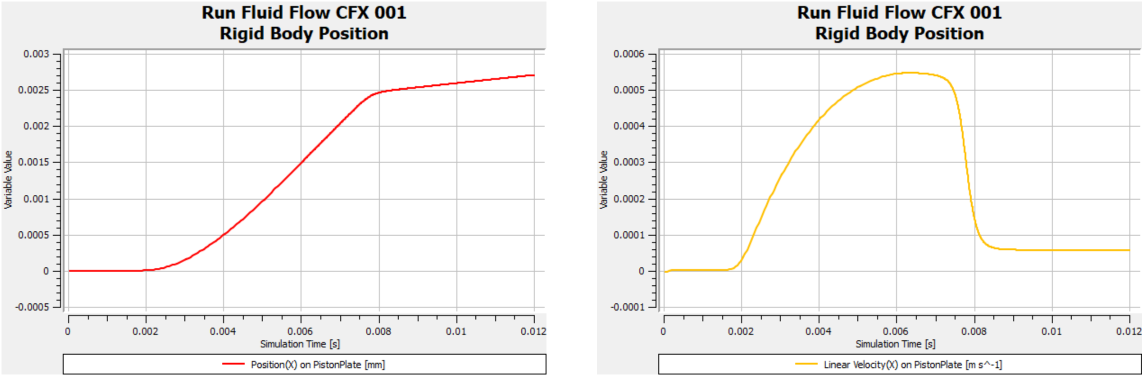

(c) Spring position in mm

(d) Spring Velocity in m/s

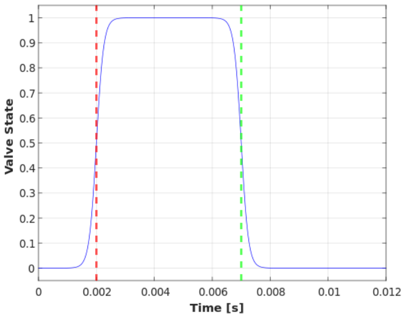

(e) Valve state for the interrupted flow: Opens at red line and closes at green line

Figure 6.13: Flow development for a $5ms$ thrust cycle, for a pressure drop $\Delta P = 500\ Pa$

Table 6.8: Model comparison for a single thrust cycle

$\Delta P = 500\ Pa$				
Variable	FEM	1^{st}	2^{nd}	Section 5.7
Mass Flow (max.)(mg/s)	246.8	244.8	244.6	700
Mass Flow (avg.)(mg/s)	105.77	104.25	104.02	337.6
Thrust duration (ms)	25.3	25.55	25.6	8
Spring displacement (μm)	5.945	5.906	5.916	6
Max. Number of Orbits(est.)	1083	1090	1088	1073
Max. Thrust time (est.)(s)	27.42	27.8	27.87	8.584
$\Delta P = 50\ Pa$				
Variable	FEM	1^{st}	2^{nd}	Section 5.7
Mass Flow (max.)(mg/s)	24.92	25.22	25	120
Mass Flow (avg.)(mg/s)	10.98	11.03	10.96	46.9
Thrust duration (ms)	24.25	24.2	24.4	4.8
Spring displacement (μm)	0.592	0.593	0.594	0.5
Max. Number of Orbits(est.)	10880	10861	10843	12882.4
Max. Thrust time (est.)(s)	263.84	262.84	264.57	61.83

6.7. Conclusion and Remarks on the Chapter

This chapter marks the conclusion of the analysis phase of this thesis, by acting as a validation measure for the design's performance seen in Chapter 5. Critical to the fruition of this study is the use of well-established software in the field of engineering, namely the *AUTODESK INVENTOR* suite for generating all geometries and the *ANSYS MULTIPHYSICS* suite as the finite element modeling workhorse. Performing a full-scale simulation on the entire assembly is quite taxing on computer resources and does not allow for comparison with the previous chapter results. Instead, the simulation strategy is based on isolated sub-assemblies to which dedicated forces are exerted, namely the envelope, the SFx spring formation, while the fluid domain required to solve the FSI dynamic model is directly extracted from the volume available between the two structural components already mentioned. For more accurate comparison, each of the load case analyses (except case E) is expanded with a grid-independence study with three levels of mesh refinement.

The static response of the envelope sub-assembly is not matching the results of Chapter 5. In particular, the equations devised for load case D fall short of the finite element model, with much better performance extracted from the latter, indicating a safer design. Better agreement is observed in load case A, although most performance metrics obtained by the FEM solver have no analytic counterpart, so this claim is left open for discussion.

The static response of the spring formation is in good agreement with the theoretical predictions of Section 5.5, an expected outcome that stems from the inherent symmetry provided by the SFx formation. As a matter of fact, the grid convergence study produced a model matching error less than 1%, proving the validity of the optimization process conducted in Section 5.5.

More problematic is the comparison of load case E, the FSI problem. The difficulty associated with a fluid-structural coupling is exponentially higher with respect to previous cases, and the assumptions made only amount to little in simplifying the model. Results are also emphasizing the accuracy difference between the analytic model and the FEM simulation, with more than double thrust duration in the latter with a better mass flow management. In the sense of purely crunching numbers, the analytic model of Section 5.7 is completely disproved despite offering the same graphical profiles as the more elaborate finite element model, but both fare poorly when seen at the larger scale of mission requirements.

As a final note in this chapter, emphasis is given to load case E and the way it has been handled in Section 6.6. Functional assumptions about the flow, mathematical workarounds and careful tuning of the solver have significantly lessened the computational load, to the extent of having a complete simulation within 20-25 minutes, depending on the run conditions, on a two-core processor clocked at $2\ GHz$ with a memory footprint of less than $1\ GB$. This speed has enabled a constructive approach to setting up the FSI model and simultaneously shows an indirect effect of the CFU configuration of the envelope.

7

Conclusion and Recommendations

The present chapter intends to draw productive conclusions about the scientific output produced in this work. Briefly said, the author has failed to deliver a convincing design that meets his own expectations, as well as the main objective that spurred this study. Section 7.1 expands upon this claim on a technical level, identifying the highlights of each intermediate design step and giving a definitive answer on the research questions posed at the beginning of this project. Section 7.2 on the other hand is more concerned with non-technical aspects that affected the workflow development. Lastly, Section 7.3 gives some recommendations about further advancing the concept of self-pressurizing storage modules.

7.1. Technical Summary

The section draws the conclusion of the entire thesis with respect to the initial objectives and the milestone research questions seen in Chapter 1. For the sake of clarity, the comprehensive objective is reformulated:

> *The project goal is to develop a self-pressurizing storage system that can be implemented within a Pocketqube-sized propulsion module and is compatible with a Vaporizing Liquid Microthruster (VLM) and a standard off-the-shelf microvalve, using compliant mechanisms.*

The objective has been only partially achieved, as demonstrated in this report. A storage module that can self-pressurize without the use of external components has been designed according to the philosophy of compliant mechanisms, by means of a multi-spring formation. The tank has performed duly when subject to static loading with a good safety margin, but it fails in keeping a sustained expulsion time by several magnitude orders, with too quick of a pressure release. This mixed outcome renders the proposed design compatible with the other propulsion components, but not the mission for which their use is intended. Compatibility encompasses all aspects of a design, so since a mismatch is found, the design cannot be regarded as successful.

With respect to the individual research questions set in Chapter 1, tentative answers are given based on the work done to justify them.

1. *What are the minimum requirements that the proposed storage solution must meet? What mass and volume budget can be allocated to the tank, taking into account any tolerances?*

   This question is successfully answered in Chapter 3, through the combined use of System Engineering methods, related works on propellant storage designs and the system requirements defined in Chapter 1. The standard method of a Requirement Discovery Tree (RDT) has generated a requirement set that should suffice to characterize the physical and functional performance of the selected design. In this work, a color-coded grouping scheme has been introduced to better discern requirements with a common trait. A maximum mass of $32\ gr$ and a maximum volume of $10.584\ cm3$ have been designated as upper limits for the tank, stemming directly from the system requirements.

2. *How does a compliant system operate? How can this principle be integrated to the system in discussion?*

   Chapter 2 explains in detail the inner workings of a compliant mechanism. The classical definition of compliant systems has been expanded to include entities that deflect beyond the typical bending actuation but nonetheless behave as elastically deforming objects. These interesting elements have been assessed in terms of function, extent of deflection and stress management, while known applications and the most highlighted assets and drawbacks complement the technical background, providing the reader with a definite answer on this research question. The integration of such a mechanism is better presented in Chapter 4, with an effort to provide as many design candidates as possible. Their elastic nature allows for a broad and enticing spectrum of concepts, such as flexure-aided bladders or springs, membrane-powered bellows, while the expanded definition has allowed torsionally deforming objects to enter the list.

3. *What is the optimal shape and configuration for the tank design? How does this configuration vary between idle and thrust conditions?*

   A conceptual design cannot by any means be the optimal solution to a problem. Still, time has been invested finding a shape and configuration that stands out from the alternatives. The answer is multi-faceted and cannot be found in a single section of this study. Instead, the proposed design is established according to trade-off analyses for all components that must be assessed qualitatively, whereas optimization studies take place for quantitative improvements of the design. Section 4.5.1 involves a complete trade-off study for the aforementioned variables, which are then optimized following the requirement limits in Chapter 5. The preliminary design containing the winning shape and configuration is summarized in Table 4.10. Size and shape optimization have also been employed for the mechanism itself, resulting in the detailed design proposal of Section 5.9. Insofar as configuration between idle and thrust states is concerned, the axial deformation of the SFx spring assembly is the only actual change, proof of the design's simplicity.

4. *What performance can be achieved by the proposed design? How well is the output replicated in a software simulation?*

   The static and dynamic performance of the module has been successfully evaluated with two different methods. First, analytic models were developed in Chapter 5 to size each component and then estimate their static load response, as per the requirements. For the non-active components, a sizing process was sufficient to observe a good response to any load case considered with safety margins being in excess of target values. For the spring-powered mechanism, a sizing process was not enough to judge its capabilities, as Requirement 6.3 is not quantified, hence an optimization study was included to lower the stiffness. The process has been further enhanced by a configuration study in order to improve the deflection levels and in turn the propellant capacity. Acknowledging the impact of manufacturing limitations, the design proposal of Table 5.12 is derived. Briefly said, the tank design is able to offer $2.9\ gr$ of water at the designated pressure, with a total mass footprint of $27.4\ gr$.

The dynamic performance of the system was treated as a Fluid-Structure Interface (FSI) problem. With a custom analytic model, thrust duration and average mass flowrate per cycle have been measured in a Simulink instance, the results being worse than anticipated. Irrespective of whether the design relied on a single spring or a multi-spring contraption, exceedingly high mass flowrates compared to literature with a much shorter thrust duration compared to the system requirement of Chapter 1 were observed. For future reference, the analysis outputted a $10\ ms$ cycle with an average consumption of $200-300\ mg/s$, disproving of the design.

Relying on analytic models was not sufficient to draw a conclusion on any of the results, even those which are obtained very simply. A validation study is conducted using dedicated engineering software that relies on Finite Element models. Results on the static response were not vastly different, with ample safety margins being observed. A grid convergence study reinforced said results, confirming the success of the tank design in this aspect. Exception to that was the calculation of stresses and deflections of the support beams, contradicting the polynomial approximation used previously. The FE model predicted a much better response, though with a slightly lower safety factor. This behavior has been replicated at the dynamic simulations, with mass flowrate and thrust durations between at least twice better (see Table 6.8). Nonetheless, the orders of magnitude lower thrust duration is a deal-breaker for the mission intended, unable to offer fine thrust control. The upper limit performance for the current tank design is a $25.6\ ms$ maneuver at the maximum stored pressure with a fuel consumption of $104.02\ mg/s$ for a pressure drop of $500\ Pa$, and a $24.4\ ms$ maneuver with a minimum mass flow of 10.96 for a $50\ Pa$ pressure drop.

7.2. Thesis Management

Referring to the final result of this study, several aspects of the workflow itself have proven challenging and at points insurmountable. Starting from the main topic, the initial MSc. proposal aimed at a complete propulsion module was reduced to a compatible self-pressurizing storage subsystem. Aside from the disproportional time and effort required to model all module subsystems in the way described here, the lack of any verified small-scale tanks with the capability of pressure control was sufficient to stand on its own as a research topic, much more so when a rather recent design philosophy is put into perspective. Still, the thesis was driven by the literature outcome rather than the goal it had set, leading to a second but much shorter literature survey on compliant mechanisms and a subsystem level list of requirements that apply only to the storage module. As a result, the project strayed from the original path and followed a completely different approach, prioritizing simplicity over innovation. From a research standpoint, though, this study is successful in generating a new solid ground for passive pressurization propellant storage that can be expanded in future efforts.

An additional consequence of the scope change was the omission of some research questions. The original thesis objective, reported in the companion literature review (see [28]), was the conception, design and implementation of a thruster-independent storage module. In particular, the tank would be ideally designed for one thruster type, then followed by an investigation to find the necessary modifications for the tank to function with the other type, which was partially achieved considering the content of this work. Logically speaking, this section would have been placed right after 6, but a detrimental issue arose: going by the conclusion of the previous section, the dynamic performance of the spring-powered pressurization is sub-par. The notion of taking an under-performing system, and modifying it to fit a completely different set of operating conditions is unreasonable and devoid of purpose, other than further disproving the design choice. Another question that had to be canceled was the advancement of the design to the experimental phase, with a physical prototype, due to both working from distance, thus not having access to a laboratory, and having a model that merits improvement of its drawbacks.

On another note, time management has been the primary cause for the major delay in delivering a complete study. Working on what is essentially an independent research study can be time-efficient only by executing a detailed plan. This study however is characterized by a number of unforeseen circumstances, such as the steeper than expected learning curve of CFX in Chapter 6, or the generation of Chapter 4 from little to no information. The lack of planning such events has had an impact to the work pace in this thesis, with an estimate of 1-2 months total time.

Even more problematic, though, was time management between the academia and personal/family life. While impossible to publicize details on sensitive matters, intermingling two very intensive time schedules is a fatal error on behalf of the researching student. For one to complete the project in a reasonable time frame, creating two distinct and non-negotiable time schedules (if such situation arises) is of paramount importance. With the exception of study-related mistakes, bad time management and planning have drastically extended the development time and reduced the quality of the work.

7.3. Recommendations

Being one of the first attempts in the field of Pocketqube-sized, self-pressurizing storage modules, the project offers ample ground for research and improvement of the concept. Hereafter, some example topics for future endeavors are presented.

- First among the potential topics is a re-evaluation of the design's secondary traits. Relying on staple materials has proven inefficient in both mass footprint and propellant capacity, or in Δv which is the final target. While the aluminum envelope along with the interface supports amount to about a quarter of the total mass, the steel spring formation is way too heavy for the deflection it offers, even after resorting to a second variation of helical springs (see Figure 4.15). The findings of Section 4.5.1 prove that switching to a *Ni superalloy* or even *titanium (Ti)* springs should cut down on mass by about $50\ \%$ due to the sheer difference in material density, allow higher deflection and therefore more prop. capacity and Δv. This material change of course cannot be applied on its own, but rather as an input to the approach of Section 5.5. On the contrary, the tank external shape and associated configuration choices have produced a sturdy envelope, with a remarkable static response to any load imposed. Improvements that can be proposed at this point is the reduction of the wall thickness to $0.5\ mm$ and the use of *topology optimization* techniques to shave off some mass from the envelope, only after improving the spring formation.

- An alternative to the above is the change in type of helical springs. Common springs have this constant-pitch form that resembles a helix, hence the name. It is though possible to vary this pitch on a turn-to-turn basis, creating a variable-stiffness spring, usually referred to as a *constant force* spring, or vary the spring diameter on a turn-to-turn basis to create *telescopic or conical* springs. Depending on the output, one can emphasize on deflection and consequently propellant capacity or pressurizing capability. This latter may be of use in a propulsion system that requires the same output at each thrust cycle.

- Insofar as the primary design is concerned, the spring alternative was preferred due to its simplicity and well-established analysis methods. Nonetheless, it is but one of the many types of springs that can be studied, and springs themselves are just a single concept out of those described in Chapter 4. Even at the stage of pure speculations, wave springs (SW), origami bellows (ORB) or *flexure-based* systems like the bladder (FB) should present better performance, despite requiring more advanced models than those found in Section 5.5.

- Taking the current design beyond its limitations, namely the low thrust duration and the measurement of a single cycle rather than intermittent operation, an experimental prototype could (and should) be considered once the aforementioned modeling problems have been resolved, ideally working in conjunction with the other propulsion components that the tank was designed for. An investigation should also be carried out on topics not discussed in this thesis, such as vibration and leaking tests. Regarding the former, some concern exists with respect to the TM-D-S interface beams (see Pages 77 and 81), which are rather thin and may induce some sloshing. As far as the latter goes, this is a mandatory experimental test for any liquid storage vessel and the current design is no exception. Lastly, Requirement 3.4 merits some future investigation, with the correlation of thermal control to the thermodynamic condition of the propellant being an interesting topic.

Bibliography

[1] Introduction to Compliant Mechanisms, August 2017. URL https://compliantmechanisms.byu.edu/content/intro-compliant-mechanisms. Accessed on 31/08/2017.

[2] The Delfi-PQ Mission, July 2017. URL http://delfispace.nl/delfi-pq. Accessed on 27/08/2017.

[3] Compliance, Definition 3. Merriam-Webster online dictionary, July 2018. URL https://www.merriam-webster.com/dictionary/compliance.

[4] FlexSys Wind Energy, July 2018. URL https://www.flxsys.com/wind.

[5] FlexFoil$^{\text{TM}}$ Compliant Control Surfaces, July 2018. URL https://www.flxsys.com/flexfoil/.

[6] Bellows Movement: HySpan Technical Notes, 2018. URL http://www.hyspan.com. Retrieved on 02-10-2018.

[7] Aluminum 6061-T6 Material Properties, 2018. URL http://www.matweb.com/search/DataSheet.aspx?MatGUID=b8d536e0b9b54bd7b69e4124d8f1d20a. Retrieved on 16-09-2018.

[8] Stainless Steel 17-7 PH Material Properties, 2018. URL https://www.spacematdb.com/spacemat/. Retrieved on 16-09-2018.

[9] Wave Spring - Technical Brochure, 2018. URL https://www.smalley.com/resource-center/catalogs. Retrieved on 16-09-2018.

[10] Space Materials Database, 2018. URL https://www.spacematdb.com/. Accessed on 20-12-2018.

[11] Metric Bolt Strength, 2019. URL http://euler9.tripod.com/bolt-database/22.html. Retrieved on 04-03-2019.

[12] Stainless steel material properties, 2019. URL http://www.powah.hk/upload/technical\information. Retrieved on 04-03-2019.

[13] Mechanical Properties of Steel Bolts, Screws and Studs, 2019. URL http://www.powah.hk/upload/technical\information. Retrieved on 05-03-2019.

[14] Circle packing in a circle, 2019. URL https://en.wikipedia.org/wiki/Circle_packing_in_a_circle. Accessed on 20/07/19.

[15] Ace Wire Spring & Form Company, Inc. Compression Springs, 2019. URL http://www.acewirespring.com/compression-springs.html. Accessed on 09/04/2019.

[16] Acxess Spring. Standard Spring Wire Diameter Sizes, 2019. URL https://www.thespringstore.com/standard-spring-wire-diameter-sizes.html. Accessed on 29/08/2019.

[17] Mohd Nizam Ahmad, Karimah Mat, and Wan Mansor Wan Muhamad. A Novel Design of Car Wiper Using Compliant Mechanism Method. *Applied Mechanics and Materials*, 465-466:39–43, December 2013. doi: 10.4028/www.scientific.net/amm.465-466.39.

[18] Timothy Melvin Allred. Compliant Mechanism Suspensions. mathesis, Brigham Young University, June 2006. URL `http://hdl.lib.byu.edu/1877/etd1322`.

[19] Ansys, Inc. CFX User's Guide, 2019.

[20] Michael F. Ashby. *Materials Selection in Mechanical Design*. Elsevier S&T, 2010.

[21] Autodesk, Inc. Autodesk Inventor Suite 2020: User's Manual, 2018.

[22] Michael S. Baker, Richard A. Plass, Thomas J. Headley, and Jeremy A. Walraven. Compliant Thermo-Mechanical MEMS Actuators. Technical report, Sandia National Laboratories, December 2004.

[23] Aleksander K. Belyaev, Tatiana V. Zinovieva, and Kirill K. Smirnov. Theoretical and experimental studies of the stress–strain state of expansion bellows as elastic shells. *St. Petersburg Polytechnical University Journal: Physics and Mathematics*, 3(1):7–14, March 2017. doi: 10.1016/j.spjpm.2017.03.003.

[24] Richard G. Budynas, Richard Budynas, and J. Keith Nisbett. *Shigley's Mechanical Engineering Design*. MCGRAW HILL BOOK CO, 2010. ISBN 0073529281.

[25] Jared J. Butler. Highly Compressible Origami Bellows for Harsh Environments. Master's thesis, Brigham Young University, November 2017.

[26] J.W. Cen and J.L. Xu. Performance evaluation and flow visualization of a MEMS based vaporizing liquid micro-thruster. *Acta Astronautica*, 67(3-4):468–482, August 2010. ISSN 0094-5765. doi: 10.1016/j.actaastro.2010.04.009.

[27] A. Cervone, B. Zandbergen, D. C. Guerrieri, M. De Athayde Costa e Silva, I. Krusharev, and H. van Zeijl. Green micro-resistojet research at Delft University of Technology: new options for Cubesat propulsion. *CEAS Space Journal*, 9(1):111–125, July 2016. ISSN 1868-2502. doi: 10.1007/s12567-016-0135-3.

[28] E. Chatzimanolis. Conceptual design of a micro-propulsion module for the Delfi-PQ: Literature research on available and prototype technologies for pico-satellite propulsion. September 2017.

[29] Chia-Chin Chen, Chien-Wei Liu, Heng-Chuan Kan, Lee-Her Hu, Guey-Shin Chang, Ming-Chih Cheng, and Bau-Tong Dai. Simulation and experiment research on vaporizing liquid micro-thruster. *Sensors and Actuators A: Physical*, 157(1):140–149, January 2010. ISSN 0924-4247. doi: 10.1016/j.sna.2009.10.025. URL `http://linkinghub.elsevier.com/retrieve/pii/S0924424709004634`.

[30] D.H. Chen and K. Ushijima. Prediction of the mechanical performance of McKibben artificial muscle actuator. *International Journal of Mechanical Sciences*, 78:183–192, January 2014. doi: 10.1016/j.ijmecsci.2013.11.010.

[31] Xing Chen and Dong-Weon Lee. A microcantilever system with slider-crank actuation mechanism. *Sensors and Actuators A: Physical*, 226:59–68, May 2015. doi: 10.1016/j.sna.2015.02.029.

[32] Peter R.N. Childs. *Mechanical Design Engineering Handbook*. Butterworth-Heinemann/Elsevier, Amsterdam Boston, 2014. ISBN 0080977596.

[33] Shyh chour Huang and Guh jyhjei Lan. Design and Fabrication of Micro-Compliant Amplifier with Topology Optimal Compliant Mechanism Integrated with a Piezoelectric Microactuator. In *2005 Conference on High Density Microsystem Design and Packaging and Component Failure Analysis*. IEEE, June 2005. doi: 10.1109/hdp.2005.251431.

[34] T.P Dao and S.C. Huang. Design and Analysis of Flexible Slider Crank Mechanism. *International Journal of Mechanical, Aerospace, Industrial, Mechatronic and Manufacturing Engineering*, 2014. doi: 10.1999/1307-6892/9998127.

[35] Ravi A Deepak and Robert J Twiggs. Thinking Outside the Box : Space Science Beyond the CubeSat. *Journal of Small Satellites*, 1(1):3–7, 2011.

[36] Sharvari Dhote, Zhengbao Yang, and Jean Zu. Modeling and experimental parametric study of a tri-leg compliant orthoplanar spring based multi-mode piezoelectric energy harvester. *Mechanical Systems and Signal Processing*, 98:268–280, January 2018. doi: 10.1016/j.ymssp.2017.04.031.

[37] E Dragoni. A contribution to wave spring design. *The Journal of Strain Analysis for Engineering Design*, 23(3):145–153, July 1988. doi: 10.1243/03093247v233145.

[38] E. Becnel, S. McAndrew, L. Strass, T. Walkinshaw and K. Worrall. PQ 60 Standard Document, March 2015.

[39] European Cooperation for Space Standardization (ECSS). Quality standard 70-71 Rev. C. Space product assurance: Materials, processes and their data selection, October 2014.

[40] Katherine Fowee, Steven Pugia, Ryan Clay, Matthew Fuehne, Margaret Linker, Anthony Cofer, and Alina Alexeenko. Quad-Thruster FEMTA Micropropulsion System for CubeSat 1-Axis Control. In *31st Annual AIAA/USU Conference on Small Satellites*, Logan, 2017.

[41] R. M. Fowler, L. L. Howell, and S. P. Magleby. Compliant space mechanisms: a new frontier for compliant mechanisms. *Mechanical Sciences*, 2(2):205–215, October 2011. doi: 10.5194/ms-2-205-2011.

[42] Juan a Gallego. *Statically balanced compliant micromechanisms*. PhD thesis, Delft University of Technology, 2013. URL `https://repository.tudelft.nl/islandora/object/uuid{%}3A081e3d0e-173b-4a36-b8d6-c29c70eb7ae3`.

[43] Y. Gao, J.T. Liu, and Y.F. Ma. A review of the vaporizing liquid microthruster technology. In *2014 ISFMFE - 6th International Symposium on Fluid Machinery and Fluid Engineering*, volume 2014. Institution of Engineering and Technology, 2014. ISBN 9781849199070. doi: 10.1049/cp.2014.1220.

[44] James Monroe Gere. *Mechanics of Materials*. Brooks/Cole-Thomas Learning, Belmont, CA, sixth edition, 2004. ISBN 0534417930. URL `https://www.worldcat.org/title/mechanics-of-materials/oclc/605724810`.

[45] Eberhard Gill. Space systems engineering: Lecture notes. October 2015.

[46] Ignacio Granero-Moneva. Design and structural analysis of the propellant tank for a water resistojet. mathesis, Delft University of Technology, July 2015.

[47] Granta Design. CES EduPack, 2018. URL http://www.grantadesign.com/education/edupack/.

[48] H. C. Greenberg, M. L. Gong, S. P. Magleby, and L. L. Howell. Identifying links between origami and compliant mechanisms. *Mechanical Sciences*, 2(2):217–225, December 2011. doi: 10.5194/ms-2-217-2011.

[49] C.A.J. Hanselaar. Evaporative Two-Phase Micro-Flow Modelling. page 148, 2016. URL https://repository.tudelft.nl/islandora/object/uuid:030573d7-42c7-4b3e-802a-5b1b9f98ed38?collection=education.

[50] Hanselaar, C.A.J. Evaporative Two-Phase Micro-Flow Modelling. Master's thesis, Delft University of Technology, April 2016.

[51] Larry L. Howell. *Compliant Mechanisms*. John Wiley & Sons, 2001. ISBN 047138478X.

[52] Larry L. Howell. *Handbook of Compliant Mechanisms*. John Wiley & Sons, Inc, Chichester, West Sussex, United Kingdom Hoboken, New Jersey, 2013. ISBN 9781119953456.

[53] Pega Hrnjak and Xiao Tu. Single phase pressure drop in microchannels. *International Journal of Heat and Fluid Flow*, 28(1):2–14, February 2007. doi: 10.1016/j.ijheatfluidflow.2006.05.005.

[54] Huub Janssen, Maurice Teuwen, Ramón Navarro, Niels Tromp, Eddy Elswijk, and Hiddo Hanenburg. Design and prototype performance of an innovative cryogenic tip-tilt mirror. In *Modern Technologies in Space- and Ground-based Telescopes and Instrumentation*. SPIE, July 2010. doi: 10.1117/12.856585.

[55] Rushikesh S. Joshi, Anirban C. Mitra, and Sachin R. Kandharkar. Design and Analysis of Compliant Micro-gripper Using Pseudo Rigid Body Model(PRBM). *Materials Today: Proceedings*, 4(2):1701–1707, 2017. doi: 10.1016/j.matpr.2017.02.010.

[56] Dan Kalapay and Charles Kim. Design of a Compliant Energy Storage Impulse Mechanism for a Desktop Stapler. In *Volume 2: 32nd Mechanisms and Robotics Conference, Parts A and B*. ASMEDC, January 2008. doi: 10.1115/detc2008-49451.

[57] K. Karthikeyan, S.K. Chou, L.E. Khoong, Y.M. Tan, C.W. Lu, and W.M. Yang. Low temperature co-fired ceramic vaporizing liquid microthruster for microspacecraft applications. *Applied Energy*, 97:577–583, September 2012. doi: 10.1016/j.apenergy.2011.11.078. URL http://linkinghub.elsevier.com/retrieve/pii/S0306261911007847.

[58] Andrew Ketsdever, Dean Wadsworth, Stephen Vargo, and E. Muntz. The free molecule micro-resistojet - An interesting alternative to nozzle expansion. In *34th AIAA/ASME/SAE/ASEE Joint Propulsion Conference and Exhibit*, number May, Reston, Virigina, July 1998. American Institute of Aeronautics and Astronautics. doi: 10.2514/6.1998-3918.

[59] Karim Khamis. Comparative Study Between MEMS and Conventional Thrusters for Small Spacecraft Micropropulsion. Master's thesis, Delft University of Technology, May 2019.

[60] Gunter Krebs. Gunter's Space Page, August 2018. URL https://space.skyrocket.de.

[61] I. Krusharev. Micro - Thruster Development: Propulsion System for the DelFFi Mission. Master's thesis, Delft University of Technology, 2015. URL http://resolver.tudelft.nl/uuid:e60e68fe-d1f6-458b-8a5a-d5036e32fb69.

[62] Wen ku Shi, Cheng Liu, Zhi yong Chen, Wei He, and Qing hua Zu. Efficient Method for Calculating the Composite Stiffness of Parabolic Leaf Springs with Variable Stiffness for Vehicle Rear Suspension. *Mathematical Problems in Engineering*, 2016:1–12, 2016. doi: 10.1155/2016/5169018.

[63] Erik Kulu. Nanosatellite & Cubesat Database, August 2018. URL https://www.nanosats.eu/. https://www.nanosats.eu/.

[64] Pijus Kundu, Tarun Kanti Bhattacharyya, and Soumen Das. Design, fabrication and performance evaluation of a vaporizing liquid microthruster. *Journal of Micromechanics and Microengineering*, 22(2):025016, January 2012. ISSN 0960-1317. doi: 10.1088/0960-1317/22/2/025016.

[65] Federico La Torre. *Gas Flow in Miniaturized Nozzles for Micro-Thrusters*. PhD thesis, Delft University of Technology, S.l, 2011.

[66] A.T. Lee and R.G.J. Flay. Compliant Blades for Passive Power Control of Wind Turbines. *Wind Engineering*, 24(1):3–11, January 2000. doi: 10.1260/0309524001495369.

[67] Haw-Long Lee and Win-Jin Chang. Sensitivity of V-shaped atomic force microscope cantilevers based on a modified couple stress theory. *Microelectronic Engineering*, 88 (11):3214–3218, November 2011. doi: 10.1016/j.mee.2011.09.001.

[68] Rh Lee, Am Bauer, and Md Killingsworth. Performance characterization of the free molecule micro-resistojet utilizing water propellant. *AIAA Paper*, 12(0704):1–11, 2007. URL http://www.aric.or.kr/treatise/journal/content.asp?idx=115611.

[69] Riki Lee, Taylor Lilly, E. Muntz, and Andrew Ketsdever. Free Molecule Micro-Resistojet: Nanosatellite Propulsion. In *41st AIAA/ASME/SAE/ASEE Joint Propulsion Conference & Exhibit*, Reston, Virigina, July 2005. American Institute of Aeronautics and Astronautics. ISBN 978-1-62410-063-5. doi: 10.2514/6.2005-4073.

[70] Kristina Lemmer. Propulsion for CubeSats. *Acta Astronautica*, 134(January):231–243, May 2017. ISSN 0094-5765. doi: 10.1016/j.actaastro.2017.01.048.

[71] J. Li, H. Godaba, Z.Q. Zhang, C.C. Foo, and J. Zhu. A soft active origami robot. *Extreme Mechanics Letters*, 24:30–37, October 2018. doi: 10.1016/j.eml.2018.08.004.

[72] Liying Liu, Jian Xing, Qingwei Yang, and Yangjun Luo. Design of Large-Displacement Compliant Mechanisms by Topology Optimization Incorporating Modified Additive Hyperelasticity Technique. *Mathematical Problems in Engineering*, 2017:1–11, 2017. doi: 10.1155/2017/4679746.

[73] Nicolae. Lobontiu. *Compliant mechanisms : design of flexure hinges*. CRC PR INC, December 2003. ISBN 9780849313677. URL https://www.ebook.de/de/product/4271970/nicolae_lobontiu_compliant_mechanisms.html.

[74] K.-J. Lu, Satyanarayana Kota, Brian Patrick Trease, Z. Kreiner, J. Arenas, and J. Geiger. Design and Application of Compliant Mechanisms for Surgical Tools. *Journal of Biomechanical Engineering*, 127(6):981, July 2005. doi: 10.1115/1.2056561.

[75] A. D. Lytle. Dynamics of bellows filled with an incompressible liquid. *Journal of Spacecraft and Rockets*, 5(1):9–13, January 1968. doi: 10.2514/3.29178.

[76] Allen B. Mackay, David G. Smith, Spencer P. Magleby, Brian D. Jensen, and Larry L. Howell. Metrics for Evaluation and Design of Large-Displacement Linear-Motion Compliant Mechanisms. *Journal of Mechanical Design*, 134(1):011008, 2012. doi: 10.1115/1.4004191.

[77] A Mancas, A Cervone, and B T C Zandbergen. Design , simulation and optimisation of a low-pressure micro-resistojet for small satellite missions. In *Space Propulsion*, page 7, Koln, 2014. URL `https://repository.tudelft.nl/islandora/object/uuid:31253f90-8e20-4993-96cc-b80b24b9c8c4?collection=research`.

[78] D K Maurya, Soumen Das, and S K Lahiri. Silicon MEMS vaporizing liquid microthruster with internal microheater. *Journal of Micromechanics and Microengineering*, 15(5):966–970, March 2005. ISSN 0960-1317. doi: 10.1088/0960-1317/15/5/010.

[79] D.K. Maurya, S. Das, and S.K. Lahiri. An analytical model of a silicon MEMS vaporizing liquid microthruster and some experimental studies. *Sensors and Actuators A: Physical*, 122(1):159–166, July 2005. ISSN 0924-4247. doi: 10.1016/j.sna.2005.04.020. URL `http://linkinghub.elsevier.com/retrieve/pii/S0924424705002402`.

[80] Gareth McKinley. 2.25 Advanced Fluid Mechanics. Technical report, Massachusetts Institute of Technology: MIT OpenCourseWare„ Fall 2013. URL `https://ocw.mit.edu.LicensedunderCreativeCommonsBY-NC-SA.` Retrieved on 05/04/2019.

[81] Juan C. Moreno, Joana Figueiredo, and José L. Pons. Exoskeletons for lower-limb rehabilitation. In *Rehabilitation Robotics*, pages 89–99. Elsevier, 2018. doi: 10.1016/b978-0-12-811995-2.00008-4.

[82] Juergen Mueller, William Tang, Andrew Wallace, Russel Lawton, Wen Li, David Bame, and Indrani Chakraborty. Design, analysis and fabrication of a vaporizing liquid micro-thruster. In *33rd Joint Propulsion Conference and Exhibit*, pages 97–3054, Reston, Virigina, July 1997. American Institute of Aeronautics and Astronautics. ISBN 9780000000002. doi: 10.2514/6.1997-3054.

[83] Mukerjee, E.V and Wallace, A.P and Yan, K.Y and Howard, D.W and Smith, R.L and Collins, S.D. Vaporizing liquid microthruster. *Sensors and Actuators A: Physical*, 83 (1-3):231–236, May 2000. ISSN 0924-4247. doi: 10.1016/s0924-4247(99)00389-1. URL `http://linkinghub.elsevier.com/retrieve/pii/S0924424799003891`.

[84] Bruce R. Munson, Alric P. Rothmayer, and Theodore H. Okiishi. *Fundamentals of Fluid Mechanics*. JOHN WILEY & SONS INC, 2012. ISBN 978-1-118-11613-5.

[85] J. Ng and B.J. Vickery. A Model Study of the Response of a Compliant Tower to Wind and Wave Loads. In *Offshore Technology Conference*. Offshore Technology Conference, 1989. doi: 10.4043/6011-ms.

[86] Nguyen, N. T. and Wereley, S. *Fundamentals and applications of microfluidics*. Artech House, Boston, second edition, July 2006. ISBN 9781580539722.

[87] Macháček Ondřej, Kubík Michal, Strecker Zbyněk, Roupec Jakub, Novák Petr, and Mazůrek Ivan. Axial and Pressure Thrust Stiffness of Metal Bellows for Vibration Isolators. *MATEC Web of Conferences*, 153:06001, 2018. doi: 10.1051/matecconf/201815306001.

[88] Kristoffer Palmer, Ville Lekholm, Henrik Kratz, Hugo Nguyen, and Greger Thornell. DEVELOPMENT OF A SUSPENDED , ROBUST , THERMALLY INSULATED MICRO CHAMBER OF THICK SILICON DIOXIDE FOR MICROTHRUSTERS AND MICROREACTORS, 2011.

[89] Kristoffer Palmer, Hugo Nguyen, and Greger Thornell. Fabrication and evaluation of a free molecule micro-resistojet with thick silicon dioxide insulation and suspension. *Journal of Micromechanics and Microengineering*, 23(6):065006, April 2013. ISSN 0960-1317. doi: 10.1088/0960-1317/23/6/065006. URL `http://stacks.iop.org/0960-1317/23/i=6/a=065006`.

[90] Sujit Pardeshi, Sachin Kandharkar, and Bhagyesh Deshmukh. Monolithic compliant slider crank mechanism for motion amplification. *Materials Today: Proceedings*, 4(2): 1677–1682, 2017. doi: 10.1016/j.matpr.2017.02.007.

[91] John J. Parise, Larry L Howell, and Spencer P. Magleby. Ortho-planar linear-motion springs. *Mechanism and Machine Theory*, 36(11-12):1281–1299, November 2001. ISSN 0094-114X. doi: 10.1016/s0094-114x(01)00051-9. URL `http://linkinghub.elsevier.com/retrieve/pii/S0094114X01000519`.

[92] Kurt A Polzin and Edgar Y Choueiri Ý. A Passive Propellant Feeding Mechanism forMicropropulsion Using Capillarity. In *38th AIAA/ASME/SAE/ASEE Joint Propulsion Conference and Exhibit*, number July. American Institute of Aeronautics and Astronautics, July 2002. doi: 10.2514/6.2002-3949.

[93] Poyck, R.M.A. Design, manufacturing and characterisation of a water fed CubeSat micro-resistojet. Master's thesis, Delft University of Technology, August 2014. URL `https://repository.tudelft.nl/islandora/object/uuid%3A87bc9f46-5f40-4a87-9716-65f7e3ac7c29?collection=education`.

[94] Willard W. Pulkrabek. *Engineering Fundamentals of the Internal Combustion Engine (2nd Edition)*. Pearson, Upper Saddle River, N.J, 2004. ISBN 0131405705.

[95] Xiao Qimin, Liu Liwei, and Xiao Qili. The Optimal Design and Simulation of Helical Spring Based on Particle Swarm Algorithm and MATLAB. *WSEAS Trans. Cir. and Sys.*, 8(1):84–93, January 2009. ISSN 1109-2734. URL `http://dl.acm.org/citation.cfm?id=1540587.1540596`.

[96] Deepak S. Ramrakhyani, George A. Lesieutre, Mary I. Frecker, and Smita Bharti. Aircraft Structural Morphing using Tendon-Actuated Compliant Cellular Trusses. *Journal of Aircraft*, 42(6):1614–1620, November 2005. doi: 10.2514/1.9984.

[97] Austin Reid, Frederic Lechenault, Sergio Rica, and Mokhtar Adda-Bedia. Geometry and design of origami bellows with tunable response. *Physical Review E*, 95(1), January 2017. doi: 10.1103/PhysRevE.95.013002.

[98] S. Silvestrini, M. A. C. Silva, D. C. Guerrieri, F. Leverone, S. Mestry, V. Pallicadath, T. Pérez Soriano, B. Zandbergen, A. Cervone and H. Van Zeijl. Pocketqube workshop: Development of a micro-propulsion system for PocketQube applications. March 2017.

[99] Mahmood M Shokrieh and Davood Rezaei. Analysis and optimization of a composite leaf spring. *Composite Structures*, 60(3):317–325, May 2003. doi: 10.1016/s0263-8223(02)00349-5.

[100] Marsil A.C. Silva, Daduí C. Guerrieri, Henk van Zeijl, Angelo Cervone, and Eberhard Gill. Vaporizing Liquid Microthrusters with integrated heaters and temperature measurement. *Sensors and Actuators A: Physical*, 265:261–274, October 2017. doi: 10.1016/j.sna.2017.07.032.

[101] Stefano Silvestrini. Closed-loop Thrust Magnitude Control System for Nano- and Pico-Satellite Applications. mathesis, Delft University of Technology, July 2017. URL http://resolver.tudelft.nl/uuid:a75bf468-2244-46d6-a905-5d52f865ab81.

[102] Pulkit Solanki and Ajay Kumar Kaviti. Design and computational Analysis of Semi-Elliptical and Parabolic Leaf Spring. *Materials Today: Proceedings*, 5(9):19441–19455, 2018. doi: 10.1016/j.matpr.2018.06.305.

[103] Phaniendra Somraj and Hung-Yao Hsu. Design of a Bistable Compliant Locking Mechanism for New Generation Mirror Actuators. In *Manufacturing Engineering and Materials Handling, Parts A and B*. ASME, 2005. doi: 10.1115/imece2005-79480.

[104] Space-Track. Satellite Catalog, August 2018. URL https://www.space-track.org.

[105] Mohamed Taktak, Khalifa Omheni, Abdessattar Aloui, Fakhreddine Dammak, and Mohamed Haddar. Dynamic optimization design of a cylindrical helical spring. *Applied Acoustics*, 77:178–183, March 2014. doi: 10.1016/j.apacoust.2013.08.001.

[106] The MathWorks, Inc. Simulink, 2019. Downloaded on 05/04/2019, from https://www.mathworks.com/products/simulink.html.

[107] van Wees, T. and Hanselaar, C.A.J. and Jansen, E. and Granero-Moneva, I. and Cervone, A. and Zandbergen, B. Design, fabrication , testing and modelling of a vaporizing liquid micropropulsion system. In *Space Propulsion*, number 7, Rome, 2016. URL https://repository.tudelft.nl/islandora/object/uuid{%}3A9811010e-75a8-4146-8175-b8c454c43d20.

[108] M. De Volder, A.J.M. Moers, and D. Reynaerts. Fabrication and control of miniature McKibben actuators. *Sensors and Actuators A: Physical*, 166(1):111–116, March 2011. doi: 10.1016/j.sna.2011.01.002.

[109] C. Wang, B.T.C. Zandbergen, Angelo Cervone, and J. Chu. Numerical studies on performance of free molecule micro-resistojet for cubesats. In *6th European Conference for Aeronautics and Space Sciences (EUCASS)*, 06 2015.

[110] Michael Yu Wang. Mechanical and geometric advantages in compliant mechanism optimization. *Frontiers of Mechanical Engineering in China*, May 2009. doi: 10.1007/s11465-009-0066-1.

[111] Xu Wang and Hanqing Jiang. Design of origami fin for heat dissipation enhancement. *Applied Thermal Engineering*, 145:674–684, December 2018. doi: 10.1016/j.applthermaleng.2018.09.079.

[112] James R. Wertz and Wiley Larson. *Space Mission Analysis and Design*. Springer Aerospace Technology. Microcosm Kluwer, Torrance, Calif. Dordrecht Boston, third edition, September 1999. ISBN 9780792359012.

[113] Jerry West. Orthoplanar Spring Based Compliant Force/ Torque Sensor for Robot Force Control. Master's thesis, University of South Florida, 2017.

[114] J. Wilkings and Iain Simpson. Mathematical Modelling for Faster Auto-Injector Design. *Innovations in Pharmaceutical Technology*, 42, 2012. URL https://www.researchgate.net/publication/296028456_Mathematical_modeling_for_faster_autoinjector_design.

[115] Joyce Wong. The University Micro / Nanosatellite as a Micropropulsion Testbed. In *13" Annual AIAAfUSU Conference on Small Satellites*, 1999.

[116] Joyce Wong, Helen Reed, and Andrew Ketsdever. Temperature and Power Predictions for Flight-testing the Free Molecule Micro-Resistojet. In *27th International Electric Propulsion Conference*, pages 15–19, Pasadena, 2001.

[117] Yunqiang Yang, Jianing Wu, Rengao Zhu, Chuchu Li, and Shaoze Yan. The Honeybee's Protrusible Glossa is a Compliant Mechanism. *Journal of Bionic Engineering*, 14(4): 607–615, October 2017. doi: 10.1016/s1672-6529(16)60426-2.

[118] X.Y Ye, F. Tang, H.Q Ding, and Z.Y Zhou. Study of a vaporizing water micro-thruster. *Sensors and Actuators A: Physical*, 89(1-2):159–165, March 2001. ISSN 0924-4247. doi: 10.1016/s0924-4247(00)00540-9. URL http://linkinghub.elsevier.com/retrieve/pii/S0924424700005409.

[119] Warren C. Young. *Roark's Formulas for Stress and Strain, 8th Edition.* McGraw-Hill Education, New York, 2012. ISBN 0071742476.

[120] Wen Zeng, Feng Gao, Hui Jiang, Chuan Huang, Jianxing Liu, and Hanfei Li. Design and analysis of a compliant variable-diameter mechanism used in variable-diameter wheels for lunar rover. *Mechanism and Machine Theory*, 125:240–258, July 2018. doi: 10.1016/j.mechmachtheory.2018.03.003.

[121] Shouyin Zhang and Guimin Chen. Design of Compliant Bistable Mechanism for Rear Trunk Lid of Cars. In *Intelligent Robotics and Applications*, pages 291–299. Springer Berlin Heidelberg, 2011. doi: 10.1007/978-3-642-25486-4_30.

[122] John C. Ziegert, Beshah Ayalew, Vincent Lee, Souharda Raghavendra, and Andreas Obieglo. Compliant Link Suspension. In *SAE Technical Paper Series*. SAE International, April 2009. doi: 10.4271/2009-01-0225.

[123] Shannon Zirbel, Shane Curtis, Rachel Bradshaw, Luke Duffield, Greg Teichert, Nicholas Williams, Ron Rorrer, Spencer Magleby, and Larry Howell. Bi-Behavioral Prosthetic Knee Enabled by a Metamorphic Compliant Mechanism. In *Advances in Reconfigurable Mechanisms and Robots I*, pages 401–409. Springer London, 2012. doi: 10.1007/978-1-4471-4141-9_36.

[124] Shannon A. Zirbel, Kyler A. Tolman, Brian P. Trease, and Larry L. Howell. Bistable Mechanisms for Space Applications. *PLOS ONE*, 11(12), December 2016. doi: 10.1371/journal.pone.0168218.

[125] Shannon Alisa Zirbel. *Compliant Mechanisms for Deployable Space Systems*. PhD thesis, University of Toronto, 2014.

[126] Shen Zupei. Approximate Calculation of U-shaped Bellows. *Tsinghua Science and Technology*, 1996.

Appendices

A

Material Index Tables

In this appendix, detailed tables of the various material indexes used in Section 4.5.1 are provided. All values are taken from [47] and are sorted in increasing order, for the materials that were considered per index.

Pressure Vessel - All Stages

Name	**Yield Resistance (m^0.5)**
Acrylonitrile butadiene styrene (ABS)	0.0347 - 0.155
Age-hardening wrought Al-alloys	0.044 - 0.288
Aluminum/Silicon carbide composite	0.0494 - 0.0804
Brass	0.0825 - 0.459
Bronze	0.0717 - 0.402
Cast Al-alloys	0.0746 - 0.512
Cast iron, ductile (nodular)	0.0449 - 0.156
Cast iron, gray	0.0334 - 0.122
Cast magnesium alloys	0.0671 - 0.214
Cellulose polymers (CA)	0.0282 - 0.0789
CFRP, epoxy matrix (isotropic)	0.00769 - 0.0276
Commercially pure lead	0.614 - 2.54
Commercially pure titanium	0.0956 - 0.213
Commercially pure zinc	0.239 - 0.706
Copper	0.144 - 1.79
Dough (Bulk) molding compound, DMC (BMC), polyester matrix	0.0699 - 0.187
Epoxies (EP)	0.00768 - 0.0449
GFRP, epoxy matrix (isotropic)	0.0466 - 0.164
Gold	0.214 - 0.386
High carbon steel	0.035 - 0.154
Ionomer (I)	0.0944 - 0.315
Lead alloys	0.407 - 1.89
Low alloy steel	0.0174 - 0.269
Low carbon steel	0.124 - 0.274
Medium carbon steel	0.0218 - 0.184
Nickel	0.104 - 1.34
Nickel-based superalloys	0.044 - 0.285
Nickel-chromium alloys	0.189 - 0.277
Non age-hardening wrought Al-alloys	0.115 - 1.11
Phenolics (PH)	0.0186 - 0.0374
Polyamides (Nylons, PA)	0.0301 - 0.0872
Polycarbonate (PC)	0.0325 - 0.072
Polyester (UP)	0.0294 - 0.0474
Polyetheretherketone (PEEK)	0.0328 - 0.0579
Polyethylene (PE)	0.0536 - 0.089
Polyethylene terephthalate (PET)	0.0751 - 0.0936
Polyhydroxyalkanoates (PHA, PHB)	0.0186 - 0.0323
Polylactide (PLA)	0.0465 - 0.0815
Polymethyl methacrylate (Acrylic, PMMA)	0.011 - 0.0261
Polyoxymethylene (Acetal, POM)	0.0281 - 0.0727
Polypropylene (PP)	0.094 - 0.186
Polystyrene (PS)	0.0148 - 0.0322
Polytetrafluoroethylene (Teflon, PTFE)	0.0594 - 0.106
Polyurethane (tpPUR)	0.0391 - 0.108
Polyvinylchloride (tpPVC)	0.0336 - 0.121
Sheet molding compound, SMC, polyester matrix	0.0706 - 0.204
Silver	0.153 - 0.275
Stainless steel	0.0925 - 0.592
Starch-based thermoplastics (TPS)	0.041 - 0.072
Tin	1.28 - 3.36
Titanium alloys	0.0505 - 0.0847
Tungsten alloys	0.0674 - 0.106
Wrought magnesium alloys	0.0353 - 0.13
Zinc die-casting alloys	0.0444 - 0.438

Pressure Vessel - All Stages

Name	Specific Strength (MJ/kg)
Acrylonitrile butadiene styrene (ABS)	0.0167 - 0.0463
Age-hardening wrought Al-alloys	0.0353 - 0.227
Aluminum/Silicon carbide composite	0.0997 - 0.118
Brass	0.0116 - 0.0609
Bronze	0.0114 - 0.0572
Cast Al-alloys	0.0186 - 0.123
Cast iron, ductile (nodular)	0.035 - 0.0951
Cast iron, gray	0.0196 - 0.0588
Cast magnesium alloys	0.0387 - 0.119
Cellulose polymers (CA)	0.0216 - 0.0408
CFRP, epoxy matrix (isotropic)	0.355 - 0.678
Commercially pure lead	3.52e-4 - 0.00106
Commercially pure titanium	0.0599 - 0.133
Commercially pure zinc	0.0105 - 0.0232
Copper	0.00336 - 0.0392
Dough (Bulk) molding compound, DMC (BMC), polyester matrix	0.0128 - 0.0284
Epoxies (EP)	0.0285 - 0.0582
GFRP, epoxy matrix (isotropic)	0.059 - 0.104
Gold	0.00853 - 0.0106
High carbon steel	0.051 - 0.147
Ionomer (I)	0.00875 - 0.0168
Lead alloys	9.09e-4 - 0.00366
Low alloy steel	0.051 - 0.191
Low carbon steel	0.0318 - 0.0503
Medium carbon steel	0.0389 - 0.115
Nickel	0.00787 - 0.101
Nickel-based superalloys	0.0366 - 0.232
Nickel-chromium alloys	0.0434 - 0.0548
Non age-hardening wrought Al-alloys	0.0111 - 0.106
Phenolics (PH)	0.0215 - 0.0389
Polyamides (Nylons, PA)	0.0442 - 0.0839
Polycarbonate (PC)	0.05 - 0.0599
Polyester (UP)	0.0253 - 0.0358
Polyetheretherketone (PEEK)	0.0496 - 0.0725
Polyethylene (PE)	0.0188 - 0.0305
Polyethylene terephthalate (PET)	0.0414 - 0.047
Polyhydroxyalkanoates (PHA, PHB)	0.0282 - 0.0323
Polylactide (PLA)	0.0444 - 0.0581
Polymethyl methacrylate (Acrylic, PMMA)	0.0451 - 0.061
Polyoxymethylene (Acetal, POM)	0.0345 - 0.0514
Polypropylene (PP)	0.023 - 0.0413
Polystyrene (PS)	0.0275 - 0.0538
Polytetrafluoroethylene (Teflon, PTFE)	0.00691 - 0.0115
Polyurethane (tpPUR)	0.0337 - 0.046
Polyvinylchloride (tpPVC)	0.0242 - 0.0371
Sheet molding compound, SMC, polyester matrix	0.0263 - 0.0476
Silver	0.018 - 0.0284
Stainless steel	0.0217 - 0.127
Starch-based thermoplastics (TPS)	0.0126 - 0.0173
Tin	9.64e-4 - 0.00206
Titanium alloys	0.163 - 0.262
Tungsten alloys	0.028 - 0.043
Wrought magnesium alloys	0.0669 - 0.241
Zinc die-casting alloys	0.0135 - 0.0769

Helical Spring - All Stages

Name	Resilience (per unit volume) (kJ/m^3)
Age-hardening wrought Al-alloys	122 - 5.05e3
Aluminum/Silicon carbide composite	845 - 1.2e3
Brass	90.7 - 2.51e3
Bronze	116 - 2.92e3
Cast Al-alloys	31.2 - 1.36e3
Cast iron, ductile (nodular)	363 - 2.68e3
Cast iron, gray	185 - 1.69e3
Cast magnesium alloys	110 - 1.04e3
CFRP, epoxy matrix (isotropic)	2.8e3 - 1.15e4
Commercially pure lead	1.15 - 10.3
Commercially pure titanium	711 - 3.51e3
Commercially pure zinc	57.2 - 281
Copper	6.99 - 952
Dough (Bulk) molding compound, DMC (BMC), polyester matrix	48.2 - 234
GFRP, epoxy matrix (isotropic)	563 - 1.89e3
Gold	344 - 533
High carbon steel	771 - 6.43e3
Lead alloys	5.44 - 87.3
Low alloy steel	759 - 1.07e4
Low carbon steel	301 - 753
Medium carbon steel	448 - 3.9e3
Nickel	24 - 3.96e3
Nickel-based superalloys	469 - 1.89e4
Nickel-chromium alloys	633 - 1.01e3
Non age-hardening wrought Al-alloys	12.9 - 1.17e3
Sheet molding compound, SMC, polyester matrix	218 - 737
Silver	508 - 1.27e3
Stainless steel	145 - 5.02e3
Tin	1.14 - 5.24
Titanium alloys	4.89e3 - 1.25e4
Tungsten alloys	797 - 1.88e3
Wrought magnesium alloys	298 - 3.78e3
Zinc die-casting alloys	77.5 - 2.46e3

Helical Spring - All Stages

Name	Toughness (kJ/m^2)
Age-hardening wrought Al-alloys	5.96 - 16.7
Aluminum/Silicon carbide composite	2.48 - 6.44
Brass	9.02 - 36.3
Bronze	6.67 - 42.3
Cast Al-alloys	4.03 - 15.4
Cast iron, ductile (nodular)	2.81 - 16.9
Cast iron, gray	0.938 - 5.56
Cast magnesium alloys	3.23 - 7.31
CFRP, epoxy matrix (isotropic)	0.363 - 3.99
Commercially pure lead	1.79 - 16.1
Commercially pure titanium	29.4 - 35.2
Commercially pure zinc	9.16 - 50
Copper	6.98 - 63
Dough (Bulk) molding compound, DMC (BMC), polyester matrix	0.693 - 2.78
GFRP, epoxy matrix (isotropic)	2.37 - 26
Gold	20.3 - 62.1
High carbon steel	3.52 - 40.8
Lead alloys	6.71 - 42.2
Low alloy steel	0.929 - 190
Low carbon steel	8.1 - 32.4
Medium carbon steel	0.693 - 40.7
Nickel	31.1 - 59.5
Nickel-based superalloys	21.4 - 65.1
Nickel-chromium alloys	30.4 - 57.8
Non age-hardening wrought Al-alloys	9.66 - 25.2
Sheet molding compound, SMC, polyester matrix	2.21 - 15.2
Silver	22.5 - 50.8
Stainless steel	19.3 - 113
Tin	5.24 - 21
Titanium alloys	26.3 - 42.8
Tungsten alloys	7.12 - 10.7
Wrought magnesium alloys	3.23 - 7.31
Zinc die-casting alloys	1.21 - 59.5

B

MATLAB and Simulink Files

In this appendix, the codes used in Chapter 5 are provided, in alphabetical order.

```
% ==========================================================================
% BEGINNING OF FILE
% ==========================================================================
% FILENAME:  BoltStress.m
% PURPOSE:  Estimate size and material of LT-B interface bolts
% ==========================================================================

%% Load external data

load OC               % Operational conditions from Requirements Section
C = 0.25;             % Approach for load distribution from P.N.Childs -
                      % Machine element design handbook
x = (5:1:15)*1e-3;    % Tank internal radius for load estimation

for i = 1:length(x)
    xR(i) = x(i)*100;
    Radius(i) = strcat('R= ', {num2str(xR(i))}, 'cm');
end


%% Materials

Grade.Placeholder = 1:6;
```

```
Grade.Name = {4.8 5.8 8.8 9.8 12.9 'A4-70'};
Grade.Sp = [310 380 580 650 970 382.5];     % Proof strength in MPa
Grade.Sy = [340 400 640 720 1020 450];      % Yield strength in MPa

%% Geometry
Size.Placeholder = 1:4;
Size.Name = {'M2' 'M2.5' 'M3' 'M4'};
Size.StressArea = [2.07 3.39 5.03 8.78]*1e-6; % In SI

%% Calculations

Stress.Mat = 0.75.*Grade.Sp;

for i = 1:length(Size.Placeholder)
    Stress.Geom(i,:) = 0.25*pi/4*OC.Pmax/Size.StressArea(i).*x.^2/1e6;
end

Stress.Sum = Stress.Mat + max(max(Stress.Geom));
Ns = Grade.Sy./Stress.Sum;                   % Yield safety factor

%% Figures
% figure(1)
%       plot(Grade.Placeholder,Stress.Mat,'-o'),grid on
%       xlabel('Material Property Class')
%       ylabel('Pre-tension Stress [MPa]')
%
%       xticks(Grade.Placeholder)
%       xticklabels(Grade.Name)
%       saveas(gcf, 'StressMat.png')
%
% figure(2)
%       plot(Size.Placeholder,Stress.Geom,'-o'),grid on
%       xlabel('Bolt Size')
%       ylabel('External Load Stress [MPa]')
%       legend(Radius)
%
%       xticks(Size.Placeholder)
%       xticklabels(Size.Name)
%       saveas(gcf,'StressGeom.png')

% ======================================================================
% END OF FILE
% ======================================================================
```

```
% ==========================================================================
% BEGINNING OF FILE
% ==========================================================================
% FILENAME:  CoilOpt.m
% PURPOSE:  Define the geometry of a helical spring
% ==========================================================================

%% Initialize
clear;clc
global OC Steel W R Lin Xabs N

%% External data

load OC
load Mat Steel

W = 1.0;     % Objective tuning factor
             % Prop. Capacity:1 <-------------------> 0:Spring Mass

Lin = 18;     % Tank length, minus 2 mm for lids
N = 7;        % Number of springs
R = sqrt(10584/pi/(Lin+2)) -1;    % Tank radius, minus 1 mm for shell


%% Problem setup for fmincon solver

Xabs = [5 2*R 16 10];                      % Max absolute bounds for [d D Na p]
x0 = [0.5 0.5 0.5 0.5];                 % Initial fraction values
lb = [0.1, 0.1, 0.125, 0.1];               % Lower bound
ub = [1.0, 1.0, 1.0, 1.0];                 % Upper bound

options = optimoptions(@fmincon,'Algorithm','sqp',...
        'MaxFunctionEvaluations',100,'display','iter');
[x,Obj] = fmincon(@O,x0,[],[],[],[],lb,ub,@nonlincon,options);

%% Optimization functions

function [DispAux] = Aux(x)
        global OC R Steel Xabs N

        xr = x.*Xabs;

        C = xr(2)/xr(1);                            % Spring index
        B = 1 + 5/(4*C-3);                          % Bergstrasser factor
        F = OC.Pmax*pi*(R/1000)^2;                  % Pressure force, in N

        Ks = Steel.G*xr(1)/1e3/(8*C^3*xr(3));       % Spring stiffness, in N/m
        y = F/Ks/N;                                 % Deflection, in m

        tau = B*8*C/pi*F/N/(xr(1)/1000)^2;          % Shear stress, in Pa

        DispAux.B = B;
        DispAux.C = C;
```

```
        DispAux.Ks = Ks;
        DispAux.tau = tau;
        DispAux.y = y*1000;

end

function [Obj,DispAux] = O(x)
        global Steel R W Xabs N

        DispAux = Aux(x);
        xr = x.*Xabs;

        O1 = -pi*R^2*DispAux.y/1000;          % Propellant capacity in cm^3/grams

        O2 = N*Steel.rho/1e6*(0.25*pi*xr(1)^2)*sqrt(pi^2*xr(2)^2+xr(4)^2)*(xr(3)
            +2) +...
        Steel.rho/1e6*pi*R^2*0.5;         % Spring mass in grams

        Obj = W*O1+(1-W)*O2;

        %  DispO.Mprop = -O1;
        %  DispO.Mspring = O2;
        %  disp(DispO)
end

function [c,ceq] = nonlincon(x)
        global Steel R Lin Xabs N

        xr = x.*Xabs;
        DispAux = Aux(x);

        load Pack.mat Pack % Packing factor from:
              % https://en.wikipedia.org/wiki/Circle_packing_in_a_circle

        PackN= Pack(N);
        ceq = [];

        c1 = (DispAux.C+1)*xr(1)/2/R -1;                       % Radius constraint
        c2 = (xr(3)*xr(4)+2*xr(1)+0.5)/(Lin-0.5) -1.001;       % Length const.
        c3 = xr(3)*(xr(1)-xr(4))/DispAux.y +1;                 % Coil overlap const.
        c4 = 2*DispAux.tau/Steel.su -1;                        % Stress const.
        c5 = DispAux.C/12 - 1;                                 % Max index const.
        c6 = 1-DispAux.C/4;                                    % Min index const.
        c7 = N/4*(DispAux.C+1)^2*(xr(1)/R)^2 - 0.95*PackN;     % Packing const.

        c = [c1;c2;c3;c4;c5;c6;c7];

        %DispC.RadCon = c1;
        %DispC.LenCon = c2;
        %DispC.OVerCon = c3;
        %DispC.Stress = c4;
        %DispC.MaxIdx = c5;
        %DispC.MinIdx = c6;
```

```
        %DispC.Packing = c7;

        %DispC.ceq = ceq;

        % disp(DispAux)
        % disp(DispC)
        % disp(xr)
end

% ========================================================================
% END OF FILE
% ========================================================================
```

```
% =========================================================================
% BEGINNING OF FILE
% =========================================================================
% FILENAME: SizeTank.m
% PURPOSE: Estimate the mass and volume footpring of the tank
% =========================================================================

%% Load External Data

global V Alum OC
load Mat Alum        % Material designation
load OC              % Operating Conditions


%% Calculations

V = 10584;           % Total volume from Requirement 1.2, in mm3
L = 10:0.2:35;       % Tank internal length (hollow), in mm
t0 = 1;              % Trial thickness, in mm

[t,R] = Pressure(L,t0); % Ignores manufacturing limit

[Vshell, Vin, Mshell] = Envelope(R,L,t); % Envelope properties
Ds = 2*R;
save Sizes Ds L Mshell

%% Figures

% figure(100)
% filename = ['Dimensions_t ' num2str(t0) '.png'];
%      yyaxis left
%      plot(L,R), grid on
%      ylabel('Tank Radius (mm)')
%
%      yyaxis right
%      plot(L,Vin)
%      ylabel('Internal Volume (mm^3)')
%
%      xlabel('Tank Length(mm)')
% %saveas(gcf, filename)
%
% figure(200)
% filename = ['Shell_t ' num2str(t0) '.png'];
%      yyaxis left
%      plot(L,Vshell), grid on
%      ylabel('Shell Volume (mm^3)')
%
%      yyaxis right
%      plot(L,Mshell)
%      ylabel('Shell Mass (g)')
%
%      xlabel('Tank Length(mm)')
%saveas(gcf, filename)
```

```matlab
%% Functions

function [y,R] = Pressure(x,y0)

        global V Alum OC

        yold = y0;
        err = 1;

        while err > 0.05
                R = sqrt(V./pi./x)- yold;
                ytemp = OC.Pmax * OC.FoSu/Alum.sy .* R;  % in mm

                err = abs(ytemp/yold - 1);
                if err <= 0.05
                        yn = ytemp;
                        break
                else
                        yold = ytemp;
                end
        end

        y = max(yn,y0);
        R = sqrt(V/pi./x) - y;
end

function [Vshell,Vin, Mshell] = Envelope(x1,x2,x3)

        global Alum

        Vex = pi*(x1 + x3).^2.*x2;
        Vin = pi*x1.^2.*(x2-2*x3);

        Vshell = Vex - Vin;
        Mshell = Alum.rho/1e6*Vshell;
end

% ==========================================================================
% END OF FILE
% ==========================================================================
```

```
% ===========================================================================
% BEGINNING OF FILE
% ===========================================================================
% FILENAME: Support.m
% PURPOSE: Structural response of TM-D-S supports
% ===========================================================================

%% Load External Data
load Mat Alum                              % Material designation

%% Constants
q = -5*9.80665*0.45/0.036/sqrt(2);         % Load per unit length
L = 0.0075;                                % Section AB length
Lx = 0;                                    % Point of Interest (w.r.t L)
E = Alum.E;

%% Beam Variables
b = 6e-3;          % Beam width
h = 2e-3;          % Beam height
I = 1/12*(b*h^3);
c = (h/2);

%% Outputs
% d represents the distributed load
% d2 represents the distributed + concentrated load

u = 0:0.01:1;    % Normalized length position

% Load Profile
f4.Mag = q/(E*I);
f4.d = ones(1,length(u));

% Shear Profile
f3.Mag = f4.Mag*L;
f3.d = (u-1);
f3.d2 = (u-1-Lx);
f3.B = f4.Mag*(L*Lx);

% Curvature Profile
f2.Mag = q*L^2/6/(E*I);
f2.d = (3*u.^2-6.*u+2);
f2.d2 = (3*u.^2-6*(1-Lx).*u+(2+3*Lx^2));
f2.B = q*L^2*Lx^2/2/(E*I);

% Slope Profile
f1.Mag = q*L^3/6/(E*I);
f1.d = u.*(u-1).*(u-2);
f1.d2 = u.*(u.^2-3*(1-Lx).*u+(2+3*Lx^2));
f1.B = q*(L*Lx)^3/6/(E*I);

% Deflection Profile
f0.Mag = q*L^4/24/(E*I);
f0.d = u.^2.*(u-2).^2;
```

```
f0.d2 = u.^2.*(u.^2-4*(1-Lx)*u+2*(2+3*Lx^2));
f0.B = q*(L*Lx)^4/24/(E*I);

%% Boundary calculations

Stress.Point1 = -E*c*f2.Mag*f2.d2(end)/10^6;
Stress.Point0 = -E*c*f2.Mag*f2.d2(1)/10^6;
DeflectB = f0.Mag*f0.d2(end)*10^6;          % Deflection at point B

%% Figures

% figure(1)   % Deflection
% plot(u.*L, f0.Mag*f0.d)
% hold on
% plot(u.*L, f0.Mag*f0.d2)
% hold off
% xlabel('Beam Position [m]')
% ylabel('Beam Deflection [m]')
% legend('Dist. load','Dist. + Conc. load','Location','best')
%
% figure(2)   % Angle
% plot(u.*L, f1.Mag*f1.d)
% hold on
% plot(u.*L, f1.Mag*f1.d2)
% hold off
% xlabel('Beam Position [m]')
% ylabel('Beam Slope [rad]')
% legend('Dist. load','Dist. + Conc. load','Location','north')
%
% figure(3)   % Curvature
% plot(u.*L, f2.Mag*f2.d);
% hold on
% plot(u.*L, f2.Mag*f2.d2)
% hold off
% xlabel('Beam Position [m]')
% ylabel('Beam Curvature [rad/m]')
% legend('Dist. load','Dist. + Conc. load','Location','northwest')
%
% figure(4)   % Shear Force
% plot(u.*L, f3.Mag*E*I*f3.d)
% hold on
% plot(u.*L, f3.Mag*E*I*f3.d2)
% hold off
% xlabel('Beam Position [m]')
% ylabel('Shear Force [N]')
% legend('Dist. load','Dist. + Conc. load','Location','northeast')
%
% figure(5)   % Distributed Load
% plot(u.*L, f4.Mag*E*I*f4.d)
% xlabel('Beam Position [m]')
% ylabel('Load Magnitude [N/m]')
%legend('Dist. load','Dist. + Conc. load','Location','best')
```

```
% ==========================================================================
% END OF FILE
% ==========================================================================
```

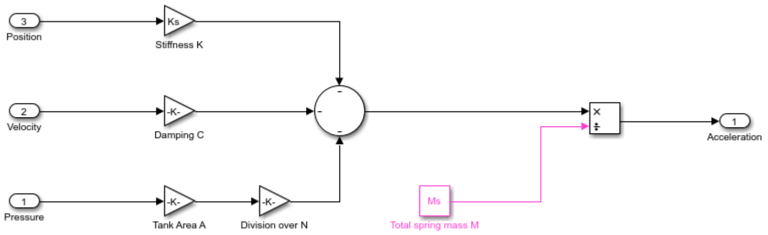

Figure B.1: A Simulink schematic of the spring solver. Based on Equation 5.7.1

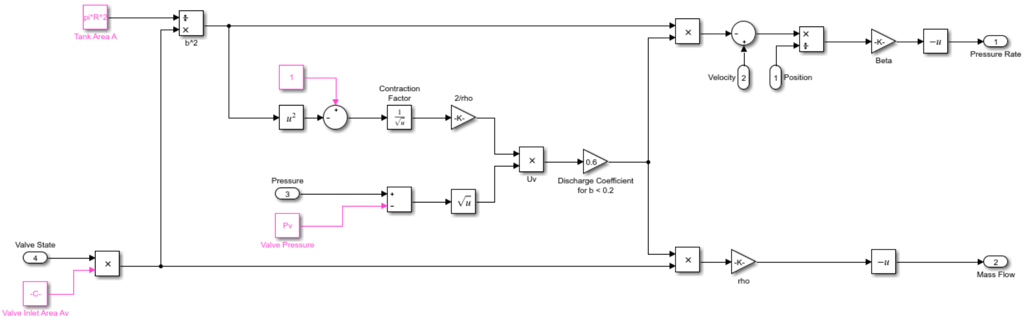

Figure B.2: A Simulink schematic of the fluid solver. Based on Equation 5.7.8

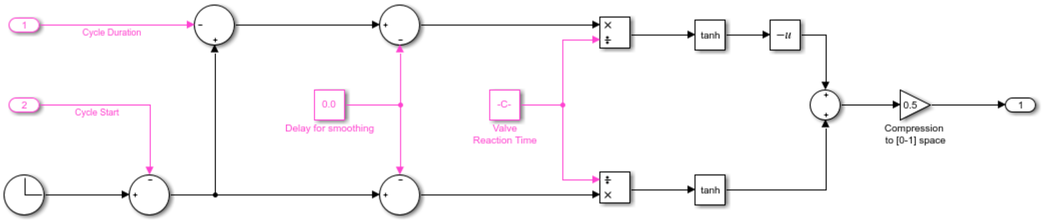

Figure B.3: A Simulink schematic of the valve controller. Based on Equation 5.7.3

C

Spring Properties Charts

U

Option B: multi-spring tank w. SFx configuration

Results not rounded to manufacturing wire dimensions

95% of Packing Factor covered

Lin	18
Vtot	10584

N	1	2	3	4	5	6	7	8	9	10
Pack Factor	1	0.5	0.6466	0.6864	0.6854	0.6666	0.7777	0.7328	0.6895	0.6878
d	2.9297	1.8727	1.5912	1.3909	1.2438	1.1305	1.0772	0.9936	0.9279	0.88
C	6.7851	5.2345	5.8131	5.9545	5.951	5.8849	6.2592	6.1126	5.9653	5.9594
Na	2	4.7261	5.2893	6.0821	6.9412	7.8337	7.8408	8.7498	9.673	10.2722
K	42756	25190	13963	9876.1	7752	6456.1	5084.5	4553.6	4120.4	3690.4
X	5.799	4.9213	5.9189	6.2761	6.3967	6.4006	6.9662	6.8361	6.6859	6.7184
Mprop,tot	2.61	2.2185	2.6682	2.8292	2.8836	2.8853	3.1403	3.0817	3.014	3.0286
Mspring,tot	15.18	10.8632	11.8363	11.9514	11.8319	11.6309	12.2156	11.9063	11.6123	11.5656
M*	**0.1719**	**0.2042**	**0.2254**	**0.2367**	**0.2437**	**0.2481**	**0.2571**	**0.2588**	**0.2596**	**0.2619**
ΔM* (%)	-	18.78	10.38	5.01	2.95	1.79	3.63	0.68	0.28	0.89

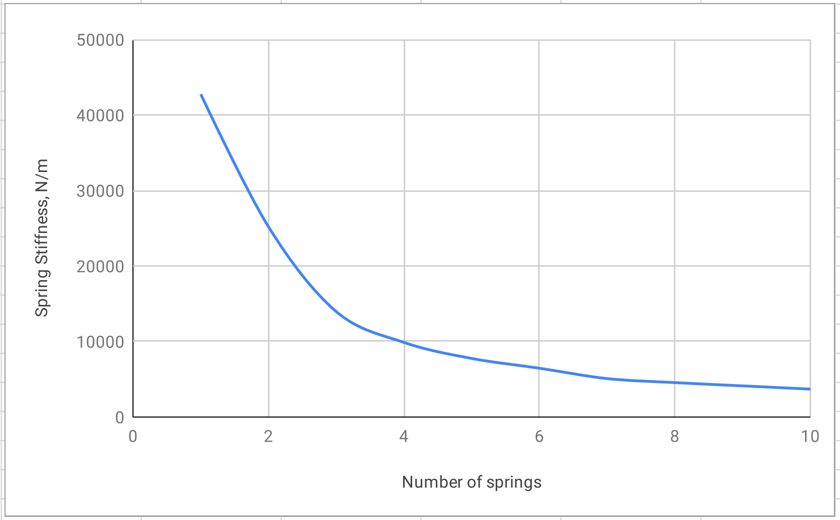

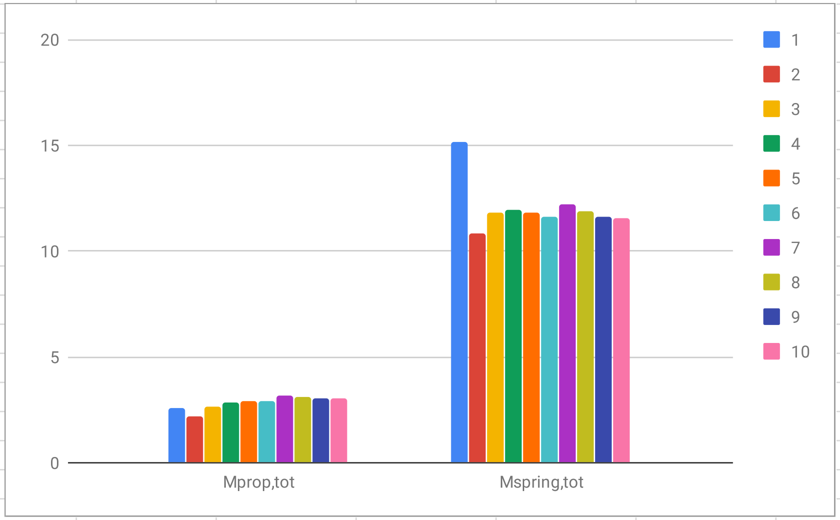

Option A: multi-compartment tank w. Vtank = Vtotal /N

Results not rounded to manufacturing wire dimensions

Lin	18
Vtot	10584

N	1	2	3	4	5	6	7	8	9	10
R	11.97	8.1774	6.4933	5.4894	4.8043	4.2986	3.9055	3.5587	3.3263	3.1043
C	6.7851	7.0511	7.0511	7.0511	7.0511	7.0511	7.0511	7.0511	7.0511	7.0511
Na	2	3.1896	4.266	5.223	6.1052	6.9368	7.7318	8.5	9.246	9.9761
K	42756	16564	9832.6	6790.3	5084.1	4003.6	3263.5	2727.9	2324.3	2010.4
X	5.799	6.9756	7.4093	7.668	7.8444	7.9746	8.076	8.1575	8.2251	8.2823
Mprop	2.61	1.4654	0.9814	0.7266	0.5688	0.4629	0.387	0.3301	0.2859	0.2507
Mprop,tot	2.61	2.9308	2.9442	2.9064	2.844	2.7774	2.709	2.6408	2.5731	2.507
Mspring	15.18	6.8523	4.1643	2.9097	2.1939	1.7358	1.4197	1.1897	1.0157	0.88
Mspring,tot	15.18	13.7046	12.4929	11.6388	10.9695	10.4148	9.9379	9.5176	9.1413	8.8
M*	**0.1719**	**0.2139**	**0.2357**	**0.2497**	**0.2593**	**0.2667**	**0.2726**	**0.2775**	**0.2815**	**0.2849**
ΔM* (%)	-	24.38	10.20	5.96	3.82	2.86	2.22	1.79	1.45	1.21